

UNIVERSITY OF LEEDS

DOCTORAL THESIS

Rationally Designed DNA Origami Carriers for
Quantitative Single Molecule Detection with Nanopipettes

by

Mukhil Raveendran

With the guidance of

Prof. Christoph Wälti and Dr. Paolo Actis

A thesis submitted in accordance with the requirements for the degree of

Doctor of Philosophy

The Pollard Institute

School of Electronic and Electrical Engineering

February 2020

DECLARATION

The candidate confirms that the work submitted is her own, except where work which has formed part of jointly authored publications has been included. The contribution of the candidate and the other authors to this work has been explicitly indicated below. The candidate confirms that appropriate credit has been given within the thesis where reference has been made to the work of others.

- **Chapter 7** contains materials published by the candidate and co–authors A. J. Lee, C. Wälti and P Actis. The work was conducted by the candidate with contributions from A. J. Lee for the design and assembly of DNA origami. C. Wälti and P. Actis are the candidate’s primary and secondary supervisors.

Publication: *M. Raveendran, P. Actis, A. J. Lee, and C. Walti, “Analysis of 2D DNA Origami with Nanopipettes,” Chemelectrochem, vol. 5, pp. 3014–3020, 2018.*

- **Chapter 8 and 9** contains materials that have been submitted for publication by the candidate and co–authors A. J. Lee, R. Sharma, C. Wälti and P. Actis. The work was conducted by the candidate with contributions from Dr. A.J. Lee for the design of DNA nanostructures, SPR studies included in the study are contributions of Dr. R. Sharma. C. Wälti and P. Actis are the candidate’s primary and secondary supervisors.

This copy has been supplied on the understanding that it is copyright material and that no quotation from the thesis may be published without proper acknowledgement

In Loving Memory of my Grandma
"Chellam paati"

A beautiful soul who painted my world full of colours

Abstract

The ability to detect small concentrations of biomarkers in patient samples is one of the cornerstones of modern healthcare. In general, biosensing approaches employed to address this need are based on measuring signals resulting from the interaction of a large ensemble of molecules with the sensor. Here, a biosensor platform using DNA origami, featuring a central cavity with a target-specific DNA aptamer, as carriers for translocation through nanopores which enables individual biomarkers to be identified and counted to compile a sensing signal is reported.

It is shown that the modulation of the ion current through the nanopore upon the DNA origami translocation strongly depends on the presence and in fact the size of a central cavity. While DNA origami without a central cavity cause a single peak in the ion current, DNA origami of the same dimensions but featuring a central cavity lead to double peaks in the ion current. This is also true for DNA origami (with and without central cavities) made of similar sized DNA but of different dimensions. It is also observed that the peak characteristics, peak amplitude and the dwell time, are different depending on the presence or absence of a central cavity.

This work exploits these parameters to generate a biosensing platform capable of detecting human C-reactive protein (CRP) in clinically relevant fluids. DNA origami frames with cavities large enough to lead to clear ion current double peaks were designed and a CRP-specific DNA aptamer was introduced into the cavity. Also, upon binding of CRP, the ion current peak changes to a single peak and the peak characteristics change.

Using this three-parameter classification, CRP-occupied and unoccupied carriers can be distinguished when they translocate through the nanopore. Thus CRP biosensing by computing the ratio of occupied vs total number of frames with a limit of detection of 3 nM is successfully demonstrated.

”The noblest pleasure is the joy of understanding”

- Leonardo da Vinci

*”There’s no such thing as perfect writing, just like
there’s no such thing as perfect despair” - Haruki Murakami*

To my Little Brother

&

My Dad, for showing me self-respect and hard work never goes amiss

My Mom, for being my constant hope and inspiration

My not so little Brother, for always setting the bar high

My Sister and Brother-in-law, for being my home away from home

My Aunts and Uncles for their tireless smiles and encouragement

My Partner, for standing by me come hell or high water

Acknowledgements

I express my sincere gratitude to Prof. Christoph Wälti and Dr. Paolo Actis, for without their direction, constant encouragement, forbearance and continued support, this project would not have been achievable. They went out of their way to motivate and guide me, every step of this PhD.

I extend my appreciation to Dr. Andrew Lee (Andy) and Dr. Rajan Sharma for their help, advice and input to this work. They are a wealth of knowledge and experience I had the fortune to befriend.

Also, I would like to thank Prof. Joshua B. Edel (Imperial College, London) for generously providing and assisting with the MATLAB script and Dr. Mark Rosamond for his support and training with SEM imaging. Further, I would like to acknowledge University of Leeds for the financial support via the Leeds Annual Research Scholarship (LARS)–PhD scholarship.

Special mention to Andy for the numerous coffee breaks and chats which kept me sane and functional throughout this PhD. And to all my friends across the globe and back home, for without them the past few years would have been dull and lonely.

Contents

Declaration	iii
Abstract	vii
Dedication	ix
Acknowledgements	xi
Contents	xiii
List of figures	xix
List of tables	xxv
1 Introduction	1
1.1 Thesis Aim	5
1.2 Outline of Chapters	6
2 Introduction to DNA and DNA Nanotechnology	9
2.1 Deoxyribonucleic acid	10
2.1.1 Structure of nucleic acid	11
2.1.2 Double helical structure–base pairing and stacking	13
2.2 DNA as building blocks	16
2.2.1 Branched structures and DNA motifs	18

2.3	DNA origami technique	20
2.4	Overview of aptamers	23
2.5	Conclusion	24
3	Introduction to Nanopores and Nanopipettes	27
3.1	Types of nanopores	28
3.1.1	Biological nanopores	29
3.1.2	Solid state nanopores	32
3.1.3	Hybrid nanopores	36
3.2	Nanopipettes	41
3.2.1	Introduction	41
3.2.2	Fabrication of nanopipettes	44
3.3	Properties of nanopipettes	46
3.3.1	Surface charge and diffuse double layer	46
3.4	Surface charge and conductance in nanopipettes	47
3.5	Electroosmosis and electrophoretic forces in a nanopipette	49
3.6	Conclusion	51
4	Review of Literature	53
4.1	Nanopores for single molecule analysis	54
4.2	Carriers for protein detection	60
4.2.1	Qualitative detection	60
4.2.2	Quantitative detection using carriers	64
4.3	DNA nanostructures in nanopore research	67

5	Methods and Materials	69
5.1	Materials	69
5.1.1	Protein and chemicals	69
5.2	Methods and techniques	70
5.2.1	DNA restriction and ligation	70
5.2.2	Polymerase chain reaction	71
5.2.3	DNA purification and quantification	73
5.2.4	DNA origami purification	73
5.2.5	Gel electrophoresis	74
5.2.6	Electrophoretic mobility shift assay	75
5.2.7	Cloning protocol	76
5.2.8	Phage transformation and expression	77
5.2.9	Chemical transformation	79
5.2.10	Miniprep protocol	79
5.2.11	DNA origami design and folding	79
5.2.12	Insertion of aptamer sequences	81
5.2.13	Sample preparation and AFM imaging in fluid	82
5.3	Nanopipette fabrication	82
5.3.1	Ion current measurements	83
5.3.2	Data analysis	84
5.4	Surface plasmon resonance	85

6	Characterisation of Nanopipettes	87
6.1	Introduction	87
6.2	Nanopipette geometry	89
6.2.1	SEM measurement	89
6.2.2	IV measurements	90
6.3	Nanopipette properties	93
6.3.1	Ion-current rectification	93
6.3.2	Ion-current conductance during DNA translocation	94
6.4	Ion-current measurements	97
6.5	Conclusion	100
7	Single Molecule Analysis with Nanopipettes	103
7.1	Introduction	103
7.2	2D DNA origami analysis	104
7.2.1	Differentiating 2D DNA origami	107
7.2.2	Frame origami Ion current signature	109
7.2.3	Double peak analysis	112
7.3	Conclusion	114
8	Double Peak Analysis using Concentric Squares	117
8.1	Introduction	117
8.2	Custom scaffold production	118
8.2.1	Scaffold assembly	120

8.2.2	Scaffold routing	123
8.3	Nanopipette translocation Experiments	125
8.3.1	Relation between double peak and cavity size	128
8.4	Conclusion	129
9	DNA Origami - Nanopipette Biosensor	131
9.1	Introduction	131
9.2	DNA origami as unique carriers	133
9.2.1	Aptamer selection	134
9.2.2	AFM and retarding gel electrophoresis	136
9.3	Nanopipette–DNA origami sensing system	138
9.3.1	Characterisation of peaks	141
9.3.2	Quantitative single molecule biosensing	143
9.3.3	Selectivity and specificity of the DNA carrier system	147
9.4	CRP detection in plasma	149
9.5	Conclusion	152
10	Conclusions and Future Developments	155
10.1	Conclusions	155
10.1.1	DNA origami as carriers	157
10.1.2	Quantitative sensing	157
10.2	Outlook and future developments	159
10.3	DNA origami barcode	159
10.3.1	Barcode assembly	160

Appendix	165
A Nanopipette pulling parameters	165
B DNA origami scaffold routing	169
C Appendix for chapter 7	179
D Appendix for chapter 8	182
E Appendix for chapter 9	189
F Appendix for chapter 10	208
Bibliography	209

List of figures

1.1	Introduction schematic	4
2.1	Central dogma of molecular biology	10
2.2	Nucleic acid chemistry	11
2.3	DNA phosphoester linkage	12
2.4	dsDNA hydrogen bonding	13
2.5	Base pairing	14
2.6	B-DNA structure	15
2.7	Schematics of sticky end hybridisation	17
2.8	Polyhedral structures	18
2.9	Schematics of crossover patterns	19
2.10	2D arrays via crossover motifs	20
2.11	DNA origami technique	21
2.12	3D DNA origami construction	23
3.1	Schematic of biological nanopore system	29
3.2	Different biological nanopores	30
3.3	Solid state nanopores via chemical etching	33

3.4	Nanopore sculpting techniques	35
3.5	Atomic layer deposition	36
3.6	Ion channel lipid bilayer on glass	37
3.7	DNA origami structures used in hybrid nanopores	38
3.8	DNA origami hybrid nanopore formation	39
3.9	Hybrid nanopore through DNA functionalisation	40
3.10	Glass nanopipettes	41
3.11	SEM images of nanopipette tip	42
3.12	Barber method of pulling micropipettes	43
3.13	Schematic of nanopipette fabrication	45
3.14	DDL: Gouy–Chapman–Stern model	47
3.15	Baseline current	50
4.1	Dwell time dependence on electrolyte	56
4.2	Biological and chemical modification of nanopores	58
4.3	dsDNA carrier molecules	61
4.4	Lambda DNA carrier	63
4.5	Quantitative sensing	65
4.6	Hybrid DNA construction using DNA nanoplates	67
5.1	Schematic of restriction and ligation	71
5.2	Polymerase chain reaction	72
5.3	DNA origami purification	74
5.4	Electrophoretic mobility shift assay	76

5.5	HiFi assembly of DNA fragments	77
5.6	DNA origami design	80
5.7	Data analysis	84
5.8	SPR	85
6.1	Schematic of nanopipette tip geometry	88
6.2	SEM micrographs of nanopipette tips	89
6.3	Pore size comparison by SEM and IV	90
6.4	Relation between pore resistance to pore size	92
6.5	I–V characteristics	94
6.6	Ion current trace of DNA sample	96
6.7	Linear and plasmid DNA detection	98
6.8	Effect of concentration and voltage	99
7.1	2D DNA origami translocation schematic	103
7.2	AFM image of 2D DNA origami structures	105
7.3	IV characteristics and SEM micrograph of ~100 nm nanopipettes	106
7.4	Ion current translocation for frames and tiles	108
7.5	Array of single and double peak ion current signatures	110
7.6	Frame DNA origami dwell time analysis	112
7.7	Double peak lag time Analysis	113
8.1	Concentric squares	118
8.2	Scaffold assembly	120

8.3	Gel electrophoresis	122
8.4	Design and routing of concentric squares	123
8.5	Concentric square–peak current and dwell time analysis	126
8.6	Concentric square–peak current signature	127
8.7	Concentric square–scatter plot	128
8.8	Double peak analysis for ConB and ConC	129
9.1	Schematic of the DNA origami–nanopipette sensing system	132
9.2	DNA origami carrier design	134
9.3	SPR analysis	135
9.4	Retarding gel electrophoresis for CRP bound carriers	137
9.5	Ion current signatures	139
9.6	Carrier molecule ion current analysis	140
9.7	Characterisation of carriers	142
9.8	Concentration dependent study	144
9.9	CRP binding study	145
9.10	CRP aptamer selectivity	147
9.11	Specificity studies with DNA origami carrier	148
9.12	Ion current traces of plasma sample	150
9.13	CRP detection in plasma	151
10.1	DNA origami barcode design	160
10.2	AFM images of DNA origami dimers and trimers	161
10.3	Data analysis for the barcode structure	162

10.4 Possible improvements	164
B.6 Tile 1 (T1)	170
B.7 Tile 2 (T2)	171
B.8 Frame 1 (F1)	172
B.9 Frame 2 (F2)	173
B.10 Concentric square A (ConA)	174
B.11 Concentric square B (ConB)	175
B.12 Concentric square C (ConC)	176
B.13 DNA nanostructure used as carrier	177
B.14 DNA origami anchor	178
C.15 F1 and F2 peak signature	180
C.16 T1 and T2 peak signature	180
C.17 Gel electrophoresis of frames and tiles	181
C.18 Pore resistance to pore size relation	181
D.19 Concentric square design map	183
D.20 Construction of concentric square B and C	184
D.21 Concentric square AFM images	185
D.22 ConA peak signature	186
D.23 ConB peak signature	186
D.24 ConC peak signature	187
D.25 Gel electrophoresis - Concentric squares	188
E.26 Binding buffer analysis	189

E.27 SPR trace aptamer 1	190
E.28 SPR trace aptamer 2	191
E.29 SPR traces aptamer with control	192
E.30 SEM image and IV curve	193
E.31 AFM image–DNA origami frame carrier	193
E.32 AFM images of CRP	194
E.33 Characterization of ion current peaks	195
E.34 Individual histogram data for carrier 1	196
E.35 Three–classification for carrier 1	197
E.36 Characteristics of disintergrated carriers	198
E.37 Characteristics of broken carriers	199
E.38 AFM images of CRP occupied carrier	200
E.39 Specificity study–AFM images	200
E.40 AFM image height sensor	201
E.41 Carrier characterization in plasma	201
E.42 AFM images for CRP occupied carrier 2	204
E.43 Characterization of carrier 2	204
E.44 Individual histogram data for carrier 2	205
E.45 Three–parameter classification for carrier 2	206
F.46 Individual histogram data for dimer and trimer	208

List of tables

5.1	Parameter for ~ 80 – 100 nm quartz	83
5.2	Parameter for ~ 100 nm quartz	83
1	parameter for ~ 20 – 30 nm quartz	165
2	parameter for ~ 10 – 20 nm quartz	166
3	parameter for ~ 250 – 280 nm borosilicate	166
4	parameter for ~ 150 – 200 nm borosilicate	167
5	Nanopipette pore size consistency	168
6	Peak count for frames and tiles	179
7	Peak count for concentric squares	188
8	Single peak count for carrier 1	194
9	Data for carrier 1	202
10	Single peak count for CRP spiked plasma	203
11	Data for CRP spiked plasma	203
12	Single peak count for carrier 2	207
13	Data for carrier 2	207
14	Peak count for dimer ConA and ConC	208

Acronyms

α -HL Alpha hemolysin pore.

AChE Acetylcholinesterase.

AeL Aerolysin.

ALD Atomic layer deposition.

AMP Adenosine 5- monophosphate.

BSA Bovine serum albumin.

ClyA Cytolysin A.

CRP C-reactive protein.

DDL Double diffuse layer.

DNA Deoxyribonucleic acid.

dNTPs Deoxynucleotide triphosphates.

dsDNA Double stranded Deoxyribonucleic acid.

DX Double crossover.

DX+J Double crossover with junction.

EBL Electron beam lithography.

EDTA Ethylenediaminetetraacetic acid.

ELISA Enzyme-linked Immunosorbent assay.

GFP Green fluorescent protein plasmid.

HPICM Hopping probe ion conductance microscopy.

IgG Immunoglobulin G.

IHL Inner helmholtz layer.

MD Molecular dynamics.

NSOM Near field scanning optical microscopy.

OHL Outer helmholtz layer.

OmpG Outer membrane protein G.

PCR Polymerase chain reaction.

PET poly(ethylene terephthalate).

PMMA Poly methyl methacrylate.

PNA Peptide nucleic acid.

PX Paranemic crossover.

RE II Restriction endonucleases type II.

RNA Ribonucleic acid.

SECM Scanning electrochemical microscope.

SELEX Systemic evolution of ligands by exponential enrichment.

SEM Scanning electron microscope.

Si silicon.

SICM Scanning ion conductance microscopy.

SPM Scanning probe microscope.

SPR Surface plasmon resonance.

ss single stranded.

ssDNA Single stranded Deoxyribonucleic acid.

STEM Scanning transmission electron microscope.

TAE Tris acetate EDTA.

TBE Tris borate EDTA.

TEM Transmission electron microscope.

TIR Total internal reflection.

Tm melting temperature.

TX Triple crossover.

Chapter 1

Introduction

Rapid and low–cost detection of disease biomarkers is becoming increasingly important in modern healthcare where a growing focus is placed on early diagnosis [1, 2, 3, 4, 5]. This presents considerable technological challenges as the relevant biomarkers are often only present at very small concentrations. Ideally, a diagnostic biosensor should be able to detect the presence of very few biomarkers in a small volume of a complex clinical sample.

The term biosensor first appeared in the 1960's to define enzyme electrodes with biocatalytic activity, and in 1962 Leyland C. Clark put forward the model of biosensor with an oxygen electrode for glucose measurement via electrochemical detection [6]. Since then, the concept has seen exponential growth particularly in medical and clinical science fields, with the advent of various types of biosensors (like immunosensors, Deoxyribonucleic acid (DNA) sensors, enzyme and tissue based sensor) and improvements in different detection techniques including optical and electrical methods [7].

However, despite the development of different sensing strategies, producing highly sensitive and selective yet simple devices for quantifying analytes remains one of the main objectives of the field. Techniques (like Enzyme–linked Immunosorbent assay (ELISA), colorimetric assays and electrochemical sensors) that explore the above objectives often

make use of ensemble methods where many biomolecules are averaged for target detection and quantification.

While ensemble techniques are valuable in a way that it reduces noise by averaging out any abnormal data, as such also becomes a handicap as there could be useful information hidden in the noise. Thus, single molecule techniques with the ability to analyse a heterogenous population one entity at a time allow us to understand better the complex larger picture of biological systems as well as functions of single molecule [8, 9, 10, 11, 12, 13, 14]. This also prevents any loss of information that could mask the relevance of that subpopulation of molecules.

From a biosensor point of view, single molecule resolution allows low concentration detection from a small sample volume, a sensitivity relevant for early stage disease diagnostics. In that regard, nanopore based biosensing for label free single molecule detection particularly using nanopipettes is one method that has received substantial attention.

Nanopipettes for biosensing:

The nanopipette technique is based on the principle of the Coulter counter or the resistive-pulse technique [15, 16], which involves charged sample molecules electrophoretically driven through a conical glass capillary (a process termed translocation) with a nanometer sized aperture. The experimental setup consists of a nanopipette filled with an electrolyte and immersed in an electrolyte chamber, a working electrode is inserted inside the nanopipette whereas a reference electrode also in contact with the electrolyte is grounded (figure 1.1).

Typically, nanopipette experiments can be conducted two ways, backward translocations where a nanopipette filled with the electrolyte solution contains the molecules of interest and upon application of voltage the molecules are pushed out through the nanopipette pore. Alternatively forward translocations, where the molecules of interest are in the electrolyte chamber and are pulled into the pore of the nanopipette. Either way, under an applied voltage, electrolyte ions and sample molecules translocate the nanopore. While

the ion flow through the nanopore is measured as the baseline current, single molecule capture, entry and translocations are characterised via the modulations in the otherwise steady current.

While substantial achievements have been accomplished with this technique (chapter 3, 4), there are chief setbacks including inefficient transport and low detection rate—as the speed of single entity translocations provides a weak signal especially when working with target protein molecule smaller than the nanopore size. Also, there remains significant difficulty in selectively detecting one particular analyte from a complex sample like blood, where thousands of similar sized background analytes are present in excess.

In response to this, a variety of strategies have been already implemented to slow down protein translocations and improve translocation rate through careful selection of electrolytes [17, 18], development of high bandwidth electronics [19, 20] or analyte modification [21].

Use of carrier to overcome setbacks:

More recently studies which examine the use of carrier molecules have also been explored for increased sensitivity and selectivity by attaching the target molecule onto a large carrier—antibody, nanoparticle, linear DNA, etc. Thus the fast travelling undetectable protein targets are effectively made visible to the nanopipette detection system. The use of a carrier also eliminates the need for any direct target labelling as the specificity can be incorporated via the carrier itself. In particular, long linear DNA with their complementarity and programmable nature is a usual carrier choice with advantages of functionalisation and as such have been repeatedly explored in different studies [22, 23, 24, 25, 26, 27] for protein detection and quantification.

However, the use of long linear DNA carrier is not without its limitations. Existing studies have shown that they are prone to forming knots and kinks [28] which are known to provide false positive signals during nanopore translocation. Moreover, notable variations in the signal depending on the translocation orientation and high blockage rates due to the passage of multiple DNA molecules through the nanopore [29, 30] have

been reported. Recent work to circumvent these problems involved combining single molecule fluorescence with nanopore detection to perform successful single molecule binding assays [27], the electro-optical system though elegant negates the key advantage of nanopore sensing, of having a simple electrical read-out system.

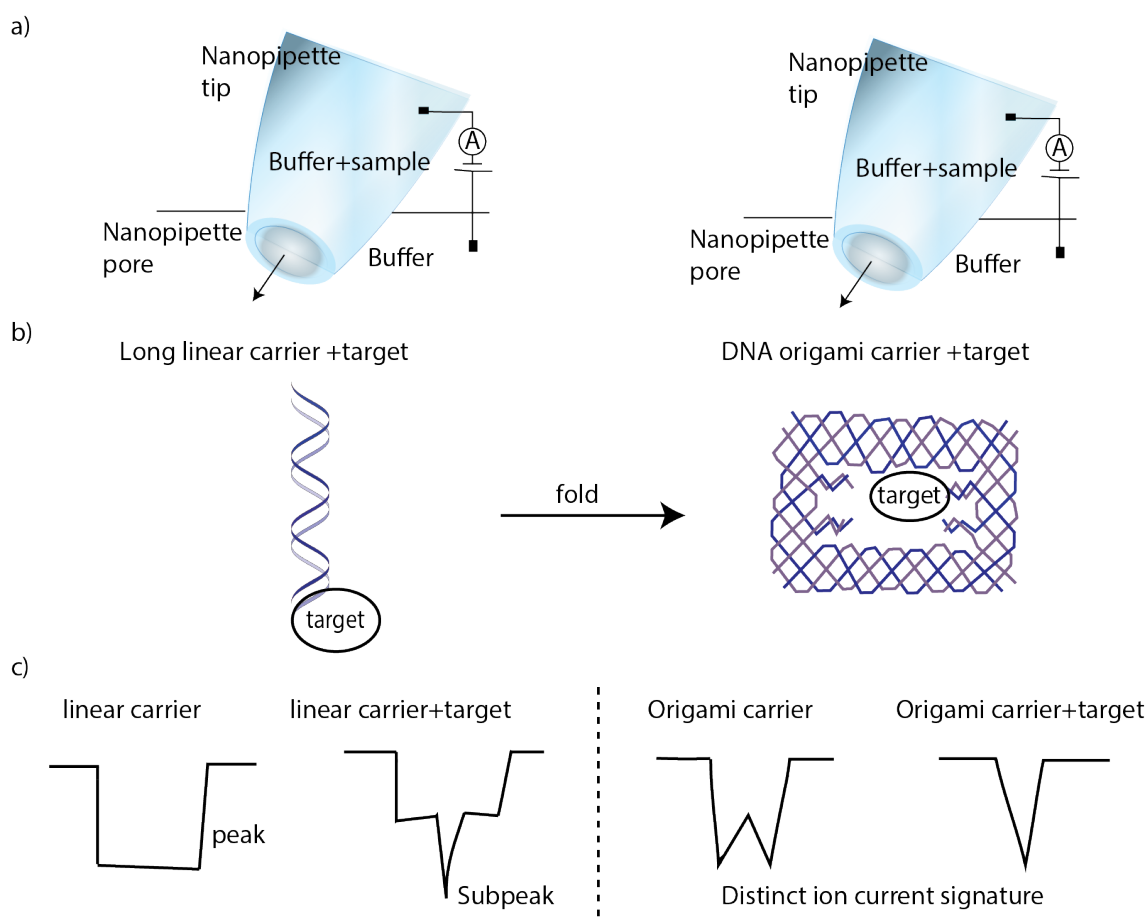


Figure 1.1: Schematic representation of a) the nanopipette experimental setup wherein the molecules of interest are translocated from inside the nanopipette to the outside, b) shows a linear DNA carrier bound to a target and how by folding the linear DNA a defined DNA origami structure that is capable of c) specific ion current signature is created, as opposed to the subpeak ion current detection.

DNA origami as carriers:

Alternatively, to completely harness the potential of DNA as carriers, we turn our attention to DNA nanotechnology, wherein the hybridisation properties of the nucleotides are

used for programmed duplex connection to produce user defined patterns. The past few decades have proved to us how DNA as functional nucleic acids and building blocks, could greatly advance single molecule research in the field of nanomedicine as drug delivery systems, probes for biosensing [31], and theranostics [32] to name a few.

Also, the possibilities of these nucleic acid nanostructures, particularly DNA origami has been explored across disciplines with applications including in the field of nanopores (chapter 3 and 4). While the structural perspective of DNA origami for constructing hybrid nanopores has had an exciting and widespread attention, what has not been looked at is its use as platforms for biosensing with nanopipettes as detectors. DNA nanotechnology especially DNA origami offers means for site specific positioning of functional materials like aptamers with nanometer scale precision, these advantages when taken together with the high sensitivity of nanopipette detection provides us a novel biosensing strategy at the single molecule level.

Thus, to truly exploit the potential of both these techniques, a multidisciplinary approach towards biosensing, DNA nanotechnology in cooperation with nanopipettes is suggested through this thesis.

1.1 Thesis Aim

With respect to the above introduction, the work put forward in this thesis aims to develop a highly sensitive, quantitative detection system combining nanopipettes with DNA origami, and attempts to improve the sensitivity and selectivity of nanopore sensing system by answering the following questions,

1. Can nanopipettes detect and differentiate different DNA origami.
2. Can these nanostructures be adopted as carriers and unique identifiers.
3. Is quantitative detection possible with DNA origami as carriers.

And by doing so demonstrate the potential of DNA nanostructures for individual protein molecule sensing via voltage driven nanopipette translocation experiments.

1.2 Outline of Chapters

Chapter 2

As per the project outlined above nucleic acids form one of the core nanotechnological procedure for this project. Thus chapter 2 provides an introduction to nucleic acids with basic explanation of their chemical makeup and structure. Further sections will introduce DNA nanotechnology and discusses the development of DNA as an engineering material which takes us to the technique of DNA origami and its many advantages. The later sections in this chapter gives a very brief overview of aptamers thus covering the introduction on the two DNA technologies (DNA origami and aptamer) used in this thesis.

Chapter 3

Another nanoscale technique used in this project for single molecule detection is nanopipettes - a class of nanopore. Intial sections in chapter 3 sets the stage with the basics of nanopore technology including, brief discussion on the types of nanopores (biological, solid state and hybrid nanopores) and their different fabrication procedure. Then the main focus of the chapter is on nanopipettes examining their history, working principle and unique nanoscale properties.

Chapter 4

Chapter 4 examines the literature available on single molecule detection using nanopores and discusses the merits and setbacks. Both electrical and optical means of nanopore detection is covered and the various solutions provided by the different groups for the betterment of the technique are looked at. The chapter also provides examples

of how DNA origami has ventured into the nanopore field and aims to highlight the uniqueness of the work carried out in this thesis by comparing the existing literature and in so provides the justification for the use of DNA origami in combination with nanopipettes.

Chapter 5

This chapter details the materials and various methods used in this thesis throughout the various chapters. For ease, the techniques are grouped into those involving DNA origami design and fabrication and those for actual nanopipette translocation experiments.

Chapter 6

The first experimental results chapter provides the detailed nanopipette characterisation studies conducted with different pore sized glass nanopipettes, both quartz and borosilicate, for establishing the indirect pore size calculation via pore resistance. This is followed by results obtained from rudimentary translocation studies with linear and plasmid DNA samples for testing the nanopipette experimental setup and for establishing the optimal sample concentration and bias voltage.

Chapter 7

In this chapter, the characterised nanopipettes from the previous chapter are used to study different DNA origami molecules via voltage driven translocation experiments. Four DNA nanostructures, two frames and two tiles, are analysed to understand the ion current characteristics in relation to the sample geometry.

Chapter 8

As continuation to the previous chapter novel DNA frame constructs of varying inner dimensions and similar outer dimensions referred to as concentric squares were designed and custom produced to better understand and prove the relation between nanostructure

geometry and ion current signatures. The chapter covers the detailed methodology for custom designing three nanostructures used in this study along with the subsequent nanopipette translocation experiments.

Chapter 9

In the final experimental chapter DNA origami and quartz nanopipettes are combined together as an effective carrier and detection system. Further, a method of quantitatively sensing protein targets through this system is proposed and demonstrated.

Chapter 10

Lastly, this chapter captures all the results observed in this thesis and also discusses the future directions and further possibilities of this work.

Chapter 2

Introduction to DNA and DNA Nanotechnology

The discovery of DNA and understanding of its structure and function has been the key factor for the enormous progress in many areas of science and technology like gene therapy, forensics, genomics etc. The simple chemistry and properties that makes DNA a successful genetic tool also favours it as a building block at the nanoscale to create artificial nanostructures, i.e., when taken out of their biological context the information embedded in them can be used to form structural and functional motifs via bottom up fabrication.

Though there are many biomolecules capable of forming synthetic structures, DNA has the most foreseeable and programmable interactions with extraordinary specificity and stability. And with development in automatic nucleic acid synthesis, any number of sequences that binds with their complementary pairs reliably can be synthesised and modified. The so designed synthetic nanostructures form an integral part of this thesis as carriers or platforms onto which our target molecule binds. Now, to efficiently take advantage of the unique properties of DNA, a sound understanding of the basic elements is imperative.

And as such in this chapter, the structure and function of nucleic acids, specially DNA from its fundamental units is discussed answering questions like what elements make up DNA and how they are arranged to pack information necessary for life. This is followed

by how the individual DNA strands can be used as engineering materials, thus outlining the field of DNA nanotechnology in detail along with various developments including the different motif designs and the DNA origami technique.

The same specificity and stability that makes DNA suitable as building blocks for nanostructures also renders them excellent functional oligonucleotides—aptamers—short strands of single stranded oligonucleotide sequences that can specifically bind various targets. These aptamers make up the functional units on the carrier nanostructures used in this thesis and hence are also discussed briefly.

2.1 Deoxyribonucleic acid

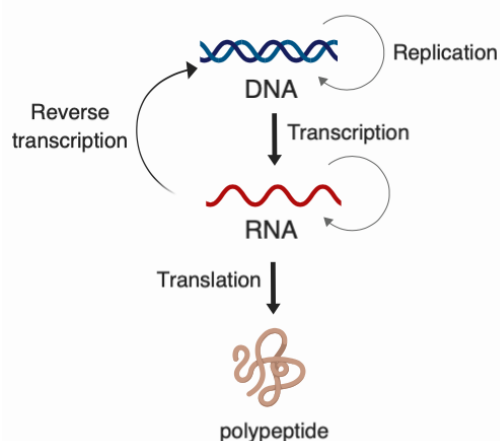


Figure 2.1: *Central dogma of molecular biology. DNA can be duplicated via replication, and information in the DNA is transferred by a process called transcription that generates RNA molecules which undergo translation to transfer the information into polypeptides.*

Deoxyribonucleic acid (DNA) is the hereditary basis of most living entities [33, 34]. A long sequence of DNA, termed the genome, carries the complete set of hereditary information required for the development of an organism and duplication of this information through generations assures the continuity of that particular species. How this “information” is stored, interpreted and transferred makes up the central dogma of molecular biology [35], see figure 2.1.

Discovery of the double helical structure of DNA was paramount for comprehending the paradigm, that genetic inheritance is conceivable because of replication, and transcription

and translation is responsible for expressing genetic information. In this section we will discuss the basic structural and chemical properties of DNA, which will be pertinent for subsequent chapters of DNA nanostructure design.

2.1.1 Structure of nucleic acid

Nucleic acid was first isolated by Friedrich Miescher in 1869, the role of DNA as the carrier of genetic information was identified by the classic experiments of Oswald Avery and co-workers in 1944 and was confirmed via the Hershey–Chase experiment.

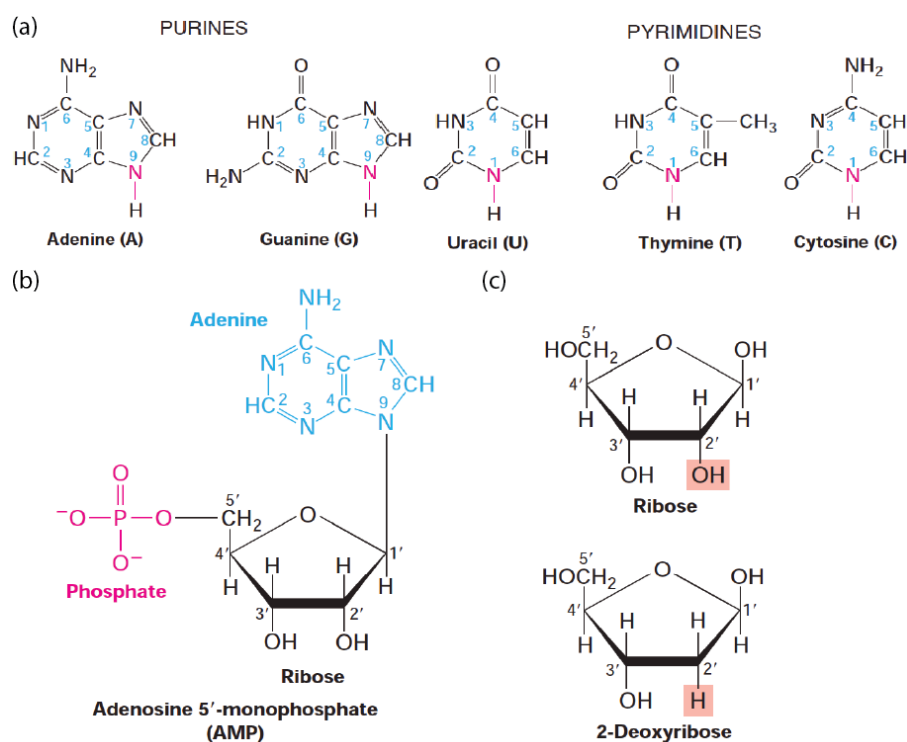


Figure 2.2: Nucleic acid chemistry, (a) Structure of the different nitrogenous bases with the bond forming nitrogen highlighted in pink. (b) Chemical structure of Adenosine 5-monophosphate (AMP), an example of a deoxyribonucleic acid structure with nitrogenous base, sugar and phosphate group indicated in different colors. (c) Structure of pentose sugar molecules with difference between ribose and 2-deoxyribose sugar highlighted. Figure adapted from Alberts et al. [36].

The chemical structure of DNA is very similar to Ribonucleic acid (RNA), they are both polymers made from units or building blocks of monomers called the nucleotides, which consists of a sugar (shown in black), a nitrogenous base (shown in blue), one or more phosphates (shown in pink), figure 2.2b. The sugars named for their type is 2'deoxyribose for DNA and ribose for RNA respectively, the difference being the sugar in RNA has a hydroxyl (OH) group on the 2' carbon of the pentose ring, figure 2.2c [36].

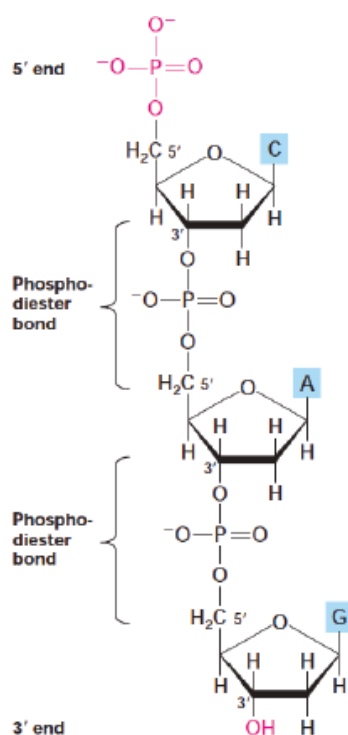


Figure 2.3: A polynucleotide chain with 5 carbon of a pentose sugar linked to the 3 carbon of the next pentose sugar through a phosphate forming the 5'–3' phosphodiester linkage. Figure adapted from Alberts et al. [36].

Each nucleic acid has four nitrogenous bases, two purines, adenine and guanine and two pyrimidines, cytosine and thymine and uracil instead of thymine in RNA. The difference between thymine and uracil is the methyl group at position C5 in thymine [35]. The bases are abbreviated A, G, C, T and U as shown in the figure 2.2a [36]. The nitrogenous base is linked to the 1' carbon on a pentose sugar by a glycosidic bond from the N1 of pyrimidines or the N9 of the purines. The pentose sugar and the nitrogenous base linked together is called a nucleoside. The sugar can be linked to a phosphate group by its 5' or 3' carbon [35]. A nucleoside with a phosphate group is called a nucleotide and a long chain of nucleotide forms a polynucleotide, figure 2.3 [36].

The nucleotide chain has a natural end to end chemical orientation or polarity, the 5' end has a free phosphate group on the 5' carbon terminal sugar and the 3' end has a free hydroxyl group on the 3' carbon terminal sugar. Due to this and because of the synthesis directionality the DNA sequences are always written and read 5' to 3' direction.

2.1.2 Double helical structure—base pairing and stacking

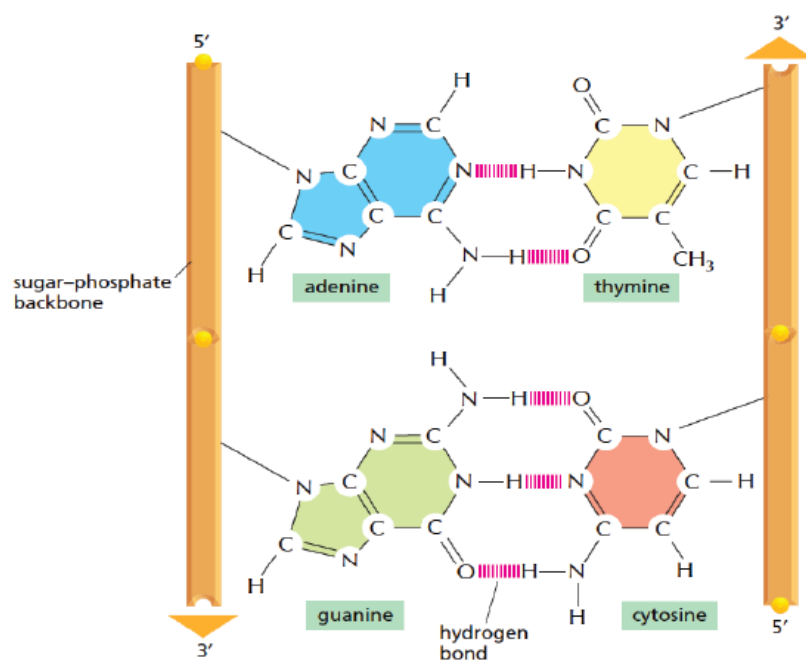


Figure 2.4: Formation of double strand via hydrogen bond between the bases, the sugar phosphate backbone with directionality of strands are indicated. Figure adapted from Alberts et al. [36].

James D. Watson and Francis H. C. Crick with Rosalind Franklin and Wilkin's X-ray fibre diffraction data built the model for the DNA double helix in 1953. The Watson–Crick structure consists of two polynucleotide chains bound together by hydrogen bonding between the nitrogenous bases to form the double helix [34][37]. This hydrogen bonding is termed as base pairing and the bases (A to T and G to C) are said to be complementary to each other.

The above said base pairing occurs between these specific bases running antiparallel (5' to 3' and 3' to 5') as they have the right functional groups in just the right geometry for the hydrogen bond to form (figure 2.4) and are thus the most energetically favourable arrangement to be packed inside the Watson–Crick double helix.

In G to C base pair three hydrogen bonds are found between G–O6 and C–N4, G–N1 and C–N3, and G–N2 and C–O2 positions, and in an A to T base pair two hydrogen bonds are found between A–N6 and T–O4, and A–N1 and T–N3 positions [38]. The two C1 atoms within a G–C base pair and an A–T base pair are equidistant (~ 10.5 Å).

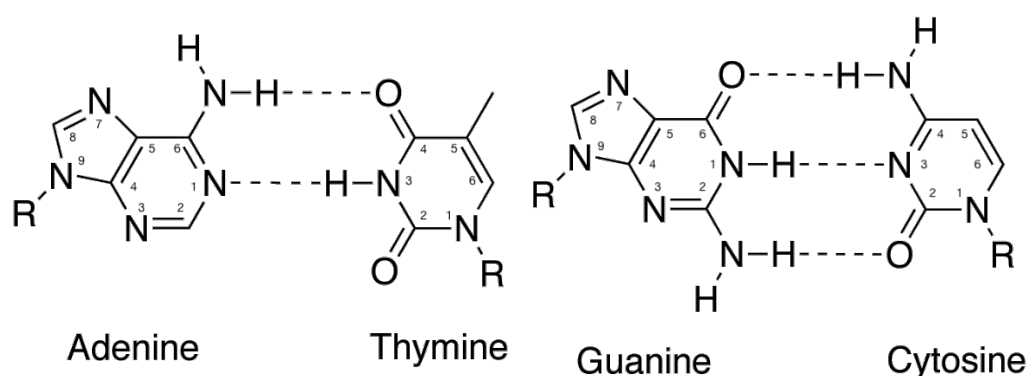


Figure 2.5: Base pairing between nucleotides, two hydrogen bond formed between A-T and three between G–C.

Thus the G–C and A–T base pairs in the Watson-Crick conformation are nearly iso-structural, from the sugar–phosphate backbone point of view [39]. The phosphate groups with the negatively charged oxygen atoms brings the DNA an overall negative charge, whilst in biological condition is shielded by proteins or cations in–vitro thus neutralising the DNA [36].

As stated above, the two polynucleotide chains run opposite to each other and thus are antiparallel, with the sugar–phosphate backbones on the outside of the double helix and base pairs on the inside [38]. Often analogised as steps to the double helical spiral staircase, the nitrogenous bases lie on top of each other (stacked), each pair rotated $\sim 36^\circ$ around the helical axes relative to the next base, so that ~ 10 bases make a full 360°

turn. The bases are stacked due to hydrophobic interactions and the stacked bases offer a stacking interaction by attracting each other via van der Waals forces [35].

Also as per the Watson and Crick base pair assembly the two deoxyribose sugars connected to the individual base pair are on the same side of it, so the stacking gives rise to continuous indentations in the surface that wind along, parallel to the sugar–phosphodiester chains, which are called grooves [39]. And consequently the asymmetry of base pairs gives rise to minor and major grooves as seen in figure 2.6.

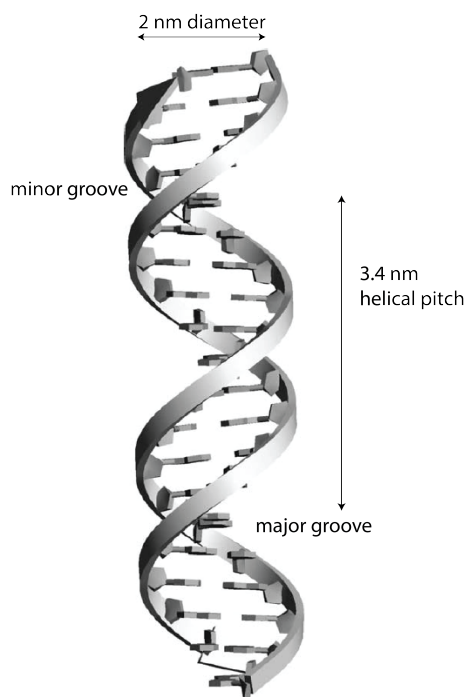


Figure 2.6: *B DNA Structure indicating minor groove and major groove with a helical pitch of 3.4 nm and diameter of 2 nm. Helical pitch is defined as the distance parallel to the helical axis between successive nucleotide units per complete turn of the helix. Figure adapted from Neidle, [39].*

These base pair interactions and governing forces determine the stability of the Double stranded Deoxyribonucleic acid (dsDNA) helix formed from the two single stranded (ss) DNA. Salt conditions like concentration, charge and size also play important roles in DNA stability and therefore its melting temperature (T_m) [40]. T_m is defined as the temperature at which 50% of the DNA strands are at random coil or in single stranded state. This dependency is also very important for folding of DNA into their native structure, because as mentioned before cations like Na^+ and Mg^{2+} are required to neutralise the negative backbone to reduce repulsive coulombic interactions between the phosphates to fold DNA [41].

DNA exists predominantly as B form in its native environment, B DNA is a right-handed helix that makes a complete turn every $\sim 34 \text{ \AA}$ (3.4 nm) and has a diameter of $\sim 20 \text{ \AA}$ (2 nm). Adjacent nucleotide distance in B DNA is 3.4 \AA (0.34 nm), and in aqueous solutions the structure averages 10.4 bases per turn [39]. Apart from B DNA, there is A and Z DNA configurations which are found in cells under certain conditions and in vitro [42].

Furthermore, the complementarity of the base pairs means that if the sequence of bases in one chain are known one could easily identify the exact sequence in the other chain, i.e., one of the chains acts as a template or base sequence to produce its complement. Thus, the discovery of DNA structure along with the earlier observations of Erwin Chargaff in 1950s, that the amount of DNA bases is different for different species, provided fundamental insight into genetic coding, the relationship between carrying genetic information in DNA and expressing it [36, 38].

Though DNA is modelled as a double helix with certain rigidity and with backbone conformation that calls for discrete torsion angles, it is also a conformationally flexible and dynamic polymer. It has been known to show specific bending directionality and stiffness that directs its packaging and functionality. And even when “free” in solution certain DNA can confer preferred axial configurations [43]. This crucial aspect of DNA for adopting a range of conformations or structural transitions from its canonical double helix along with its programmable nature as said above is what enables it as a very efficient coding system, and a very suitable building material as described in the following sections.

2.2 DNA as building blocks

The many features of DNA such as defined nanosize (2 nm diameter), structural repeat (3.4 nm) with stiffness and persistence length of $\sim 50 \text{ nm}$ combined with the predictable and programmable interface makes it extremely fit for small molecular manipulations. And so, the fabrication of nanostructures through DNA bottom up technology provides a

huge advantage as a parallel self-assembly technique to fashion many sophisticated and application oriented patterns as discussed further.

An early start to DNA nanotechnology was with the in-vitro genetic manipulations [44, 45] with sticky ends, wherein a short single stranded overhang protruding from the end of the double stranded DNA hybridises with the complementary protruding end of another double stranded DNA. The protruding ends like flaps of velcro stick together due to their complementarity to form a single molecular complex. In nature, sticky ends are products of restriction enzyme cleaving a double helix (figure 2.7a). This can be used as an efficient tool for control of intermolecular association and predictable geometry at the point of cohesion.

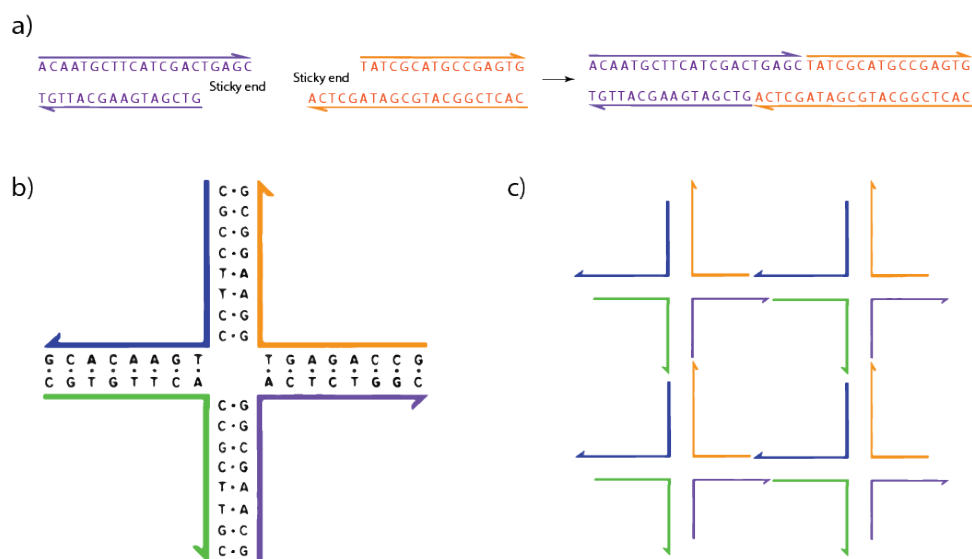


Figure 2.7: Schematic representations of a) sticky end hybridisation of two DNA duplexes to form one DNA complex. b) A four way holliday junction formed from four partially hybridised asymmetric strands producing a immobile junction,.c) Sequential assembly of asymmetric strand junctions via sticky ends to create 2D lattice structure. Figure 2.7b and c adapted from Seeman [46].

2.2.1 Branched structures and DNA motifs

The only limitation is that the axes of DNA are linear unbranched helices and joining them via sticky ends will result in longer linear helices in one dimension, to make multiple dimensions branched DNA is a requirement. There are several examples of branched DNA structures naturally found as intermediates during replication, genetic recombination, strand displacement, and gene expression [46].

One such motif of branched DNA called the Holliday junction [47], first described by Robin Holliday in 1964, is found in the biological system as intermediates of genetic recombination [48]. The Holliday junction contains four strands of DNA bound together to form four double helical arms abutting a branch, such that each strand is complementary to the other partially (figure 2.7b). Biologically these junctions migrate the length of the DNA due to homologous sequences and resolve into two double helices, a process called branch migration.

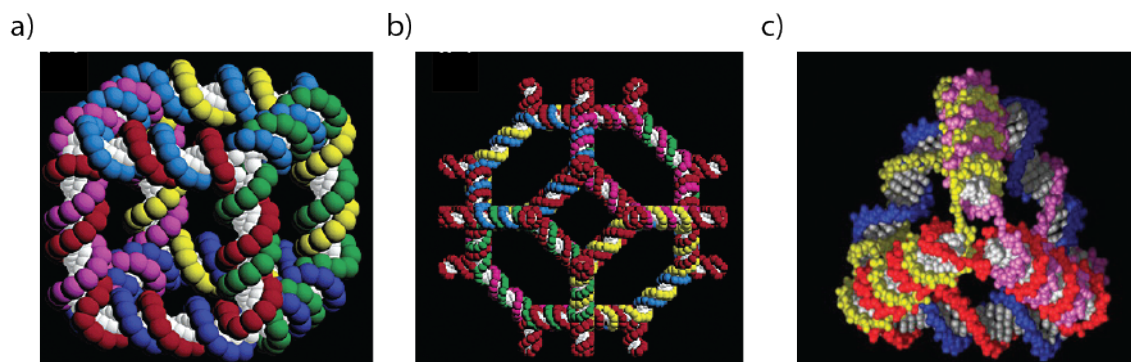


Figure 2.8: Polyhedral structures. a) A stick-cube formed from six different cyclic strands each represented by a colour, the strands are linked to each other twice on every edge making the structure a hexacatenane. b) A top down view of the fourfold axis of a truncated octahedron with six squares and eight hexagons, the molecule is made of 14 cyclic strands. c) Tetrahedron formed by annealing 4 DNA sequences. Figures adapted from Seeman [49], Zhang and Seeman [50] and Goodman et al. [51] respectively.

Nadrian C. Seeman in 1982 [46] proposed omitting the sequence symmetry by making use of artificial DNA sequences designed to be asymmetrical thus forming immobile

junctions or fixed branch points. The artificial oligonucleotide sequences also allowed for the construction of branched junctions with multiple arms [52]. Thus, via self-assembly using branched DNA molecules with programmed sticky ends 2 dimensional arrays [46] (figure 2.7c) and 3D structures including a stick-cube [53], multiple polyhedral constructions [51, 54, 55, 56, 57, 50] and borromean rings [58] were achieved, figure 2.8.

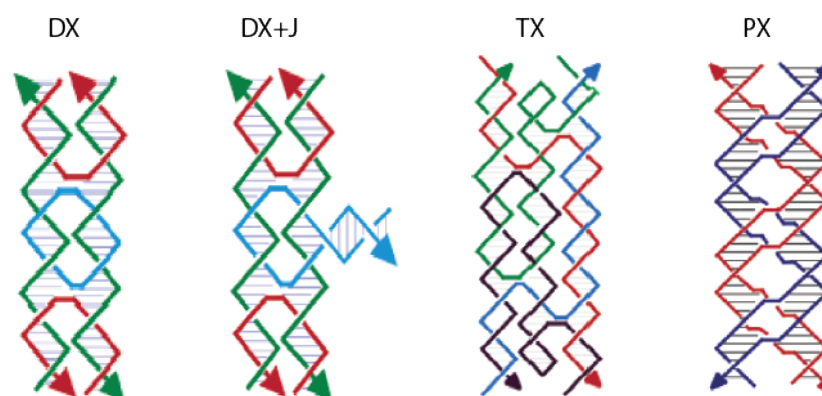


Figure 2.9: Schematic of different crossover structures for Double crossover (DX), Double crossover with junction (DX+J), Triple crossover (TX) and Paranemic crossover (PX). Figure adapted from Fu and Seeman [59].

This development to form higher order structures as shown in figure 2.8 was possible due to DX molecules [59] that consisted of two DNA double strands linked together by two strand exchange or crossover (see figure 2.9) rather than the single exchange seen in holliday junction [60]. The double cross over offered the rigidity and stability needed to construct extensive DNA structures with precise topology and geometry.

Subsequently DX junctions with sticky ends were used to achieve many 2D arrays and 3D DNA structures [56, 61, 62, 63, 64, 65, 66]. Progress in the structural motifs based on DX motifs were also crucial for expanding DNA nanotechnology, for example, to create highly ordered geometries different types of crossovers like TX [67], PX [68] and multiple cross motifs [49], three-point and six point star motifs [69, 62], tensegrity triangles [55] and T-junctions [70] were used to deliver the much needed core integrity and individual component rigidity by weaving multiple strands together.

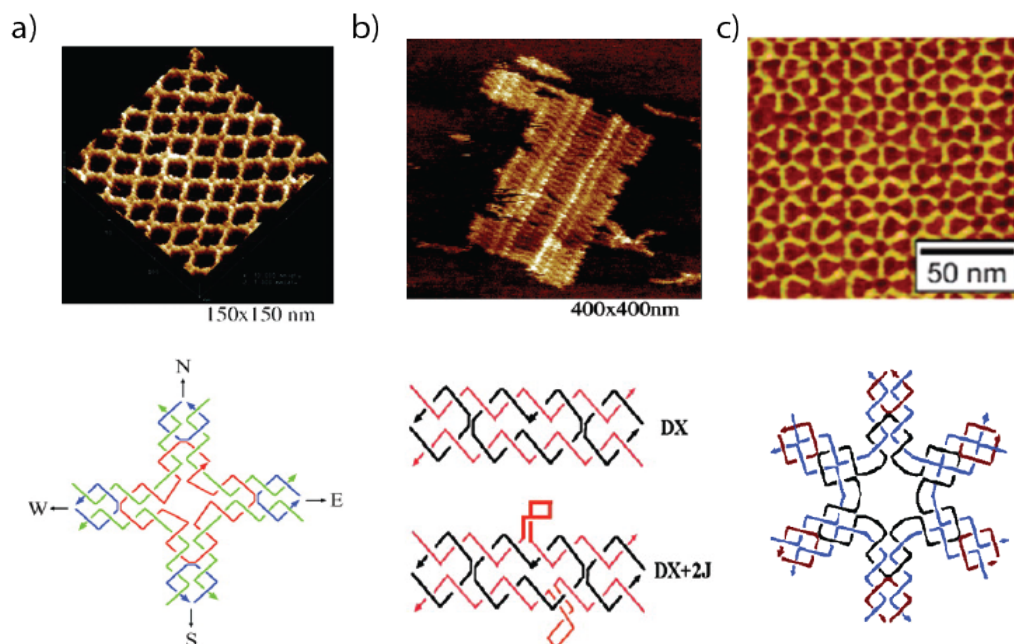


Figure 2.10: *Different DNA nanostructure crossover motifs and AFM image of the resulting 2D arrays formed via the respective motifs. a) Four-way double crossover junction, b) combination of DX crossovers and DX with 2 junctions, c) six point star motif structure. Figures adapted from Zhang et al. [71].*

2.3 DNA origami technique

In contrast to Seeman's motif junction construction, Paul Rothemund in 2006 [72] proposed a method for DNA nanostructure assembly that transformed DNA nanotechnology. In his article he described a self-assembly technique that made use of long single stranded viral DNA, called the scaffold DNA, that folded onto itself into a desired pattern with the addition of complementary short strands called staple or helper strands that bring together the specific parts of the Single stranded Deoxyribonucleic acid (ssDNA) (figure 2.11a and b).

The technique similar to Seeman's is based on the interconnection of several DNA strands via cross over branches. But in the origami technique the strength and rigidity of the DNA nanostructures is from DX contributed by both the scaffold and staple strands all

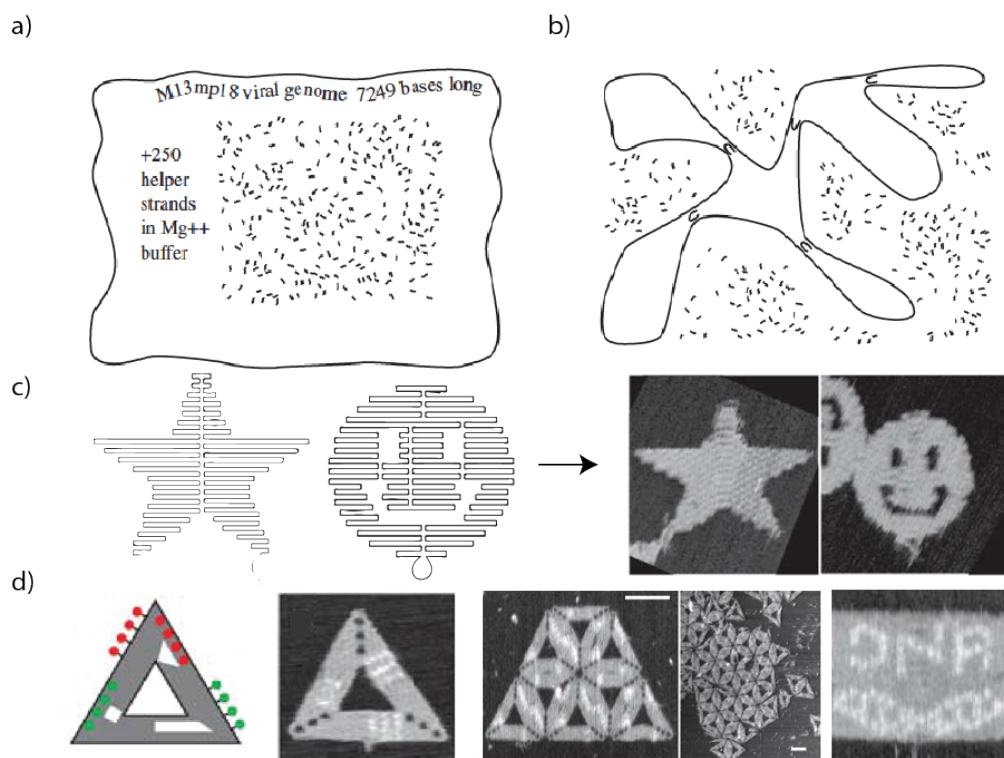


Figure 2.11: *The DNA origami technique. a) Large ssDNA scaffold mixed with an excess of short strands of staple DNA, b) staple strands complementary to particular regions of the scaffold help pinch the scaffold together through complementary hybridisation, c) scaffold strand routed in a raster pattern for two arbitrary structures and AFM images of the formed star and smiley design upon addition of staple strand, d) schematic example of patterned triangle DNA structure with protruding hairpin DNA sequences (white swatches) that show up as bright pixels under the AFM, triangles combined to form lattices via the extended staples (shown as protruding dots in the schematic) that are complementary to the scaffold. Adapted from Rothemund, [72].*

throughout the structure (see chapter 6). Use of scaffolds in DNA nanotechnology was already reported by Yan *et al.* [73] to build one dimensional barcode array and by Shih *et al.* [54] for constructing an octahedron structure from a 1.7 kb scaffold folded with DX and PX motifs. But neither of these studies could show the comprehensive impact of Rothemund's DNA origami structures.

Rothemund through his paper showed the generality of his method to form different

arbitrary shapes including stars and smiley faces as shown in figure 2.11c. The method provided an easily addressable surface area of around 100 nm and enabled creation of well-defined structures. Also, the use of a single scaffold overcame the problem of stoichiometry and purification thus simplifying the assembly process and increasing yield even for complex structures.

He also demonstrated patterned DNA origami with protruding dumbbell hairpin structures thus labelling them to be visualised via AFM as bright pixels due to their height difference (figure 2.11d). Thus, the versatility of DNA origami scaffold technique was demonstrated, ranging from well-formed structures to patterned pixels onto which molecules could be added transforming them into platforms or ‘nano-breadboards’ for carrying out various diverse experiments.

Subsequently in 2009, Douglas and group [74, 75] extended the DNA origami technique to build three dimensional structures by stacking multiple layers of DNA helices in parallel which held to the porous honeycomb lattice assembly. The honeycomb lattice connects each DNA helix to three neighboring strands placing crossovers every 7 bp thus providing 0° , 120° and 240° between the crossovers which corresponds well with the B form DNA with 10.5 bp per helical turn of 360° . This way every two DNA duplex will contain a double crossover every 21 bp.

Alternatively square lattice assembly [76] connects one DNA helix with four neighbors, here the crossovers are separated every 8 bases causing a fourfold symmetry with a 270° backbone angle. This is achieved by extending the helical pitch to 10.67 bp per turn which causes a global twist in the structure but results in a tighter packing of duplexes. The global twist can be rectified manually via deletion or slightly varying the position of crossovers by deviating from the 8 bp count at certain points.

Similarly, deliberate strains and twists can be applied to the DNA structure via targeted insertions and deletions of basepairs [77], this enabled the development of 3D structures [78] with high curvatures. The open source software caDNAno released by Douglas and colleagues [74] has become the go to tool for designing DNA origami scaffold-staple

layouts using honeycomb or square lattice packaging.

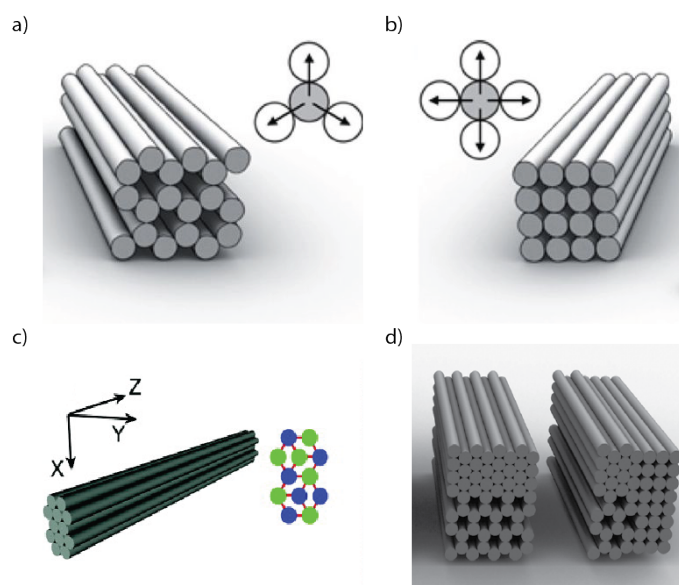


Figure 2.12: *a) Honeycomb lattice assembly b) Square lattice assembly c) Hexagonal assembly and d) Hybrid assembly. Adapted from Castro et al. [79] and Ke et al. [80].*

Apart from square lattice, hexagonal lattice assembly [80] for close packing of DNA helices were also introduced wherein a DNA helix connect 6 surrounding strands. If one desires and the construct warrants hybrid designs consisting of multiple assemblies in combinations of square, honeycomb and hexagonal lattices are also possible (figure 2.12).

2.4 Overview of aptamers

From the above discussions, it is clear that nucleic acids are multifunctional, in that oligonucleotides that can specifically bind various targets is yet another valuable contribution. These short single stranded nucleotides (DNA or RNA) that can bind target molecules with high specificity and affinity are called aptamers. The interactions that drive the formation of specific aptamer–target complex could be hydrophobic and electrostatic interactions, hydrogen bonding, van der Waals forces, shape complementarity and base stacking [81].

The aptamers selected through different approaches including Systemic evolution of ligands by exponential enrichment (SELEX) and computational methods like molecular dynamics and in silico identification [82] can discriminate between closely related conformational isomers, molecules with different functional groups and amino acid mutations. Compared to very huge antibodies aptamers are small and flexible which permits binding of small molecule targets that are inaccessible to antibodies. They are also cheaper to produce compared to the laborious in-vivo screening involved for antibody generation. Moreover, aptamers can be chosen against a large spectrum of targets including toxic and non-immunogenic molecules that cannot be recognised by antibodies [83].

In this thesis, aptamers specific for CRP protein adapted from Jarczewska *et al.* [84], Lee *et al.* [85], Huang *et al.* [86], and Piccoli *et al.* [87] were utilised as functional groups attached to DNA origami for successful quantitative detection.

2.5 Conclusion

In this chapter, the chemical structure and function of DNA was discussed. Detailed chemical structure of DNA showed that genetic information is stored and carried within the DNA in a linear sequence, and the complementary nature of the four nucleotide bases (A to T and G to C) forms the base for its hierarchy, to form duplex structures. This programmable molecular recognition of DNA brings about its versatility other than as carriers of genetic information.

Accordingly, the chapter provided a detailed observation of the potential of nucleic acids in the field of DNA nanotechnology including its progress starting from the development of different types of motifs and crossover structures to the introduction of DNA origami and subsequent evolution to design 3D structures and arrays.

While one technique followed multiple strand hybridisation via motifs the other utilised a long ssDNA scaffold and hundreds of short nucleotide strands to form a desired shape.

Despite their technical differences both Seeman and Rothemund's approach successfully exploited the basic complementary nature of DNA for creation of nanostructures. These nanostructures have been developed into and incorporated in a variety of applications as breadboards for biomolecular interaction studies, molecular tweezers, nano robots, carriers in targeted therapy, etc [88, 31, 89].

Apart from nanostructures, short oligonucleotides few tens to few hundreds of base pairs in length that function as aptamers thus capable of specifically recognising target molecules were discussed. The experimental results chapters in this thesis will further explain how we made use of DNA origami and aptamers for designing a single molecule sensing system.

Chapter 3

Introduction to Nanopores and Nanopipettes

Another important element in this thesis is the use of nanopipettes, a class of nanopore, for the detection of target molecules via translocation. Translocation of molecules (salts, nucleotides, peptides, etc) through the membrane of cells is a fundamental and universal process in the biological system. This basic yet sophisticated transport system functions through passive pores, active ion channels, and viral motors with elegant and highly-ordered structures [90]. These functional biological arrangement motivated the development of different nanopores for single molecule detection.

Before diving into the wealth of knowledge on the different types of nanopores, it is important to note the history that led to the birth of this technique. In 1940s, Wallace H Coulter invented a resistive cell counting tool for blood cells in haematology [91] which was later patented as ‘Means for counting particles suspended in fluid’ in 1953 [15]. The technique consisted of two electrodes placed across a pore filled with an electrolyte solution and measured the electrolyte conductivity as a function of time using an electrometre connected to the electrodes and a chart plotter.

Suspension of cells being pushed through the pore produced discrete resistive spikes or pulses in the otherwise unvarying electrolyte conductivity due to the temporary obstruction of the pore. The frequency of these pulses with time is associated to the total amount of cells present in the sample and the distribution of the electrical pulse

amplitude is related to the cell size distribution. Though the simplicity of the Coulter counter was met with reluctance at first, it became clear that the speed and accuracy of the technique cannot be matched with the traditional manual process of cell counting and it has revolutionized clinical practice since then.

Coulter's resistive pulse technique was later refined in 1970s by DeBlois and Bean [92] for detection of viruses and nanoscale particles by translocating them through submicron pores. Later in 1990s the much exciting jump to nanoscale happened with ion channel studies in lipid bilayers playing a crucial role [93]. This time period saw two major advancements, development of pore size from millimetre to nanometre dimensions and the target analytes were no longer whole cells but individual ions, biomolecules and single particles [16].

This chapter will briefly discuss the different types of biological and solid state nanopores, along with their fabrication techniques used for various single entity analysis. Later sections will discuss how development in microelectrodes and patch clamp techniques lead to tip based nanopipettes. Since glass nanopipettes will be the technique of choice for the entirety of this project, the last section of this chapter will focus on its history, fabrication technique, working principle and properties.

3.1 Types of nanopores

There are different types of nanopores, distinctly they can be divided into naturally occurring biological pores and artificially made nanopores. The artificially made nanopores can further be divided into solid state nanopores, glass nanopipettes, and hybrid nanopores. Though in this thesis we only use glass nanopipettes for all of our experimentation, we will very briefly discuss about the different types of nanopores and then in detail about the nanopipettes.

3.1.1 Biological nanopores

Naturally occurring biological pores have been explored over the years as nanopore detection systems with the early study involving biological nanopore Alpha hemolysin pore (α -HL) for ss DNA and ssRNA detection demonstrated in 1996 [94]. These pore forming proteins embedded in lipid membranes, liposomes or polymer membranes and immersed in an electro-chemical chamber (figure 3.1) offer distinct advantages as a nanosensor for single molecule detection and have been largely exploited especially for nucleotide sequencing.

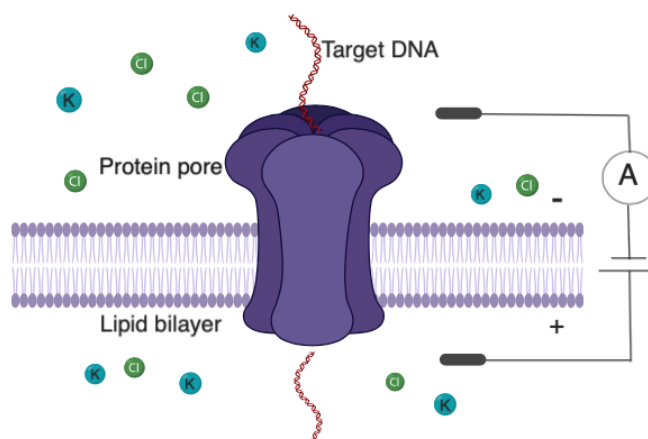


Figure 3.1: A representation of a protein pore embedded in a lipid bilayer immersed in a buffer system.

Traditionally and most widely used biological pores include the Staphylococcal α -HL, Aerolysin (AeL) a β pore forming toxin, Outer membrane protein G (OmpG) pore a monomeric protein from *E.Coli*, Cytolysin A (ClyA) pores and the phi29 connector protein. Each of these pore forming proteins have their advantages and relevance.

For example, α -HL, a heptameric transmembrane pore forms a 5 nm length barrel when it self-inserts into the lipid bilayer. The formed nanopore has a very small dimension of 1.4 nm diameter which limits translocation to ssDNA structures alone [95]. Thus for dsDNA, Phi29 Motor and ClyA pores are preferred as they are large enough to allow dsDNA and

protein translocations. But the protein pore α -HL is utilised extensively because of its ability to stay open for a long time interval, a specific function that results in a stable baseline signal which is important for single molecule detection. Several studies have also demonstrated easy modifications within α -HL pores that makes translocation and detection events specific and highly sensitive [96].

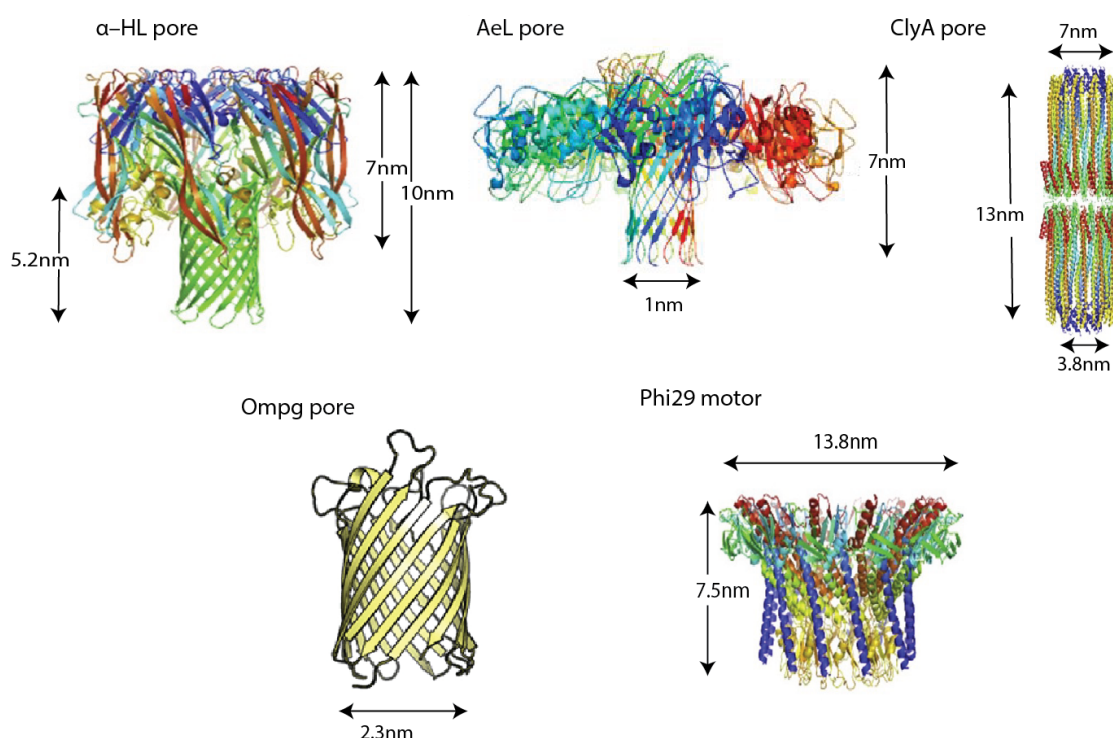


Figure 3.2: *Biological nanopores. Structure of different biological pore forming proteins discussed in this section represented with pore diameter and channel length. Figures adapted from Shi et al.[97].*

Likewise, the spontaneous assembling nature of AeL into 1.0 –1.7 nm pores make them suitable for single molecule analysis. Utilised first in 2006 as a nanopore sensor for α -helix collagens, both wild-type and modified AeL pores have been studied through the years for various applications like DNA and protein detection [98, 99], analysis of various oligosaccharides, peptides and chimera molecules.[100, 101, 102]. Furthermore, AeL pores are used for their ability to enhance negatively charged target interaction, due to their positively charged residues.

On the other hand, OmpG pores are exploited for their simple modification procedures. The analyte-target molecule interaction with the pore loop results in a characteristic signal for different proteins which also varies in frequency, duration and open pore current respective to the analytes. Thus the bound targets can be identified by studying the current signal. Furthermore, modified OmpG pores have also been found useful for protein analyses like streptavidin analysis by trapping them through specific ligand attachments to the pore loop [103, 104].

Yet another biological pore used widely for DNA translocation is ClyA nanopores. The pores with a 13 nm long central channel is narrow (~ 3.3 nm) in one end and wider at the other (~ 6.4 nm). As opposed to AeL pores the ClyA nanopores have negatively charged residues within the pore constriction. Though the narrow opening of the ClyA pores are large enough for double stranded DNA transport, the negatively charged residues prevent entry of dsDNA due to electrostatic repulsion. Thus high ionic conditions (2.5 M) are required to screen the pore charge to allow successful transport of dsDNA [105]. Modified ClyA pores by addition of positive charged residues or removal of the negative residues were also found useful [106, 107, 108].

Alternatively a nanochannel made from a viral nanomotor inserted into a lipid bilayer is the Phi29 connector protein. The bacterial virus Phi29 DNA packaging nanomotor consists of a channel made of 12 copies of gp10 protein that encircle to form a channel of ~ 7 nm in length and 3.6 nm diameter at the narrow and 6 nm at wider end [109]. The connector inserted into a lipid bilayer has been shown to be robust and generate extremely reliable, precise and sensitive conductance signatures which have been used for real time chemical sensing, gating studies and fingerprinting DNA translocations including controlled ratcheting of DNA [90, 110, 111].

Even though biological nanopores have been used widely for their remarkable ability to be precisely engineered and altered they do have certain disadvantages because of their fixed small size and limited stability, thus rendering them unable to be used for various analytes or under different parameters (pH, salt concentration, temperature, etc). It should be noted that due to the limits of this thesis, the review has not touched upon

the huge field of ‘biological nanopore sequencing’ which has an overwhelming academic and technological interest.

3.1.2 Solid state nanopores

It is for the above said reasons that solid state nanopores are considered more advantageous, and though earlier nanopore based applications mostly adopted biological nanopores, solid state nanopores have slowly gained popularity. Fabricating a solid state nanopore with control over pore size and channel length is an obvious advantage it offers over the biological counterpart. In addition, high stability, adjustable modifiable surfaces and choice of integration into devices or expansion into arrays makes them all the more favourable.

Fabrication of solid state nanopores

There are many ways to fabricate solid state nanopores, a few techniques including chemical etching, focussed beam sculpting and Atomic layer deposition (ALD) are briefly discussed in this subsection. The many other different types of fabrication procedures and the various substrates for nanopore along with their advantages are explained elsewhere [112, 113, 114, 115].

Chemical etching

Etching holes into insulating layers has always been one way to create pores both micro and nano. Though it has a major advantage of low cost massive parallel production of nanopore arrays, it does suffer from low efficiency [113]. One of the more delicate etching technique is guided etching or ion track etching where ‘tracks’ are formed using high energy heavy metal ions (figure 3.3a) in a thin polymeric membrane (like polyimide, polycarbonate, polyethylene terephthalate) followed by chemical wet etching [116, 117, 112]. Nanopores as small as $\sim 1\text{--}2$ nm have been created via this technique but one

detriment is the very narrow pore angle of the pores formed through this technique that precludes translocation of polynucleotides [114].

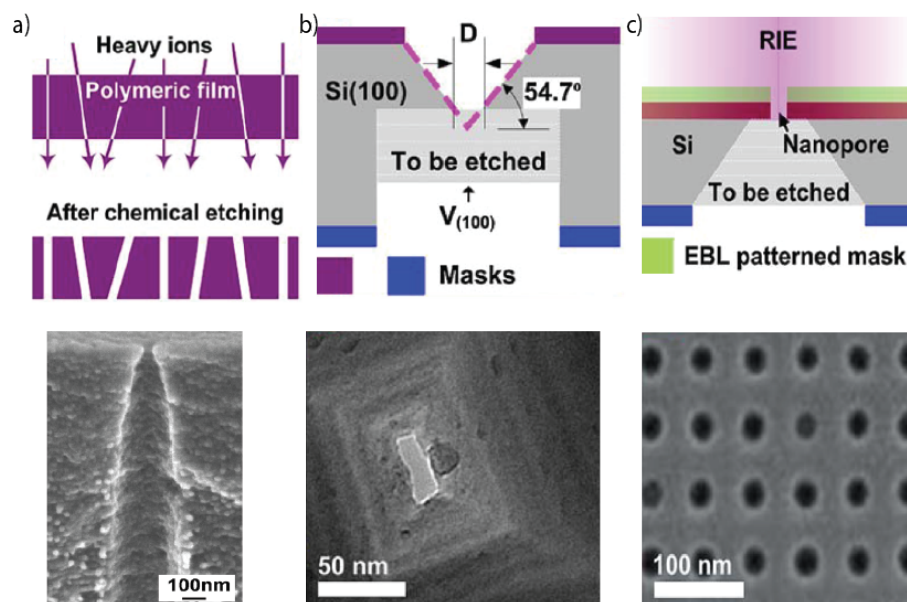


Figure 3.3: Chemical etching. The top panel explains the different etching processes in a schematic and the bottom panel contains Scanning electron microscope (SEM) images of example nanopores fabricated through the different techniques. a) Ion track etching mechanism depicting the path of heavy ions and resulting pore channels after chemical etching, the SEM image below shows the geometry of one such nanopore, b) anisotropic wet etching procedure wherein a standard micrometre pattern is created by a typical lithography process and then an inverted pyramid like structure is formed, then nanopores are created by etching the other side of the substrate using alkaline solution to produce pyramidal nanopores as seen in the SEM image underneath (15×38 nm pore size). c) Electron beam lithography (EBL) assisted reactive ion etching, first the pores are defined using electron beam etching and transferred onto the target layer with reactive ion etching, then the underside is etched away to create free standing pores, SEM image shows a representative array of sub 20 nm pore size. Figures adapted from Storm et al. [118].

On the other hand, anisotropic wet etching of semiconducting substrates like silicon (Si) offer robust, biocompatible integrated nanopore system. Figure 3.3b, shows the etching

process through which pyramidal nanopores are formed in Si membranes. Large arrays of pyramidal Si nanopores down to ~ 30 nm can be produced through this method and can also be easily tuned by changing the wet etch mask length–width ratios [113, 115]. Etching processes to produce even smaller nanopores (~ 13 nm) with feedback control mechanisms are also available [112].

In addition to the above, metal assisted chemical etching and metal assisted plasma etching are other ways of nanopore fabrication through etching. These methods can be used to form conical, cylindrical and even helical nanopores. More recently EBL assisted reactive ion etching [119] and improved techniques to fabricate nanopores of sub 20 nm sizes with embedded metal electrodes have also been proposed (figure 3.3c) [120].

Focused ion and electron beam sculpting

To overcome the challenges in chemical etching and realising controlled nanometre scaled nanopore fabrication became possible with direct nanodrilling of membranes with ion beam. Focussed ion beam was reported as a technique for fabricating solid nanopores first by Li *et al.* [121]. An Ar⁺ ion beam was used to drill a nanometre size hole in a silicon nitride Si₃N₄ membrane, the size of the pore was determined by the strength and heat of the ion beam and fine tuning of the pores were achieved through feedback mechanism of the detectors [121].

This gave rise to the ion beam sculpting technique that paved way for single molecule translocations through solid state nanopores that were of controlled nanometre dimensions. Further research on pore shrinking rates and different ions allowed fabrication of pores as small as 1.8 nm and nanopores have progressively been sculpted in various membranes including SiO₂, SiN, SiC, Al, Cr, Poly methyl methacrylate (PMMA) and polyimide [112].

Different sculpting techniques were then studied, including EBL of Si, SiO₂ and SiN [122, 123, 124]. Storm *et al.* in 2003 put forth the technique of using electron beams for nanopore sculpting [118]. Si, SiO₂ and SiN membranes produced via standard microfabrication technique and drilled into nanopores of about 20–200 nm by electron

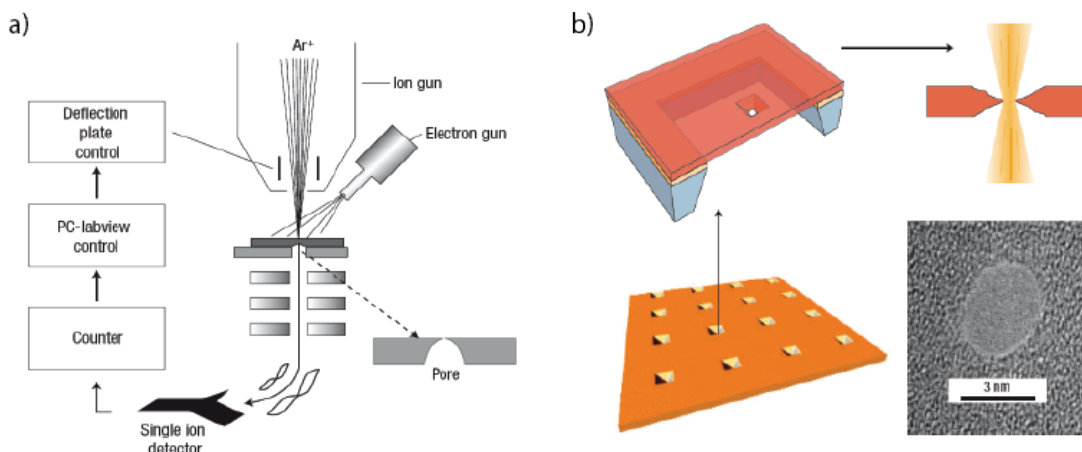


Figure 3.4: Schematic depicting nanopore sculpting techniques, a) the Ion beam technique that uses a focused ion beam to drill nanopores and b) A series of images explaining the electron beam sculpting process by Storm et al. [118] an array of pyramidal nanopores prefabricated by combined electron beam lithography and etching is then sculpted using TEM electron beam. Adapted from Li et al. [121].

beam lithography and etching were successively tuned down to ~ 2 nm with electron beam (figure 3.4). With wide field high intensity illumination using Transmission electron microscope (TEM), holes with pore size larger than the membrane thickness were enlarged whereas small holes shrunk, due to carbon deposition [118, 114].

Alternatively it was also observed that lower electron beam intensity will cause nanopore shrinkage as well [124]. Based on this technique and with further improvement boron doped silica nanopores and magnesium nanopores with sub 10 nm pores have also been rendered possible [125, 126]. Thus electron beam sculpting offers a nanometre scale modification technique with high precision and direct visual feedback at sub– nanometre resolution.

Direct milling of nanopores entirely by focusing the electron beam through TEM and SEM has also been studied extensively, nanopores produced through this method can be further modified with wide field electrons or ions as described above or any other shrinking techniques if required. SiN film modification in stable nanopores using Scanning transmission electron microscope (STEM) is yet another option, advantage of

STEM being the ability for lateral movement and pore size control essential for high nanometre level precision resulting in fine tuned pores of about 1.3–2.4 nm diameter [127].

Atomic layer deposition

ALD is another method of fabricating and shrinking nanopores with controlled nanopore size. ALD can deposit layers as thin as 0.1 nm, and its homogenous surfaces (conformed coating) also helps prevent any defects from prior fabrication processes. ALD has been used to deposit high dielectric constant materials like Al_2O_3 and TiO_2 to shrink nanopores. Alternative to silica counterparts Al_2O_3 surface possesses a positive charge and also score high on stability and signal to noise performance. In addition, the tuneable thickness of the Al_2O_3 membranes and diameter of the nanopore makes it a competitive candidate for nanopore sensing [112, 115].

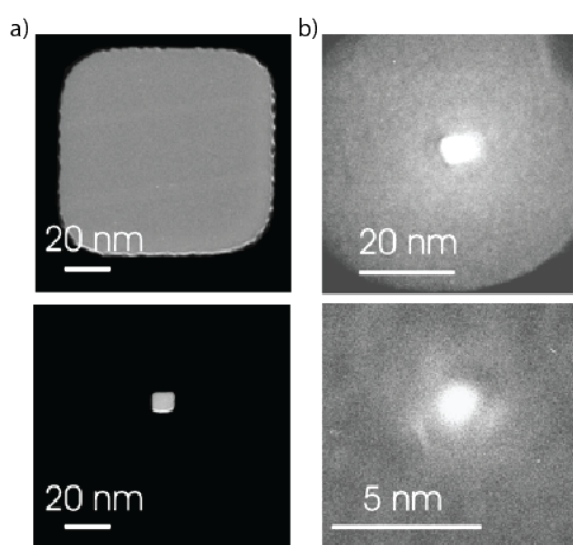


Figure 3.5: TEM images of nanopores before and after ALD. a) A square shaped nanopore fabricated via focused ion beam is shown retaining its shape after 500 layers of Al_2O_3 deposition to produce sub 10 nm pore diameter. b) A ion beam sculpted ~ 7 nm nanopore surface was deposited with 24 layers of Al_2O_3 using ALD to arrive at a 2 nm pore. Figure adapted from Chen et al. [128].

3.1.3 Hybrid nanopores

Integrating biological nanopores with their solid state counterpart gives rise to a new field of nanopores called the hybrid nanopores, thus the major limitations of the individual nanopores as discussed earlier could be overcome by combining them. The

idea of combining components of various nanopore systems include earlier reports of ion channels formed via lipid bilayers supported on teflon membranes (with 2 micron diameter pores) [129] and tens of μm glass pores [130].

Further improvement by White *et al.* saw generation of long-lived lipid bilayer suspended on 100 nm glass nanopores [131]. These glass pores were fabricated by first sealing a platinum wire inside a glass capillary and subsequent polishing and electrochemical etching to expose the platinum and produce a truncated cone shaped glass nanopore. Lipid monolayer deposition was achieved through modification of the glass nanopore with 3-cyanopropyltrimethylchlorosilane producing a hydrophobic surface. The lipid monolayers deposited on the inner and outer glass nanopore surfaces merge to form a stable bilayer (figure 3.6), that was found to be persistent for at least 2 weeks at room temperature and successful stochastic detection of heptakis-(6-O-sulfo) β cyclodextrin was demonstrated via the inserted α -HL.

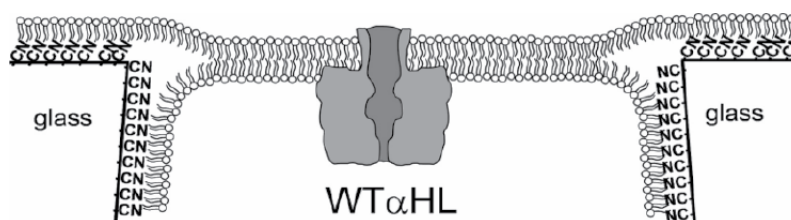


Figure 3.6: Ion channel lipid bilayer on glass, α -HL inserted in the lipid bilayer which was suspended on a glass nanopore, thus forming a hybrid capable of successful single molecule detection. Adapted from White *et al.* [131].

Moving forward, with the advent of solid state nanopores Hall *et al.* proposed α -HL insertion into SiN membrane nanopore [132]. For α hemolysin-SiN membrane hybrids, electrophoretic insertion was achieved by modifying the protein pore with a 3 kbp dsDNA at the end of the channel and the long overhang was used to pull the channel end into the SiN pore. Every stage of the protein pore entry into SiN could be monitored via the ion current traces such as, initial dsDNA translocation, pre-insertion of protein pore and finally hybrid formation. The stability of the hybrid nanopore was then tested via ssDNA translocation experiments.

Lately, an entire class of hybrid nanopores formed from DNA origami that allows for fabricating nanopores with desired structure and dimension have opened up various new possibilities in the field of nanosensing. Hybrid nanopores designed till now use two types of DNA origami structures, funnel and plate shaped (figure 3.7) and are incorporated with solid nanopores and glass nanopipettes (section 3.2) via different means. For example, Hernandez-Ainsa *et al.* [133] combined glass nanopipettes and DNA origami (figure 3.8a), this was achieved by simple trapping of the DNA origami onto the nanopipettes by applying a positive bias.

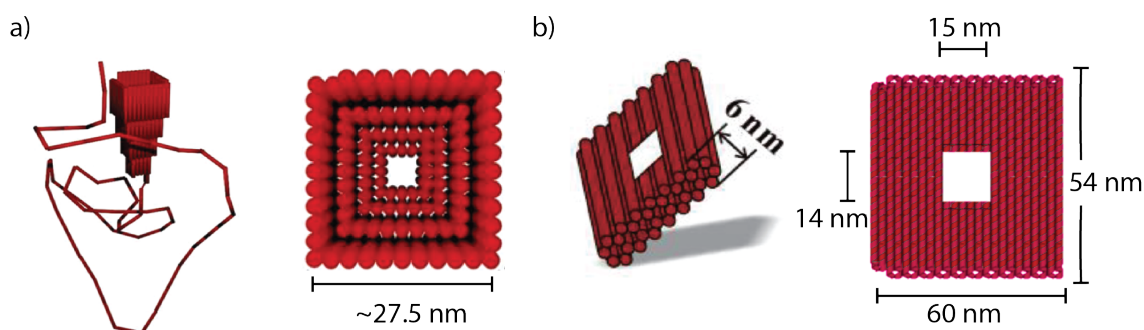


Figure 3.7: Two types of DNA origami structures used in hybrid nanopore formation. a) A funnel shaped DNA origami with a wider 27.5 nm opening with a pore size of ~ 7 nm and a vertical view of the same. b) Nanoplate DNA origami and the vertical view of the same. Adapted from Hernandez-Ainsa *et al.* [133] and Bell *et al.* [134].

Successful trapping was evident via the drop in ion current and increase in baseline noise and since the DNA origami cannot translocate through, as they are designed to be slightly larger than the pore of the nanopipettes, ejection of the trapped origami was also possible with reversal of voltage. Also by incorporating fluorphores onto the DNA origami, they were able to perform single molecule fluorescence detection of the hybrid nanopore formation in addition to ionic current detection. This setup was used for detection and controlled translocation of lambda DNA, moreover, the hybrid structures were further extended for specific ssDNA detection via modification of the DNA origami with complementary single stranded overhangs. A very similar integration system of trapping DNA origami nanoplates onto nanopores was also put forth by Wei *et al.* [135] for specific protein and ssDNA capture.

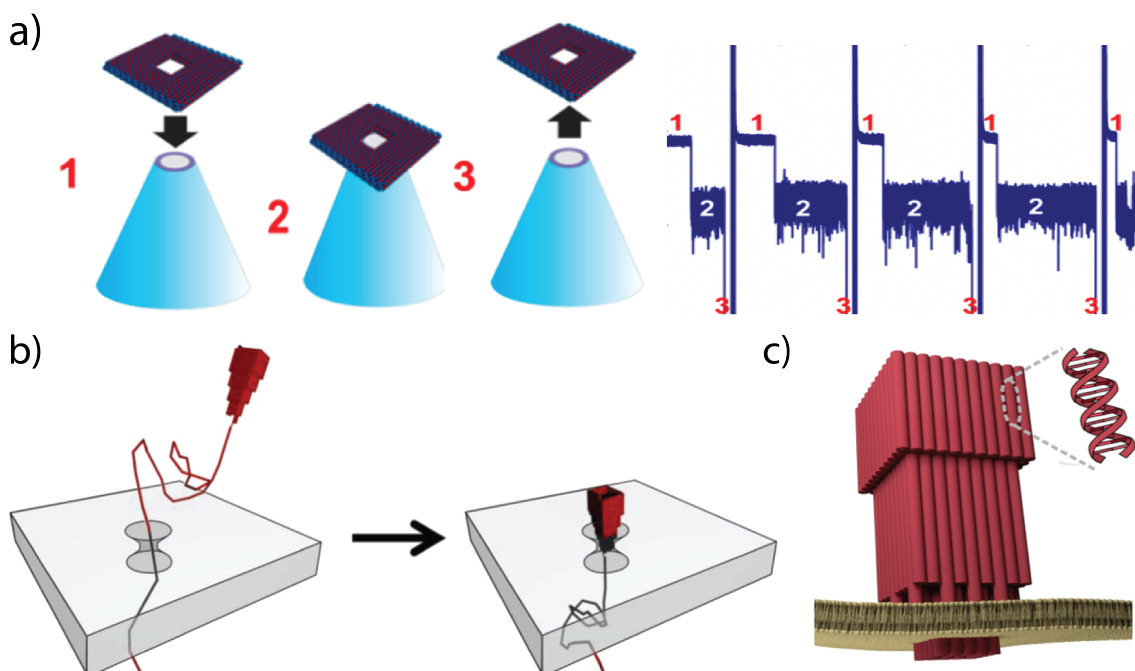


Figure 3.8: a) DNA nanoplatform–glass hybrid construction via application of voltage and ejection of the same with a opposite voltage. b) Hybrid nanopore formed by inserting DNA origami into silica nanopore via voltage application, the long strand of overhang DNA or leash helps the DNA origami to self–orient and insert into the nanopore. c) The first hybrid nanopore fashioned by inserting DNA origami in a lipid membrane. This artificial porin exhibited a pore size of 6 nm, large when compared to the naturally occurring pore forming proteins and such are also ideal to study and mimic large toxins and nuclear pore complex apart from molecular sensing. Figures adapted from Hernandez-Ainsa et al., Bell et al. and Gopfrich et al. [133, 134, 136].

On the other hand DNA origami can also be incorporated within nanopores via insertion (figure 3.8b), i.e., using solid state nanopore as a frame conical DNA origami can be inserted into the solid nanopore as a top piece via voltage application, through this approach hybrid nanopores have been successfully formed in solid state silica [134], these hybrid nanopores can also be dismantled and reformed in a controlled manner via voltage. Using this system the authors successfully detected translocation of dsDNA. This system was later developed into a multiplexing setup by replacing silica nanopores with glass nanopipettes. The glass nanopipettes with their own set of advantages as explained in

the following chapter allow simple integration to a common reservoir with multichannel analyte detection system [137].

This fashion of DNA origami insertion is also used to produce hybrid nanopores in lipid membranes, a representative example being formation of the largest synthetic pore in lipid membrane as shown in figure 3.8c [136]. These DNA origami hybrids constructed via insertion into lipid membranes are termed protein like DNA pores, and large amount of research has been conducted using them in the span of few years for various single molecule detection applications [138, 139, 140, 141].

Apart from DNA origami incorporation nanopores have also been modified biologically and chemically to impart specificity and sensitivity, for example, Iqbal *et al.* reported a hybrid nanopore design by functionalising biological probes on silicon solid state nanopore channels. These specifically modified nanochannels, which were used to detect short ssDNA, are very sensitive towards the particular target of interest, and can detect single bp mismatch [142] (figure 3.9).

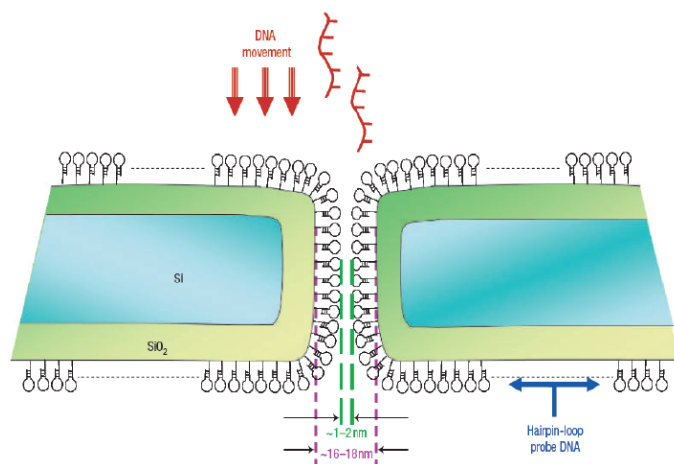


Figure 3.9: Hybrid nanopore formed through amine modified hairpin loop functionalisation on nanopore channel, shown with nanopore size before and after the modification. Schematic adapted from Iqbal *et al.* [142].

These selective solid state nanopores functionalised with amine modified DNA probes (hair-pin loop) were successfully used for ssDNA detection with high selectivity, thus by reducing the size of the nanopore effective selective translocation and detection of ssDNA targets were made possible.

Selectivity towards a specific target for high sensitivity detection through nanopores have

been a constant target in both biological and solid state nanopore design and development. Hybrid nanopores formed by combining biological and solid state nanopores discussed above show clear ways to overcome that challenge by imparting improved specificity, sensitivity and the much needed adaptability for molecular sensing and DNA sequencing experiments. Hybrid nanopores formed via DNA origami also overcame the issue of fixed pore size thus expanding the range of analytes that could be detected through the system. Hybrid nanopores also widen the options of nanopore functionalisation for selective target capture and also extend the possibilities of integration with other systems.

3.2 Nanopipettes

3.2.1 Introduction

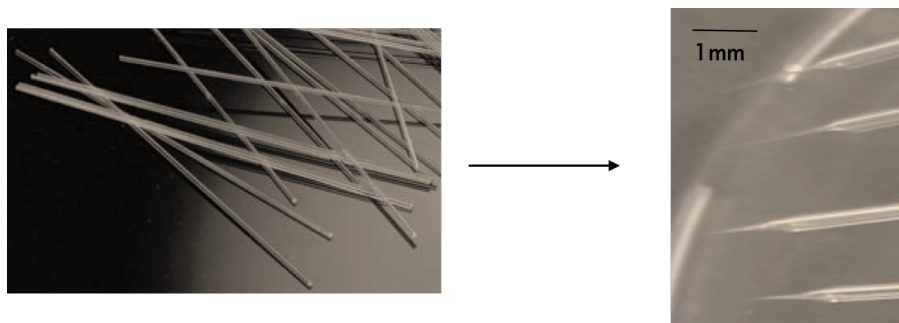


Figure 3.10: *Nanopipettes fabricated from glass capillaries.*

Alternative to all these nanopores are the glass nanopipettes, nanopipettes are a type of solid state nanopores fabricated from glass capillaries with highly tuneable pore sizes with nanometre resolution. As their name suggests they are shaped like the macro glass pipettes with a long base of a few millimetre diameter that forms a conical shank and terminates with a nanometre scaled opening. Figure 3.10 shows images of glass capillaries and how the resulting nanopipettes look to the naked eye.

Nanopipettes in this work strictly refer to glass pipettes upto few hundreds of nanometre in pore size, although the definition could also be extended to nanoelectrodes made from

these pipettes and ultra-microelectrodes primarily used for electron transfer studies as explained elsewhere [143]. There are also carbon nanopipettes which are produced by depositing the carbon tube inside glass substrate and then exposing the carbon tip via etching [144, 145]. But to stay within the scope and relevance of this PhD thesis we will discuss in detail only about glass nanopipettes.

The quickest and easiest method of glass nanopipettes fabrication is through laser pulling. With a high reproducibility rate and controlled size, shape and geometry the process can be carried out on the bench and do not need clean lab facilities like other solid state nanopores. Also, unlike their biological counterparts, glass nanopipettes are robust and stable chemically and could be operated under a variety of pH buffer conditions [143, 146, 147]. Quartz and borosilicate (figure 3.11) are the most used substrate of choice today for nanopipette fabrication via laser pulling. With a higher melting temperature than borosilicate, quartz or fused silica is preferred due to their low electrical noise [148, 149] superior quality and mechanical strength (to penetrate tissues and cells without impairment) [150].

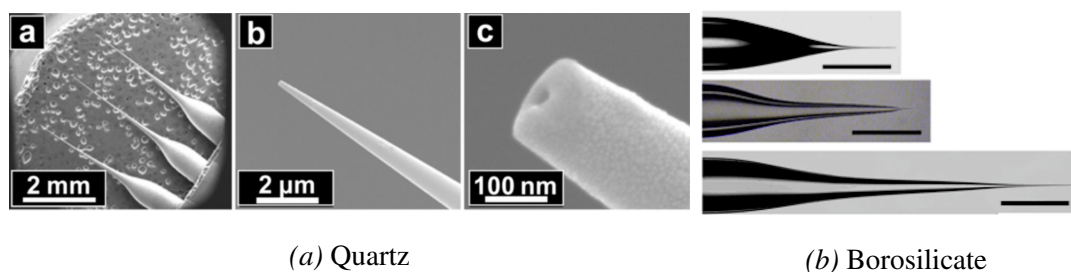


Figure 3.11: Representative Scanning electron microscope (SEM) image of (a) quartz and (b) borosilicate nanopipettes. Figures adapted from Sa and Baker [151] and Bafna et al. [152].

History of nanopipettes

Glass capillary micropipettes with very fine tips were first fabricated via hand by Barber in the early 20th century [153]. The methodology involved the exact procedure of the modern laser pullers but made use of a burner to heat and soften the glass capillary which

was then manually pulled at both ends with tweezers (figure 3.12). These micrometre sized pipettes were successfully used for delivery of single cells (bacteria) and extraction of fluids from cells [154, 155]. Barber's method of micropipette fabrication was then sophisticated and improved to pull needles less than one half micron in size from jena glass tubing about 5 mm diameter, as mentioned by Kite *et al.* for studying marine ova [156, 157, 158]. The following years saw Barber's micropipettes adapted, modified and improved for many applications [159, 160, 161] including electrical stimulation of living cells [162] and for use in electrophysiology as intracellular electrodes [163, 164, 165, 166, 167, 168, 169].

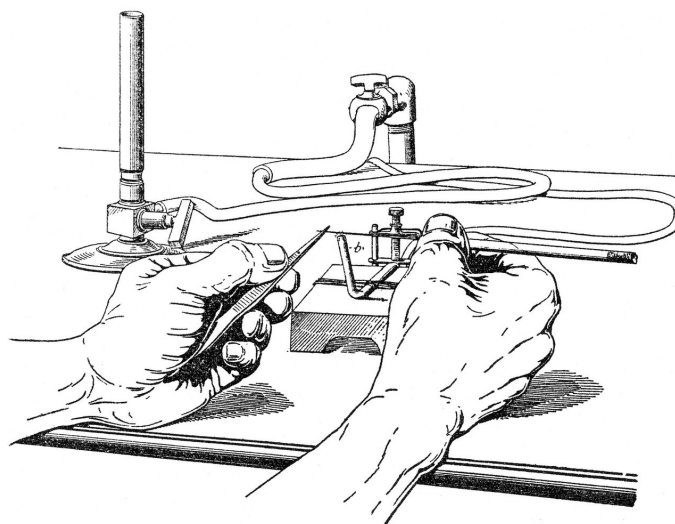


Figure 3.12: Barber method of pulling glass micropipettes, adapted from Barber [155].

This time period also saw advancement of plant cell microelectrodes to be used successfully in single animal cells [170, 171, 172, 173]. Hand pulled pipettes that were consistently sharp and fine, and could pierce animal cells without damage were successfully used to measure potentials in frog muscle cells with minimal pipette resistance with hardly any junction potential [174, 175]. From 1950s glass micropipettes were no longer hand pulled, but via mechanical and electrical means [176] and later glass pipette fabrication reached even more sophisticated mechanisms [177].

Apart from their use as electrophysiological tools another famous application is detecting voltages and currents from ion channels. The famous patch clamp technique using the

micropipettes for current and voltage detection in microchannels was developed in the 1970s, and nanopipettes with diameters as small as 45 nm to be used as reference electrode was produced by Brown and Flaming for intercellular measurements in 1977 [178]. The Nobel prize in 1991 for medicine was awarded for the patch clamp technique. From there on several single ion channel studies involving micro and nanopipettes were conducted [179] and thus began the use of nanopipettes in analytical chemistry.

Slowly the use of micropipettes spread to various fields, micropipettes as probes for Scanning electrochemical microscope (SECM) was investigated by Solomon and Bard in 1995 [180] and the first ever ionic current rectification behaviour by nanopipettes [181] was reported in 1997. Also, the unique geometry and tip size made nanopipettes widely adaptable for use in analytical measurements and as probes for Scanning probe microscope (SPM), and subsequent years witnessed nanopipettes widely employed in various techniques like SECM [182, 183], Scanning ion conductance microscopy (SICM) [184, 185, 186], Hopping probe ion conductance microscopy (HPICM) [187, 188], Near field scanning optical microscopy (NSOM) [189] and AFM [190, 191, 192].

Recent years have seen nanopipettes, with their nanoscale characteristics along with the wide choice of modification, and ease of integration, capable of many applications in various fields including nanofluidics, sensitive analytics and diagnostics, electrochemical and optical biosensing, nanobiopsy, and nano deposition and writing [2, 147, 146, 193, 194].

3.2.2 Fabrication of nanopipettes

While past decades have seen Flaming/Brown type pullers for micro and nanopipettes production from borosilicate and quartz capillaries, laser pipette puller P2000 (Sutter instruments) are more commonly in use nowadays. The laser pipette puller makes use of a CO₂ laser heat source to melt the glass capillaries instead of a heating filament (Platinum: Iridium 90: 10) as used by the Flaming/Brown models. The laser heat source provides a huge advantage to work with quartz (fused silica) capillaries as a pure and

strong form than other standard glass capillary. Also, the high precision to apply user defined heat (amount and distribution of laser) onto the glass makes it possible to obtain variety of nanopipette pore dimensions and taper length.

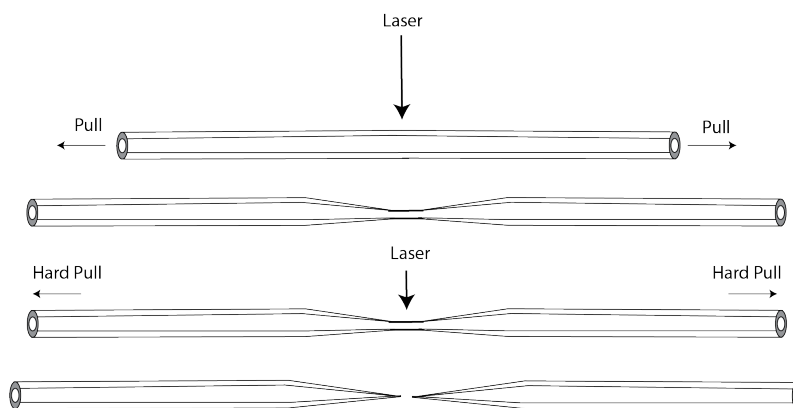


Figure 3.13: Schematic of nanopipette fabrication from glass capillary.

The mode of operation comprises a beam of laser of specified power and spread (distribution) focused on the glass capillary for a specific time thus melting the glass producing a taper, then the taper is further heated and pulled by the ends by specified force producing two symmetric conical nanopipettes. The nanopipette pore size and pore geometry can be tailored via the pulling parameters namely HEAT –specifies the output power of the laser, and the amount of energy supplied to the glass, FILAMENT (FIL) –the scanning pattern and scanning length of the laser beam, VELOCITY (VEL) –the velocity of the initial pull before the hard pull is executed, DELAY (DEL) –controls the timing of the start of the hard pull in relation to the deactivation of the laser after the initial pull, PULL –the force of the hard pull [195].

The right parameters for producing a nanopipette with specific tip geometry and size is through replication, trial and error. Generally, increasing heat, velocity and pull parameters increases taper length and decreases pore diameter [195], but these parameters for a specific pipette size and geometry would change from puller to puller. Also, as the quality and reproducibility of a puller will also vary with room temperature, humidity and alignment of the laser itself, it is very important that the same puller is used for all experiments of a study and that the puller is kept in the same environment and not

moved in-between studies. A representative table showing consistent nanopore size for nanopipettes pulled on different days using the same parameter and puller is shown in appendix A table 5.

3.3 Properties of nanopipettes

The very small size coupled with the asymmetrical geometry of the nanopipette tip gives rise to many unique features. A number of intriguing phenomena arise due to the anisotropy of the nanopipette system including asymmetric electroosmotic flow [196], ionic current rectification and concentration polarisation [197, 198]. Some of these phenomena will be discussed in detail to understand transport of molecules through the pore of the nanopipette and the resulting ion current.

3.3.1 Surface charge and diffuse double layer

Surfaces immersed in an electrolyte solution carries a surface charge because of specific ionic adsorption on the surface or dissociation of protons from surface groups. This leads to the formation of an electrical double layer at the interface between surface and the electrolyte solution due to the accumulation of diffuse ionic layer in solution to compensate the surface charge [199]. At the same time there will be homogeneous distribution of ions in the solution due to thermal motion. Thus the solid/liquid interface would be rather complex with multiple layers.

Gouy–Chapman–Stern model explains surface–electrolyte interface as a layered structure with an immobile inner layer and an outer diffuse layer. The model proposes that the inner layer made up of specifically adsorbed ions and solvent molecules is bound to the surface, called the Inner helmholtz layer (IHL) or stern layer. Whereas the outer layer has mobile solvated ions in solution exhibiting long range electrostatic interaction with the charged surface, this is termed the diffuse layer or Outer helmholtz layer (OHL) and the nonspecifically adsorbed ions in this layer extends from the OHL into the bulk solution

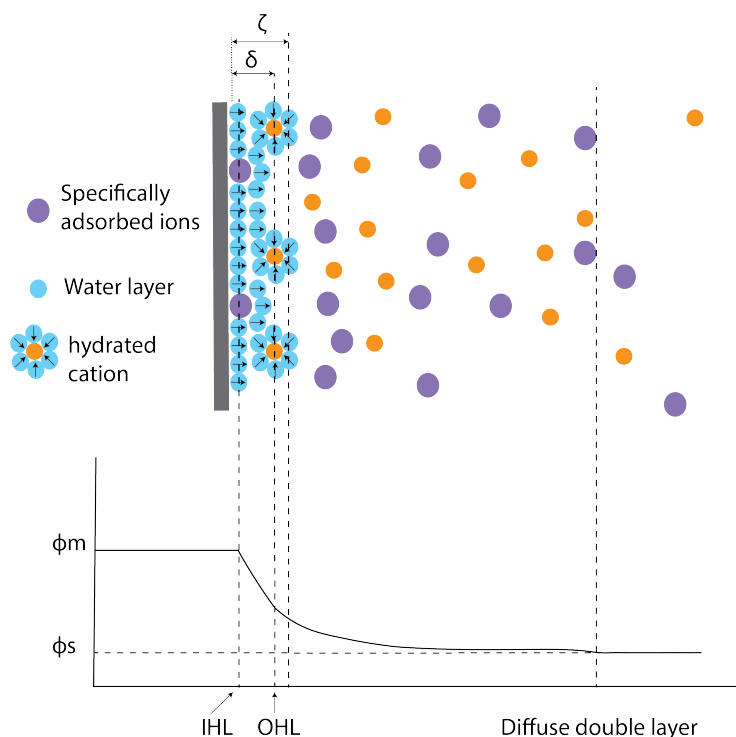


Figure 3.14: Gouy–Chapman–Stern model explaining the distribution of ions in a double diffuse layer at the solid–liquid interface.

the thickness of which approximately equal to the Debye length. This is called the Double Diffuse Layer (DDL).

So the DDL formed to neutralise the charged surface in turn causes an electrokinetic potential (surface potential) between the surface and any point of mass of the electrolyte. The surface potential is related to the surface charge and thickness of the double layer and this potential drops off linearly in the Stern layer and exponentially in the diffuse layer until zero at the imaginary double layer boundary in the bulk solution [200, 201].

3.4 Surface charge and conductance in nanopipettes

Transport of ions through the confined geometry of a nanopipette is effectively dependent on their surface properties due to their large surface area to volume ratios. A diffuse layer of a quartz nanopipette in KCl (pH 6.8) electrolyte will carry a negative

charge (due to the ionisation of functional groups ($-\text{OH}$) on the surface) which will be compensated by an excess of K^+ ions accumulation near the surface through electrostatic interactions. And consequently clouds of excess K^+ ions and depleted Cl^- ions exist near the glass surface–electrolyte interface thus forming the DDL. The DDL in presence of an electric field will contribute to the electric current (flux of ions) across the nanopipette depending on the pore size, electrolyte concentration and thickness of the DDL [181, 202, 203].

For example, when the DDL thickness is comparable to the diameter of a nanometre sized tip, the current (ion flux) must pass through the diffuse layer and the electrostatic interaction between ionic species and surface charges will affect ion transport properties. On the other hand, if the DDL thickness is negligible compared to the tip diameter, it will not affect ion movement, because most of the ions migrate through the electrically neutral (bulk composition) zone of the electrolyte. Thus the I–V characteristics of nanopipette will be strongly affected by the DDL thickness at the orifice of the quartz pipette [181, 204, 205, 206]. Ion current rectification is further discussed in the chapter 7.

Now, a nanopore with charged inner wall will thus have a varied ion distribution inside the pore to that is in the bulk solution. At high salt concentrations influence on the ion current is exerted by the charge carriers in bulk solution and so the conductance will increase with increase in number of charge carriers, but the counter–ions that shield the nanopipette negative surface also contribute to the conductance. Thus the overall ion current through the pore is thus a sum of the contributions from bulk ions and counter ions shielding the surface and is represented by equation 3.1 adapted from Smeets *et al.* [207].

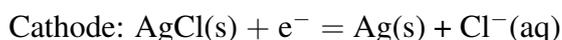
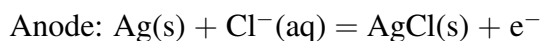
$$G = \frac{\sigma d_{\text{pore}}^2}{4 L_{\text{pore}}} [(\mu_{\text{K}} + \mu_{\text{Cl}}) n_{\text{KCl}} e + \mu_{\text{K}} \frac{4\sigma}{d_{\text{pore}}}] \quad (3.1)$$

where, d_{pore} is the pore diameter, L_{pore} is nanopore length, n_{KCl} is the number density of potassium or chloride ions, e is elementary charge, σ is surface charge density in the pore, μ_{K} and μ_{Cl} are electrophoretic mobility of the respective ions.

In the equation, the first term is in relation to the bulk conductance and the second term represents the surface charge contributions. At KCl densities higher than $n_{\text{KCl}} \gg \frac{2\sigma}{d_{\text{pore}}}e$ the bulk conductance takes over as mentioned before and as n_{KCl} is lowered surface effects dominate the conductance. For more detailed experimental measurements on the salt dependence of ion and DNA translocation, refer Smeets *et al.* [207].

3.5 Electroosmosis and electrophoretic forces in a nanopipette

Consider a quartz nanopipette filled with and immersed in KCl electrolyte, two Ag/AgCl (non polarisable) electrodes inside the nanopipette and outside in the bulk electrolyte completes the connection. On application of a voltage, the transport of ions in and out of the pore of the nanopipette provides the baseline current signal [208], as shown in the figure 3.15. Two reversible electrochemical reactions occur at the electrodes, an oxidative reaction at the anode results in an electron migrating through the wire to produce current (generating a charge imbalance) which results in K^+ cation migration towards the nanopore. A reverse reaction at the cathode produces Cl^- that migrates towards the pore.



In such a nanopipette system with nanoscale pore size and conical geometry the applied potential results in a large pore resistance in the Mohms to Gohms range and the field gradient occurs almost entirely at the tip and vicinity of the nanopipette [209]. Thus, the electric field inside the pore becomes the driving force for the electrophoretic translocation of charged analytes. If a negatively charged analyte (DNA) is added inside the nanopipette and a negative potential applied, the analyte is electrophoretically translocated towards the anode from inside of the nanopipette to the outer bulk electrolyte

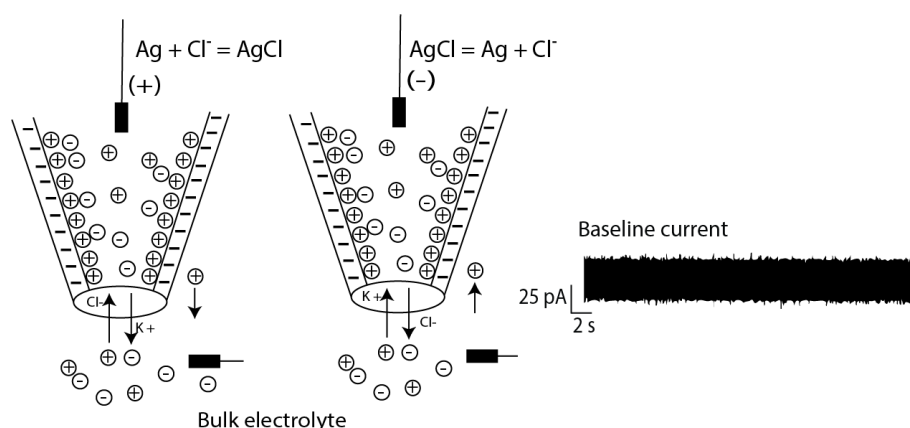


Figure 3.15: Schematic of the processes that occurs at the electrode/electrolyte interface. The quartz nanopipette surface has a negative charge and the arrows indicate the movement of the ions in and out of the pipette with respect to the voltage applied.

thus causing a transient modulation in the otherwise stable baseline current [210].

Now, a charged surface immersed in a liquid electrolyte in the presence of an electric field parallel to the surface, also results in a flow of ions adjacent to the surface. The interface between the surface and the electrolyte forms a double layer, with excess cations (K^+) relative to the bulk concentration as explained before. Under an applied electric field, the ions in the diffuse part of the double layer will move along the gradient and drag their solvation shells thus resulting in a net flow of liquid in the direction of the electric field, an effect known as electroosmosis.

Electroosmosis may play a role in nanopipette translocation experiments with their influence dependent on nanopipette and analyte surface properties, and concentration of electrolyte [211, 212, 213]. For example, electroosmotic effects are negligible with DNA samples (potentially due to its sizable fixed charge) with translocations driven largely via electrophoretic force whereas, proteins with variable charge with respect to electrolyte conditions (pH, ionic strength) could have combined electroosmotic and electrophoretic forces governing their translocation [200].

3.6 Conclusion

Thus this chapter discussed how research with biological nanopores and their development and further advancement to fabricate synthetic nanopores lead to a truly nanopore regime of detection. Nanopipettes, after their inception many years ago for applications in electrochemistry, with their facile and low cost fabrication coupled with versatility have had significant impact in various fields including analytical science and bionanotechnology.

Also, as described in previous sections, the adaptable use of glass nanopipettes to produce hybrid nanopore system further extends their applicability and as such have been extensively researched for biosensing studies, liquid–liquid interface studies and as probes for microscopy techniques.

The chapter also described the principle of translocating charged molecules using resistive pulse sensing and also presented some key theories like surface charge, double diffuse layer and ion conductance effects which are important to understand single molecule detection and sensing which makes up the work presented in the following chapters.

Chapter 4

Review of Literature

In this chapter existing literature on single molecule detection using nanopores including nanopipettes as well as related background about DNA nanostructures is reviewed to rationalise this project. The sections explain the application of nanopipettes in the field of single molecule analysis. Predominantly papers that utilize change in current as cue for biomolecular translocation for various functions are discussed, but the review will also consider the significance of optical detection and combined electrical and optical detections in nanopipette translocations.

Moreover, the review will explore the challenges in single protein molecule detection using nanopores in general and highlight the various strategies that have been implemented in the recent years. Particularly, emphasis will be placed on the use of ‘carrier molecules’ including long linear dsDNA, Lambda DNA, nanoparticles and antibodies.

Moving forward, the review will introduce the existing literature of DNA nanostructures in the field of nanopores for hybrid nanopore formation. Subsequently, discussions on the potential of DNA origami nanostructures as a versatile tool for combination with nanopipette translocation and detection of single entities is put forward. Thus a justification between the existing carrier molecule approaches and the usage of DNA origami carrier approach used in this thesis is drawn.

4.1 Nanopores for single molecule analysis

Since the first implementation of biological [94] and solid state nanopores [121] for single nucleic acid detection, a plethora of research has been conducted covering a wide range of nanopore applications in both biotechnology and analytical fields. While the field has seen significant achievement in nanopore DNA sequencing [208], it has also empowered a vibrant area of research for interrogating biomolecules [4] including linear DNA, RNA, proteins, nanoparticles, biological nanostructures and plasmids.

To portray more specifically, DNA translocation experimental studies to monitor DNA translocation dynamics and conformation, analysis of several nanopore factors and their effects including criteria like bias voltage, surface charge of nanopores and electrolyte concentration on DNA translocation have been studied [214]. Another important research area that has been extensively looked at is the use of nanopipettes for biosensing, especially for detecting protein biomarkers in clinical and medical diagnosis.

In a standard nanopore experiment target molecules are translocated through the pore via an applied external electric field, which results in a transient change to the otherwise steady current. Information extracted from these modulations is used to detect and characterise different target analytes. However, while numerous protein biomarker detection in biological and solid state nanopores and nanopipettes both directly and indirectly have been successfully demonstrated, chief setbacks such as reduced selectivity, nonspecific interactions with pore walls and poor signal to noise ratio (especially if the analyte size is smaller than the nanopore opening) still remain to be tackled.

Recent simulations showed that translocating a <100 kDa protein via solid state nanopores with pore size ~ 10 nm or less using a 10 kHz bandwidth current amplifier only detects 0.1% of the total translocation events. Thus while direct protein detection via nanopores is possible, it seriously suffers from low temporal resolution and results in only a fraction of events to work with [215, 216]. Hence a more robust nanopore

detection system capable of high sensitive detection becomes imperative. Moreover, the need for specificity while working with complex samples demands improved alternatives with ability to differentiate similar sized proteins.

Thus a variety of strategies have been implemented to overcome the above mentioned problems including development of high bandwidth electronics [19, 20] and careful selection of electrolytes [18, 17] to slow down translocations. Fraccari *et al.* built custom made electronics capable of high bandwidth low current detection in ~ 20 nm pore sized quartz nanopipette translocations, their platform combined ultra-low noise current reading and voltage biasing with zapping and automatic reverse biasing for versatile nanopore sensing.

Similar improvements with high measurement bandwidth was put forward using SiN nanopore integrated with custom CMOS-integrated nanopore (CNP) amplifier. With ultra thin solid state nanopores the authors were able to detect transient features within translocation events with a signal as large as 30 nA and temporal resolution down to 100 ns, which are otherwise masked at lower bandwidths. Another study by Larkin *et al.* [217] combines high bandwidth electronics with ultrathin hafnium oxide (HfO_2) and silicon nitride (SiN) membranes of around 5 nm pore size for effective detection of sub 30 kDa proteins (Proteinase K and RNase A). The pore-amplifier combination was able to detect short current events down to $2\text{--}2.5 \mu\text{s}$ dwell time with a 250 kHz bandwidth which resulted in a reasonable capture rate.

Alternatively, the bandwidth requirements can be reduced by an order of magnitude by slowing down the molecule translocation speed. For example, the viscosity of the electrolyte solution plays an important role in analyte translocation, studies show that increasing the electrolyte viscosity results in a linear increase in translocation dwell time with as much as 5 times increase in temporal resolution [17].

Also, experiments with respect to bias voltage indicate a linear relationship to current blockages and inverse proportionality to translocation dwell times. But it should be noted that DNA translocation for an applied voltage with respect to target size and nanopore

size is also strongly influenced by the nanopore energetic barrier [218], which the target molecule needs to overcome for successful translocations.

For example, in a protein nanopore, DNA translocations are not detectable below ~ 50 mV but SiN nanopores were shown capable of DNA translocation at a bias voltage as small as ~ 20 mV [17]. A strong dependency of target translocation towards temperature has also been demonstrated in both solid state and biological nanopores, with decrease in temperature leading to decrease in current blockage and increase in dwell time.

Though by a combination of the above discussed electrolyte factors one could slow down analyte translocation, this is achieved at the expense of signal levels, i.e., slowing down translocation could also result in decrease of conducting ions and inhibit molecular flux into the pore which decreases current blockage signal.

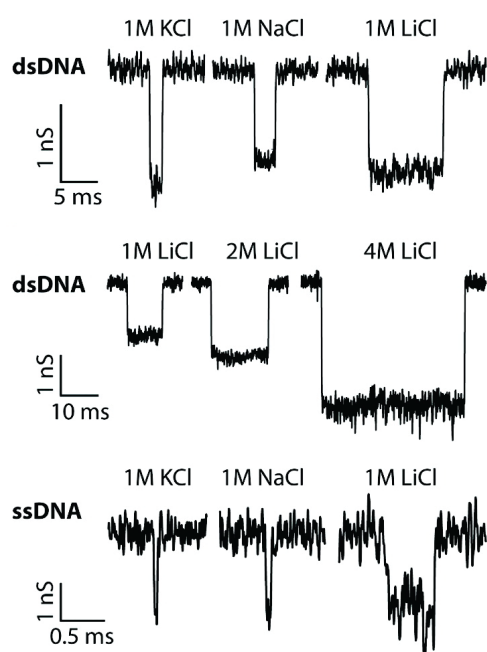


Figure 4.1: Ion current traces of dsDNA and ssDNA translocation events in different concentration of various ionic solutions, first and last row shows a clear correlation of increase in dwell time with change in electrolyte from KCl to NaCl to LiCl, centre row shows further decrement of translocation time with increase in LiCl concentration from 1 M to 2 M to 4 M. Figure adapted from Kowalczy *et al.* [18].

Instead one could simply use different electrolytes like LiCl and NaCl in the place of KCl to considerably slow down molecules in a nanopore. Various monovalent ions (K, Na, Li) have different effects on analyte molecules, and therefore the charge of the analyte due to analyte-counterion interactions impacts an effect on translocation. As shown by Kowalczy *et al.* [18] 48.5 kbp dsDNA molecule translocation in 1 M KCl, NaCl and LiCl

ionic solution showed increasing translocation time in that respective order. With respect to LiCl, further increase in electrolyte concentration to 4 M slowed down the DNA by a factor of 10 resulting in a very good signal to noise ratio.

Molecular dynamics (MD) simulations at a molecular level with a 8 nm pore also demonstrate that the minimum bound duration for 4 M ion concentration is again dependent on the type of ions, with the most durable bonds formed by LiCl followed by NaCl and then KCl. Though the study indicates that LiCl at high concentrations offer certain advantages for analyte translocation, such as increased ion current signal, the electrolyte system becomes a hinderance when one wants to extend the technique to physiological conditions and sensitive biological samples.

Another way around the setbacks is to modify the nanopores, both chemical and biological modification of nanopores [142, 219] have been attempted. For instance, Yusko *et al.* made use of a bio-inspired (pheromones detection by insects) approach to detect single molecules (streptavidin, anti-biotin fab fragments and anti-biotin antibodies) by coating solid state nanopores with lipid bilayer. The biotinylated lipid bilayer formed by small unimellar liposomes was utilised as means for fine tuning the nanopore size via choice of lipids with respect to the target and for functionalising target specific ligands in and around the nanopore (figure 4.2a).

Due to the fluid nanopore coating, translocation of molecules after ligand capture was possible with increasing frequency as the specific ligands on the mobile sheet of lipid layer helped bring the proteins from the bulk solution to near the pore and subsequent translocation via 2 dimensional diffusion, as opposed to detection of analytes with permanently fixed surface modifications [220, 221]. Translocation of lipid bound proteins also helped with slowing down the translocation due to the high viscosity of the lipid bilayer making possible time resolved detection.

The study was also extended to demonstrate the ability of fluid bilayer to prevent nonspecific interactions or absorption and facilitate smooth translocation of aggregate prone proteins (AB peptides) preventing clogging of nanopores.

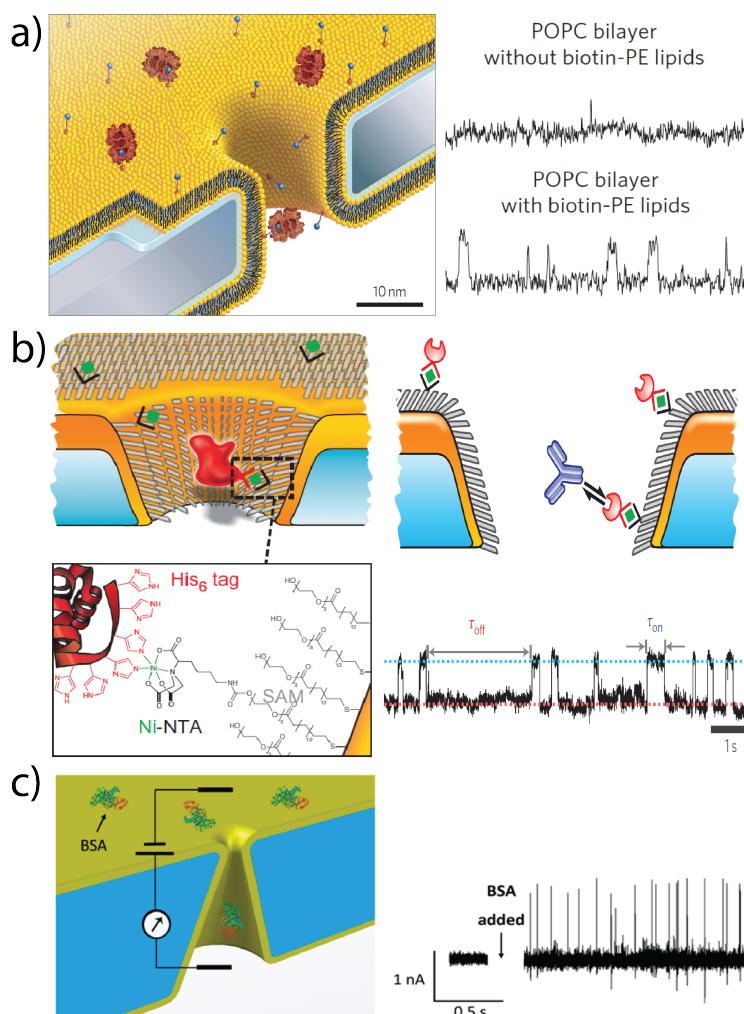


Figure 4.2: Biological and chemical modification of nanopores and resulting ion current traces a) lipid (POPC) coated SiN nanopore with illustrative streptavidin binding to the specific lipid anchored biotin-PE. b) Gold coated nanopore with SAM of matrix thiol and NTA receptor thiols, the image also shows the NTA receptor specifically binding to a His6-tagged protein. c) Single conical nanopore etched from poly(ethylene terephthalate) (PET) foil irradiated with Au ions coated with Al_2O_3 and ion current trace events corresponding to translocation of BSA. Abbreviations POPC: 1-palmitoyl-2-oleoyl-glycerol-3-phosphocholine, Biotin PE: 1-oleoyl-2-(12-biotinyl(aminododecanoyl))-sn-glycerol-3-phosphoethanolamine. Adapted from Yusko et al. [219], Wei et al. [222] and Wang et al. [223].

Apart from biological functionalisation solid state nanopores (SiN) have also been chemically modified, metallic (gold)–solid state nanopores chemically modified with nitrilotriacetic acid (NTA) receptors was used for detecting protein molecules [222] with ion current trace representing long lasting dwell time events observed for target binding and translocation.

For this, a mixture of ethylene glycol terminated SAM and NTA receptors were assembled on the gold surface, while the NTA binds His–tagged proteins specifically and the SAMs prevents nonspecific protein binding onto the pore walls of solid state nanopores. Detection of proteins binding to the receptor was deduced from the ion current jumps and analysing the dwell time. The system was also used to detect antibody binding to the same protein, thus demonstrating a sandwich sensing assay, figure 4.2b.

Fine–tuning properties of nanopore inner surface has also been shown to facilitate direct detection of proteins, for example Bovine serum albumin (BSA) detection through Al_2O_3 modified nanopores was reported by [223] as shown in figure 4.2c. Atomic layer deposition of Al_2O_3 onto PET conical nanopores both reduced its pore size just about a little greater than the BSA and imparted an positive charge, capable of weak interactions with the protein target, onto the otherwise negatively charged wall. This weak interaction served to reduce translocation time and subsequent well defined signals were obtained.

Another option, is to simply use single molecule fluorescence and attain optical detection of the translocations. Since optical approach allows for direct observation of translocations it also prevents any misinterpretation regarding single molecule translocations. Recently, SiN nanopores was used for studying 2.8 kbp dsDNA end labelled with fluorophore Cy3 using both ion current and fluorescence for detecting translocations [21], the native fluorescence of SiN was effectively reduced by treating the membrane with a dose of He ions. Though simultaneous synchronised electro–optical measurements was not possible with this system, the study successfully demonstrated parallel optical detections in an array of nanopores.

4.2 Carriers for protein detection

Alternatively, several research groups have also examined the use of carrier molecules to overcome the above said setbacks. This includes the novel method of utilising long dsDNA strands to detect biomolecules bound to the DNA, the underlying principle is to make use of the secondary level current (sub level) that transpires in addition to the blockage current of dsDNA upon target binding. As a consequence, by monitoring the ion current pattern one could detect the biomolecules in the sample and also extract information on their binding process.

Thus a large carrier molecule—like dsDNA—acting as an anchor could effectively slow down the protein target, impart specificity and selectivity and also provide a good signal to noise ratio. Recently, several groups have in effectuation applied this concept for several promising applications, several different carriers apart from dsDNA have also been experimented with. This section will discuss a few representative examples.

4.2.1 Qualitative detection

Among the work with dsDNA carriers, Bell and Keyser [23] made use of long linear DNA strands as backbone to form dumbbell shaped protrusions and modified some regions of the DNA to conjugate antigen molecules thereby essentially forming a barcoded antibody detection system.

The double stranded backbone was formed by using a 7.2 kbp long ssDNA hybridised to several 38 bp long oligonucleotides, the DNA dumbbell hairpin structures were made of 28 bp that projected from the dsDNA backbone with an additional 20 bp for attachment to the backbone. The dumbbells were placed 20 bp apart and forms a left handed helix around the backbone, dsDNA with varying number of dumbbell projections (5, 17 and 29) were tested to arrive at a compromise between number of hairpins needed and space left on the backbone for high accuracy read and signal size. A five section 11 hairpin

projection was thus constructed by labelling the first and fifth sections as controls for start and stop of the barcode, and changing the 2nd 3rd and 4th section as ON (with hairpins) and OFF (remove hairpins to form dsDNA) signals.

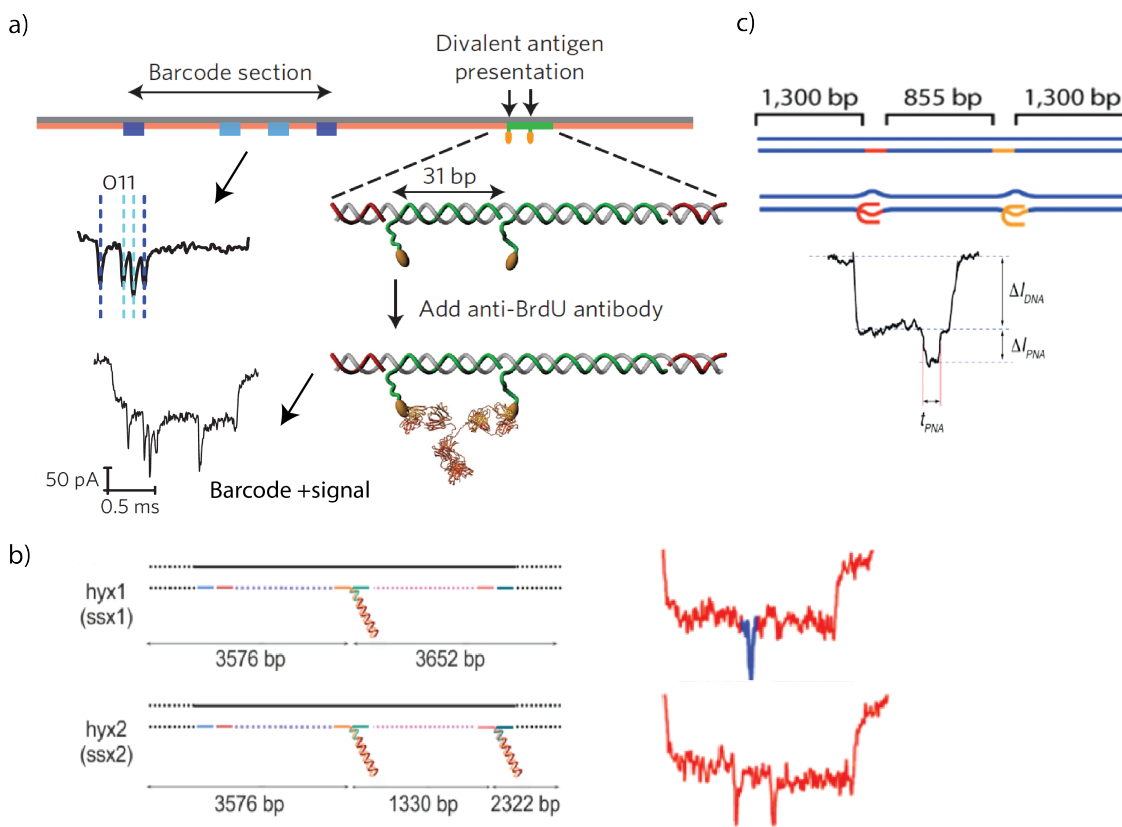


Figure 4.3: Schematic of dsDNA carrier system and respective sub-level ion current events a) the dsDNA carrier modified with antibody binding probes and encoded with a dumbbell barcode scheme, b) dsDNA carrier with ssDNA overhangs, c) dsDNA PNA carrier system. Figures adapted from Bell and Keyser [23], Yue et al. [26] and Singer et al. [22] respectively.

Thus a library of different codes were designed through which successful detection of IgG antibody isotopes was achieved by specific placement of antigen sites in the dsDNA backbone. They were also able to demonstrate multiplexing of the system, to detect four target antibodies (biotin, bromodeoxyuridine (BrdU), puromycin and digoxigenin) by attaching different antigens to the backbone structure.

A similar idea, but for detecting short (~ 100 nucleotide) DNA fragments was proposed by Yue *et al.* [26]. Their system utilises long linear dsDNA (7.2 kbp) with short DNA sequences as probe overhangs at specific locations to bind ssDNA fragments and detect and differentiate them via sub-level ion current using quartz nanopipettes of 20–30 nm pore size. The overhangs were composed of short 12 bp sections with the carrier backbone and a 88 nucleotide long ssDNA protrusion that could be hybridised with the target DNA.

Alternatively, Singer *et al.* [22] studied the sensitivity of SiN nanopores by threading long linear DNA molecules with and without bound Peptide nucleic acid (PNA) molecules, wherein they successfully demonstrated the identification of PNA probe specific sequences via increase in signal to noise of sub-ionic current. The detection system consisted of SiN nanopore fabricated via focussed electron beam in the range of 4–5 nm pore size for unfolded DNA entry and slow translocation. The 3.5 kbp length fragments taken from the lambda phage one with regions of bis-PNA complementarity and one without recognition sites acted as target and control sequence. The 8 bp PNA regions in the dsDNA contributed to a 200 fold increase in translocation time of the PNA–DNA complex compared to the control sequences of same length.

The authors relate this to non-specific interactions of the complex with the nanopore and formation of kinks at the PNA binding site as described elsewhere [224]. Thus an electrical method of label free single and multi specific PNA tagged dsDNA recognition approach via simple nanopore translocation was put forth.

Yet another single molecule detection system based on Lambda DNA modified with aptamers was put forward by Sze *et al.* using ~ 16 nm quartz nanopipettes [25]. Whence dsDNA carriers in previous works were constructed from ssDNA templates hybridised with short complementary strands, starting with an intact dsDNA lambda strand and utilising the single stranded terminal for probe modification simplifies the preparation process but also introduces design limitations.

Proof of concept was demonstrated with incorporation of thrombin molecule at two and three different sites separated by 96 bp length in the carrier at concentrations as low as 1.6

nM. Translocation resulted in distinct ion current peaks consisting of two levels of events with the 1st level pertaining to the dsDNA carrier and the second level contributed through target binding, the sub level count also varied with respect to the number of bound proteins i.e two subpeaks for two thrombins and three for three bound thrombin at the aptamer positions. The significant difference in current and dwell time for the unbound and bound carrier were also used to successfully detect and differentiate the multiple protein targets. In addition multiplexing by simultaneous detection of thrombin and Acetylcholinesterase (AChE) was also carried out in both buffer and biological sample.

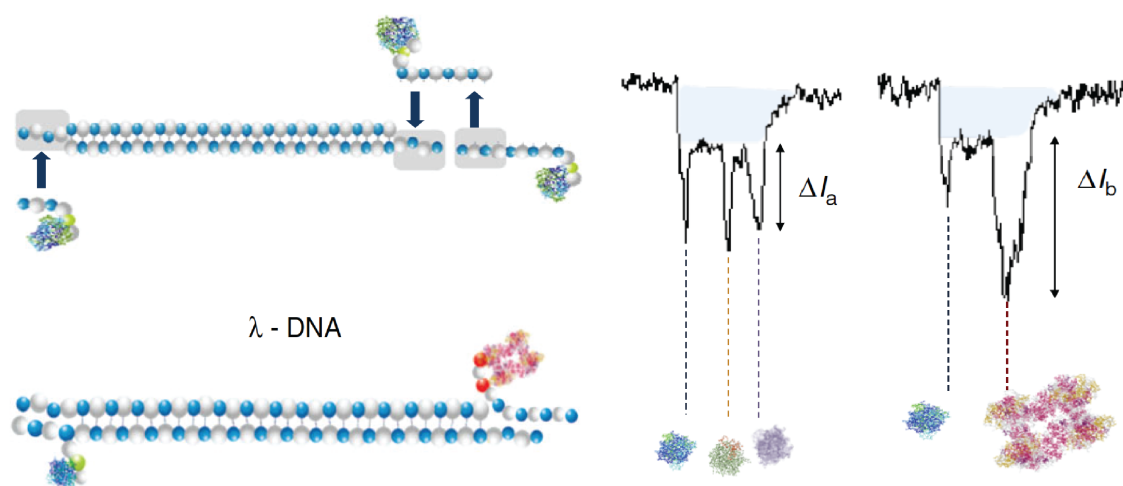


Figure 4.4: Schematic of Lambda DNA end modified with different target specific aptamers for multiplexing study along with the respective ion current event for 2 and 3 protein detection, adapted from Sze et al. [25].

Further interestingly apart from use of long dsDNA, gold nanoparticles modified with aptamers and antibodies have also been used as carriers for direct detection of proteins. Specifically, DNA aptamers functionalised onto gold nanoparticles about 5 nm in size (AuNPs) were used for selective target protein binding [225]. The aptamers were 5' end modified with thiol group for easy attachment onto the gold nanoparticle surface, the aptamer also included an additional 10 thymine bases as spacer for reducing steric hinderance with the AuNPs and lyzozyme bound aptamers if any. The nanoparticles imparted an increase in both event frequency and ion current signal which was very

advantageous in detecting single lysozyme.

Differentiation between the nanoparticles, lysozyme bound and unbound aptamer modified nanoparticles were achieved through the current amplitude change from current enhancement to blockade at different polarity of voltage applied. The detection technique was also demonstrated for complex mixtures containing excess of other components.

Another label free protein detection technique [226] made use of nanopipettes to detect single α fetal protein via antibody specific binding. Traditional method of comparing translocation dwell time and ion current amplitude was made use of to detect protein bound antibodies and also differentiate them from unbound antibodies, deep current blockades (~ 2.7 fold increase) were observed for even low concentrations (1 nM).

4.2.2 Quantitative detection using carriers

The above mentioned examples mostly involve qualitative detection of single molecules, but with the help of long DNA as carriers, quantitative detection of the single analytes has also been achieved [24, 27]. Keyser and group in 2016 were able to show quantitative detection of single molecules by utilising the secondary ion current signal upon target binding as explained in previous examples. For this, the linear single stranded M13mp18 virus genome (7.2 kbp) hybridised with 190 complementary strands each of 38 bp was modified at specific locations with a 5' extension of three thymines which then anchored the probe. Two systems biotin–streptavidin and digoxigenin–antidigoxigenin were tested with a quartz nanopipette separately to detect target binding via translocation ion current. Even though the study employed high ionic concentration buffer system (4 M LiCl) that raises concerns with biological samples, it was a first of a kind quantitative biosensing system that made use of carrier occupancy to evaluate the protein concentration.

Despite the many successes of long linear DNA carriers for both qualitative and quantitative sensing, it is not without its limitations, existing literature shows translocation of long strands of DNA through the nanopore are prone to forming knots and kinks [28, 29] which are known to provide false positive signals. Also the notable variations

in the signal depending on the translocation orientation and varying blockage rates due to the passage of multiple DNA molecules [30] through the nanopore makes long dsDNA debatable as carriers especially when working with sensitive electrochemical detection.

In order to circumvent these problems, recent work by Cai *et al.* [27] combined single molecule spectroscopy with electrochemical nanopore detection to provide a two factor conformation of binding events. The electro–optical set consisted of ~ 21 nm quartz nanopipettes aligned precisely with the diffraction limited optical volume, the alignment confirmation was carried out through translocation of YOYO–1 fluorescently labelled 5 kbp DNA and monitoring the percentage synchronisation between the electrical and optical channels.

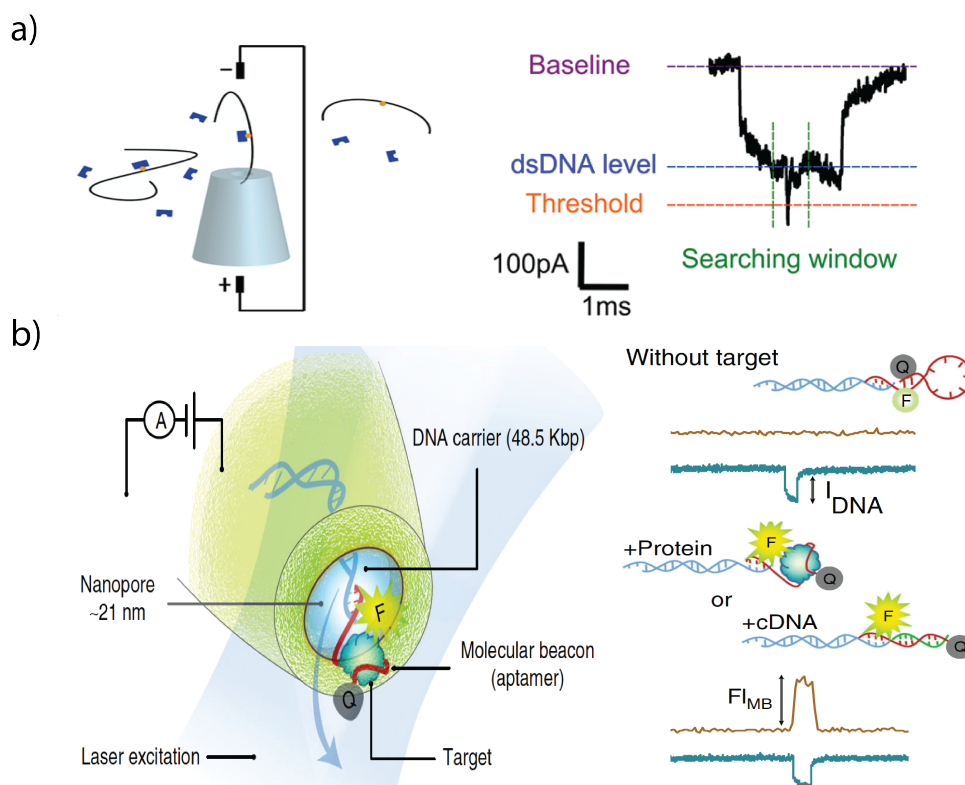


Figure 4.5: Quantitative protein sensing using dsDNA carrier, a) makes use of sub level current spike, adapted from Kong *et al.* [24] and b) utilises the synchronised electrical and optical translocation trace, adapted from Cai *et al.* [27].

The authors as in their previous study [25] used double stranded lambda DNA with overhangs to hybridise target specific probes but in addition included a flurophore label, this allowed for simultaneous translocation and detection of the target as well as confirmation of binding electrically and optically. The proof of concept was demonstrated with two schemes, one by labelling the target with flurophore and two a carrier design with molecular beacon utilising aptamer and flurophore–quencher pair.

In the target labelled approach, flurophore labelled streptavidin detection and quantitation using biotinylated oligonucleotide hybridised with the carrier was demonstrated via a concentration dependent study. While free carriers produced event signals in the electrical channel and free streptavidin in optical channel, synchronised signals are observed for target bound carriers in both electrical and optical channels. The percentage of this synchronised events over the total electrical signal was used to calculate a binding affinity of 7.6 pM.

Further, with the molecular beacon system, attachment of target molecules resulted in separation of the flurophore and quencher and again using the synchronised detection signals thrombin molecules were detected at the single molecule level with a K_d of ~ 5 nM and detection limit of 0.5 nM. This clever contraption was found to be sensitive down to single bp mismatch when tested with control sequences. The system was also successfully used to detect target molecules in serum and urine samples to demonstrate its physiological relevance.

Their approach, although elegant, negates the key advantage of nanopore sensing where complex optical setups are required, compared to the relatively simple electrical detection systems. To explore the full potential of nanopores for health diagnostics, medical applications and even as environmental monitors, it is eminent for the system to be simple for advancement as real time sensing systems and portable devices. On that regard an all electrical sensing system is advantageous.

4.3 DNA nanostructures in nanopore research

A significant difference with carrier molecules and target bound carrier molecules is important in achieving clear differentiation in their ion current, this can be imparted either via charge or mass difference. Most of the carrier based systems discussed in this chapter that makes use of long linear DNA threading into ~ 20 nm or less nanopores relies on the extra mass of the bound target that results in a sub-current in addition to the carrier current. While this scheme has been effectively used in many detection systems for both proteins and DNA, a more specific ion current change with respect to bound target would bring about further advantages to the nanopore based sensing system.

As such, instead of complex optical integrations or modifying the target or nanopore walls, one could simply take the long DNA and form defined compact DNA origami structures.

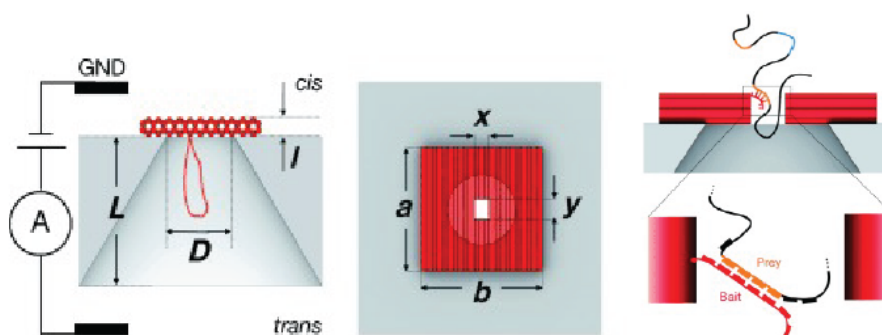


Figure 4.6: Nanoplate on nanopore (SiN) setup. DNA origami nanoplate (50×50 nm) with varying central apertures electrically placed on top of a 18–25 nm SiN nanopore to act as size selective gatekeepers, the right most image shows target specific modification of the nanoplate named as ‘bait–prey’ capture technique. Figure adapted from [135].

While DNA origami has already ventured into nanopore research, its use has mostly been towards hybrid nanopore formation or as selective gatekeepers, figure 4.6. For example use of DNA nanoplates [135] placed onto solid state nanopores fabricated via e–beam

lithography effectively reduced the pore size from $\sim 18\text{--}25$ nm to $\sim 5 \times 7$ nm or 9×14 nm with respect to the nanoplate aperture design. Placement was achieved through a bias voltage that sucked the nanoplate to the pore and translocation of the nanoplate itself was prevented as the nanopore diameter was slightly smaller than the nanoplate.

While reducing the pore size led to the successful detection of 52 kDa single streptavidin molecule translocations it also significantly increased the baseline noise. Moreover the nanoplate aperture was too small for larger Immunoglobulin G (IgG) (150 kDa) molecule translocation. These hybrid nanopores were also used for detecting ssDNA and were capable of specific interaction with the target molecule via the DNA origami nanoplate and hence produced selective highly differentiable signals, an approach the authors called bait–prey mechanism.

So far DNA origami as hybrid systems have been used for detecting variety of single molecules but research in DNA origami–nanopore combinations still needs improvement to address many problems. Specifically, ion current noise upon attachment, current leakage and insufficient pore space for larger protein molecule studies and analysis [227]. Nevertheless, the many excellent characteristics of DNA origami such as ease of design, stability, versatility in size shape and dimension makes them very attractive for single molecule detection.

Thus, in this project we attempt to make use of the appealing features of DNA origami in an alternative way—as carriers—in combination with quartz nanopipettes towards designing a highly selective biosensing tool.

Chapter 5

Methods and Materials

5.1 Materials

5.1.1 Protein and chemicals

CRP protein (human) was purchased as an aqueous solution from Sigma Aldrich (St. Louis, MO, USA) in 0.02 M Tris, 0.28 M sodium chloride, 0.005 M calcium chloride, pH 7.8–8.2, containing 0.1% sodium azide. The restriction enzymes and T4 ligase were purchased from New England Biolabs (NEB) Inc, Ipswich, MA, USA.

Potassium chloride (KCl) made up to 100 mM, magnesium acetate (MgAc) made up to 100 mM and tris-acetate (Tris-Ac) that was made up to 100 mM (pH 7.4), glycerol, Ethylenediaminetetraacetic acid (EDTA) 0.1 mM, Tris acetate EDTA (TAE) buffer: 10× concentrate that can be diluted to a 1× solution containing 40 mM tris, 40 mM acetate, and 1 mM EDTA, pH ~8.3 were all also purchased from Sigma Aldrich (St. Louis, MO, USA).

All the accompanying figures in this section were created using Adobe Illustrator and biorender.com unless specified otherwise.

5.2 Methods and techniques

5.2.1 DNA restriction and ligation

There are several enzymes that can modify a DNA sequence by addition or removal of particular chemical groups, one such enzyme called Restriction endonucleases type II (RE II) can cut DNA at precise locations close to or within their recognition sequence in a reproducible manner. There are several restriction endonucleases and each has its own specific recognition sequence where it cleaves the DNA and nowhere else. For example, restriction endonuclease PvuI cleaves DNA only at CGATCG sequence and EcoRI cuts only at GAATTC as shown in figure 5.1.

The way these RE cleaves the dsDNA results in either blunt or sticky ends. Many of them cut the dsDNA at the middle of the recognition sequence and thus results in a blunt or flush end, example, PvuII and AluI are blunt ends cutters. Some other restriction enzymes cleave dsDNA in a staggered pattern, so that the resulting dsDNA strands have short single stranded overhangs. These are called sticky or cohesive ends, which can then be joined together due to the complementary base pairing between them.

A restriction digest reaction is carried out by adding the specific restriction enzyme to the required concentration of DNA and buffer. And the mixture is incubated at the right working temperature (37°C for most of the RE) for 1 hour after which, the enzymes are most commonly deactivated via incubation at 70°C for few mins.

Ligase is an enzyme produced by all living cells to carry out functions of repair in case of discontinued base pairs or breakage in a DNA molecule and simply ligate strands of DNA during replication and recombination.

In laboratory conditions ligase (T4 ligase from T4 bacteriophage) can be used to stick together individual DNA molecules or two ends of a same DNA molecule. The enzyme catalyses the formation of phosphodiester bonds between the juxtaposed 5' phosphate and 3' hydroxyl termini thus bridging the two ends.

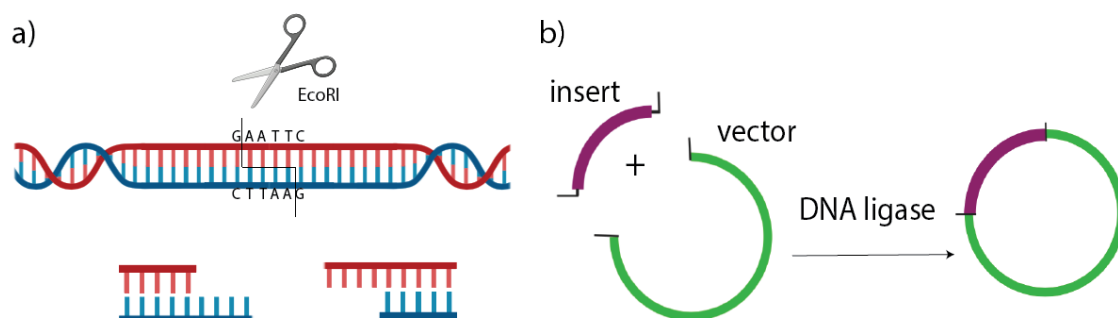


Figure 5.1: Schematic of a) restriction reaction using *EcoRI* enzyme (the schematic unwinding of the dsDNA is only a representation for clearly denoting the bp) and b) ligation example of an insert into a vector.

The reaction follows the steps of adding T4 DNA ligase and T4 ligase buffer (50 mM Tris-HCl, 10 mM MgCl₂, 10 mM Dithiothreitol 1 mM ATP, pH 7.5) with the DNA molecules of interest and incubating them at 16°C overnight or room temperature for 10mins, followed by heat inactivation at 65°C for 10 mins.

The different restriction enzymes namely EcoRI, NcoI, NspI, KasI, BmtI, and T4 DNA ligase were used for the construction of DNA origami structures used in chapter 8.

5.2.2 Polymerase chain reaction

Polymerase chain reaction (PCR) is a selective amplification technique for copying specific regions in a DNA. The region of amplification is defined by two short oligonucleotides primers, the primers each bind to one strand of the dsDNA thus flanking the sequence of interest. Amplification proceeds with the help of thermostable DNA polymerase enzyme that catalyse the formation of phosphodiester bonds between the neighboring nucleotides with respect to the template strand.

Typical PCR comprises of 30 to 40 cycles with repeats of three major steps, denaturation (94°C), annealing (50°-65°C) and extension (68°-74°C) of tiny amounts of DNA as template and results in accumulation of the product in an exponential fashion through each cycle (figure 5.2). For example, after 30 cycles one would have 130 million short

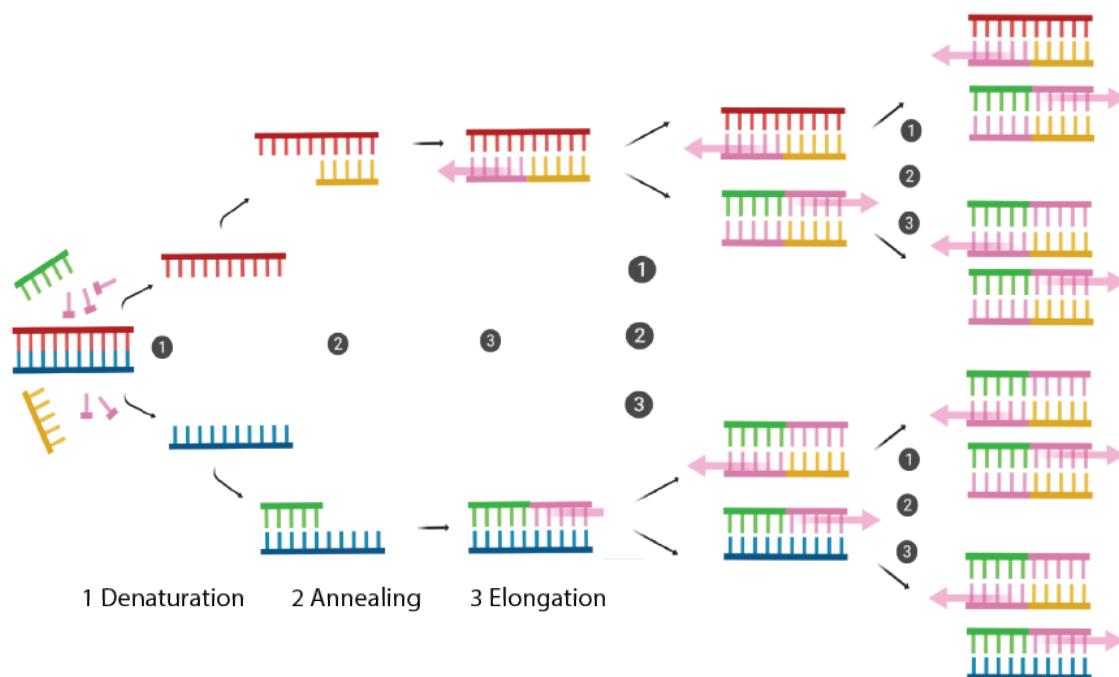


Figure 5.2: *Polymerase chain reaction illustrated with denaturation, annealing and extension steps numbered 1 2 and 3 respectively.*

products derived from each starting molecule, i.e., several micrograms from nanograms or less. For a PCR reaction to occur the DNA template is mixed with DNA polymerase enzymes, the primers and nucleotides mixture (A, T, G, C) in appropriate concentrations and subjected to the respective heat cycles.

Colony PCR

Colony PCR is a method for determining the presence or absence of a particular sequence (insert) in a plasmid construct (vector). It allows for a convenient way to check insertion of the target in the vector upon transformation by directly adding the cells in the PCR reaction. The colony PCR reaction follows the traditional PCR steps, but in the initial heating step the cells are lysed causing release of the plasmid DNA which will then serve as the template for the rest of the reaction as shown in the figure 5.2. Colony PCR can also be used to check if the insert is of the correct molecular size and orientation in the vector.

In this thesis, PCR was used in the amplification of the different scaffold fragments for the construction of nanostructures in chapter 8, and colony PCR was used for confirmation of formed scaffold.

5.2.3 DNA purification and quantification

All nucleic acid products used for DNA origami scaffold construction were purified to remove residual components including enzymes and Deoxynucleotide triphosphates (dNTPs) from the reaction mixture and to exchange them into a storage buffer. Purification was directed using spin columns from Roche (Roche Diagnostic Ltd, West Sussex, UK) High pure PCR product purification kit, that makes use of silica to selectively bind DNA in the presence of chaotropic salts and high ionic buffers.

The protocol follows the steps of binding DNA to silica surfaces, repeated washing and elution from the columns using a low ionic buffer. The spin steps were carried out on a table top microcentrifuge (Eppendorf) at 13,000 rpm in room temperature and eluted to 30–50 μ l volumes. Quantification of the eluted products was carried out with a Nanodrop 2000 UV spectrophotometer (Thermo scientific, Wilmington, DE, USA). 1 μ l of the sample was loaded onto the pedestal and quantified after proper cleansing and blanking with distilled water and elution buffer respectively.

5.2.4 DNA origami purification

Nanostructure purification was carried out via gel filtration process using Sephacryl S400 (GE healthcare, UK). Molecules in the sample are separated depending on their size and with respect to the size exclusion resin used, molecules larger than the largest pores elude the gel and elute first while intermediate size molecules and very small molecules enter the matrix to varying extents and elute later.

It is important to note that exclusion limits of the gel filtration resins are only meaningful in continuous flow processes. In spin column gel filtration chromatography, the product

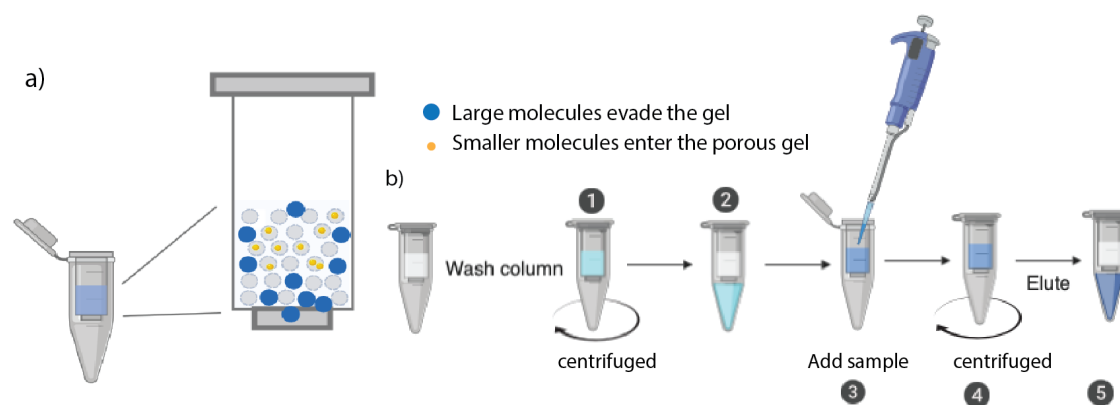


Figure 5.3: DNA origami purification via S-400 column, a) schematic represents small molecules entering the gel and large molecules eluting first b) the purification steps where in the step 1 the column is washed with the DNA origami storage buffer (10 mM MgAc, 10 mM TrisAc, 1 mM EDTA), and samples added in step 3 and eluted into the storage buffer in step 5.

pass through the gel whereas the smaller impurities are retained depending on resin, sample volume, product size and the g force used in the purification process.

In this thesis, the folded nanostructures are purified by removal of excess staples via a size inclusion matrix and eluted into the same folding buffer.

5.2.5 Gel electrophoresis

Electrophoresis is a technique where molecules in a sample mixture are separated under the influence of an applied electric field. The rate of migration is determined by the shape and charge to mass ratio of the molecules. As many proteins and nucleic acids have identical charge to mass ratios and as most DNA molecules are the same shape, electrophoresis of different size molecules in solution results in little or no separation.

The size of the nucleic acid becomes a factor, when electrophoresis is performed in a gel. The gel, commonly made of agarose, polyacrylamide or the combination of both consists of intricate network of pores through which the molecules migrate through under the applied electric field. Thus, using gel electrophoresis molecules (DNA, RNA or proteins)

in a sample mixture is separated based on their size, charge and shape.

A slab of gel is made using an electrically conductive mildly basic buffer TAE or Tris borate EDTA (TBE), the percentage of agarose or polyacrylamide by mass creates a molecular sieve, with a pore size in relation to the percentage used, i.e. higher percentage of gel yields smaller pores and vice versa. The solidified slab of gel is immersed in the same conducting buffer between an anode and cathode. The alkalinity of the buffer brings a uniform charge to the sample molecules and the electric field causes them to migrate through the gel matrix towards the positive or negative end depending on their net charge.

5.2.6 Electrophoretic mobility shift assay

Electrophoretic mobility shift assay (EMSA) is a technique based on the principle that protein bound nucleic acids migrate the gel slowly in comparison to the free nucleic acids. Thus the technique is also called gel shift assay or retarding gel electrophoresis as the rate of migration of the complexes is shifted or retarded. Non-denaturing agarose or polyacrylamide gels with TAE or TBE buffer are used to resolve the protein–DNA complexes and the success is largely dependent on the stability of the complex. While the gel matrix provides a caging effect, the low ionic strength of the electrophoresis buffer helps stabilise the interactions [228]. Wide range of nucleic acids sizes and structures and various sizes of proteins are compatible with this assay. But the technique is not without limitations, for example, samples at disequilibrium, and rapid or slow dissociation of samples. It is also important to note that several variables like the electrophoresis run time, applied voltage, buffer conditions, protein binding conditions and use of additives should be optimised from sample to sample so that one does not underestimate the binding density. Thus, though the non-denaturing EMSA could resolve protein bound DNA from unbound DNA, it was only used as an additional technique to validate the results and does not provide a straightforward evaluation in this thesis.

All the gel electrophoresis images shown in this thesis are agarose gels, gels used in chapter 8 are 1% gels run in 1×TAE buffer for 60mins and the agarose gels for EMSA

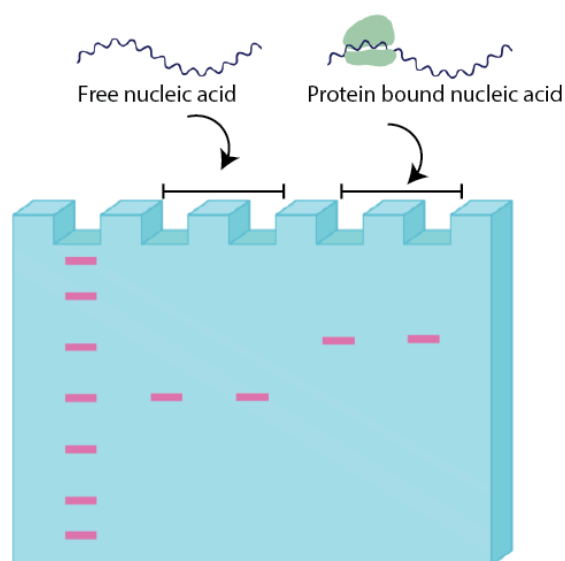


Figure 5.4: *Electrophoretic mobility shift assay, schematic shows shift in bands with protein bound nucleic acid samples whereas unbound free nucleic acid samples runs further down the lane.*

studies in chapter 9 are 0.5% gels in $1\times$ TAE and 11 mM MgAc with runtime of 2 hours at 4°C . Typically 100 ng of the products were loaded in the wells for proper visual identification along with 1 kbp ladder. The separation voltage was applied at 80 V.

5.2.7 Cloning protocol

The NEBuilder HiFi DNA assembly (NEB Inc, Ipswich, MA, USA) is a high efficient and accurate protocol that makes use of a mixture of enzymes that work together to assemble multiple fragments of DNA regardless of end compatibility or fragment length, producing a double stranded sealed DNA molecule.

The reaction mixture consists of exonuclease—to create single stranded 3' overhang which allows for annealing of fragments with complementary ends. For this, the fragments should be designed with overlapping end sequences (15–25 nt) with T_m equal to or greater than 48°C (assuming A–T pair = 2°C and G–C pair = 4°C) as shown in the figure 5.5. The overlaps can be split between the vector and insert (orange) in any combinations to make a short primer or can be entirely made of vector sequence (blue) depending on the fragments to be assembled.

Polymerase—to fill the gaps within the annealed fragments and DNA ligase—to seal the

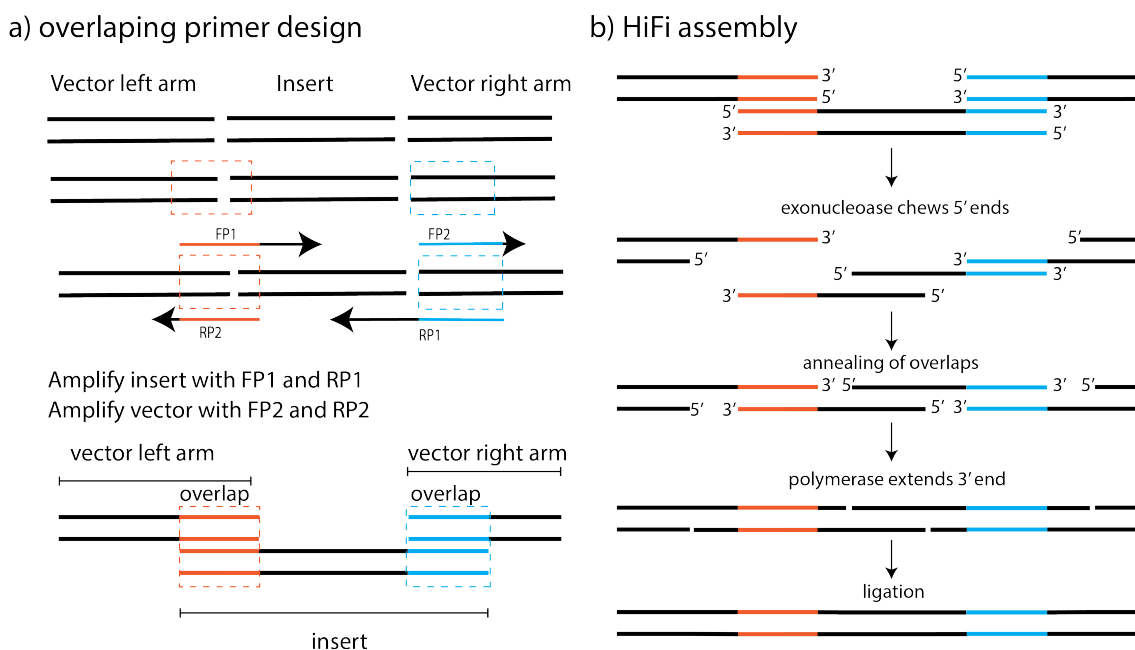


Figure 5.5: Schematic of the NEBuilder HiFi DNA assembly a) primer design and b) protocol to form dsDNA.

nicks to form a circular dsDNA. The reaction mixture along with the fragments were incubated in a thermocycler at 50°C for 15 minutes or 60 minutes if more than 2 fragments are assembled.

In this thesis, the vector (f23) and insert (f1) fragments (see chapter 8 section 8.2.1) for the custom scaffold (phagemid) was assembled using inserts with overlapping vector sequences.

5.2.8 Phage transformation and expression

The successfully constructed custom scaffold from the HiFi cloning protocol was chemically transformed in competent *E.Coli* cells (DH5 α from NEB Inc, Ipswich, MA, USA) and 100 μ l of the culture was spread onto 2 \times YT agar (16 g tryptone, 10 g yeast extract, 5 g NaCl, 15 g agar) plates containing ampicillin (100 mg/ml) and incubated overnight at 37°C.

Individual colonies were then selected and grown in 200 μ l 2 \times YT broth (16 g tryptone,

10 g yeast extract, 5 g NaCl) containing ampicillin for 2 hours at 37°C in a shaking incubator at 250 rpm. The colonies were also simultaneously tested for successful transformation via colony PCR. This was followed by scale up to 5 ml 2× YT cultures containing ampicillin, the rest of the 200 µl cultures were frozen for future use in 80% glycerol. After overnight incubation at 37°C, DNA extraction from the 5 ml cultures was carried out via miniprep protocol as explained below.

The extracted DNA was then taken forward for chemical co-transformation with mp13cp cells (a gift from Dr. Simon White, University of Leeds). Similar protocol of inoculation and incubation was carried out onto 2× YT agar plates containing ampicillin (100 mg/ml) and chloramphenicol (25 mg/ml).

Again individual colonies were picked and first grown in 200 µl 2× YT broth containing both ampicillin and chloramphenicol and then transferred to 5 ml cultures. Glycerol stocks of the selected colonies grown in 200 µl 2× YT broth were also made. Successful co-transformation was confirmed both via colony PCR and restriction digestion tests followed by gel electrophoresis (chapter 8, section 8.2.1).

Now the 5 ml culture was scaled up to 500 ml flask cultures and incubated overnight at 37°C in a shaking incubator for phage expression. After overnight growth the culture was centrifuged (1000 g at 4°C for 10 mins) to separate the bacterial cells (pelleted) from the phagemid (supernatant). The supernatant was then incubated overnight with 3.5% PEG and 0.5 M NaCl at 4°C to precipitate the phagemid, which was separated via centrifugation (1000 g at 4°C for 30 mins). The resulting pellet was resuspended in 10 ml PBS.

Repeated cycles of centrifugation and PEG precipitation was carried out until a clear supernatant is obtained containing only the phagemid, the final resuspension volume was kept as low as possible (1 ml PBS) to obtain a concentrated sample. This was followed by phenol–chloroform DNA extraction and ethanol precipitation.

5.2.9 Chemical transformation

Chemical transformation is one way to introduce foreign DNA into a cell. Briefly competent cells (bacterial cells with increased permeability to DNA after treatment with calcium (Ca^{2+})) are incubated with the DNA of interest and subjected to heat shock at 42°C for 30 seconds. This allows for passage of the DNA into the cells, which are then grown out in nutrient rich medium at 37°C as explained above.

In this thesis we use competent E.Coli cells (DH5 α from NEB Inc, Ipswich, MA, USA to transform our custom scaffold.

5.2.10 Miniprep protocol

Purification of the plasmid DNA was carried out using the Monarch plasmid miniprep kit (NEB Inc, Ipswich, MA, USA). The procedure goes through the steps of cell resuspension, alkaline lysis and neutralisation via addition of respective buffer solutions provided in the kit.

Further centrifugation steps under high salt concentration in the spin column tubes binds DNA to the silica matrix. This is followed by washing steps to remove RNA, proteins, salts and other cellular components and final elution into a small volume storage buffer for high concentrated high purity DNA.

Plasmid DNA scaffolds purified using this protocol resulted in hundreds of $\text{ng}/\mu\text{l}$ in an 30 μl elution volume.

5.2.11 DNA origami design and folding

The DNA origami concentric squares used in chapter 8 were designed using the custom made ssDNA scaffolds of 9073 bp, 8515 bp and 6307 bp whereas the DNA nanostructures used in chapter 7 and DNA nanostructure carriers in chapter 9 were designed from 7249

bp M13mp18 ssDNA from tillibit (Germany). The procedure for producing custom made scaffolds is explained in detail in chapter 9 and in previous sections of this chapter. All the complementary short staple strands for the respective nanostructure designs were ordered from Integrated DNA technologies (IDT), Coralville, IA, USA.

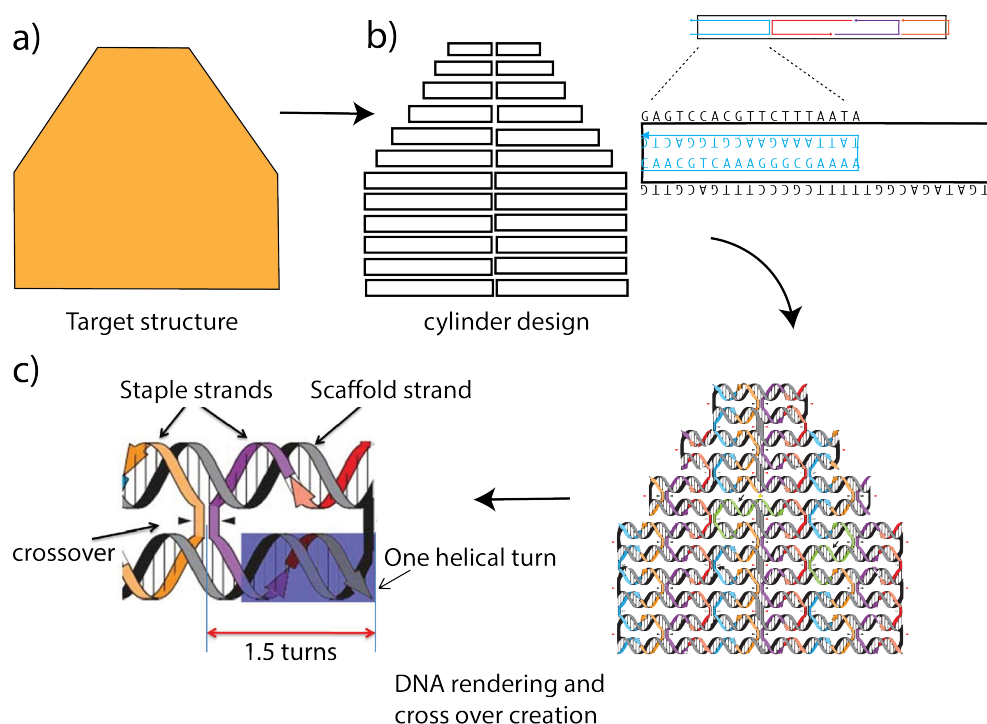


Figure 5.6: Schematic of *a) target structure b) placement of cylinder representing dsDNA and the DNA origami routing as seen in caDNAno software c) DNA rendering illustrating scaffold and staple crossovers created all throughout the structure thus resulting in a stable structure.*

All the nanostructures were designed using caDNAno software, first a scaffold strand represented in black runs throughout the design back and forth progressing from one helix to other so that it makes one of the two strands in every double helical domain. This is done by envisioning the desired target with rod structures representing duplex DNA. Then staple strands (different colors) complementary to the scaffold is derived with respect to the scaffold routing. The staple sequences can then be easily exported through the software for synthesis. The routing design for each nanostructure used in this thesis is included in appendix B.

In this thesis, the ssDNA scaffold mixed with a tenfold excess of the staple strands in the folding buffer (10 mM TrisAc (pH 7.4), 10 mM MgAc and 1 mM EDTA (Sigma Aldrich, USA)) was folded via thermal annealing where the sample mixture is initially heated to 95°C and then cooled down to 20°C in steps of 1°C/minute.

5.2.12 Insertion of aptamer sequences

The DNA origami carriers used in chapter 9 includes a aptamer sequence containing a modified end sequence with 5' amine attachment. This was incorporated into the carrier design in a second thermal annealing step (heat up to 35°C and decrease 0.5°C per minute) or inclusive with the staples. Either way, folded frame DNA origami carrier with precise insertion of aptamer was achieved. The sequences of the hCRP aptamers adapted from Jarczewska *et al.* [84], Lee *et al.* [85], Huang *et al.* [86], and Piccoli *et al.* [87] and nonspecific random sequences used in chapter 9 are as follows,

Specific hCRP aptamer 1 –16 bp anchor + 44 bp aptamer

NH₂–AAGCCTTTATTTCAACGCCTGTAAGGTGGTCGGTGTGGCGAGTGTGTT
AGGAGAGATTGC

Specific hCRP aptamer 2 –16 bp anchor + 72 bp aptamer

NH₂–AAGCCTTTATTTCAACGGCAGGAAGACAAACACGATGGGGGGGTATGA
TTTGATGTGGTTGTTGCATGATCGTGGTCTGTGGTGCTGT

Specific hCRP aptamer 3 –16bp anchor + 52bp aptamer

CGAAGGGGATTTCGAGGGGTGATTGCGTGCTCCATTTGGTGTTTTTTTTTTTTT
GCAAGGATAAAAATTT–NH₂

Nonspecific random aptamer

NH₂–CTGAACAAGAAAAATAGCAGAACTTACGAGCCAGGGGAAACAGTAAGG
CCTAATTAGGTAAAGGAGTAAGTGCTCGAACGCTTCAGA

5.2.13 Sample preparation and AFM imaging in fluid

The DNA origami samples reported in this study were imaged in fluid as per the following protocol. Firstly, mica surfaces were freshly cleaved using tape lift off and incubated with 10 mM NiCl₂ (10 μl for 60 seconds). Excess NiCl₂ was then removed and 20 μl of samples prepared in the scanning buffer (10 mM TrisAc (pH 7.4), 10 mM MgAc and 1 mM EDTA) were immediately applied and incubated for 15mins. The mica surface was topped off with 200 μl of the same buffer prior to imaging. For the DNA origami carrier samples used in chapter 9 for CRP binding study, 2 mM CaCl₂ was included to the scanning buffer similar to the nanopipette translocation experiments.

The samples were imaged in tapping mode in aqueous fluid using a Dimension Fastscan (Bruker, Santa Barbara, CA, USA). The images were captured with scan rates of 20 kHz (256×256 pixels) using Fastscan D Si₃N₄ cantilevers containing a Si tip (Bruker, Santa Barbara, CA, USA) with a nominal tip radius of 5 nm.

5.3 Nanopipette fabrication

The glass nanopipettes used in this thesis were fabricated from quartz capillaries with filament (QF100-50-7.5) with outer diameter 1.0 mm, inner diameter 0.50 mm and 7.5 cm length (World precision instruments, UK) via laser pulling using P2000 laser puller. The laser pulling technique along with its principle is explained in detail in chapter 3. Briefly nanopipettes with different pore sizes were utilised according to the samples analysed, the pore size of the final pulled glass pipette depends on the different pulling parameters. For detailed description of individual parameters please refer to chapter 3, section 3.2.2.

The tables 5.1 and 5.2 portray the pulling parameters utilised for obtaining ~100 nm quartz pipettes which are predominantly used throughout this thesis in chapter 7, 8 and 9. Parameters for obtaining ~20 nm quartz and ~180 nm borosilicate pipettes used for

Table 5.1: Pulling parameters for quartz capillaries of 0.5 mm inner diameter and 1.0 mm outer diameter, producing pore diameters of 80–100 nm.

HEAT	FIL	VEL	DEL	PULL
575	3	35	145	75
900	2	15	128	150

nanopipette characterisation studies in chapter 6 are provided in appendix A along with all other tested parameters.

Table 5.2: Pulling parameters for quartz capillaries of 0.5 mm inner diameter and 1.0 mm outer diameter, producing pore diameters of ~ 100 nm.

HEAT	FIL	VEL	DEL	PULL
625	3	35	145	75
900	2	15	128	150

5.3.1 Ion current measurements

For the translocation experiments of DNA origami the nanopipettes with the working electrode were filled with the translocation buffer (0.1 M KCl with 10 mM TrisAc, 10 mM MgAc and 1 mM EDTA) containing the DNA origami at a final concentration of 500 pM. For the DNA origami carrier–CRP binding studies 2 mM CaCl₂ was also included (chapter 9). The Mg is required to maintain the stability of the DNA origami, and the Ca to match the buffer conditions used to select the DNA aptamers employed as binding moieties. For linear and plasmid DNA samples the buffer used was 0.1 M KCl.

The grounded counter electrode was immersed in a 0.1 M KCl solution to complete the circuit. On application of a negative potential to the working electrode inside the nanopipette, DNA origami from inside the nanopipette are translocated out into the electrolyte solution resulting in a modulation of the ion current. Ion current data were acquired using an Axon instruments–patch clamp system (Molecular devices, USA).

Measurements were recorded using the Axopatch 700b amplifier, and the data were acquired at a rate of 100 kHz and 20 kHz low pass filtered.

5.3.2 Data analysis

Initial data analysis was carried out with a custom MATLAB script (provided by Prof Joshua Edel, Imperial College, London, UK) and further data analysis was carried out using ProFit (QuanSoft, Switzerland). The MATLAB script is capable of picking out individual events in a given ion current trace using defined thresholds, usually 7 standard deviation and above of baseline noise. The baseline is traced via asymmetric least square smoothing algorithm and fit determined by poisson probability distribution function. The first and last data points above baseline for each event is taken as the start and end of the event.

Individual events are then further processed to obtain event duration and event maximum peak amplitude to generate scatter plots and histograms. The distributions are fitted using gaussian probability density function. The ion current trace event data generated from the MATLAB script was also exported in excel format for further data analysis and producing plots and histograms with ProFIT software.

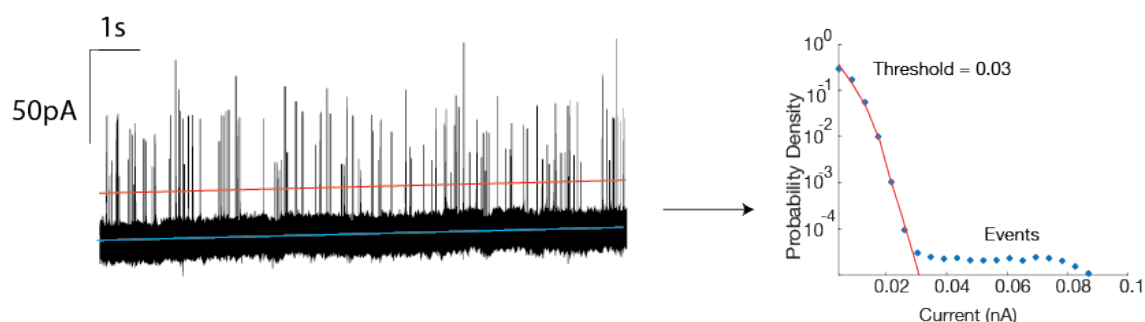


Figure 5.7: Raw ion current translocation trace (inverted) of a sample, with baseline trace (blue) and threshold line (red), data analysis using MATLAB script shows a threshold of 0.03 nA above which is counted as events.

5.4 Surface plasmon resonance

Surface plasmon resonance (SPR) is a process that occurs when parallel polarised light hits a thin metal film under total internal reflection. When a parallel polarised light travelling from higher to lower refractive index medium changes its path (angle), at a critical angle of incidence, the light does not leave the medium and reflects at the interface of the two media. This is called Total internal reflection (TIR).

In the SPR situation, with the Kretschmann configuration, a thin metal film (usually gold) is placed at the interface of the two dielectric media, a prism with high refractive index medium and a low refractive index medium which can be air or the solution of interest. The presence of a dielectric medium on top of the gold creates a special situation with the

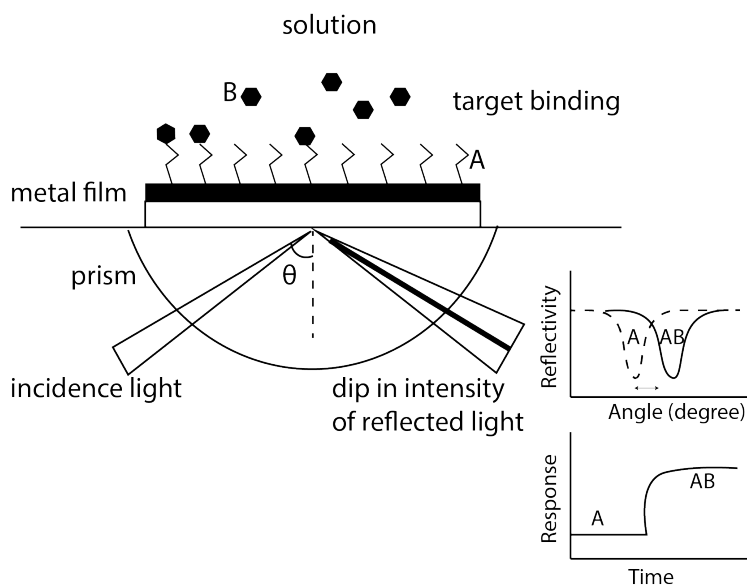


Figure 5.8: Surface plasmon resonance theory explained in a schematic along with the reflectivity and resonance.

photons causing evanescent waves and if the medium is of an opposite or higher dielectric constant than the metal, the free electrons in the metal will fluctuate. And when the light hits the gold at a particular angle of incidence the photon energy interacts with the free fluctuating electron in the metal surface producing surface plasmons (electromagnetic

surface wave). This is called surface plasmon resonance [229].

Thus under TIR when the energy of the light is ideal, the photons are converted to resonating plasmons and there will be no reflecting light (a sharp decrease or 'gap' in the reflected light intensity). Plotting the light intensity vs angle of incidence will result in a dip at the specific SPR angle. The SPR angle is dependent on the refractive index of the solution near the interface. Thus binding of molecules on the surface of the metal film changes the refractive index which can also be measured as the change in resonance angle.

In this project, aptamer–protein binding studies were carried out via an ESPRIT SPR instrument from Metrohm Autolab B.V (Utrecht, The Netherlands). The ESPRIT configuration contains a replaceable glass disk with a thin layer of gold, placed on a hemi cylinder prism coated with a thin layer of oil. For this, the end-modified aptamers attached with an amine group were anchored onto the gold SPR surface functionalised with a self-assembled monolayer (SAM) of C₁₁PEG₆COOH via EDC (1-ethyl-3-(3-dimethylaminopropyl) carbodiimide) NHS (N-hydroxysuccinimide) coupling chemistry. The gold SPR surface from XanTec bioanalytics was cleaned by sonication twice in acetone for 10 minutes and then immersed in an ethanolic 1mM SAM solution containing 5% acetic acid and allowed to stand at room temperature for 48 hours.

Following the incubation, the surface was rinsed with 100% ethanol, quickly dried with nitrogen and was mounted on the SPR system. To attach the DNA aptamers to the gold surface, the COOH–terminated SAM surface was activated with 50 mM EDC and 200 mM NHS in 100 mM MES buffer at pH 5.5 for around 15 min. The surface was washed with the MES buffer, followed by a 30 minute incubation with 5 M of DNA aptamer in 10 mM sodium acetate buffer at pH 5.5. Any remaining activated COOH sites were quenched by exposing the surface to 100 mM ethanolamine in water for around 10 min. The surface was then washed with the binding buffer (10 mM TrisAc, 10 mM MgAc, 2 mM CaCl₂ and 1 mM EDTA in water) and then challenged with varying concentration of human CRP as explained in chapter 9. The binding was measured as the change in resonance angle.

Chapter 6

Characterisation of Nanopipettes

6.1 Introduction

As per the aims explained in chapter 1, to translocate and study DNA origami molecules via nanopipette, it is essential to fabricate nanopipettes with pore sizes capable of translocating and detecting the samples with a good signal to noise ratio. Predominant nanopore research indicates improvement in geometry of nanopore, electrolyte selection, electrolyte concentration and applied voltage as important factors for improving the signal quality of biomolecular translocations [208]. Particularly, controlling the shape, size and thickness of nanopipettes is of critical importance as the behaviour and response of a nanopipette is influenced by the geometry and also their surface chemistry [230]. Though one could essentially reduce noise via electrical and vibrational shielding, this does not contribute to the enhancement of ion current signal. Thus the pore size plays an important role in high signal to noise ratio of the ionic current, specifically it is essential to obtain a nanopipette pore diameter similar to that of samples in order to observe their translocation through the pore.

This chapter describes the procedure for characterising the pore size of nanopipettes filled with 0.1 M KCl electrolyte solution, which is the electrolyte used in this thesis. The most convenient method to estimate the pore size of a nanopipette is through

resistance measurements via voltammetry [231, 232], where the ionic current is measured as a function of the voltage applied across the nanopipette. Alternative and more direct measurements are through SEM and TEM, some researchers also make use of simulations to supplement the characterisation of geometry and inner surface properties of nanopipettes with high accuracy [151, 205, 230, 233].

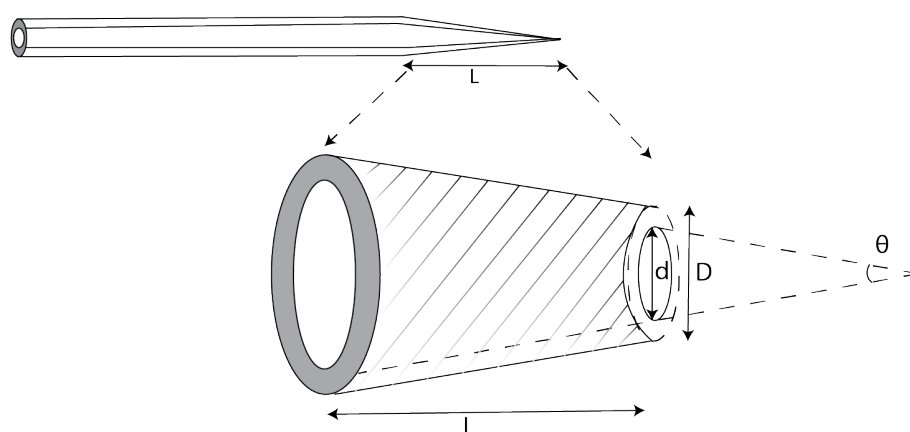


Figure 6.1: Schematic of a nanopipette tip geometry representing pore size (d), outer pore diameter (D), taper length (L) and inner pore angle θ .

Here, in the first instance different pulling parameters were devised as shown in appendix B and direct SEM imaging was employed to confirm the nanopipette pore size obtained for the respective pulling parameters. Once consistent and reproducible parameters for particular pore sizes were established and confirmed via SEM, the geometric features (pore size and outer pore angle) obtained from the same were used to check the resistance calculations. This was done in order to utilise nanopipette pore resistance as a quick means of pore size approximation.

This involved characterisation experiments with two pore sizes ~ 20 nm and ~ 200 nm, fabricated from two types of glass capillaries quartz and borosilicate, including ion current asymmetry and conductance studies. Later sections of this chapter involves preliminary translocation studies involving simple DNA configurations, linear and plasmid, via the ~ 20 nm pore nanopipettes.

6.2 Nanopipette geometry

6.2.1 SEM measurement

As mentioned in the introduction, nanopipettes fabricated from quartz and borosilicate capillaries through different pulling parameters were imaged by SEM, and after numerous trials, programs with high reproducibility ($\geq 90\%$) were identified for a range of pore sizes (see appendix A). Figure 6.2 portrays representative SEM images of nanopipette pores for the different pulling parameters used in this thesis.

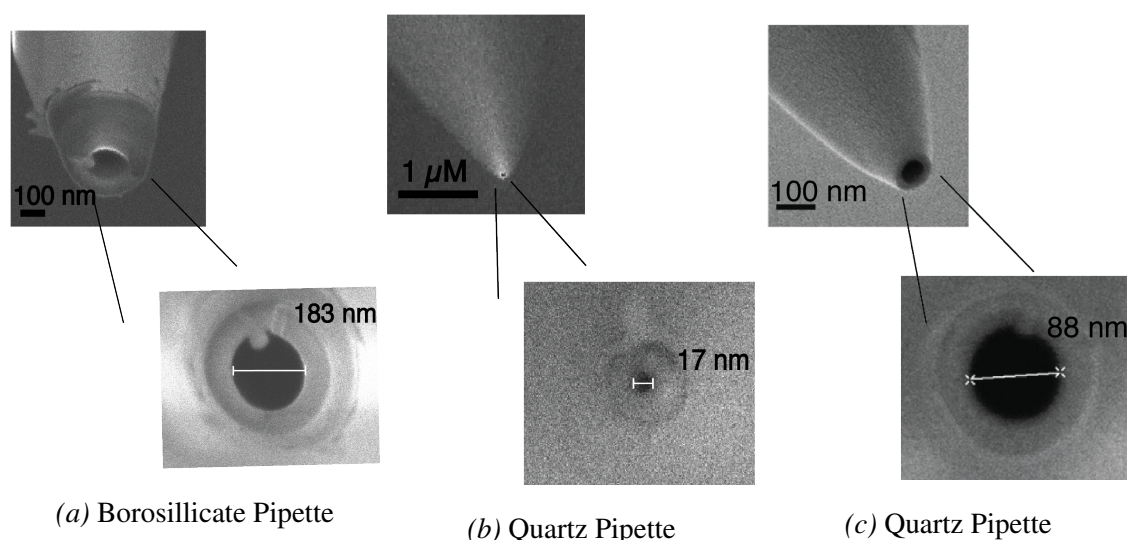


Figure 6.2: SEM micrographs of representative borosilicate and quartz nanopipettes with a) 183 nm, b) 17 nm and c) 88 nm diameter.

Though SEM of a nanopipette tip is the most common method for pore size determination [218, 234, 235], it is a time consuming process. Also, imaging nanopipettes of pore size <50 nm is challenging as the pipette constantly goes out of focus due to charging. The charging can be minimised by coating the nanopipette tip with a thin layer (few nanometers) of conducting material e.g. gold, but for nanopipettes of small pore size (20 nm and below) this is problematic as the metal layer significantly affects the observed pore size.

6.2.2 IV measurements

Thus as an alternative, we turned to pore size verification through pore resistance calculation as a more convenient and quicker means to determine the geometrical features of the nanopipette tip. As one glass quartz capillary produces two identical nanopipettes, one was used for pore size determination via SEM (D_s) while the other was used for determining the pore size through electrochemical means (D_a), figure 6.3.

Thus it was possible to test the reproducibility of the nanopipette fabrication parameters and also establish if, the electrochemical measurement could be used to approximately determine the pore diameter and subsequently to select the right sized nanopipettes. Two sets of pulling parameters that produced a small ~ 20 nm and larger ~ 200 nm pore sized pipettes (figure 6.2) were chosen for this purpose.

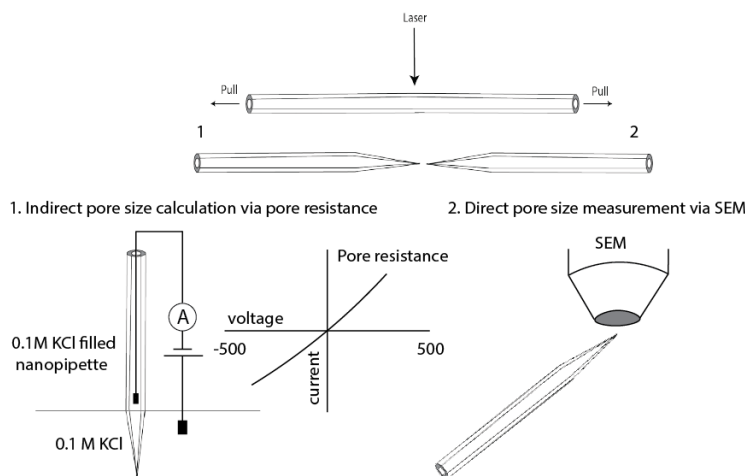


Figure 6.3: A schematic showing one twin of the nanopipette being directly imaged via SEM (D_s) and the other used for pore resistance calculation via IV measurement (D_a). The two nanopipettes fabricated from the same capillary is then compared.

Obtaining nanopipette pore size via IV measurements relies on the pore radius and inner angle as shown in equation 6.1, adapted from Actis *et al.* [3].

$$R_p \cong \frac{\cot\left[\frac{\alpha_{inner}}{2}\right]}{\kappa\pi r_i} \quad (6.1)$$

Where R_p is the pipette resistance, r_i the inner pipette radius, κ is the solution conductivity, and α_{inner} is the inner nanopipette cone angle. The conductivity of 0.1 M KCl of 1.278 S/m is used.

Additionally, as SEM imaging of the nanopipette pore opening does not provide full details on the lumen of the nanopipette inner wall especially for small pore sized nanopipettes, indirect ways to calculate nanopipette inner features consider the ratio of outer to inner pore diameter remaining constant at the pore opening. Thus the outer nanopipette angle estimated from SEM images is used to calculate the inner pipette angle through equation 6.2, adapted from Perry *et al.* [230].

$$\tan \alpha_{inner} = \frac{\tan \alpha_{outer}}{r_{o/i}} \quad (6.2)$$

Where, α_{inner} is the inner pore angle and α_{outer} the outer pore angle. $r_{o/i}$ is the ratio of outer to inner pore radii.

The outer pore angle calculated for the quartz (~ 20 nm) and borosilicate (~ 200 nm) pipettes were $\sim 14^\circ$ and $\sim 28^\circ$ respectively. The nanopipette resistance (R_p) can also be estimated by inputting the pore parameters, or the pore size could be calculated by inputting the pore resistance from IV measurements (R_a), using equivalent equations adapted from [206, 236, 237].

For our experimental purpose a batch of 18 borosilicate and 18 quartz capillaries pulled using different pulling parameters at a time were used to test the above equation and to validate the consistency of the fabrication procedure. The nanopipettes were imaged by SEM to evaluate the inner and outer diameter and outer pore angle. The values were equated to ultimately determine the pore resistance R_p of the pipette as per the equations 6.1 and 6.2. Pore resistance, R_a was obtained via IV measurements of the pipette in electrolyte solution using the patchclamp amplifier (Axopath 700b) through an inbuilt measurement procedure. The two values R_p and R_a were then compared to establish if the electrical measurement which yield R_a , could be used to approximately determine the pore diameter and vice versa.

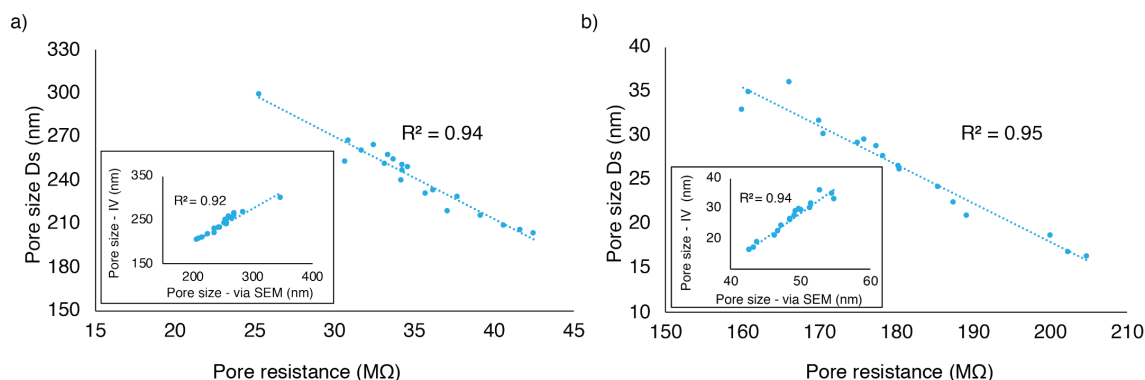


Figure 6.4: Graph showing the correlation between pore resistance and pore diameter for a) borosilicate ($n=18$ and $R_a = 180 \pm 16.4 \text{ M}\Omega$), b) quartz ($n=18$, $R_a = 36.1 \pm 5 \text{ M}\Omega$) nanopipettes fabricated using parameters as outlined in appendix A. The inset shows the correlation between the measured and calculated pore diameter, D_s and D_a respectively. The dotted lines represent least square fits of a first order polynomial to the data.

This was achieved by plotting R_a against D_s as shown in figure 6.4. It can be seen that the pore diameters (D_a) back-calculated via the equation 6.1 by substituting the pore resistance values (R_a) from the electrical measurements is in line with the pore sizes (D_s) measured via SEM for both pore sizes. The inset of the figures indicate the pore diameter values (D_a and D_s) plotted against each other showing a good correlation for both quartz and borosilicate nanopipettes. It could be observed that for the borosilicate nanopipettes the calculated and measured diameters are almost identical, on the other hand for quartz nanopipettes, which have a much smaller pore diameter, the calculated and measured diameters are not identical.

Nevertheless, they are linked in a linear relationship and therefore the actual pore diameter can accurately be estimated via the electrical measurements. With the correlation between D_a and D_s established, the equation was used to estimate the nanopipette pore diameter using R_a . The graphs 6.4a and b also indicate that quartz nanopipettes of pore size $\sim 20\text{--}35 \text{ nm}$ exhibit a pore resistance (R_a) of $180 \pm 16.4 \text{ M}\Omega$ and borosilicate nanopipettes with $36.1 \pm 5 \text{ M}\Omega$ resistance (R_a) fall into a pore size range of ~ 190 to 250 nm diameter. Thus, the electrical measurements form a solid basis for estimating the pore size and if in

doubt was always confirmed under SEM.

6.3 Nanopipette properties

6.3.1 Ion–current rectification

These different–sized nanopipettes filled with 0.1 M KCl, also exhibited different ion current properties. Here, with the glass nanopipettes exhibiting a negative surface charge under the experimental condition, a very slight ion–current rectification or more of an asymmetry in the ion current is observed with respect to the direction of the bias for the nanopipettes which can be seen in the figure 6.5. Ion–current rectification in glass nanopipettes has been attributed to the charged surface and asymmetric tip geometry. When the pore size is comparable or less than the DDL for a particular electrolyte concentration, the uneven electrostatic potential due to the conical shape on the nanopipette tip has been used to explain the rectification [181] (chapter 3 for detailed DDL and surface properties of nanopipettes). This can be quantified through the rectification ratio r [3] defined by equation 6.3.

$$r = \frac{I_{-}}{I_{+}} \quad (6.3)$$

Where I_{-} is the ion–current at the given negative voltage and I_{+} the ion current at the same positive voltage. With our 20 nm quartz and 200 nm borosilicate nanopipettes we show a rectification ratio of 1.28 ± 0.4 and 1.07 ± 0.2 respectively, indicating an increased current in the negative voltage bias. This is consistent with other studies using similar pore size pipettes [238, 181]. While the rectification in 0.1 M KCl typically with 1 nm DDL [3] makes it negligible in larger pore sizes of 100 nm and above, for smaller pore sized nanopipettes of few nanometers, the DDL influences the asymmetric ion current which in turn affects the ion flux and conductance. This can be seen clearly from the I – V graphs in figure 6.5 for ~ 200 nm and ~ 20 nm borosilicate and quartz nanopipettes.

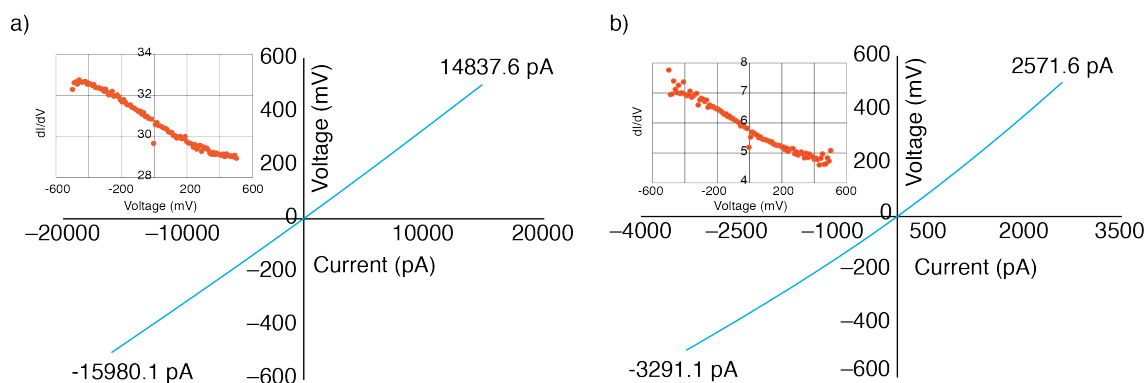


Figure 6.5: Representative I - V plots of average of 18 a) borosilicate and (b) quartz nanopipettes represented by blue lines highlighting that both nanopipettes exhibit ion-current asymmetry; the insets represent the derivatives (dI/dV) graph for current-voltage curves.

This ion current asymmetry also affects the indirect pore diameter calculation as reported in previous studies [230], as the pore resistance calculation does not take into account potential asymmetries in the I - V characteristics or even ion current rectification. This is evident from the I - V graphs (figure 6.5), for larger borosilicate pipettes the I - V curve is almost linear with only a slight ion current asymmetry and thus the pore resistance equation results in a pore size that is comparable to the pore size measured by SEM. But as the pore size decreases the calculation could not be associated to pore size with high correlation with respect to inner pore angle and ion-current asymmetry and it generates a slightly larger pore size than what is found through SEM. Nevertheless, this only results in a systemic error and therefore correctable.

6.3.2 Ion-current conductance during DNA translocation

Thus the transport of ions through the nanopipette is dependent on the surface charge of the nanopipette and the conductance is influenced by the ions and counterions in the pore. And during translocation of a biomolecule, the nanopipette conductance is governed by two factors.

Briefly, the nanopipette pore blockage due to the physical presence of the sample will cause a decrease in the flux of ions available for transport, this is called the geometric exclusion effect. At the same time the presence of a charged molecule (DNA) will introduce additional counterion charge carriers into the ion flux in addition to the counterions on the nanopipette surface. Thus the conductance change G can be represented as a combination of bulk ions and counterions as explained by Smeets *et al.* [207], given in the equation 6.4 below .

$$G = \frac{1}{L_{Pore}} \left[\frac{-\pi}{4} d_{DNA}^2 (\mu_K + \mu_{Cl}) n_{KCl} e + \mu_k^* q_{lDNA}^* \right] \quad (6.4)$$

Where L_{Pore} is the length of the pore, d_{DNA} is the diameter of the DNA sample, μ_K and μ_{Cl} are electrophoretic mobility of the respective ions moving with the DNA and q_{lDNA}^* is the effective DNA charge per unit length, n_{KCl} is the number density of potassium or chloride ions, e is elementary charge.

Studies also show that the surface charge on the nanopipette walls along with the charged DNA induce a cloud of positively charged counterions and the magnitude of this ion concentration near the pore tip changes with respect to the position of the DNA in the nanopipette [198]. Thus the conductance change and shape of the ion current during translocation can be represented as a combined effect of bulk ions and counterions shielding the surface charge.

For high electrolyte concentrations the first term in equation 6.4, the ion carriers in the bulk solution, dominate the ion current resulting in $G < 0$ but for low KCl concentrations the counter ion charge carriers dominate thus increasing the ion current ($G > 0$). This is observed in the representative ion current trace below and all throughout the experiments.

Figure 6.6 shows an ion current trace (~ 100 s) of 3.5 kb linear dsDNA molecule translocating from inside the nanopipette of ~ 20 nm pore size in 0.1 M KCl at -300 mV. With our nanopipette experimental setup with respect to DNA samples, an applied

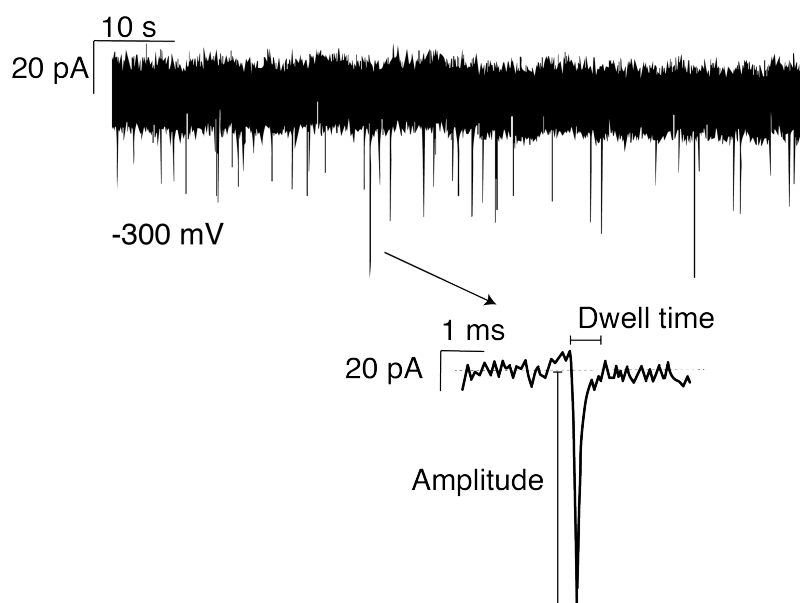


Figure 6.6: A representative ion-current trace for a 3.5 kb dsDNA sample translocating a ~ 20 nm pore with pore resistance of ~ 180 M Ω , exhibiting current enhancement in 0.1 M KCl at -300 mV applied voltage. The baseline current represents the flow of KCl ions and the individual events represent dsDNA molecule passage one at a time. The zoom in of an individual ion current peak shows the translocation time or dwell time and peak amplitude using which the biomolecules are characterised.

positive voltage to the electrode inside the nanopipette does not result in events, but a negative voltage drives the negatively charged DNA molecule towards the nanopore. As could be seen, this results in an absolute increase of ion current upon translocation of DNA molecules.

This observation is in agreement with previous studies [28, 29, 207, 239] involving translocation of dsDNA through nanopores reporting a decrease or increase in ion current conductance with regard to the concentration of electrolytes. In particular, salt concentration dependent conductance studies [207] shows that there is a gradual change in ion current from blockage to enhancement with a crossover point at KCl concentration of around ~ 300 mM. Recent studies by Wang *et al.* [240] also show that this cross over concentration is much lower (~ 100 mM) for bundled DNA nanostructures than that observed for linear dsDNA.

Thus the increase in ion current (amplitude) and the time taken for events to occur (dwell time) is used for ascertaining the characteristics of the sample biomolecules as shown in the next section.

6.4 Ion–current measurements

Initial translocation studies were conducted with 3.5 kb linear and 4.7 kb circular (Green fluorescent protein plasmid (GFP) [241]) DNA configurations, this allowed for the estimation of variables like appropriate voltage required for translocations and concentration of samples needed to achieve a good capture rate before moving on to folded DNA origami structures.

For this, nanopipettes of ~ 20 nm pore size was used and experiments were performed by addition of samples in 0.1 M KCl into the nanopipette with the translocation direction from inside to outside unless stated otherwise. Upon translocation, it was observed that depending on the DNA sample size and conformation, a magnitude of current blockage and translocation dwell time is produced. This could be observed from the data analysis of the ion current events of the two samples.

The circular plasmid with higher basepair length exhibited a higher peak amplitude and dwell time of 69 ± 19 pA and 0.13 ± 0.1 ms than that observed for linear DNA (47 ± 14 pA and 0.11 ± 0.04 ms) as seen in the figure 6.7. This could be explained through the different ion and counter ion distributions in the nanopipette due to the varying conformation of linear and circular DNA samples in solution combined with their size differences. Thus the two samples were detected and differentiated via their significantly varying peak amplitude.

Also, the ion current signal observed for the biomolecules is with respect to the nanopipette pore size, i.e., translocation of linear and plasmid DNA in ~ 200 nm pore nanopipettes resulted in very low or no ion current events when compared to the 20 nm pore. Further, a final sample concentration of about 500 pM inside the nanopipette was found to be ideal

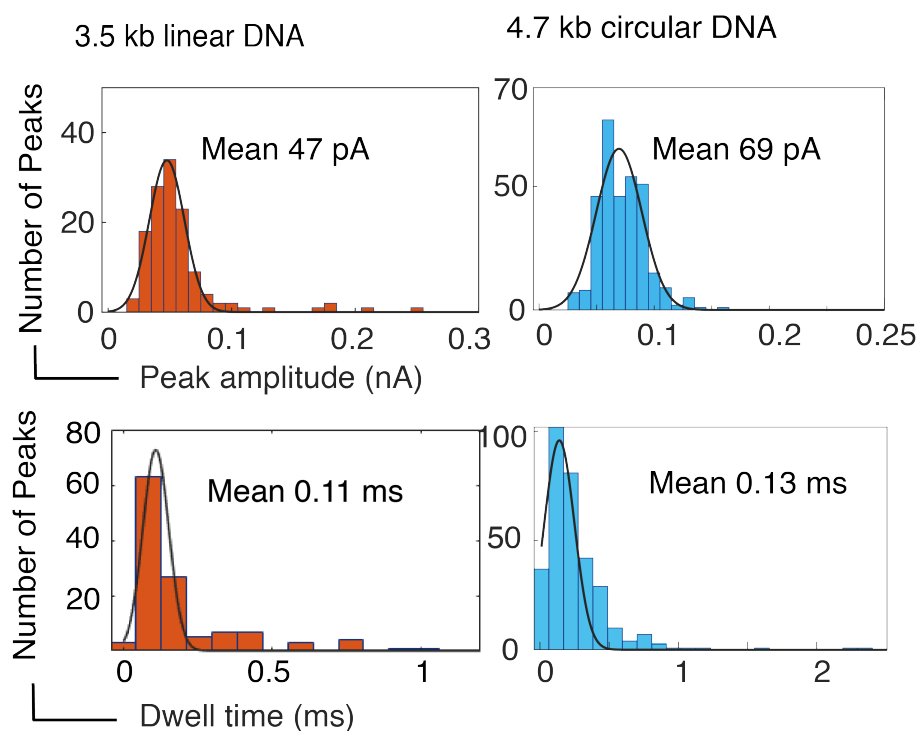


Figure 6.7: Single entity detection, The histograms represent the peak amplitude and dwell time for a) linear DNA molecule (3.5 kb) and b) 4.7 kb circular DNA obtained upon translocation via ~ 20 nm pore size nanopipettes with pore resistance ~ 186 M Ω . The data represents >80 events for each sample.

for translocation without clogging the pipette, also, while a negative voltage bias of 200 to 250 mV is sufficient for occurrence of events, negative 300 to 350 mV is appropriate for obtaining good number of events within a short recording time (2 minutes).

Next, the effect of sample concentration and applied voltage on ion current was studied using plasmid samples, for this, increasing concentrations of GFP plasmids (from 10 to 500 pM) were translocated at a constant applied voltage (-350 mV). The observed ion current trace presented with a steady increase in the number of events with respect to sample concentration as shown in figure 6.8a and b and exhibited a constant dwell time of 0.12 ± 0.1 ms.

Alternatively application of increasing voltage to a fixed sample concentration (500 pM) also presented with increased event capture rate and enhanced event signal. It can be

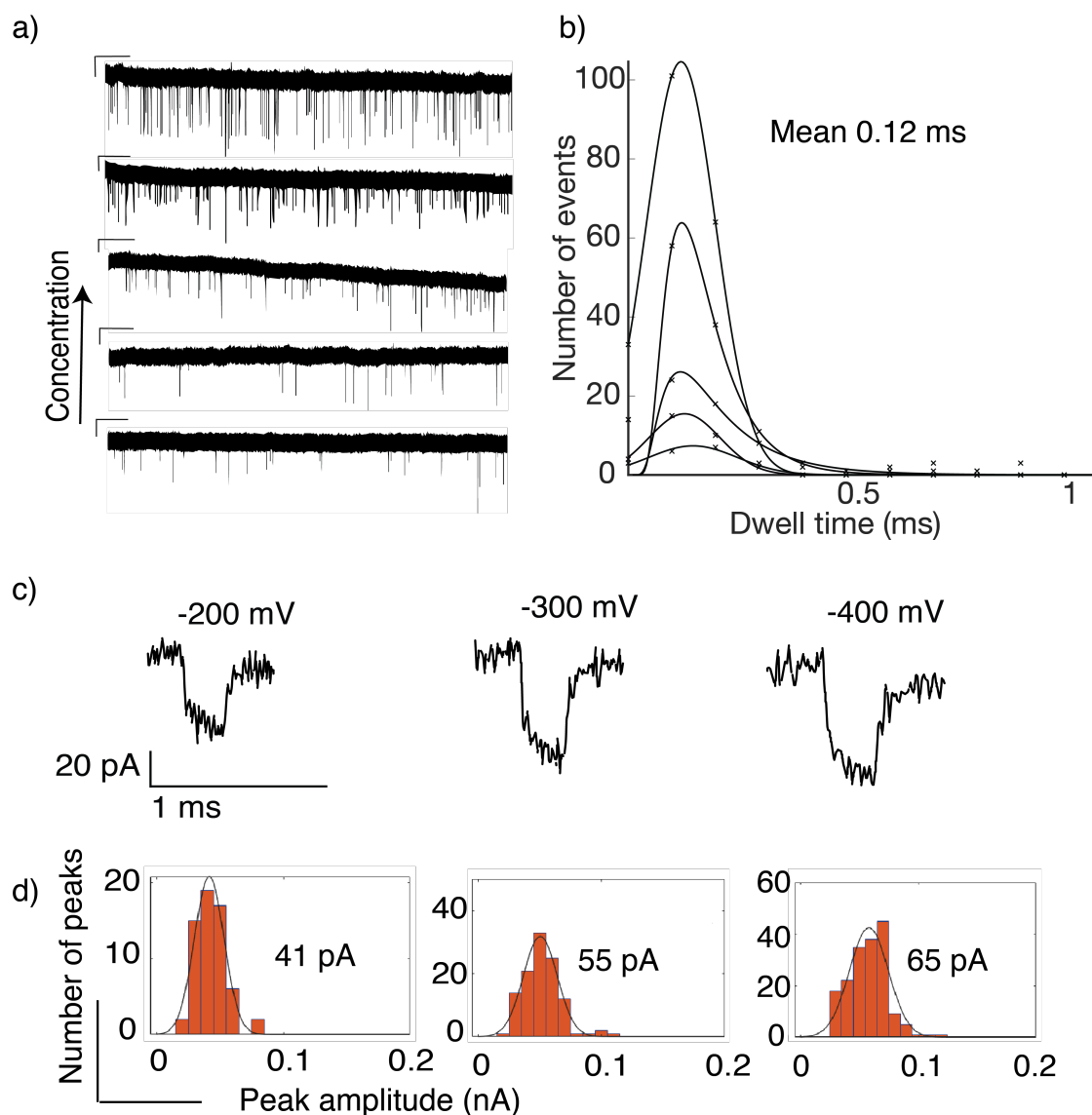


Figure 6.8: Effect of concentration and voltage on ion current translocation. a) Ion current traces for increasing concentration of circular DNA samples indicating increase in events with b) constant dwell time as shown in the histogram. c) Increase in applied voltage increases peak amplitude. d) individual histograms of peak amplitude for varying voltages, $n > 40$. The nanopipettes used exhibited a pore resistance of $\sim 180 \text{ M } \Omega$.

observed from the peak amplitude histograms (Figure 6.8d), the mean amplitude slowly shifts from $41 \pm 11 \text{ pA}$ for -200 mV to $55 \pm 13 \text{ pA}$ for -300 mV and $65 \pm 15 \text{ pA}$ for -400 mV indicating occurrence of events with higher peak amplitude. This voltage dependent

increase in ion conductance is also in agreement with previous linear DNA translocation studies [29] and could be explained due to the predominant electrophoretic force upon the negatively charged DNA backbone [242].

6.5 Conclusion

This chapter covered the detailed characterisation studies performed to confirm the pore size of nanopipettes fabricated using particular pulling parameters. It was demonstrated that IV measurements provide a quick and reliable approximation of the nanopipette pore size and SEM visualisation could be used to confirm the same. The pore sizes estimated were in good agreement with SEM and different sized nanopipettes pulled via various parameters could be easily characterised for pore size with high accuracy.

In particular, a pore resistance of approximately $180 \pm 16.4 \text{ M}\Omega$ represents pore size from $\sim 20\text{--}35 \text{ nm}$ and $36.1 \pm 5 \text{ M}\Omega$ resistance is for pore size range ~ 200 to 250 nm diameter. The study also showed that it is important to choose nanopipette pore sizes in accordance to the sample to be detected in order to actually detect the sample other than to enhance signal to noise ratio. Specifically, while 20 nm sized pipettes were sufficient for detecting both linear and plasmid DNA samples with good signal to noise ratio, the samples were very small to be detected with the larger 200 nm pore sized pipettes.

The 20 nm nanopipettes were successfully used to translocate, detect and differentiate linear and circular DNA samples via the ion current characteristics, peak amplitude and dwell time. In that, the linear DNA sample presented with $\sim 47 \text{ pA}$ amplitude and the larger plasmid DNA showed an increasing $\sim 69 \text{ pA}$, whereas the dwell times observed for both the DNA samples were similar 0.11 ms and 0.13 ms respectively.

The pipettes were subsequently used to translocate different concentrations of plasmid DNA samples and their respective ion currents analysed. While dwell times for the different concentration were similar, the capture rate showed significant difference with increasing number of events in relation to the sample concentration. Similarly

translocation at different voltages while keeping the sample concentration constant revealed an increasing ion current amplitude with difference in the ion current mean.

Thus the experiments in this chapter helped to confirm that I–V voltammetry can be reliably used to correlate pore resistance with pore size using our setup and also evidenced the ability of nanopipettes to detect and differentiate different biomolecules. The preliminary translocation studies also provided an estimation of appropriate sample concentration (~ 500 pM) and voltage bias (-350 mV) required for translocating the samples with an ion current signal discernible from the background noise.

Chapter 7

Single Molecule Analysis with Nanopipettes

7.1 Introduction

In the previous chapter successful translocation of linear and circular DNA molecules through glass nanopipettes was demonstrated, this was important for proof of concept of biomolecular translocation using the nanopipette setup and for initial characterisation.

Moving forward, this chapter focuses on the next aim of the thesis, to study larger DNA molecules translocation, particularly DNA origami. These nanostructures, as opposed to circular and linear DNA that tend to form random coils in solution [243], are designed to be structurally defined (see chapter 2) thus resulting in a rigid geometry .

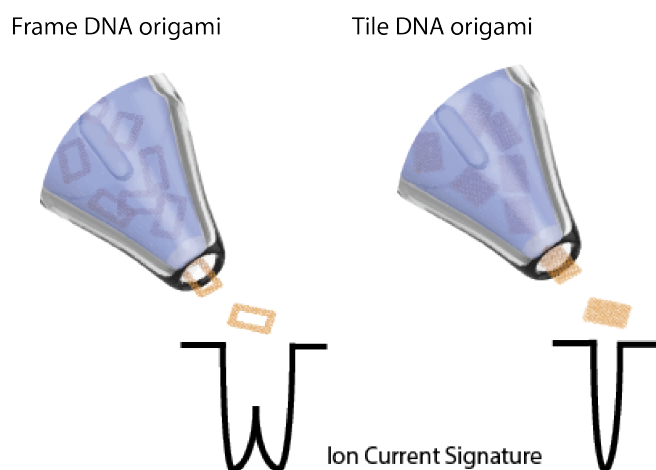


Figure 7.1: A schematic representation of the nanopipette for translocating 'Frame' (left) and 'Tile' (right) DNA origami.

Translocation of such DNA nanostructures through nanopores has been recently investigated. In particular, the differentiation of DNA cubes from RNA rings was demonstrated using variations of the peak dwell time and the peak ion current through a 50 nm silicon nitride nanopore membrane [244]. Similarly, nanopipette detection of double helix concatamers examining the translocation dwell time to extract information on sample length and folding state was demonstrated [245]. Further work using DNA origami as a molecular breadboard to isolate nuclear pore complexes enabled the differentiation between wild type and mutant forms by analysis of their characteristic ion current traces [246].

However, despite these remarkable successes, the relationship between the structure of the DNA origami and the corresponding ion current during translocation remains largely unexplored which hinders the adoption of these nanostructures for various nanopipette applications like as carriers and unique identifiers. In the following sections differently structured DNA origami samples are studied in relation to their ion current signature for the above said purpose utilising two structures, frames and tiles as shown in figure 7.1.

Herein, the DNA origami translocation data is discussed using traditional methods of analysing ion current measurements, i.e., through dwell time and ion current amplitude, but also the importance of ion current structure and its correlation with sample geometry is discussed in detail which would be the basis on which this study is built on.

7.2 2D DNA origami analysis

Four different DNA origami samples of similar size assembled using the same 7249 nt M13mp18 ssDNA as scaffold were investigated via nanopipette translocation experiment to understand, if the structural differences in DNA origami correlated with the ion current signals. The four origami designs, two frame structures (F1 and F2) and two solid tile structures (T1–plain tile and T2–same as T1 tile but with 44 additional protruding loops on one side), were formed through different folding of an identical ssDNA scaffold in

the presence of >200 pooled short staple oligonucleotides as explained in chapter 5. Importantly, the plain tile and frame DNA structures differ only in geometry and not their constituent sequence, and as a consequence their charge and molecular weights remain identical, hence any differences in the observed ion currents are directly related to the structural variation of the DNA origami and not a change in mass or charge.

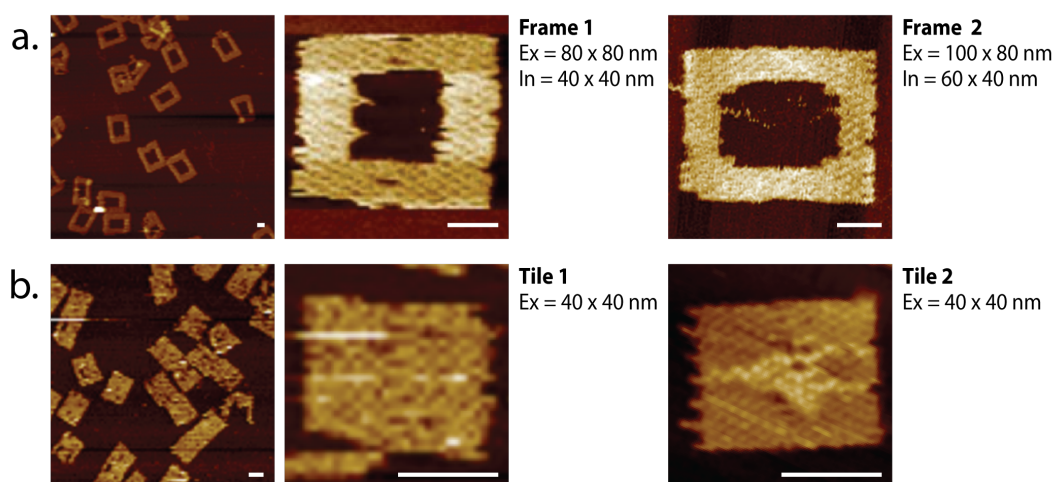
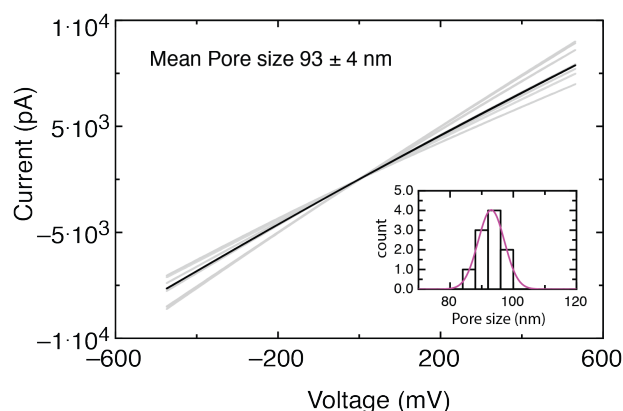


Figure 7.2: AFM images of the different DNA origami structures, showing a range of uniformly formed structures along with an individual representative AFM scan of both frame and both tile DNA origami. a) Frame DNA origami F1 and F2 with the internal (In) and external (Ex) dimensions indicated. b) Tile DNA origami T1 and T2 with external dimensions indicated. The scale bars for all images are 20 nm.

The successfully folded structures were resolved in a 0.5% agarose gel (appendix C figure C.17). The folded rigid structure can be seen as a distinct band running slightly above the m13mp18 scaffold run as a control in the second lane. The gel electrophoresis also shows the successful purification of the folded structures from excess staple oligonucleotides, seen at the bottom of the lane, via S400 size exclusion columns (chapter 4). The purified successfully assembled DNA origami structures were then imaged through AFM as shown in figure 7.2. From the AFM image the folding efficiency was estimated about 70–80% for the various structures. The observed sizes were found to be in

excellent agreement with the designed dimensions for both frame and tile origami. F1 is approximately 80×80 nm with an internal cavity of 40×40 nm, and F2 is 80×100 nm with a 40×60 nm internal cavity (Figure 7.2a). In comparison, both DNA tile designs (Figure 7.2b), T1 and T2, are approximately 40×40 nm. The different routing designs employed for formation of these structures are provided in appendix B.

a. IV plot of nanopipettes



b. SEM image of nanopipette tip

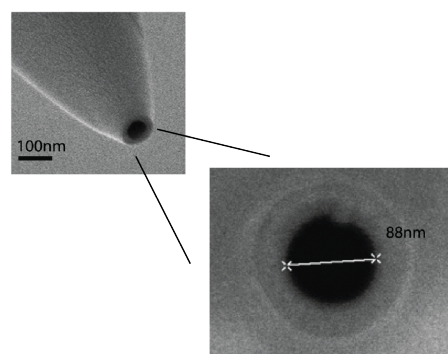


Figure 7.3: a) IV characteristic for a set of 10 quartz pipettes with 76 ± 10 M Ω pore resistance (80–100 nm) pulled using parameters in chapter 5, the inset shows a histogram for pore size data fitted with a Gaussian curve and b) shows a SEM micrograph of one representative nanopipette pore size pulled using the same parameters.

For translocation studies, nanopipettes with pore sizes in the range ~ 100 nm were fabricated, to closely match the DNA origami sample size utilised in this chapter and following chapters 8 and 9. The pulling parameters established via the SEM characterisation study from chapter 6 (tabulated in table 5.1 in chapter 5) resulted in pore sizes 93 ± 4 nm, as perceived from the histogram shown in inset of figure 7.3a, which represents a batch of 10 pipettes pulled on the same day. Pore size estimation via pore resistance in comparison with SEM images were also in good correlation (appendix C, figure C.18) and the IV curves as shown in the figure for the respective pore sized pipettes also provide further evidence of consistency. It was found that pore sizes of nanopipettes pulled on different days slightly varied, but the distribution range remained consistent between few tens of nanometers with 76 ± 10 M Ω pore resistance.

7.2.1 Differentiating 2D DNA origami

The nanopipettes were filled with a solution of 0.1 M KCl containing 500 pM of the DNA origami. Similar to previous chapter 6 involving dsDNA, for a 500 pM sample concentration a voltage of -350 mV applied between the electrode inside the nanopipette and the electrode in the surrounding electrolyte translocated the origami through the nanopore causing a temporary increase in the absolute value of the ionic current. This increase in ion current is in agreement with linear DNA and plasmid samples in chapter 6 and existing literature [240]. Figure 7.4a shows examples of ion current traces representing more than 90 single molecule events obtained for each of the DNA origami structures, and figure 7.4b shows a selection of zoomed-in current peaks for the different origamis i.e., F1, F2, T1 and T2.

Interestingly, noteworthy differences were observed between the respective peak current amplitudes and dwell times of the translocation events of the four origami samples. From Figure 7.4c, which displays the frequency of observed peak ion current amplitudes for the different origamis, it can be seen that the ion current observed during the translocation of F2, which is slightly larger in dimension than F1 (100×80 nm vs 80×80 nm), exhibit a higher mean absolute current amplitude of 59 ± 15 pA compared to 37 ± 10 pA. In contrast, both the solid tile origami T1 and T2 show a higher mean absolute current amplitude of 65 ± 11 pA and 75 ± 10 pA, respectively, than either of the frame origami structures.

This may suggest that the counterion distribution of the tile origami during translocation differs from that of the frame origami, thus increasing ion flux and respective current when compared to their frame counterparts. The small difference in current amplitude between T1 and T2 might stem from the fact that T2 contains additional DNA loops on its surface which may impact the counterion distribution and thus lead to a further increase in ion transport during translocation. Considering that F1, F2 and T1 DNA origami are formed from the same ssDNA scaffold and hence possess the same charge, it is noteworthy that the geometry of the origami appears to play an important role in the translocation ion current and thus can be differentiated via peak amplitude averages.

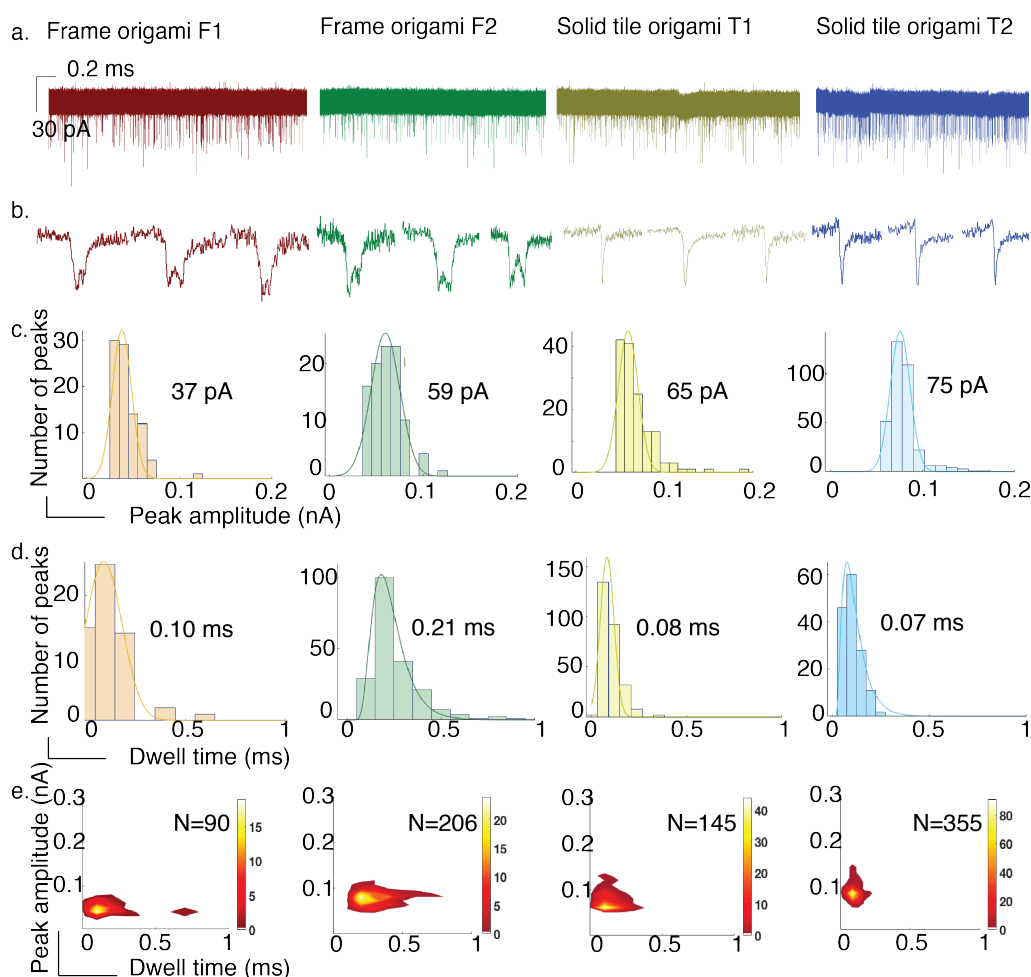


Figure 7.4: *a)* Ion current recordings for each of the frame and solid tile origami samples via nanopipettes with $\sim 82\text{ M}\Omega$ resistance. The data consists of at least 100 events each. The recordings are of approximately 100 seconds in duration, sampled at 100 kHz and low-pass filtered at 20 kHz to remove high-frequency noise. *b)* Representative selection of current peaks observed for individual translocation events for the frame and tile origami. Dwell time and peak amplitude histograms depicting *c)* frequency of observed peak currents and *d)* dwell times for each origami. The solid lines represent Gaussian fits, from which the respective mean peak currents and dwell times are obtained. *e)* Colour maps, displaying the frequency of events with different current amplitudes vs dwell times, revealing that wider distributions are observed for the frame origami compared to the tile origami.

These results corroborate the results of a recent study by Alibakhshi *et al.* wherein the ability of silicon nitride nanopores to differentiate ring-shaped RNA and cube-shaped DNA nanoparticles using similar means was demonstrated [244]. Similar to the differences in mean peak current amplitude, significant differences in the dwell times of the translocation events of the different DNA origami were also observed. The mean of the observed dwell time for both T1 (0.08 ± 0.04 ms) and T2 (0.07 ± 0.03 ms) are slightly smaller than that of the frame origami F1 (0.10 ± 0.09 ms), and much smaller than that of frame origami F2 (0.21 ± 0.07 ms). The dwell time provides an indication of how long the DNA origami spends in the nanopore, and can therefore be used as an indicative measure of the speed of translocation. Hence, the mean dwell times of the different origami suggest that the tiles travel through the nanopipette opening faster than both frames.

Also, the distribution of dwell times observed for the different DNA origami structures are significantly narrower than those found in previous studies with DNA nanostructures [244], DNA concatemers [245], and DNA origami [246] where prolonged dwell times were reported. However, the nanopores employed for this work differ significantly from the ones in the cited studies and hence the results are not directly comparable.

7.2.2 Frame origami Ion current signature

In addition to the differences in mean current peak amplitude and dwell time between the different DNA origami, it can be seen from the selection of current peaks shown in figure 7.4b that a distinct difference in peak shape is observed between the frame and tile origami. These results suggest that perhaps the peak shape can be used as a unique fingerprint of the origami to deduce small structural changes between differently folded DNA origami. Here, the tile origami was found to produce a single peak upon translocation, as would be expected for a single entity passing through the nanopore.

However, where the frame structures were translocated, a characteristic double peak, or W-shaped peak, was observed. The absence of such double peaks in any of the tile origami samples suggests that the double peaks are characteristic of the frame structure,

and likely specifically of the presence of a cavity in the structure's centre. Figure 7.5 portrays an array of representative peak shapes obtained from translocation events of the frame and tile origami.

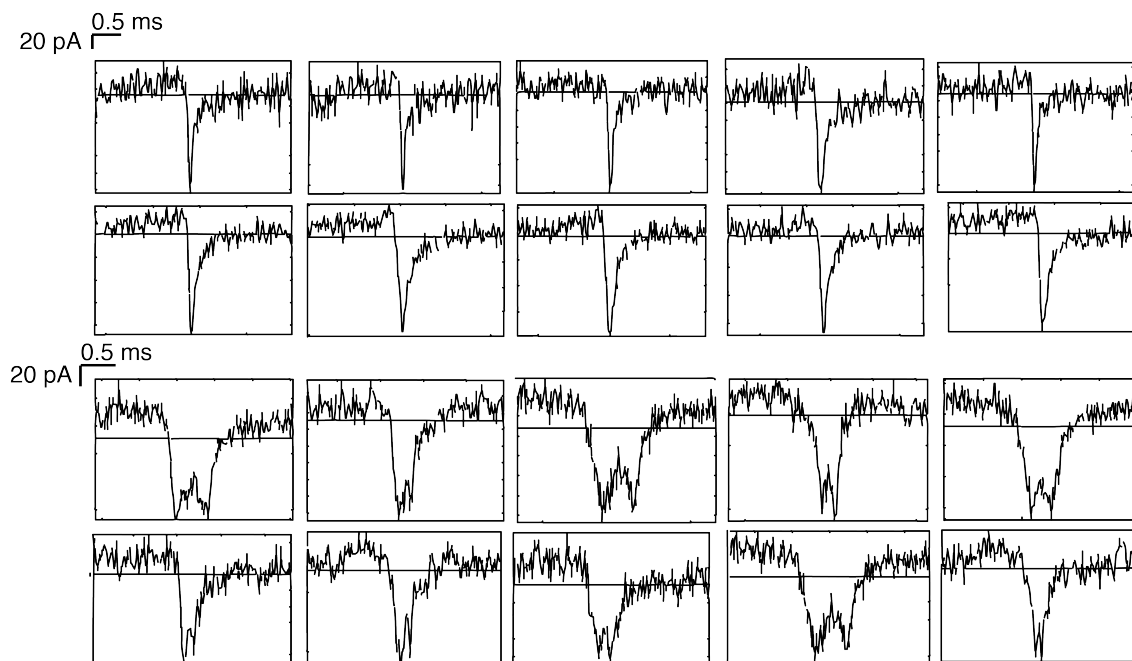


Figure 7.5: Array of single and double peak ion current signatures observed for tile and frame samples represented in the top and bottom rows respectively.

References to double or multiple peaks within a single event have been reported in previous studies. In that, Zhang *et al.* show multiple peaks including double peak for Au nanorod sample translocation due to the tumbling motion or rotation of the individual structures during translocation [247]. Another example for multiple peak observance is reported by Steinbock *et al.* and Maglia *et al.* [248, 96] for long linear DNA samples. In these reports the multiple peaks are because of the different states in which the DNA pass through the nanopore due to random folding.

The multiple peak occurrences in the above mentioned studies are arbitrary and vary from event to event perhaps depending on the orientation of the molecule in question as they translocate the nanopore. However, the double peak like structures observed in this study are consistent throughout most of the events, and a third or multiple peaks was

not observed for any of the samples. Also the absence of double peaks for the solid tile further strengthens the argument to attribute double peak observance to the geometry of the nanostructure itself. Table 6 in appendix B, shows the number of double peaks observed for F1 and F2 frame DNA origami to be 50 to 60%, whereas T1 and T2 exhibit >94% single peaks only.

Dwell time analysis of frame origami

Moreover, translocation of F1 DNA origami was investigated at different translocation voltages -250 mV and -300 mV in addition to the -350 mV reported above. Figure 7.6 shows a number of different translocation peaks of the sample at different translocation voltages, and it can be seen that double peak structures are observed for all investigated translocation voltages. The dwell times of the individual translocation events are indicated in the panels, and a notable increase is observed with decreasing translocation voltage.

This is corroborated by the frequency plots of events vs observed dwell time for the different translocation voltages (figure 7.6b). Given that the translocation of the DNA origami is driven by the applied voltage, it can be expected that the translocation speed decreases with voltage and therefore the origami will spend more time in the nanopore, resulting in an increase in observed dwell time. Similarly, the number of observed events per unit time decreases with applied translocation voltage, and while at a translocation voltage of -250 mV still a significant number of events is observed, at -200 mV, no translocation events were registered.

In contrast, increasing the translocation voltage to greater than -350 mV resulted in very high translocation speeds and consequently a rapid flux of DNA origami through the nanopipette pore leading to clogging of the pore and eventually termination of the transport. The slower translocation speed at the lower translocation voltages is also expected to improve the ability to resolve potential double peaks, and this is indeed reflected in the data, where more prominent double peaks are observed at lower translocation voltages, figure 7.6a.

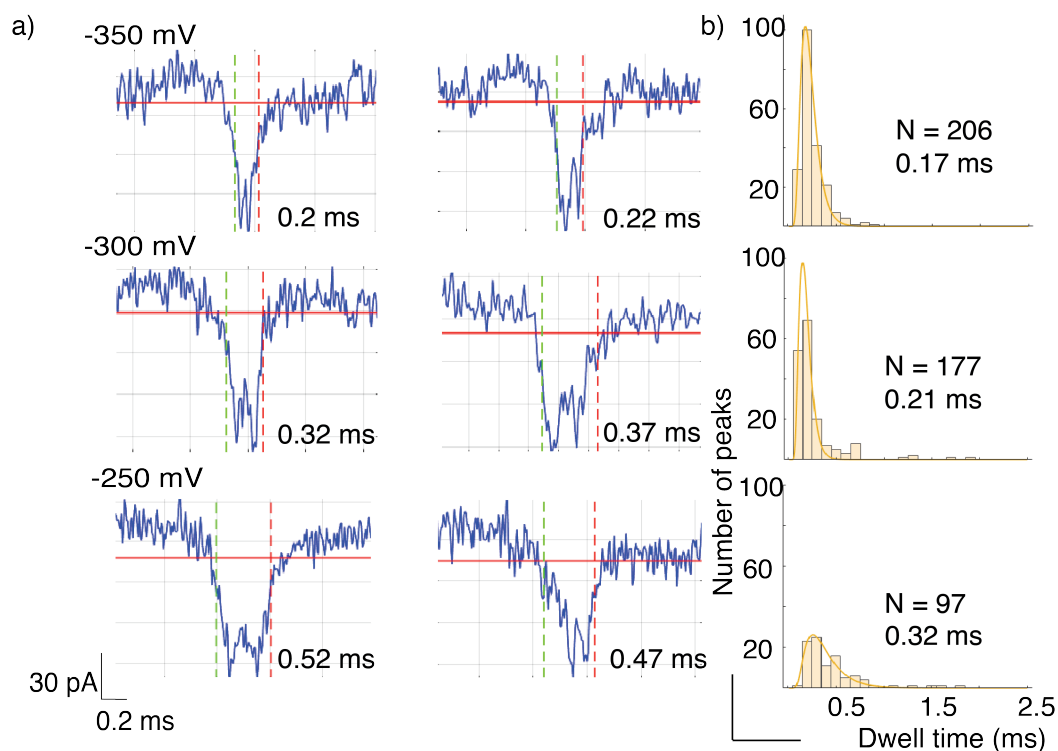


Figure 7.6: *Frame DNA origami dwell time analysis using nanopipettes exhibiting $\sim 79 M\Omega$ pore resistance. a) Representative set of translocation current peaks for frame origami F1 at different applied voltages. The dwell times of the different peaks are indicated in the figure. It can be seen that double peaks are observed for all applied voltages. b) Frequency of dwell times for translocation of frame origami F1 at different voltages; a wider distribution of dwell times is observed at lower translocation voltages, and an increase in the frequency of events is observed with increasing translocation voltage.*

7.2.3 Double peak analysis

Interestingly, the shape and composition of the double peaks were also found to differ for the two different frame origami F1 and F2. Figure 7.7 shows the distribution of the dwell times of the two constituent peaks P1 and P2 of the characteristic double peaks observed during the translocation of frame origami. While the dwell time for P2 is similar for origami F1 and F2, the dwell time of peak P1 for frame F2 is twice as long as that of P1

for frame F1.

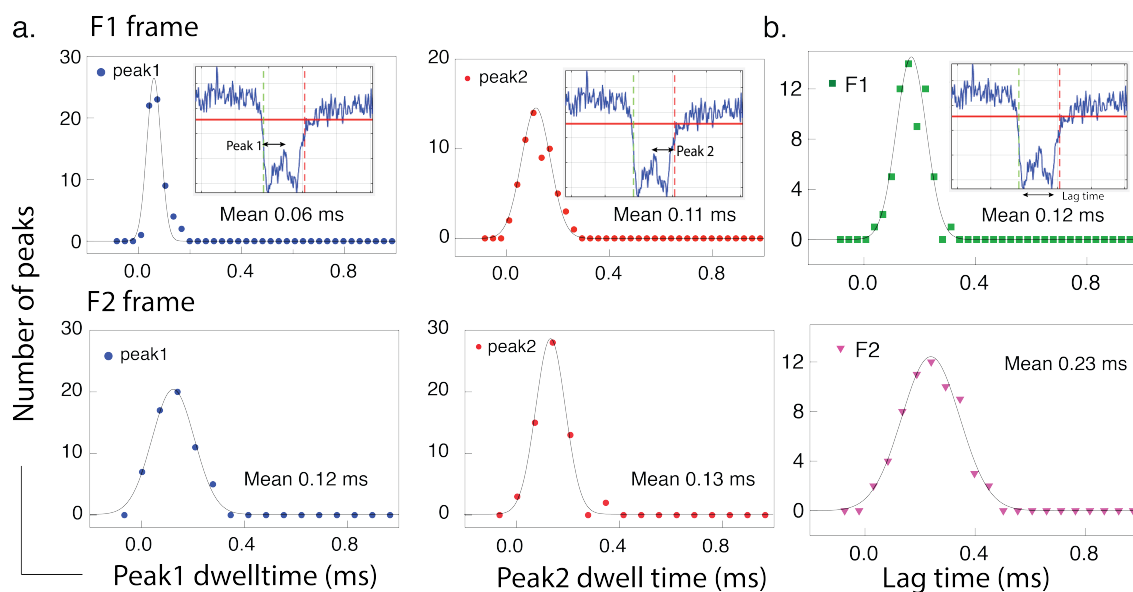


Figure 7.7: Lag time analysis of the double peaks of the frame DNA origami translocated through nanopipettes with $\sim 84 \text{ M}\Omega$. a) Frequency plot of the individual dwell times for individual peaks P1 and P2 for F1 (top panel) and F2 (bottom panel); the insets show a typical double peak with peak 1 and peak 2 dwell time indicated, respectively. b) Frequency plot showing the number of observed translocation events with different lag times for frame origami F1 (top) and F2 (bottom); the inset depicts the lag time between peak 1 and peak 2 of a typical peak. The solid lines represent Gaussian fits to the data, and the observed mean values as extracted from the fit are given in the individual panels. The data represents >80 events for each analysis.

Furthermore, the lag time between the two constituent peaks P1 and P2, determined by the time difference between the occurrence of the maxima of the two peaks, has been measured and the results for both frames are shown in Figure 7.7b. Given that the occurrence of the double peak is linked to the frame-like shapes of the DNA origami, it can be argued that the double peak arises as a consequence of the passage of one arm of the frame through the nanopipette pore, giving rise to P1, followed by the central cavity, and finally the other arm of the frame, giving rise to P2.

Therefore, the lag time between P1 and P2 would be related to the dimensions of the

internal cavity of the frame. Indeed, the lag time for frame F2 which has a central cavity of 60×40 nm is almost twice as long as the that of F1 which has a smaller central cavity of 40×40 nm.

Moreover, in addition to an overall longer lag time, the distribution of observed lag times for F2 ($0.23 \pm 2\%$) is significantly broader than that for F1 ($0.12 \pm 2\%$). This may be a consequence of the symmetry of the central cavity. F1 has a symmetrical central cavity (40×40 nm), resulting in a tight distribution of double peak lag times as the relevant cavity dimension is independent of the orientation with which it travels through the nanopore. In contrast, F2 has an asymmetric cavity (40×60 nm) which would give rise different lag times depending on the direction of travel and hence to a broader distribution of lag times.

7.3 Conclusion

Here, the ability of glass nanopipettes to detect structural differences between different DNA origami, in particular to distinguish different 2D origami structures (frame from tile) is demonstrated, which shows that nanopipettes can be employed as a highly sensitive detection tool to analyse individual molecules.

Specifically, it is shown that both the dwell time as well as the amplitude of the ion current peak can be used to differentiate nanostructures of different types, which is in line with previous studies. In addition, it is demonstrated that the structure of the peak can be used to distinguish different DNA origami structures.

The observation that the ion current peak structure holds sufficient information to be correlated to a particular DNA origami structure was established through the investigation of different frame and tile DNA origami structures, i.e., the frame DNA origami led to a characteristic double peak, while the solid tile origami only led to single peaks in ion current.

Furthermore, preliminary evidence that the shape and composition of the double peak and the individual constituent peaks are related to the dimension of the frame and in particular

that the lag time of the two constituent peaks varies with the dimension of the central cavity of the frame is put forward. This suggests that the ion currents observed during the translocation of DNA origami through nanopipette pores can be used to distinguish not only coarse structural differences (frame from tile) but also more subtle variation in relation to the central cavity.

Chapter 8

Double Peak Analysis using Concentric Squares

8.1 Introduction

As indicated in the previous chapter nanopipettes are capable of detecting and differentiating subtle geometric differences between DNA origami structures, it was also observed that the frame DNA structure has a characteristic ion current signature in relation to its central cavity. Therefore, in order to exploit the central cavity signature for further applications, it was first necessary to define the relationship between the ion current peak structure and cavity size. This was achieved via translocation studies of a set of rationally designed nanostructures, which will be the objective of this chapter. Till the previous chapters, the approach to deriving these different nanostructures required the rerouting of the same 7249 nt ssDNA scaffold in order to create a central cavity within the design. As such, the entire geometry and all the dimensions of the DNA nanostructures used were different between solid and frame-like designs.

However, to validate and demonstrate the potential of the double peak characteristics, frame DNA nanostructures with specific geometries were required in order to establish the geometric influence on translocation ion current. To this end, this chapter will first elaborate the steps for designing and assembling DNA origami structures with specific fixed geometry via custom made scaffolds. Three different lengths of scaffolds were

produced to design three nanostructures in a way that they resembled a nested square, i.e., while the outer length and width remained constant only the inner frame window differed, figure 8.1.

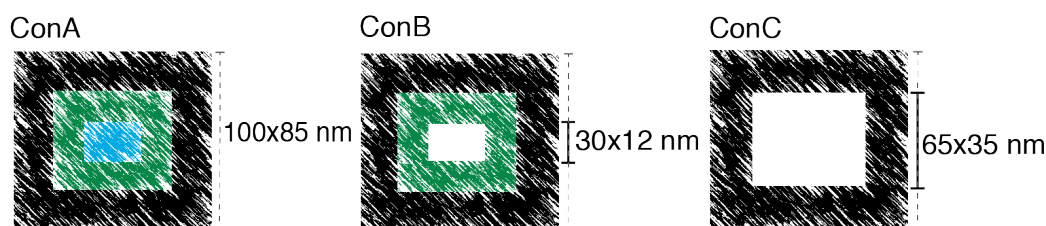


Figure 8.1: Schematic of concentric square design, the DNA frames were designed to have the same outer dimension and varying cavity size.

Later sections in the chapter will include nanopipette translocation studies of the constructed concentric square nanostructures and subsequent analysis to test if the double peak ion current could be influenced through the frame dimensions especially the size of the cavity. This systematic study will also be used to determine the sensitivity of the nanopipette to detect the central cavity, as such a limit of detection for the double peak occurrence.

8.2 Custom scaffold production

Many DNA nanotechnology applications requires DNA origami structures made from different lengths of scaffold DNA apart from the commercially available scaffold. The ability to produce custom scaffold sequences is of great benefit to the design process, for example, it allows for creation of larger structures, provides better control over the final size and shape and control of basepair placement at specific locations within the structure. A variety of enzymatic methodologies are available that enable production of custom-made scaffolds, including rolling circle amplification of a circular template

[249, 250], site specific mutagenesis [251] or nicking and sequential digestion of one strand of a plasmid [75]. Though these methodologies offer sequence customisability, production yield and scale up is difficult due to the many enzymatic processing steps.

On the other hand, large scale production of ssDNA using filamentous bacteriophages along with fast multiplying *E.coli* cells as host is another way of producing custom scaffolds [252]. Filamentous bacteriophages like M13 are bacteria-specific viruses that can package and transport their single stranded genomes into rod-like particles with a protein coat. These phages can be separated from the culture media and the ssDNA purified via molecular biology techniques. However, sequence customisability in the M13 phage is limited because most of its genome (<6 kb) contains protein coding and regulatory sequences that cannot be easily altered without hindering phage growth.

Alternatively, phagemids, engineered vector that contains plasmid and M13 components, are an efficient way to produce ssDNA. Phagemids contain two replication origins, a standard plasmid origin and the other derived from M13 that is essential for ssDNA synthesis but lacks the enzymes and proteins required for ssDNA packaging and production. Thus the cells containing custom phagemids must be co-infected with helper phage or co-transformed with a helper plasmid for successful production of ssDNA [253], and are ideal for sequence customisation. Helper plasmids and phages usually are devoid of origin of replication or contain defective packaging signals, this allows for preferential packaging of phagemid and also prevents helper DNA from being packaged. Successfully packaged phagemids can then be identified using two different antibiotic resistance gene present in the helper plasmid and phagemid.

In this study, pBluescript II SK(+) phagemid (PBS) was used to create three scaffolds of varying lengths through molecular biology techniques to design DNA origami constructions with similar outer dimension and different inner dimension. The DNA constructs were termed concentric squares (Con) A, B and C and the scaffolds required for these were stitched together from two fragments derived from lambda (λ) phage DNA along with PBS, as shown in the figure 8.2a. The PBS (+) are plasmids containing the phage origin (f1 ori) of replication and an ampicillin resistance gene. The helper plasmid

used is M13cp which is based on M13 phage without its packaging signal and contains a chloramphenicol resistance gene.

Thus the 9 kb custom scaffold required for achieving the envisioned DNA origami design was produced by inserting 6.1 kb sequence, derived as two separate fragments from λ phage, into the 2.9 kb phagemid. These two fragments (approximately 1.8 kb and 4.2 kb) were selected devoid of protein coding regions to eliminate any interference in the phage growth and downstream process. The elaborate map for scaffold assembly is provided in the appendix D.

8.2.1 Scaffold assembly

Briefly, the fragments that make up the scaffold referred to as f1, f2 and f3 were PCR (see chapter 5 section 2.2) amplified from the respective λ and PBS plasmid DNA templates using appropriate primers. The primers used in the amplification procedure were designed to incorporate the restriction sites EcoRI and NspI flanking the product f2 and NcoI and NspI flanking f3 respectively.

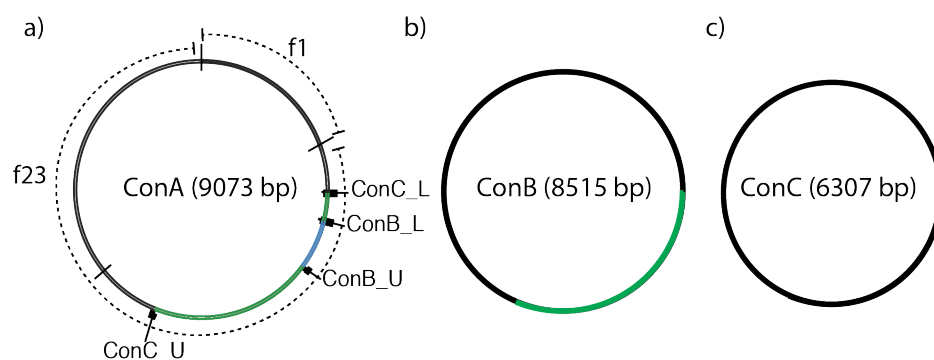


Figure 8.2: Scaffold assembly, Schematic portraying fully assembled ConA scaffold consisting of fragments f1 and f23 (formed via f2 and f3 ligation). ConB scaffold is produced by PCR amplification of regions ConB–L and ConB–U which incorporates *KasI* restriction sites at the ends and ConC via amplification of Con–L and Con–U primers incorporating *BmtI* sites.

The two fragments were then restriction digested with the respective enzymes to form

sticky ends which were used for ligation (chapter 5 section 2.1), thus resulting in one long fragment (f23). This long fragment was then combined with f1 using the NEBuilder HiFi DNA assembly protocol (chapter 5 section 2.7) by considering the long fragment f23 as vector and short fragment f1 as insert, resulting in f123 dsDNA.

Subsequently the circular dsDNA (f123) was chemically transformed in competent E.Coli cells to produce the custom scaffold. The transformed cells with the f123 plasmid were selected using their antibiotic resistance gene and recovered with a miniprep (chapter 5 section 3.0) to be co-transformed with helper plasmids (M13cp cells) to produce ssDNA f123. The transformation and ssDNA expression steps are further explained in methods and materials (chapter 5). The final ssDNA f123 product constituted 9073 bp and made up the largest scaffold for the DNA construct ConA.

The two smaller scaffolds for the DNA constructs ConB and ConC were produced by PCR amplification with double stranded f123 as template. As before the primers were designed to incorporate the restriction digest site KasI for the product ConB and BmtI for the product ConC respectively as shown in the figure 8.2. Subsequent restriction and ligation followed by similar co-transformation protocol with helper plasmids as above results in 8515 bp and 6307 bp ssDNA scaffolds for Con B and C.

In the first instance the scaffold strains were produced in 5 ml tubes and was then followed by large scale scaffold harvesting by scaling up to 500 ml cultures. The cultures were harvested by separating the bacteria from the phagemid and subsequent phenol chloroform DNA extraction. The single stranded scaffold yield for the three samples were upto ~ 1200 ng/ μ l (in 50 μ l volumes).

Scaffold formation confirmation

The different fragments formed were verified for correctness every step of the assembly protocol via gel electrophoresis, figure 8.3a shows the successfully amplified and ligated f1 and f23 fragments and the final double stranded ConA, B and C DNA respectively.

Additionally the double stranded scaffolds were also double digested with multiple

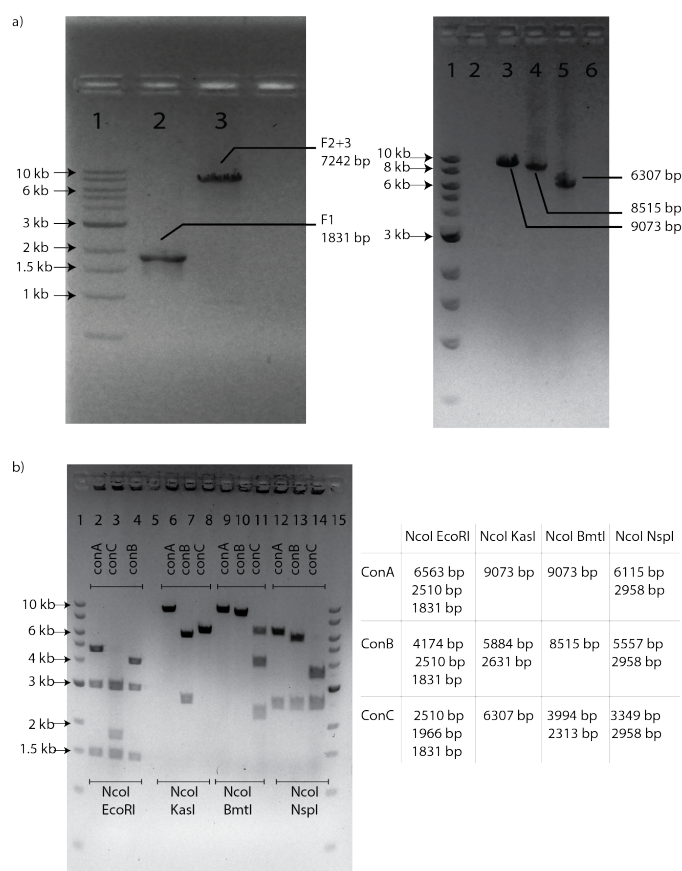


Figure 8.3: Gel electrophoresis confirmation images of a) the fragments used in hifi cloning to form the final ConA construct and the final custom scaffolds. b) The three different scaffolds were subjected to restriction digestion with NcoI and EcoRI, NcoI and KasI, NcoI and BmtI and NcoI and NspI pairs. The fragments are visualised in 1% agarose in $1\times$ TAE buffer at 80 V with minimum run time of 60 mins.

restriction enzyme for further confirmation. Restriction digestion with NcoI and EcoRI, NcoI and KasI, NcoI and BmtI and NcoI and NspI enzyme pairs were performed and visualised in agarose gel as presented in figure 8.3b. The lanes contain 4 sets of Con A, B and C scaffolds restriction digested with the different enzyme pairs as labelled.

The adjacent table indicates the expected basepair lengths of the restriction digest combination with respect to the restriction sites located in the scaffold design for each DNA nanostructure. As observed the fragment lengths correlated well with the restriction digest sites on the constructs thus validating the correct formation of scaffolds.

8.2.2 Scaffold routing

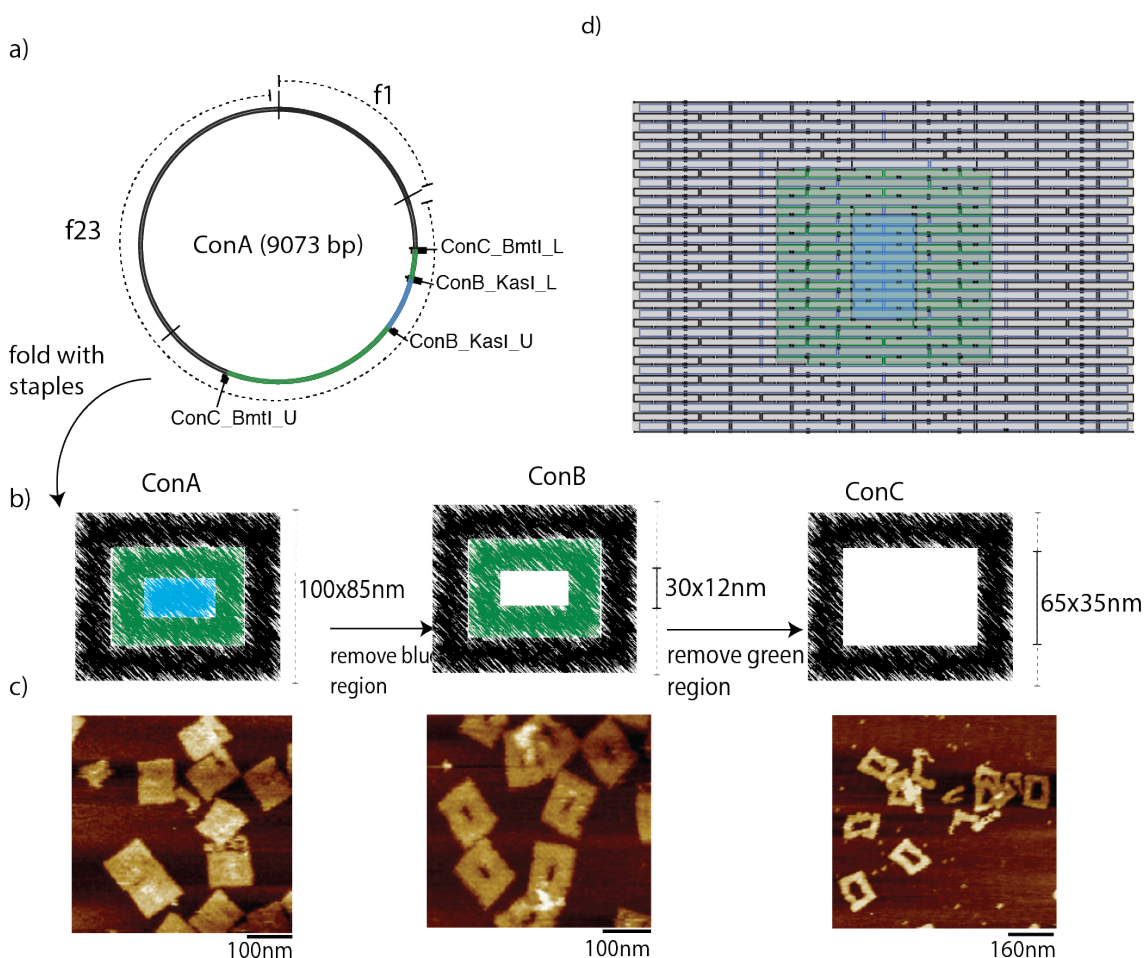


Figure 8.4: Schematic of a) ConA scaffold and b) the design for the concentric squares showing concentric squares ConB and ConC formed via systemic removal of inner scaffold portions of ConA. c) The AFM micrographs show the successfully folded nanostructures with identical outer dimensions and varying inner cavity. d) The upper right panel shows the scaffold routing of concentric squares (ConA, ConB, and ConC). The full tile comprising the black, green and blue regions represents the ConA DNA origami, whereas excluding the blue region in the centre from the full tile represents ConB and the black region alone represents ConC.

The longer scaffold that forms ConA was routed such that it formed the outer portion

(black) in its entirety prior to folding in to the middle (green) and then subsequently the inner portion (blue) of the design. As such, a specific reduction in the scaffold length could be used to remove the inner and middle portions of the design specifically whilst maintaining the same outer dimensions and arrangement of DNA oligonucleotide staple sequences (figure 8.4). Thus the novel DNA nanostructures were designed to resemble a set of three nested squares as shown in the routing diagram.

The concentric square designs were all folded using a thermal annealing gradient (chapter 5 section 2.9) from the same pool of DNA oligonucleotide staples with their respective ssDNA scaffolds and their formation confirmed by AFM. From figure 8.4b ConA, ConB and ConC can all be seen to have identical outer dimensions of 100×85 nm. ConA is noted to be a solid structure whereas ConB and C contain cavity with dimensions of 30×12 nm and 65×35 nm, respectively. These dimensions measured via AFM on mica under buffer were found to differ slightly to the envisioned design. External dimension of 72×86 nm for ConA B and C and internal cavity of 20×11 nm and 44×38 nm for ConB and ConC respectively, calculated by considering 1 helical turn (10.67 bp) to be 3.6 nm in length i.e., basepair length as 0.34 nm and double helical width of the stacked helices as 2 nm. While the width calculation using bp length was a useful approximation, the length (top to bottom) of the concentric structures turned out to be extended, as reported in previous studies [72, 254].

The AFM images revealed that the concentric squares stretch vertically along the stacked helices resulting in the additional ~ 20 nm increase in the total length. This extended length is because of the inter-helical gap likely due to the electrostatic repulsion between the helices. Thus an estimated inter-helical gap of ~ 1 nm [72, 255] was taken into account when engineering the length of the DNA origami, resulting in 107×86 nm external dimension and internal voids of 29×11 nm (Con B) and 65×38 nm (ConC) which matches to a close approximation with the AFM measurements.

As said before, the exact length of a DNA origami structure depends on the helical gap and this in turn varies with cross over spacing [255]. It should be noted that removal of inner and middle portions of ConA to form ConB and C also results in decrease of number of

crossovers between the helices, though the structure remains intact this causes a decrease in the structural rigidity with increased flexibility and stretch. This can be seen in the AFM images (figure 8.4c and 8.6a), ConB stretches slightly with ~ 10 nm increase in length, whereas ConC after losing the entire central portion of ConA stretches ~ 20 nm. Nevertheless, the DNA origami dimensions via AFM images are consistent throughout and still suits the purpose of this study.

The assembly efficiency of the concentric squares as observed via AFM images for the solid ConA sample and ConB with the smaller void was estimated to be $>80\%$ ($n > 50$), whereas the number of intact ConC DNA structure was found to be comparatively lower with $\sim 65\%$ ($n > 40$) as shown in appendix D figure D.25.

8.3 Nanopipette translocation Experiments

The folded DNA origami samples were subjected to translocation experiments with ~ 100 nm pore glass nanopipettes with related pipette resistance of around 86 ± 10 M Ω . The experimental setup similar to previous nanopipette translocation experiments, included the samples inside the nanopipette at a final concentration of ~ 500 pM and upon application of a constant voltage (-350 mV) the target moves from inside the nanopipette to the outside thereby causing an increase in ion current. As discussed previously, the peak characteristics like peak signature, peak amplitude and dwell time derived from the ion current events were then used as a signature for differentiating DNA origami concentric squares.

As seen in previous DNA based translocation studies (chapter 6 and 7), ConC, with a large inner void and low mass translocates through the nanopore slowly (dwell time = 0.31 ± 0.14 ms) and has a small ion current increase (peak amplitude = 86 ± 19 pA) when compared to that of ConB (dwell time = 0.22 ± 0.06 ms, peak amplitude = 97 ± 13 pA) with a smaller inner void and slightly higher mass. In contrast, the solid ConA nanostructure with the highest mass is seen to produce the largest ion current increase

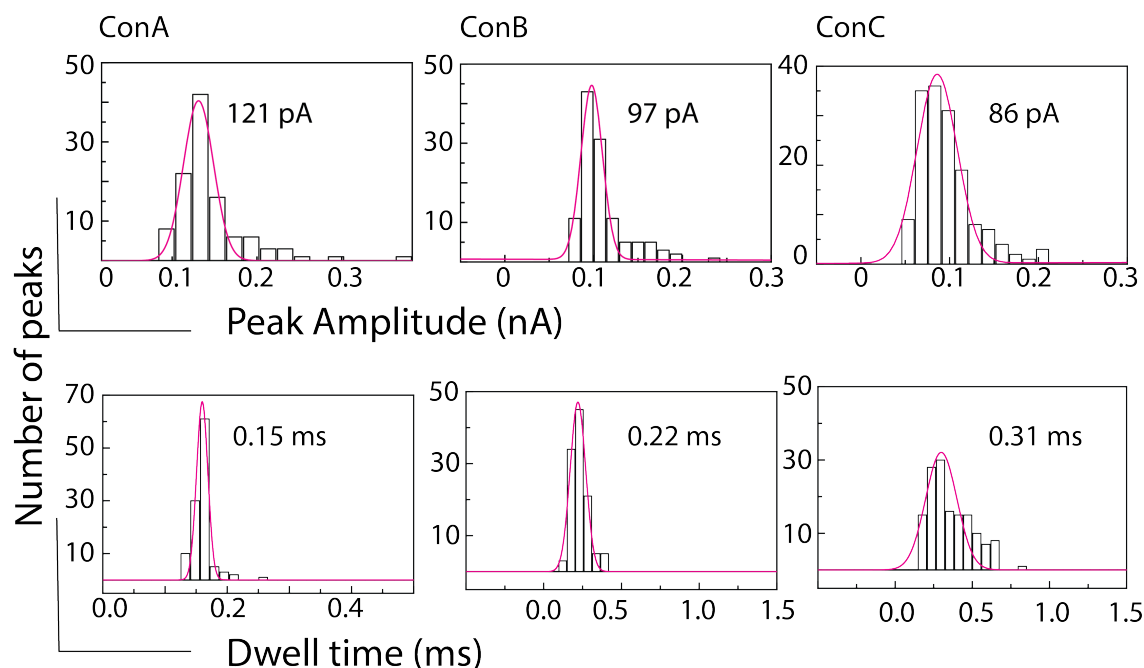


Figure 8.5: Peak current and dwell time histograms of the concentric square samples with Con A, B and C, translocated via nanopipettes with $\sim 90\text{ M}\Omega$ pore resistance, exhibiting averages around 121 pA and 0.15 ms, 97 pA and 0.22 ms and 86 pA and 0.31 ms respectively. The plots are fitted with a Gaussian curve and represents $n > 100$ events each.

(peak amplitude = 121 ± 23 pA) as it translocates swiftly through the nanopore, with a short dwell time (0.15 ± 0.01 ms), see figure 8.5.

It is possible that these differences in peak amplitude and dwell time could represent the combined contribution of the overall charge and geometry of the DNA nanostructures, due to the variable scaffold length used in these designs. It is, however, notable that the distinct ion current signatures consistently correlates with the cavity geometry between both our studies in this chapter and chapter 7, which strongly attributes the difference in ion current signatures to the geometry of the DNA nanostructures.

As shown in figure 8.6a the ion current signature for the concentric squares change according to the dimensions of the DNA origami and decreasing the size of inner cavity had a correlation with the ion current signature.

While ConA a solid tile presented with a single peak signature, ConB and C presented double peaks in their ion current structure, data analysis of about 100 events for each concentric square structure shows ConA presenting 95% single peaks, ConB and ConC presented with >80% double peaks. In that, ConB with the smaller cavity exhibited a slight split in the ion current while ConC samples showed a distinctive double peak in accordance with the large cavity at its centre as shown in figure 8.6. The double peak count for the concentric squares obtained from two different nanopipettes on different days are represented in table 7 of appendix C.

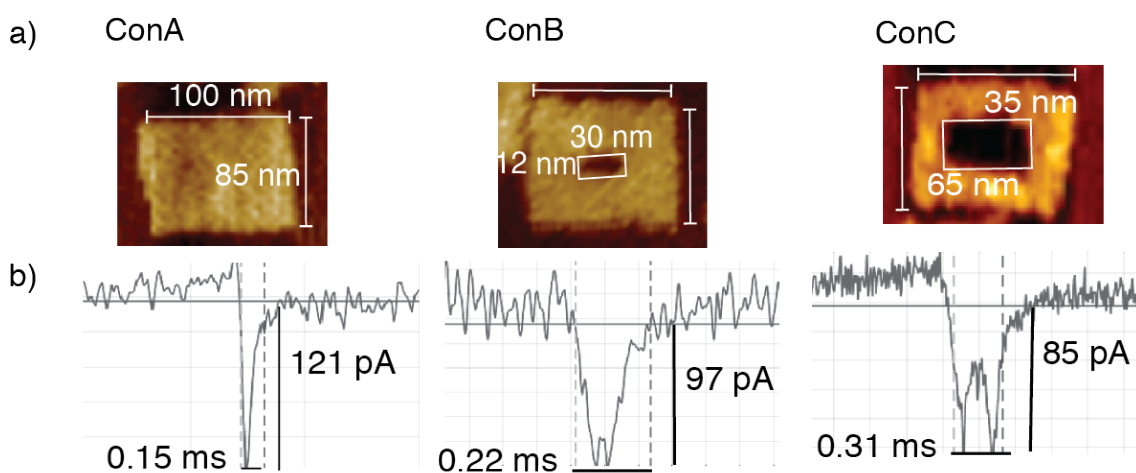


Figure 8.6: a) AFM image of the concentric squares along with the respective b) peak current signatures. ConA the solid tile exhibits a single peak, ConB with a small inner void exhibits a double peak with a small split and ConC with the larger void produces a significant double peak structure

This sensitivity of nanopipettes to differentiate DNA origami in relation to their geometry with respect to dwell time, peak amplitude and ion peak signature provides a three parameter system with which the DNA origami could be identified. Figure 8.7 shows the scatter plot for ion current events of the respective concentric square samples plotted with dwell time against peak amplitude. It is evident from the plot that the concentric squares could be identified with specific distribution range within which most of the respective events fall as follows; ConA <0.2 ms dwell time and >100 pA peak amplitude, ConB between 0.15 ms and 0.25 ms dwell time and between 90 pA and 100 pA peak amplitude,

ConC >0.25 ms dwell time and <90 pA peak amplitude. In that ConA and ConC have significantly distinguishable distribution range whereas ConB overlaps with both ConA and ConC as seen in figure 8.7.

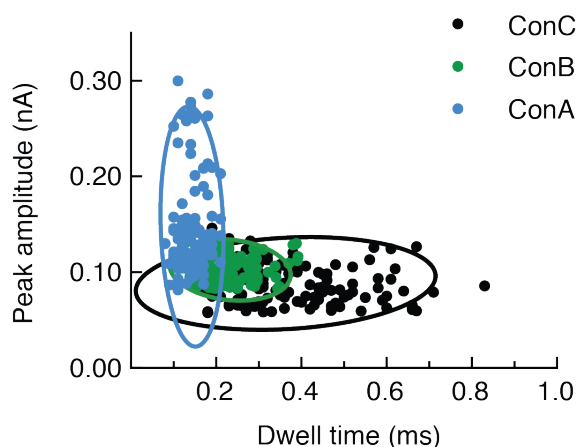


Figure 8.7: Peak amplitude vs dwell time scatter for concentric square constructs ConA (blue), ConB (green) and ConC (black) with >100 events each. The events are fitted with a 95% confidence ellipse.

Individual analysis of the ion current events (>100) using dwell time and peak amplitude together matches about 70–82% of the events with the respective concentric square structures. But, ion current signature taken together with these parameters allow us to identify distinct populations of DNA nanostructures and better distinguish the overlapping events. This would also allow for fewer false positives.

8.3.1 Relation between double peak and cavity size

Interestingly, analysis of the double peak structure is also found to correlate strongly with the cavity geometry, where the lag time (peak to peak distance) and amplitude (dp height) increases with increasing cavity dimensions. Data analysis of at least 50 events for ConB and C shows 80% of the peaks presenting with respective lag time and dp height as shown in figure 8.8. The analysis also shows that though ConB samples were successfully detected and differentiated with mean peak amplitude and dwell time, the ion current signature with mean lag time of 0.03 ± 0.01 ms and double peak height of 14 ± 4 pA (see figure 8.8) falls within the baseline noise (20 pA) indicating the frame void size (30×12 nm) to be too small.

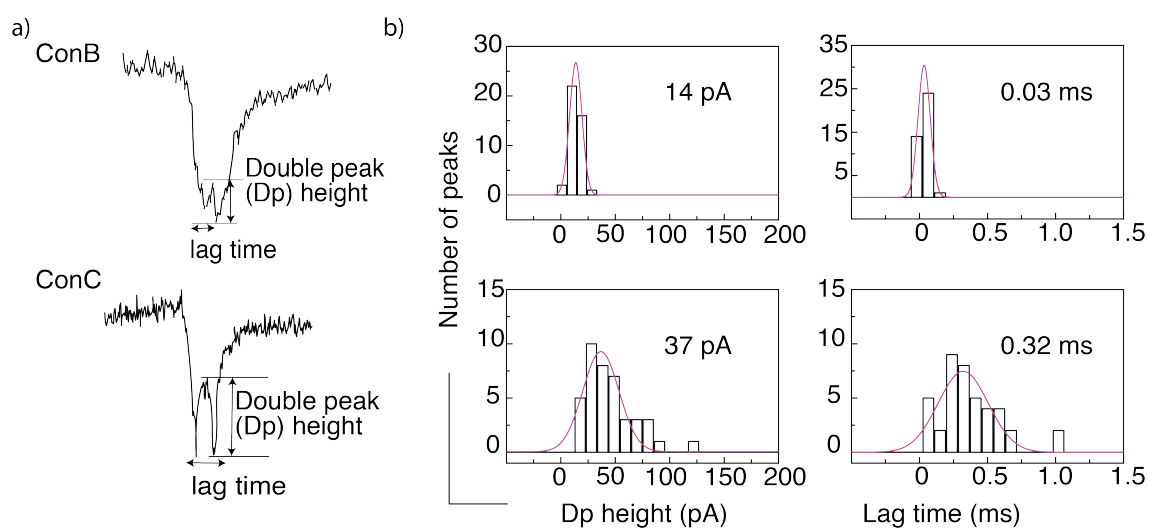


Figure 8.8: Double peak analysis for ConB and ConC ($n > 30$ events each) with the first column portraying a mean Dp height of 14 pA and 46 pA for ConB and ConC respectively. The second column with the lag time histogram shows a narrow short lag time of 0.03 ms for ConB double peaks whereas the ConC peaks present with a wider and longer lag time of 0.37 ms. Translocation experiments were conducted via nanopipettes with $\sim 92 \text{ M}\Omega$ pore resistance.

Whereas notably, there is a higher dp height of 37 ± 2 pA for the larger ConC void size 65×35 nm. The broader distribution (0.32 ± 0.1 ms lag time) of peak amplitudes also suggests the variable orientation of the rectangular nanostructure ConC during nanopore translocation, which is also consistent with the DNA origami design, indicating the flexible nature due to the thin frame geometry. Thus to obtain a distinctive high signal to noise double peak ion current signature, an inner frame dimension (cavity) of $> 30 \times 12$ nm along with a rigid outer frame is required.

8.4 Conclusion

In this Chapter, successful custom designed scaffolds for three DNA origami structures with a novel design strategy was demonstrated. The DNA nanostructures were assembled to resemble a set of three nested squares so that removal of specific portions in the scaffold

led to removal of the inner sections of the designed square. This facilitated maintaining the outer dimension constant with the same scaffold arrangement and staple sequence for all three structures.

Using these structures, the association of ion current to changes in DNA origami structure was studied and confirmed. By manipulating the frame inner dimensions, concentric squares with varying cavity size were created which resulted in specific ion current signatures upon translocation. Thus a direct correlation (>80%) of peak signature to cavity space, with respect to the frame DNA origami structures is provided.

While the traditional peak parameters, dwell time and peak amplitude, could successfully distinguish 72–80 % of the events to the ConA, B and C structures inclusion of ion current signature further increased the predictability especially in the overlapping regions where the structures presented with similar dwell time or peak amplitude. The study with varying inner void size also allowed the determination of a suitable void size (>30×12 nm) for high signal to noise double peak (dp height>baseline noise 20 pA) signature.

Thus, the potential of these DNA nanostructure for applications that take advantage of the cavity space with respect to the double peak signature is apparent. The next chapter will discuss how these well defined geometric (frame) nanostructures could be utilised for target attachment and subsequently detected through nanopipette translocation experiments making use of the unique ion current signature.

Chapter 9

DNA Origami - Nanopipette Biosensor

9.1 Introduction

From previous experiments as discussed in chapter 7 and 8, we had identified a unique ion current fingerprint denoting the presence or absence of void within 2D DNA nanostructures. With regards to biosensing applications, then this ion current fingerprint could be exploited to provide a readout of the presence or absence of a bound entity obscuring the cavity where a specific binding agent like an aptamer is presented internally.

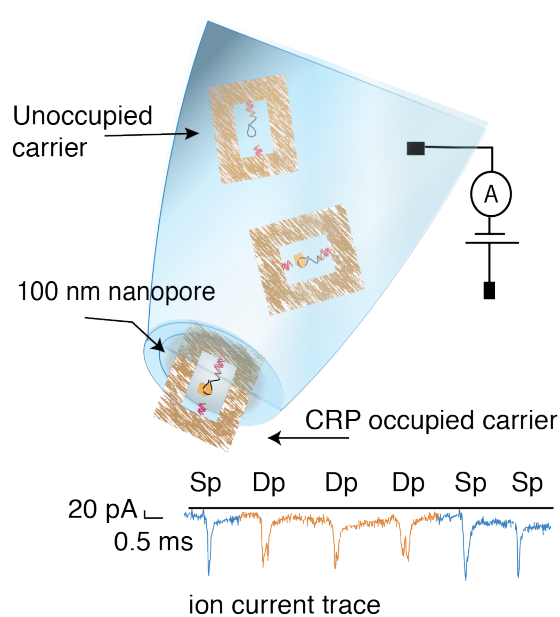


Figure 9.1: Schematic of the DNA origami-nanopipette sensing system, the ion current trace shows a mixture of single and double peaks as observed for CRP incubated carriers.

The currently employed clinical diagnostic assays are generally based on ensemble-averaging immunoassays such as ELISAs. In these, an antibody or antibody mimetic is used to capture relevant biomarkers in the sample, and in general, each antibody-biomarker interaction contributes a small amount to the accumulated assay signal. However, the individual immuno-interactions cannot be identified anymore and only manifest themselves as part of this ensemble-averaged signal.

In order to explore this and as a proof of principle, we demonstrate the quantitative detection of human CRP, which is an established inflammation biomarker. In a healthy adult the median CRP concentration is $0.8 \mu\text{g/ml}$, and its concentration in blood exceed 1 mg/ml ($8 \mu\text{M}$) [256] as a result of an inflammatory response. Thus detection of CRP for various clinical applications as a general inflammation marker and as an indicator for cardiovascular problems is of interest.

Arguably, the ability to detect biomarkers with single entity resolution rather than via ensemble-averaging techniques provides significant advantages for the detection of ultra-small biomarker concentrations. A promising approach to this is to detect single protein biomarkers using carrier molecules through a nanopore under an applied voltage.

Thus, with regard to all the challenges and the response strategies reviewed in chapter 4 towards nanopore protein detection, we propose DNA origami as an alternate carrier with a defined geometry which can host the subject biological entity, in an analogous approach to that used to study single biological reactions with high speed atomic force microscopy [257].

The initial sections of this chapter describes the design and construction of DNA origami carrier including selection and insertion of specific aptamer sequences for CRP. The binding affinity of the aptamer towards CRP is confirmed via SPR experiments and binding within the carrier itself is studied with AFM and gel retardation assays. This is followed by nanopipette translocation experiments for detection of CRP bound carrier molecules. Further sections explain our methodology of three-parameter usage for quantitatively detecting CRP molecules.

Thus this chapter shows that the DNA origami structure provides a versatile and robust carrier platform to circumvent the limitations of the existing carrier based approaches with the potential for quantitative single molecule sensing that is both sensitive and highly selective.

9.2 DNA origami as unique carriers

As discussed in the previous chapter, the correlation of translocation peak signature to cavity geometry within these DNA nanostructures provides a unique and robust approach to detect the presence of a much smaller analyte. By placing a binding agent specific to the molecule of interest within the cavity of the DNA nanostructure, and upon binding the target analyte, the volume of the cavity changes resulting in a change in the ion current peak signature.

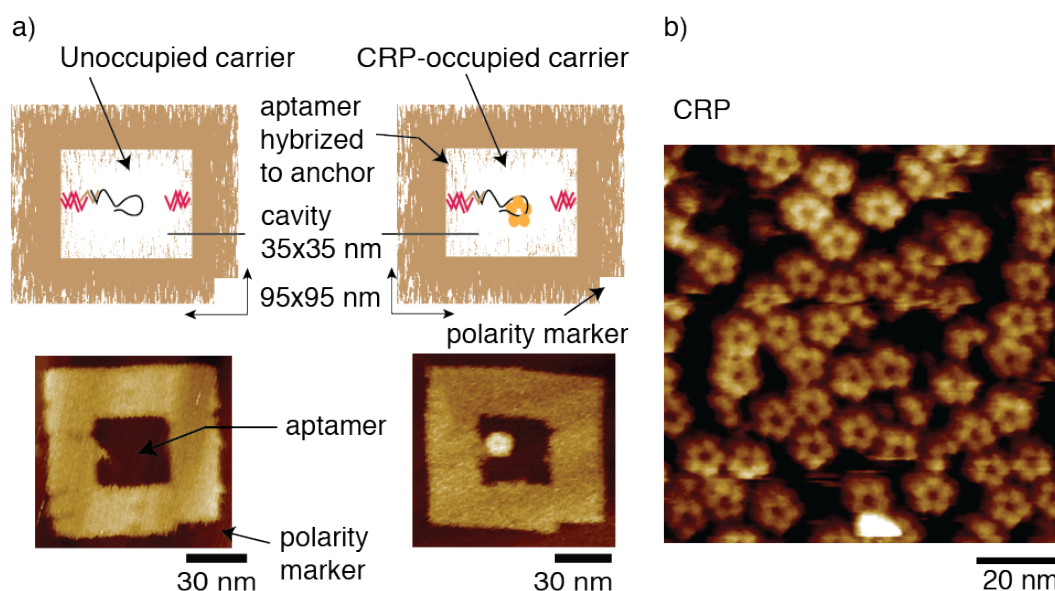


Figure 9.2: a) Schematic and AFM image in the first column shows the placement of the aptamer opposite to the polarity marker with help of the anchor sequence and the second column shows the subsequent protein occupied frame. b) The right panel shows the AFM image of CRP protein

In order to explore this strategy and as proof of principle, quantitative detection of CRP is shown here. A DNA frame nanostructure was produced from a 7249 nt scaffold to include internal anchor sequences within a central cavity to which DNA aptamers could be hybridised and presented (figure 9.2). This DNA nanostructure contained a small cavity (35×35 nm) sufficient to provide a distinctive double peak signature as informed by the concentric square studies chapter 8. Whilst its outer frame structure (95×95 nm) was rigid and closely matched in dimensions to the nanopipette pore size of 100 nm, providing a robust signal to noise at each translocation event. The additional inclusion of a notch at one corner acted as a polarity marker for confirmation of correct aptamer placement by AFM. The complete DNA nanostructure and aptamer assembly is herein referred to as the carrier. Figure 9.2 shows the schematic and AFM micrographs of the empty DNA origami frame functionalised with the aptamer on the top left (opposite) of the polarity marker and the same bound with CRP.

9.2.1 Aptamer selection

Initially, three CRP specific aptamers selected from previous works [84, 85, 86, 87] were analysed via SPR to confirm target specificity. This was necessary to verify CRP binding to aptamers with end modified anchor sequences as required for this study. Figure 9.3b portrays SPR results of the three end modified aptamers showing positive binding towards CRP. Firstly, the gold SPR chips were deposited with self assembled monolayer (SAM) of $C_{11}PEG_6COOH$ which was then used for amine end modified aptamer attachment by activation with 1-ethyl-3-(3-dimethylaminopropyl) carbodiimide (EDC) as shown in figure 9.3a. The cross linking occurs via activation of carboxyl groups for direct interaction with primary amines through amide bond formation. The SAM spacers prevents any nonspecific target binding onto the surface and also helps placement of the aptamer well above the surface for efficient binding. Then, CRP at specific concentration was flowed over the aptamer immobilised Au film surface. The binding of CRP to the specific aptamer causes a change in resonance angle which is measured in millidegrees. The SPR experiments were carried out as per protocol explained in chapter 5 section 4.

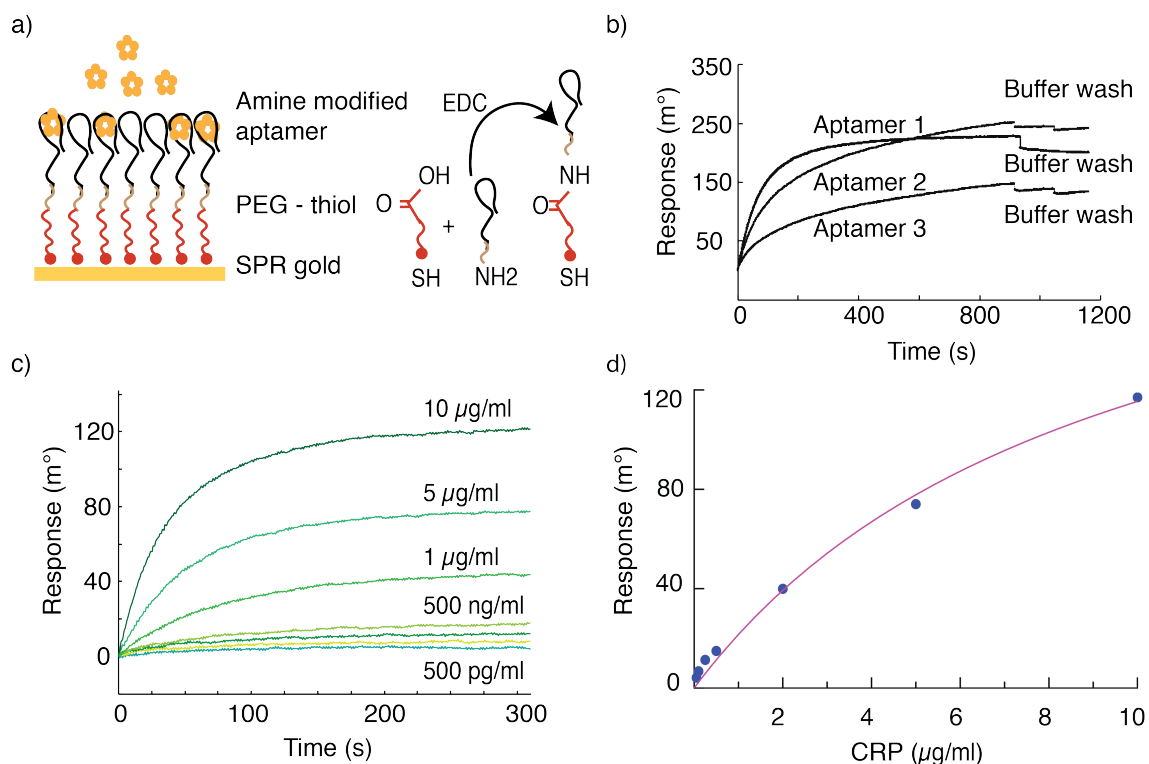


Figure 9.3: a) A schematic of SAM functionalised SPR gold chip for attachment with amine modified aptamer sequences for CRP detection. b) The SPR data shows positive binding of CRP with all three tested aptamers. c) Concentration-dependent signals for different concentration of CRP from 500 pg/ml to 10 g/ml against aptamer 1. d) SPR response plotted against the respective CRP concentration follows a Langmuir isotherm with a K_d of ~ 40 nM.

Though all three aptamers showed positive binding with CRP via SPR analysis, aptamer 1 and 2 showed the largest SPR angle shift with aptamer 1 exhibiting the faster binding kinetics compared to aptamer 2 and were selected for all further experiments. Aptamer 3 with the lowest response was excluded, and also for the reason that there was no conclusive binding after insertion within the DNA origami carrier via AFM imaging. The selected aptamer 1 was then tested against different buffer conditions and it was noted that there was a substantial shift in SPR angle indicating increased CRP binding in presence of Ca^{2+} (appendix E figure E.26). This is in agreement as noted in previous studies [258, 85]. Thus a binding buffer (10 mM MgAc, 10 mM TrisAc, 1 mM EDTA) with an appropriate

concentration of calcium (2 mM CaCl₂) suitable for DNA origami (appendix E figure E.36 and E.37) was selected for nanopipette translocation and analysis. The aptamer was also tested against nonspecific targets to rule any false positive signals, as shown in the appendix E figure E.29.

A concentration dependent SPR analysis was also carried out to identify the appropriate concentration of CRP required for further experiments to obtain a significant signal. Figure 9.3c shows SPR angle shifts upon flowing different concentrations of CRP (from 500 pg/ml to 10 μg/ml) over the aptamer immobilised Au film surface as explained in chapter 5. The response plotted against the different CRP concentration was used to calculate the binding affinity (K_{dSPR}) of the end modified aptamer sequence, as shown in the graph (9.3d) following the Langmuir equation $y = x \times Bmax / (x + K_d)$; , $K_{dSPR} = \sim 40$ nM. In comparison, the study by Lee *et al.* [85] and Jarczewska *et al.* [84] resulted in a K_d of 3.5 nM and 6 pM respectively. Also from the concentration study, a lower CRP concentration (1 μg/ml or ~ 9 nM) exhibiting a significant SPR response was chosen for the nanopipette and AFM experiments. The complete SPR traces for all the experiments are provided in the appendix E.

9.2.2 AFM and retarding gel electrophoresis

The performance of the DNA aptamer within the context of the carrier was established by incubating 36 nM (4.4 μg/ml) CRP with 9 nM concentration of carrier in the translocation buffer (0.1 M KCl containing 10 mM MgAc, 2 mM CaCl₂, 10 mM TrisAc and 1 mM EDTA) at room temperature for 30 minutes and then characterised by AFM (figure 9.2 and appendix E, figure E.38). Incubating the samples in similar buffer conditions as required for nanopipette translocation experiment also facilitated direct study of carrier molecules stability in the respective buffer and also check suitability of the buffer for CRP–aptamer binding. From the AFM images, the efficiency of CRP binding was calculated to be >60% (n=50) for a 1 : 4 (carrier to CRP) ratio.

In addition, retarding gel electrophoresis experiments (chapter 5 section 2.6) were carried

out to further confirm CRP binding to the carrier. Gel electrophoresis of carrier sample (9 nM) incubated with increasing concentration of CRP (9, 18, 27, 36 nM) in the translocation buffer as mentioned above was carried out for 2 hours at 80V at 4°C in 0.5% agarose. The samples were incubated for 30 minutes prior to electrophoresis. The gel is shown in figure 9.4a with a 1 kb ladder in lane 1 and control samples in lane 2, 3 and 8. Surprisingly, a concentration-dependent shift of the carrier bands can be seen, in lanes 4 to 7 which could be due to successful CRP binding to the carrier.

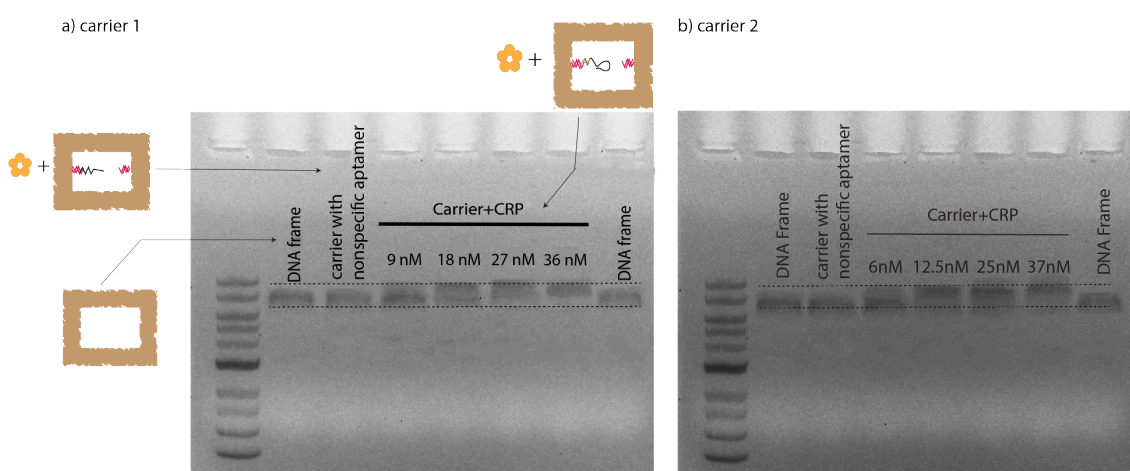


Figure 9.4: Retarding gel electrophoresis study for a) carrier 1 and b) carrier 2 attached with aptamers 1 and 2 respectively exhibiting positive CRP binding as seen in lane 4 to 7. The gel also consists of a 10 kb ladder in the 1st lane, lane 2, 3 and 8 act as controls with DNA frames in 2nd and 8th lane and carriers with non-specific aptamer in 3rd lane.

For 9 nM (1: 1) CRP a light upper band and darker lower band is observed, for 18 nM (1: 2) and 27 nM (1: 3) CRP we could observe the lower band gradually shift. The lower bands in the carrier-CRP complex runs similar to the controls and represent the unbound DNA origami carrier, at 36 nM (1: 4) CRP concentration only the upper band is visible suggesting carrier molecule saturation. Whereas the carrier with nonspecific aptamer (lane 3) shows no CRP binding and runs parallel to the empty DNA frames (lane 2 and 8) both acting as control bands. Similar electrophoresis study was also carried out for aptamer 2 as represented in figure 9.4b which further suggested positive CRP binding

to the respective aptamers in the carrier. While CRP bound carriers could be resolved from free DNA origami carrier and negative controls, the separation is not significant for concentration depending binding confirmation. The slight smearing of the bands and the occurrence of light and dark bands could be due to disequilibrium of the samples and the long run time of 2 hours could also cause low dissociation of the DNA origami itself. Thus the results were only taken as a qualitative validation of carrier–CRP binding.

9.3 Nanopipette–DNA origami sensing system

CRP detection via nanopipette translocation experiments for both aptamer 1 and 2 were successfully conducted, and they both presented with similar data and results. While we do compare and relate data for both aptamers where necessary, only one of the two is discussed and presented in detail in this chapter and elaborate data for the other is provided in appendix E.

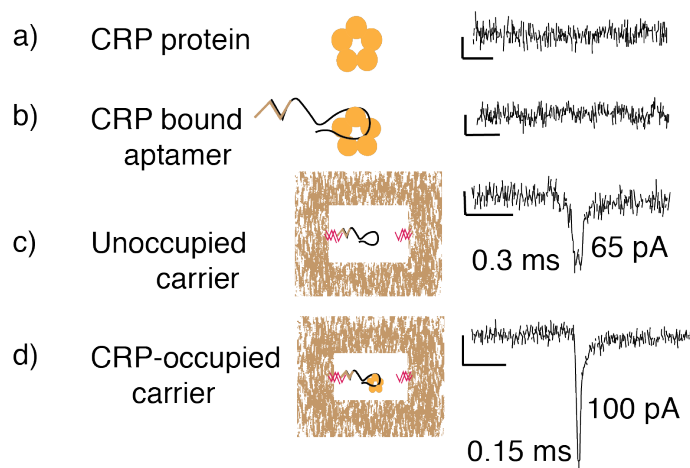


Figure 9.5: Ion current signatures for a) free CRP, b) aptamer bound CRP, c) empty carrier and d) CRP bound carrier. c) and d) portrays the clear ion current structure difference between the bound and unbound sample molecules. The traces also show that CRP free and aptamer bound were undetectable with the ~ 100 nm pore sized pipettes. The scale bars represent ms and 20 pA in the x and y direction.

Initially, nanopipette translocation experiment of DNA frames and carriers (DNA frames incorporated with aptamers) were carried out in 0.1 M KCl buffer at a final concentration of 500 pM. Data analysis of more than 100 ion current events revealed double peaks with peak amplitude around 65 ± 6 pA and dwell time of 0.29 ± 0.1 ms for carriers and a mean peak amplitude of 62 ± 4 pA and dwell time of 0.32 ± 0.05 ms for DNA frames (figure 9.5c and 9.6). These peak characteristics were also consistent with similar sized DNA frames (F1 and F2) tested before in chapter 7. Thus we note that, the addition of a single stranded DNA aptamer of few tens of bp in length within the DNA structures has a negligible effect on the resulting ion current, when compared to empty DNA nanostructures.

Similarly, to analyse the CRP-occupied carriers, an equimolar solution of CRP and carriers at 9 nM incubated under the same conditions as for AFM and gel electrophoresis studies was used with the aim of having a mixed population of occupied and unoccupied carriers. Ion current measurements obtained from these revealed a mixture of double and single peaks with the latter accounting for 30% of the total number of events for the above mentioned carrier to CRP ratio. This is consistent across different nanopipettes ($n=3$) with a average single peak percentage of 31 ± 2 .

Further data analysis on the ion current events ($n > 100$) indicates that the double peaks have a mean ion current amplitude of 62 ± 4 pA and dwell time 0.33 ± 0.03 ms (see figure 9.6) which is similar to those observed for carriers and DNA frames on their own as seen above. In contrast, analysis of the single ion current peaks ($n > 50$) demonstrates a substantial shift in both dwell time and peak amplitude, where 0.15 ± 0.05 ms and 90 ± 9 pA are observed, respectively.

From previous experiments in chapter 7 and 8, the frame DNA structure's characteristic double peak has already been evidenced to the presence of the cavity in the structure. It should also be noted, due to the large dimensions of the nanopipette pore (100 nm) compared to the measured diameter of CRP (11 nm), it is impossible to directly detect free CRP or free aptamer in this system, figure 9.2 and figure E.32. This taken together with the results of the concentric squares study (chapter 8) which showed that the peak shape changes from a double peak to a single peak upon filling in the central cavity, we

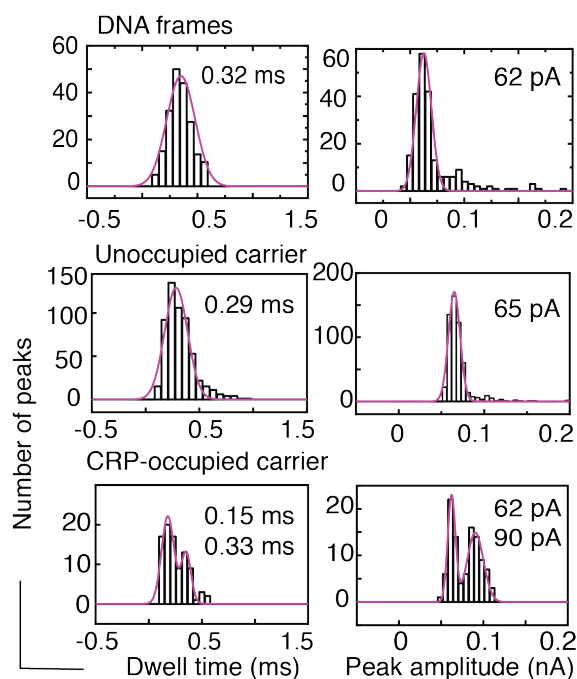


Figure 9.6: Histograms of dwell time and peak amplitude for DNA frame, carrier on its own and carrier incubated with CRP at a 1:1 ratio. The DNA frames and unbound carriers showed a dwell time average and peak amplitude average that was significantly different from the CRP bound carriers. The histograms are each fitted with a Gaussian fit, data represents $n > 100$ events obtained through nanopipettes with $\sim 95 \text{ M}\Omega$ resistance.

speculate that the single peak events correspond to occupied carriers, i.e. carriers with a CRP bound to the specific aptamer.

Furthermore, the double peaks accounting for approximately 40% of the total number of observed events (appendix E section 2, table 7), is in line with the percentage of occupied carriers that would be expected based on the K_d SPR obtained from the SPR experiments (figure 9.3), which suggests that the percentage is concentration dependent as expected. Thus the carriers CRP bound and unbound could be differentiated from the sample mixture by considering the structure of the ion current peak or its mean characteristics (dwell time and amplitude).

9.3.1 Characterisation of peaks

Next, in order to use this approach for high sensitivity biosensing, a reliable way of classifying the different ion current events is required. Figure 9.7(i) shows the scatter plots of the peak amplitudes versus dwell times of the ion current peaks observed for the translocation of unoccupied carriers. All events which resemble the shape of double peaks

are shown in orange, and all other events as black triangles, indicating that they cannot be classified.

To eliminate outliers and to ensure robust classification, ion current events will only be classified as a true double peak representing an unoccupied carrier if the measured peak amplitude and dwell time fall within the 95% confidence ellipse (indicated by orange circles), which is indicated in the figure. Peaks which fall outside of this boundary are indicated by orange triangles and will not be considered as events representing unoccupied carriers.

Similarly, figure 9.7(ii) shows the scatter plots of the peak amplitudes versus dwell times of the ion current events observed for the translocation of a mixture of carriers with ten times excess of CRP expected to lead to the majority of carriers being occupied. All events which resemble the shape of double peaks and single peaks are shown in orange and blue, respectively, and all other events as black triangles, indicating that they cannot be classified.

As above, to ensure a robust classification for single peaks to represent CRP-occupied carriers, the 95% confidence ellipse (indicated as a blue ellipse) is employed as an in-out filter. Only single peaks which fall within this 95% confidence area are considered as resulting from the translocation of a CRP-occupied carrier (indicated by blue circles), all other single peaks are considered unclassified (indicated by blue triangles).

To classify the double peaks, and thereby establishing the number of events representing unoccupied carriers, the confidence ellipse from panel (i) is indicated in orange, and hence only double peak events which fall within this area are considered (orange circles), while the ones outside this area are dismissed (orange triangles).

This now enables the classification of observed ion current peaks into three categories, double peaks representing unoccupied carriers, single peaks representing CRP-occupied carriers, and unclassified peaks which resemble neither a double nor a single peak. A step wise schematic of this classification is shown in appendix E, figure E.33. This multi-parameter classification enables the discarding of ambiguous translocation events,

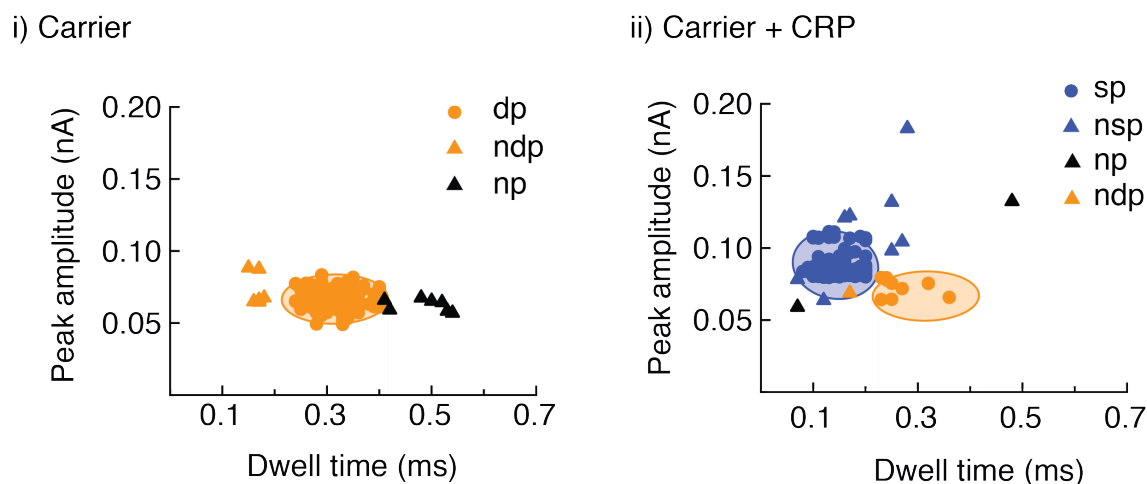


Figure 9.7: Scatter plot of peaks for unoccupied carriers (left) and carriers incubated with a $10\times$ excess of CRP (90 nM). Ion current events which are double peaks are plotted on orange, and the ones that fall inside the 95% confidence ellipse are plotted as circles, the others as triangles. Only events that fall within the 95% confidence ellipse are considered double peaks. The same analyses was carried out for single peaks (plotted in blue). Ion current events which resembled neither a double nor a single peak are shown as black triangles and are excluded from the analysis. Data represents at least 100 events for each analysis.

for example resulting from broken carriers, in a robust way. Such events would likely resemble single peaks and hence represent false positives.

To illustrate this, the DNA nanostructures were deliberately disrupted by incubating in 10 mM CaCl_2 for 30 min to substitute the constituent Mg^{2+} with Ca^{2+} prior to translocation. The AFM micrographs in figure E.36i of appendix 5 demonstrate that the carriers have been degraded significantly. This is in accordance with previous studies demonstrating that the affinity of DNA towards calcium is greater than magnesium [259] and high mM concentrations of Ca^{2+} can denature the DNA origami structure [260].

During the translocation experiments only very few events were recorded, and the peak amplitude vs dwell time scatter plot shows that none of the recorded peaks fall within the relevant confidence ellipse (appendix 5, figure E.36ii and iii), demonstrating the

robustness of the classification approach. As such, the counting of false positives from broken or truncated carriers in the sample is limited effectively by the filtering of the single peaks via the classification procedure discussed above.

We note that the small concentration of Ca^{2+} in the translocation buffer does not affect the carriers significantly. Even after incubation of the carriers for 4 hours in the translocation buffer, only a small number (approximately 10%) of the translocation events would be classified as CRP-occupied carries with the above classification method (appendix E, figure E.37).

9.3.2 Quantitative single molecule biosensing

To demonstrate quantitative sensing using the translocation of carriers with specific DNA aptamers, and the concept of counting single individual carrier molecules classified through the three-parameter approach (peak amplitude, dwell time, and shape), we analysed the ion currents of a range of translocation experiments at different CRP concentrations.

Figure 9.8a shows the distinct ion current signature for occupied and unoccupied carrier and a collection of representative ion current peaks for a range of different CRP concentrations indicating an increase in the occurrence of single peaks with increasing CRP concentration. For each concentration, the observed ion current events were classified as described above. Where single or double peaks did not satisfy the filtering criteria they were marked as “unclassified” and were not taken into account for the concentration analysis. Such unclassified peaks represented between 9–36% of the total number of events in a 2 minute trace. Consequently with respect to the occurrence of dp and sp there was a gradual shift in the histograms of mean dwell times and peak amplitudes across different concentrations, see figure 9.8b.

Now by considering the three-parameter approach the ion current events obtained for different CRP concentrations were plotted with their dwell time against peak amplitude and overlaid with the 95% confidence ellipse obtained from figure 9.7 (appendix E figure

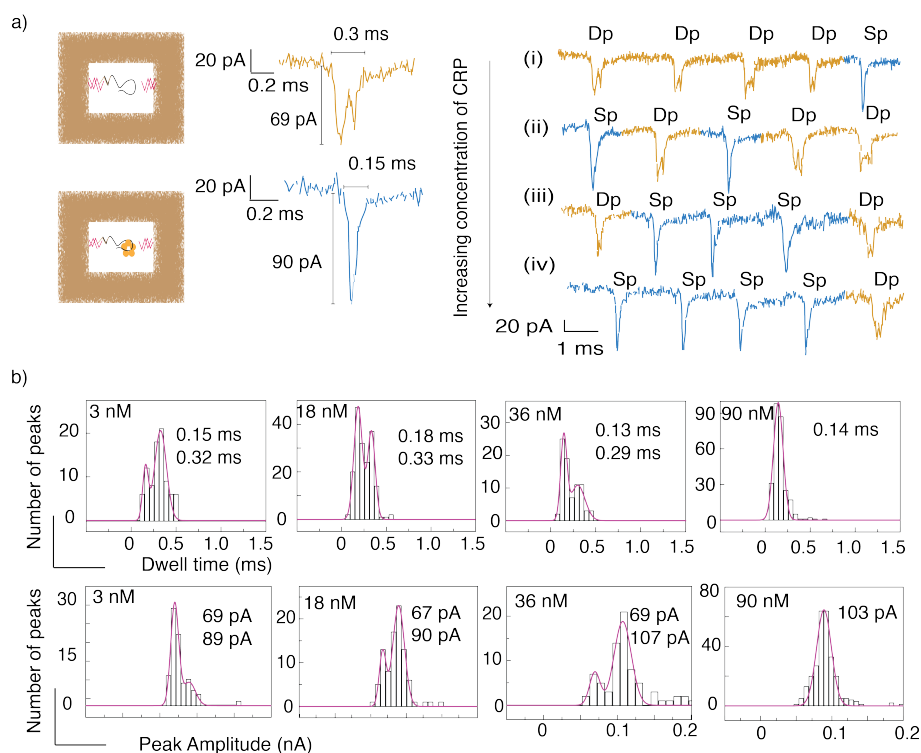


Figure 9.8: Concentration dependent study, a) Ion current signatures observed for CRP–unoccupied and occupied carriers and representative selection of ion current signatures for increasing concentration of CRP. The peak traces are stitched together from individual peaks of a longer trace to remove regions with no events for the purpose of illustration. b) Dwell time and peak amplitude histograms ($n > 80$ each, table 9) of the ion current events for the CRP–occupied samples depicting gradual shift in the averages with respect to concentration of CRP, the histograms are fitted with Gaussian fit. The nanopipettes used for these experiments exhibited a pore resistance of $95 \pm 3 \text{ M}\Omega$.

E.35). Figure 9.9a represents ion current translocation events for 9 nM concentration of CRP and carrier, where the double and single peaks represented as orange and blue circles and unclassified events are denoted by triangles.

Thus by counting the number of single and double peaks within the ellipses, quantitative detection of occupied and unoccupied carriers was achieved. Subsequently, the normalised single peak count, i.e., classified single peaks vs total number of classified

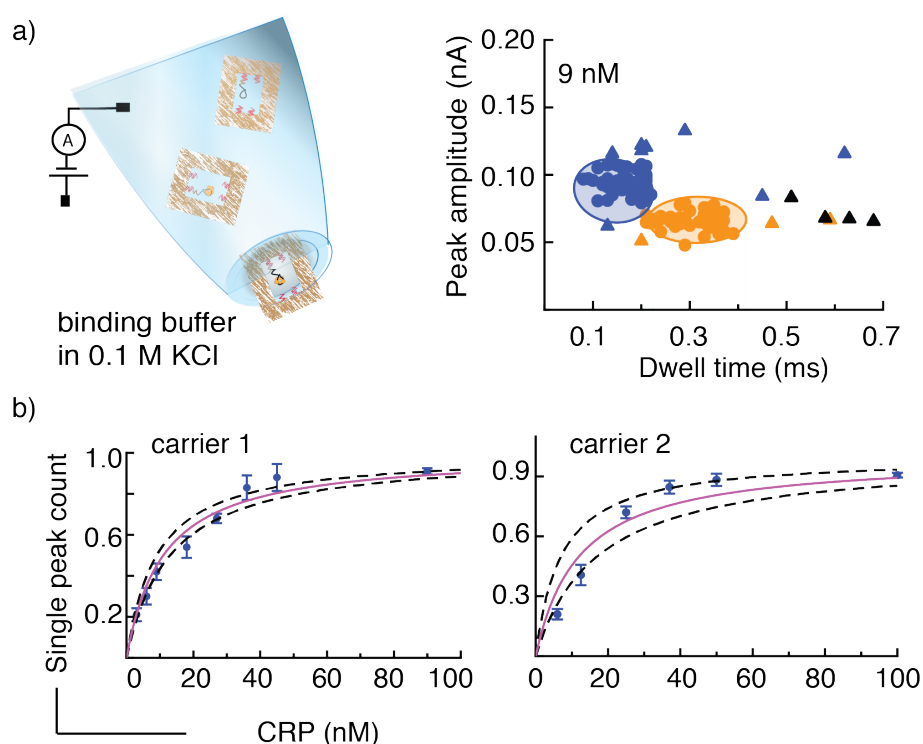


Figure 9.9: CRP binding study a) Translocation events of carriers (9 nM) incubated with different concentration of CRP with their peak amplitude plotted against dwell time. The single peaks in the ion current data are coloured blue while the double peaks are coloured orange, and the unclassified events discarded from the quantitative analysis are represented as triangles. The plots are overlaid with the 95% confidence ellipses from figure 9.7. b) Ratio of single peaks vs total classified peaks against CRP concentration for carrier 1 and carrier 2 (table 8 and 12). The data were fitted with Langmuir isotherm $y = x \times B_{max} / (x + K_d)$ (solid line) and revealed a K_d of 11 ± 2 nM and K_d of 12 ± 5 nM for the two carriers. The dashed lines represent the confidence boundaries of the fit. The error bars denote standard deviation of events from ion current translocation experiments conducted on different days using three different nanopipettes.

peaks, was used to calculate the binding affinity of the carrier for the analyte at the single molecule level. Figure 9.9b shows the normalised single peak count, for different concentrations of CRP from 3 nM to 90 nM for carrier 1.

As expected, the normalised single peak count increases with increasing CRP concentration. The data were fitted with a Langmuir isotherm, using the dissociation constant K_d as the only fitting parameter, and the result is shown as a solid line. The K_d obtained from the fit is 11 ± 2 nM for carrier 1, which is a same order of magnitude with the results from our SPR study of DNA aptamer 1. Similar data analysis was also carried out for carrier 2 and normalised single peak count plotted against CRP concentration following a similar Langmuir curve with a K_d of 12 ± 5 nM is shown in figure 9.9b.

Using the parameter classification (amplitude, dwell time and ion current signature) quantitative detection down to 3 nM CRP in $\sim 5 \mu\text{l}$ sample volume was achieved within a 2-minute sampling window, lower concentrations than 3 nM were not attempted as the number of single peak vs total classified peak ratio was very close to that of empty carrier and control samples for a 2 minute ion current recording. However, the sensitivity of this system can be improved by reducing the size of the confidence ellipses to increase the stringency of the classification which in turn would need an extension of the sampling time and employing different designs of DNA origamis to reduce the number of broken carriers in the sample.

Thus a quantitative technique using nanopipette translocation with two different aptamers for a target of interest is presented, demonstrating the robustness of the biosensing approach.

9.3.3 Selectivity and specificity of the DNA carrier system

To further validate the specificity of our sensing system, in particular of the carriers to the CRP target, a random DNA sequence was selected to act as a non-specific aptamer (NspApt) and the translocation ion current was measured for carrier concentration of 9 nM and CRP concentration of 90 nM, i.e., the highest concentration reported for carrier 1. The analysis of the ion current events is shown in figure 9.10a .

A single distribution of peak amplitudes and dwell times with averages of 69 ± 5 pA and 0.3 ± 13 ms, respectively, were found, consistent with the values measured with

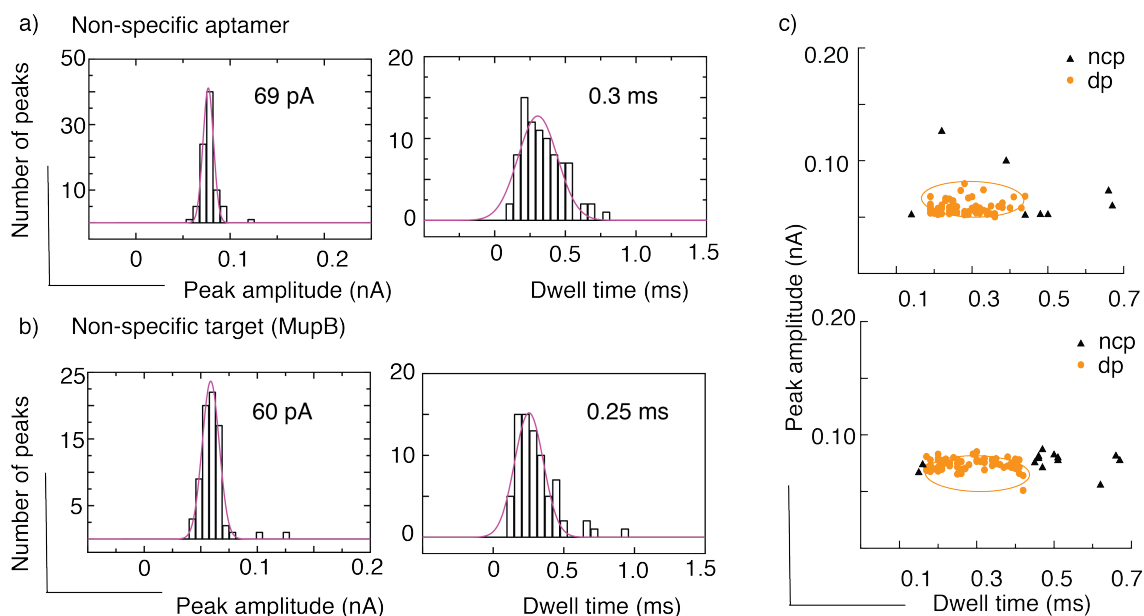


Figure 9.10: Control experiments conducted using nanopipettes with $\sim 90 M\Omega$ resistance for a) non-specific aptamer sequence and b) a random protein (MupB) resulted in dwell time and peak amplitude mean (0.3 ms and 0.25 ms and 69 pA and 60 pA) similar to empty carrier samples. The histogram plots are fitted with a Gaussian fit. c) The scatter plot analysis which shows the classification of the ion current events shows that no occupied carriers were detected, demonstrating the high specificity of the sensing approach. The data represent $n > 80$ events each.

unoccupied carriers. The scatter plot clearly shows that only double peaks were identified, and no single peaks, demonstrating that a non-specific aptamer does not lead to any detection signal.

Furthermore, the CRP specific carrier (at a 9 nM concentration) was subjected to 90 nM of a control protein (MupB) of similar size as CRP, and the results of the ion current analysis is shown in figure 9.10b. Similar to the non-specific aptamer, single distributions of dwell time and peak amplitudes (averages of 0.25 ± 0.1 ms and 60 ± 7 pA) were observed which are in line with those for unoccupied carriers. The scatter plot clearly shows that no single peaks were identified ($n > 50$) demonstrating that no MupB bound to the CRP-carriers. These control experiments are also in accordance with the SPR data,

which involved testing a random protein against the surface bound aptamer sequences as discussed previously.

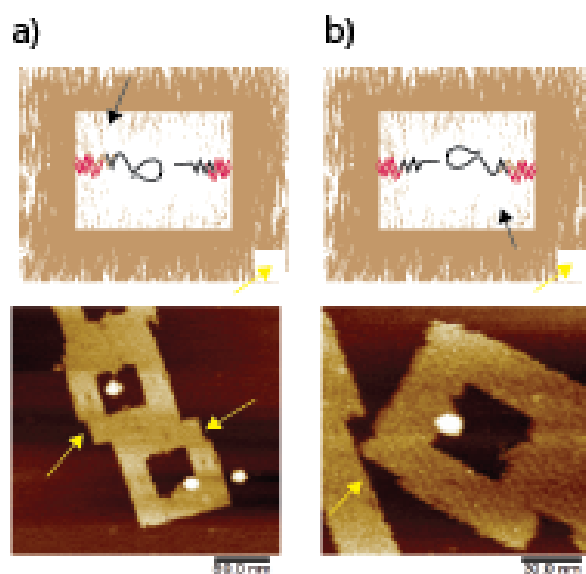


Figure 9.11: *CRP to carrier molecule specificity studies consisted of positioning aptamers in different positions. a) carriers with CRP bound to the left aptamer, b) CRP bound to the right aptamer. The positions right and left are with respect to the orientation marker indicated by the yellow arrow.*

Evidence for high specificity of the selected aptamer towards CRP within the carrier was further corroborated by placing both specific and nonspecific aptamer in the carrier and detecting the correct binding of CRP to the specific aptamer via AFM. The carrier (9 nM) samples were incubated with CRP at 36 nM in translocation buffer at room temperature for 30 mins and imaged on mica. AFM images in figure 9.11 shows DNA origami frame with both specific and non-specific aptamers incorporated in two different arrangements and the CRP molecule bound to the appropriate aptamer.

In the first instance we have the aptamer opposite (top left) and nonspecific aptamer adjacent (bottom right) to the polarity marker. From the AFM images we can clearly note the CRP binding to left of the polarity marker and not to the nonspecific aptamer. Swapping the specific and nonspecific aptamer placement again shows corresponding

CRP binding to the correct side of the DNA frame structure, i.e. adjacent to the polarity marker this time. Analysis of the AFM images (appendix E, figure E.39) show CRP bound to the correct aptamer about 47–55% of the total carriers in the image, the few incorrect binding (7–20%) seen via AFM could be due to nonspecific protein–surface or substrate interactions.

9.4 CRP detection in plasma

For applications in clinical diagnostics, it is important that quantitative detection of analytes such as CRP can also be performed in complex biological fluids. To demonstrate the performance of our sensor system with such fluids, nanopipettes translocation studies in plasma was conducted. Initially translocation study for different concentrations of plasma was performed to assess the complexity and signal to noise ratio obtainable for these biological samples.

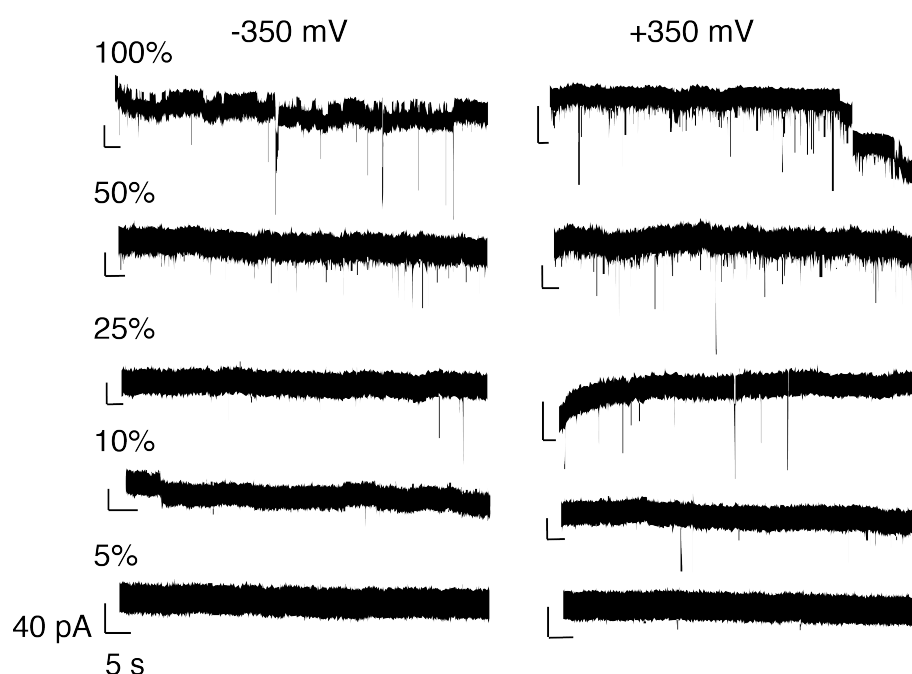


Figure 9.12: Ion current trace of plasma sample at different dilutions subjected to negative and positive voltage bias.

As expected the undiluted plasma sample presented with high noise, i.e., many number of events with various different translocation time and peak amplitudes were visible due to the complex nature of plasma. Step wise dilutions and subsequent ion trace data acquisition was done till a clean baseline was attained at both voltage polarities (figure 9.12).

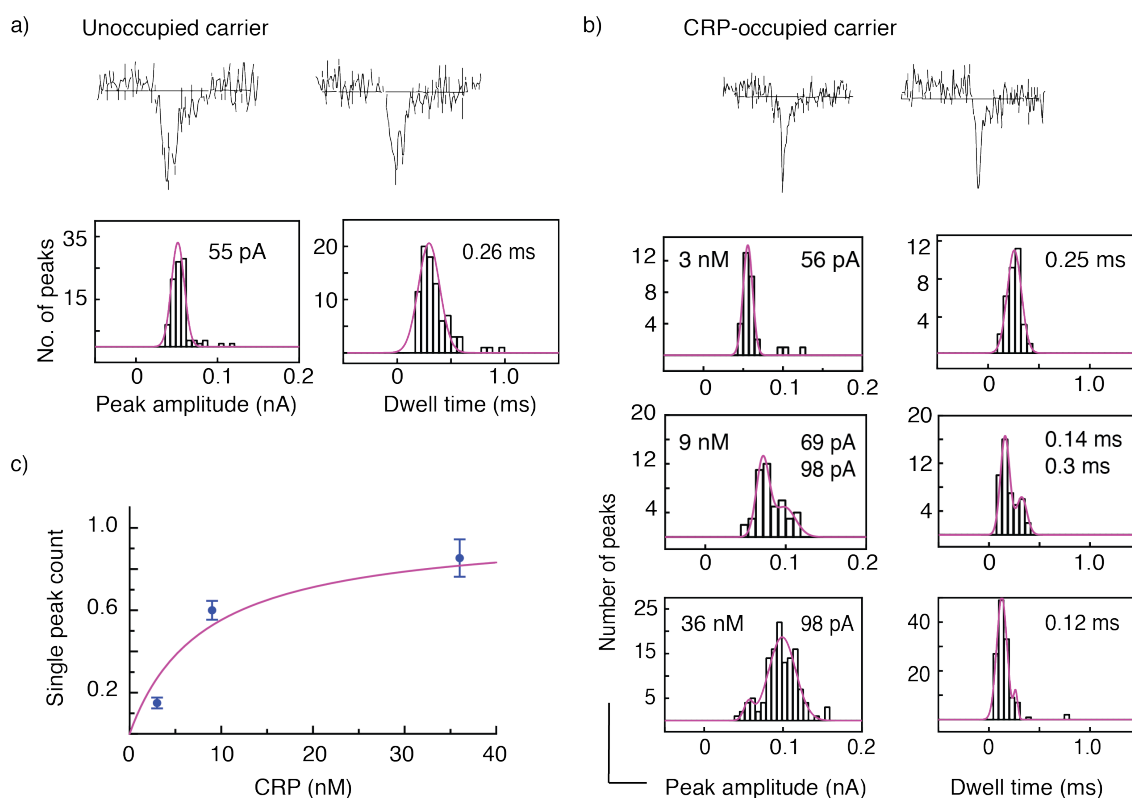


Figure 9.13: CRP detection in plasma. CRP detection in diluted plasma. Typical ion current traces, and peak amplitude and dwell time histograms for a) unoccupied carriers and b) CRP-occupied carriers in different concentrations of CRP in 5% plasma. c) Normalised single peak count, i.e., ratio of single peaks vs total classified peaks against CRP concentration, table 10. The solid line is a guide to the eye using a Langmuir isotherm. Data represents $n > 30$ for 3 nM, $n > 40$ for 9 nM, $n > 100$ for 36 nM.

A solution of (5%) human plasma diluted in buffer and spiked with the different concentrations of CRP ranging from 3 nM to 36 nM was used for further nanopipette translocation experiments as shown in the figure 9.13. The carrier molecules on their own

in 5% plasma produced double peak ion current events similar to the situation in buffer, but with a slightly lower dwell time around 0.26 ± 0.10 ms and peak amplitude of 55 ± 6 pA. Nevertheless the peak characteristics for occupied carriers (0.12 ± 0.04 ms and 98 ± 1 pA), i.e. the single peaks observed in 5% plasma spiked with CRP, were found to be consistent with the experiments in 0.1 M KCl buffer.

The different ion current events observed during a translocation experiment with 5% plasma can be classified into single peaks, double peaks and unclassified peaks in the same way as in buffer. Figure E.41 in appendix 5 shows the scatter plots for peak amplitude versus dwell time for all CRP concentrations with the single and double peaks which were selected as representing CRP-occupied and unoccupied carriers, respectively, indicated in the same way as for the buffer experiments. The ratio of single peak versus total number of classified peak is shown in figure 9.12c together with a Langmuir isotherm-like guide to the eyes using the K_d as established for the buffer experiments.

We successfully detected CRP bound carriers at concentrations as low as 9 nM (compared to 3 nM in pure buffer), with a good signal to noise ratio and the normalised single peaks count also correlated with increasing CRP concentration. Based on the counting statistics the number of unclassified events observed for various CRP concentrations in plasma sample were similar (9–25%) to those observed in pure buffer.

9.5 Conclusion

In this chapter, a biosensing approach based on identifying and counting individual biomarkers being translocated through a nanopore on a DNA origami carrier macromolecule which features a central cavity with a target-specific DNA aptamer is demonstrated.

By utilising the definite structural property of DNA origami towards translocating ion current, DNA origami structures were designed with central cavities large enough to lead to a clearly identifiable double peak in the translocation ion current, but small enough that

if the biomarker of interest—human CRP—is inserted into the cavity, the translocation ion current peak becomes a single peak.

To facilitate the specific and selective binding of the biomarker of interest into the cavity, a biomarker-specific DNA aptamer was weaved into the DNA origami structure on the edge of the cavity. Translocation studies with unoccupied DNA origami carriers and highly CRP-occupied carriers revealed two distinct dwell time-peak amplitude clusters, which correlated with single and double peak shapes, respectively. This ability to differentiate between biomarker-occupied and unoccupied carriers provides solid foundations for biosensing.

Using the three-parameter classification, i.e. the peak shape and the 95% confidence ellipse in the peak amplitude-dwell time scatter plot, quantitative detection down to 3 nM and 9 nM CRP in $\sim 5 \mu\text{l}$ sample volume of buffer and diluted human plasma, respectively, was achieved within a 2 minute sampling window.

Using robustly folded rather than long linear DNA which is often the carrier of choice for nanopore experiments, many of the setbacks were overcome. The easily identifiable ion current signature of the DNA origami carrier not only minimises false positives owing to knots and folds often occurring in linear DNA, but also eliminates the ‘tail to head’ and ‘head to tail’ ambiguity which is encountered with long linear DNA strands with respect to its translocation direction.

Importantly, this carrier-nanopore biosensing approach is based on counting individual biomarkers rather than relying on an ensemble-averaged signal. As such, the sensitivity of this system can be improved, for example by reducing the size of the confidence ellipses used to eliminate outliers and thus to increase the stringency of the classification. This, in turn, would require an extension of the sampling time to ensure statistically relevant numbers of occupied and unoccupied carriers are recorded.

Furthermore, improving the DNA origami designs with increased robustness will reduce the number of broken and thus unclassifiable carriers in the sample, contributing to increased sensitivity and specificity. Finally, the presented biosensing system has the

potential to be advanced to multiplexed detection, e.g. through using ribbons of DNA origamis with integrated barcoding as indicated in the next chapter.

Chapter 10

Conclusions and Future Developments

10.1 Conclusions

The accessibility of a robust single molecule technology that is both sensitive and specific, like with the use of nanopores and nanopipettes, will indubitably advance biomolecular research techniques. One such milestone in the field that conveys the translatability of this technique is the successful commercialisation of nanopores for DNA sequencing (MinION by Oxford Nanopore Technologies).

Apart from the important goal of rapid and reliable genome sequencing, the applications of nanopore sensing technique is broad ranged and extensive with lot of opportunities for improvement. This includes commercial use in biomedicine (molecular diagnostics and drug development), biotechnology (food industries and water quality control) and forensics (bioterrorism, crime scene detection). For example, the analysis and study of individual proteins molecules to develop new protein–biomarker based diagnostics is one application that is of importance and relevance to this thesis.

An ideal biosensor should be robust, simple, highly sensitive and selective for rapid detection of a specific target molecule in real time. Biosensor research targeted towards realising these criteria also includes, integration of nanomaterials for various functions in the design of biosensors to improve its utility. Especially with the advent of DNA

nanostructures, nanoscale functional devices using biological molecules have opened up enormous opportunities in bio–nanotechnological applications.

The DNA nanostructures produced via bottom up molecular self–assembly have been researched extensively in the last few decades with advances in scaffold design to form arbitrary DNA origami designs in both two and three dimension. Many of these nanostructures have been utilised as molecular breadboards for biosensing, also, previous research in bioelectronics group have evidenced DNA origami as a molecular platform for molecular interaction studies including proteins [257].

Usually, the role of nanoscale materials used in the biosensor scheme would be different according to their distinctive properties and biosensor design, for example, as immobilisation support, as mediators, or as signal amplifiers. With the use of DNA nanostructures one could satisfy the aforementioned parameter objectives in a label free manner if combined with nanopore sensing technology.

Thus in this project, by effectively making use of the expertise within the bioelectronics group, DNA frame nanostructures that are capable of anchoring the analyte and subsequently impart sensitivity and specificity to the biosensor via nanopipette based resistive pulse detection, were designed. This was done with an aim towards tackling few of the challenges in the field of nanopore sensing, particularly 1) screening single protein molecules 2) imparting specificity and sensitivity 3) achieving quantitative sensing.

Previous work in literature discusses translocation of different DNA nanostructures of few tens of nanometer that could be successfully differentiated by using the variations in translocation peak dwell time and current amplitude, thus demonstrating the relation between ion current and sample geometry. Also, it has been shown that via examination of the translocation dwell time one could extract properties of the sample like their length and folding state. In this thesis, the potential of nanopipettes is extended further to differentiate differently folded DNA origami nanostructures and their subsequent use as carriers conveying target bound state via specific ion current signature.

10.1.1 DNA origami as carriers

This way of anchoring analytes to a biomolecule ‘carrier’ has been studied previously with the use of linear DNA molecule. Barcoding and multiplexing for different protein molecules have also been researched, as presented previously in the literature review, for both qualitative and quantitative detection. The main idea in these approaches is to search for events within events (sub–peak ion current).

In this thesis, it is shown that the many setbacks of the long linear DNA carriers could be overcome via the use of well formed DNA origami as carriers. First, the use of DNA origami implies a definite structure designed with specific dimensions and they are not in random coil or folded state in solution and during their passage via nanopore. This eliminates the occurrence of false positive events due to folds and knots which are always observed in long DNA translocations. We also remove the various ion current signatures that stem from directional ‘tail to head’ and ‘head to tail’ translocations.

Moreover, through chapter 7 and 8 it is evidenced that the DNA frame origami nanostructures give rise to double peak ion current signature that is characteristic to the shape of the nanostructure. Thus unlike the linear DNA carrier, DNA nanostructure carriers have a specific ion current signature that can be visually recognised.

10.1.2 Quantitative sensing

Further in chapter 8 it is evidenced that the specific ion current signature of frame DNA origami structures could be influenced by manipulating the frame dimension. The dimension of the outer frame in relation to the inner cavity produces a split in the ion current structure due to an increased flow of ion and varied counterion distribution. Also, the split in ion current (double peak) becomes less significant with decrease in cavity size and eventually merges to present a single peak.

Thereupon in chapter 9, this direct correlation of cavity space to ion current signature is made use of for arriving at a unique and robust mechanism for detecting analyte occupied

DNA origami carrier. By placing an aptamer within the cavity space, and upon capture of the target analyte, results in a change in the ion current peak signature of the carrier. Here, a true or false biosensing signal can be directly encoded into the ion current peak signatures, single and double respectively, due to the presence and absence of the bound analyte within the central cavity of the DNA origami.

Also, it is important to note that the inner cavity of the DNA origami should be sufficient enough to provide a distinguishable double peak and the outer frame structure should be rigid and sized in dimension comparative to the nanopipette pore size thus presenting a high signal to noise at every signal translocation. More importantly the inner cavity dimension should also be in relation to the bound target size that upon binding the peak signature changes. In this thesis for detecting CRP the DNA nanostructure contained a small inner window (35×35 nm) whilst its outer frame structure was 95×95 nm, which was adequate to produce double peaks and transpire as single peaks upon CRP capture which is of ~ 11 nm in diameter.

Additionally, the translocation experiments revealed that the CRP-occupied and unoccupied carriers can be differentiated via dwell time and peak amplitude as shown in the 95% confidence ellipse in the peak amplitude-dwell time scatter plots. This taken together with the distinct ion current signatures allows for a three-parameter classification wherein the capture rate is calculated by number of single peaks against the total classified events observed in an ion trace. Using this strategy quantitative detection down to 3 nM was possible.

Diagnostic devices for detecting and sensing biomarkers for disease identification or therapeutic intervention need to be highly selective and sensitive thus capable of identifying the target analytes in clinical samples with no or very less sample preparation. While most proof of concept studies present their abilities in purified samples or clear buffer solutions, the real scenario with biological samples is much more complicated with presence of complex protein mixtures, salt and other background molecules. Thus, this work also demonstrates the ability of DNA origami carriers to quantify CRP in human plasma samples at concentrations as low as 9 nM, using the three-parameter classification.

10.2 Outlook and future developments

Our highly sensitive nanopipette–DNA origami sensing system also has enormous possibilities for future improvements, for one it could be easily extended as a multiplex system with barcodes for labelling.

10.3 DNA origami barcode

As is evident from this thesis, the concentric squares in chapter 8 exhibit different peak amplitude, dwell time and ion current signatures that are significant enough to differentiate each other via nanopipette translocation. Thus these structures were further exploited to form dimers and trimers by linking individual DNA origami monomers together in order to study the potential of these structures as barcoding system. This was achieved by end modifying the staple sequences present at the ends of the concentric square DNA origami to form linkers with sticky ends that extended out. Assembly of the dimer and trimer chains were driven via Watson–Crick hybridisation of multiple sets of sticky ends. The end modification concept was adapted according to our needs from Zenk *et al.* [261].

For this purpose, four sets of 6 linkers that can be arranged on either or both sides of the concentric square structure, as shown in figure 10.1 were designed. Since the concentric squares have a common outer scaffold region and consequently similar staples, the linkers can be interchangeably used between the 3 DNA nanostructures. The end modification consisted of a linker sequence, polyT blockers and spacer sequence. The linkers 6 bp in length facilitates specific interactions between the concentric squares, the polyTs (4 bp) allow linkers to transverse helices flexibly, and lastly the 7 or 8 bp spacer sequences are intra complementary within the monomer. These end modifying sequences were designed so that after hybridisation of the concentric squares the distance between two DNA nanostructures would be 21 bp (~ 2 helical turns), this spacing ensured there was

torsional twist between the monomers resulting in an effectively planar structure.

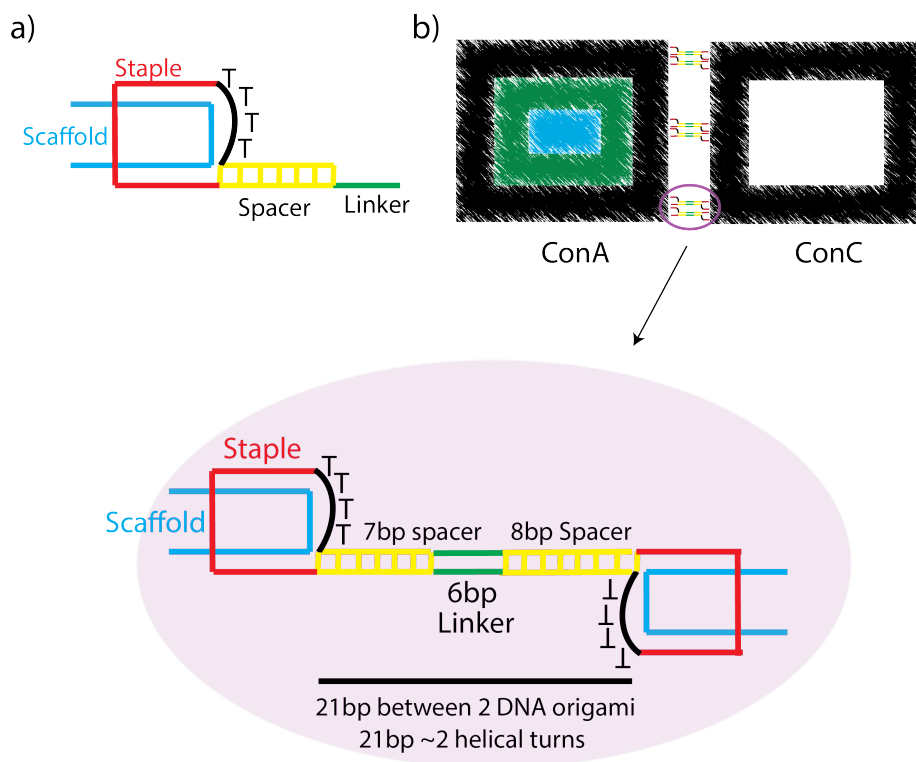


Figure 10.1: DNA origami barcode design. Schematic illustrating a) the linker sequence designed as part of the staple sequence (red) so that it is partially complementary with the scaffold edge sequences (blue). b) A representative example of linking two monomers ConA and ConC using 6 linker pairs between the monomers.

10.3.1 Barcode assembly

The concentric squares ConA B and C with modified end staples were individually folded and purified to result in nanostructures with sticky ends. Subsequently, different combinations of DNA nanostructures, were pooled together and subjected to thermal annealing by heating upto 30°C with a 0.5°C/minute reduction to 15°C. And as such two combinations of dimers (ConA+ConB and ConA+ConC) and one trimer (ConB+ConA+ConC) was studied. AFM micrographs of the successfully hybridised dimers and trimers are shown in figure 10.2.

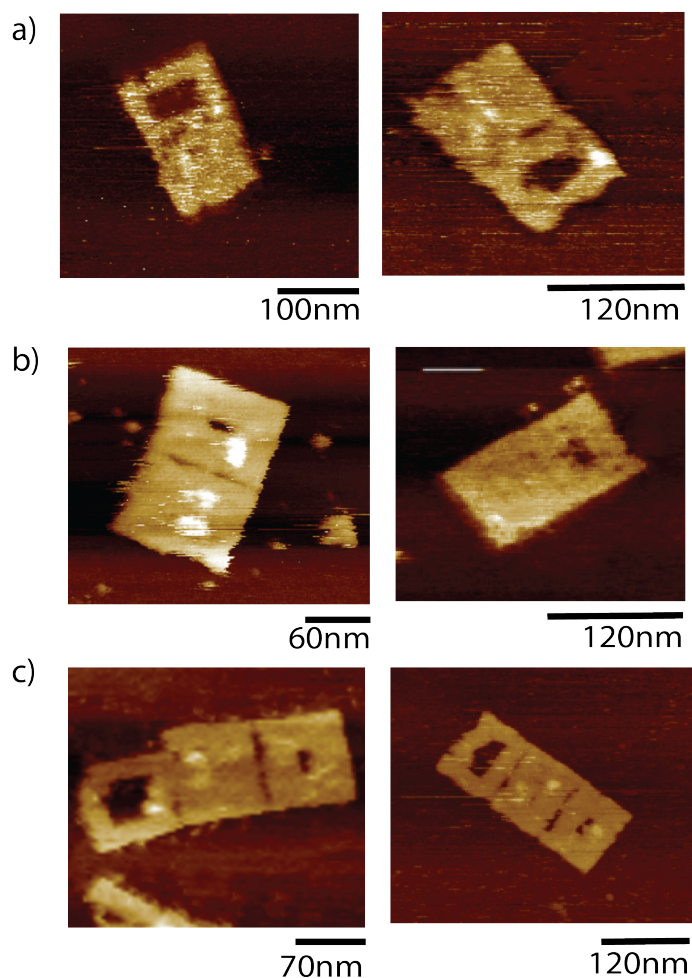


Figure 10.2: *Representative examples of the successfully formed dimers and trimer each measuring a total of $\sim 200 \times 85$ nm and $\sim 300 \times 85$ nm in external dimension respectively. a) Dimer formed between ConA and ConC b) ConA and ConB dimer c) ConA B and C trimer.*

Preliminary translocation experiments of these dimers and trimers generated interesting data, of the three combinations the dimer formed with ConA and ConC resulted in a mixture of ion current peak signatures, in that, ion current peak signatures that were distinct from those observed for the monomers were evident. While the ion current trace events did exhibit single peaks and double peaks as observed for the monomers, there were also countable number of events representing three peaks (see figure 10.3). These three peak structures accounted for $\sim 30\%$ of the total peak count as shown in table 14 in appendix F. While the single peaks could be from the broken dimers and unformed monomers, the multiple peak signatures could represent intact dimers. Data analysis of the events revealed a dwell time mean of 0.41 ± 0.05 ms, which is greater than that observed for the monomers ConA (0.15 ms) and ConC (0.31 ms) individually, thus suggesting evidence for translocation of dimers. Also the peak amplitude data of the

dimer (ConA+C) presented with a wider peak amplitude distribution with 99 ± 2 pA.

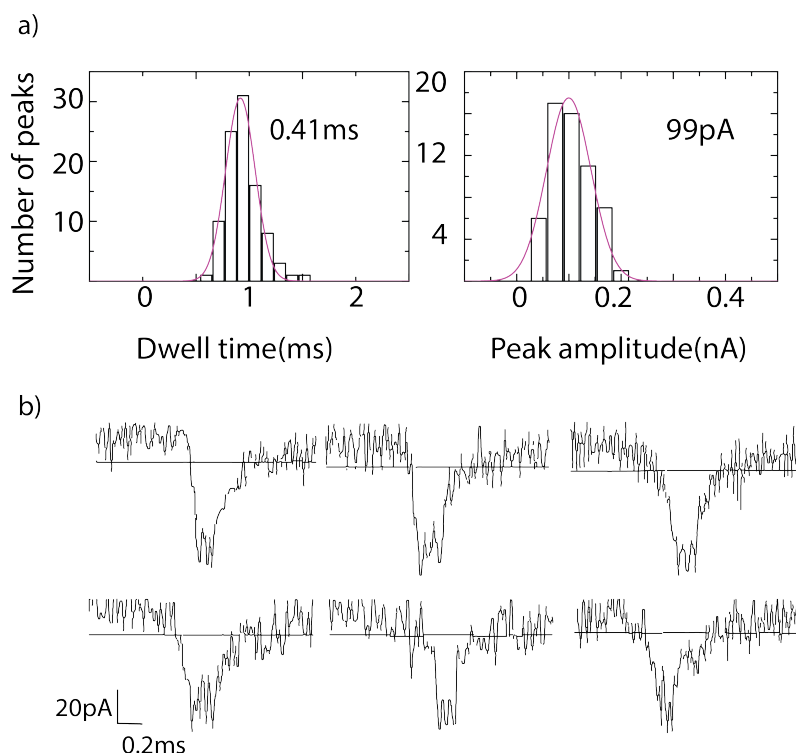


Figure 10.3: Data analysis of the nanopipette translocation ion current trace for ConA+C dimer samples. a) Histogram graphs representing a mean dwell time of 0.41 ms and peak amplitude of 99 pA along with b) some examples of observed ion current signatures.

However, ConA+B dimers and ConA+B+C trimer samples did not present with a distinctive ion current signature. Data analysis of the trimers showed a dwell time of 0.6 ± 0.01 ms, which is larger than that observed for the dimers and individual monomers. Also, peak amplitude histogram revealed two clusters with mean peak amplitude of 155 ± 36 pA and higher. Whereas, ConA+B dimers produced a mean peak amplitude of 73 ± 4 pA and dwell time of 0.36 ± 0.1 ms. Individual histograms and ion current signatures observed for both these samples are provided in the appendix F.

Thus, while the ability of the DNA origami structures to be modified for successful dimer and trimer formation is evidenced through this preliminary work (as visualised via AFM), translocation characteristics via nanopipettes requires further study for absolute

confirmation and differentiation between the samples.

Possible improvements to the barcode design

The indistinguishable peak signatures observed for these samples upon translocation could stem from the inability of the nanopipettes to separate out the individual components of the dimers and trimers, this could be rectified via modifications as suggested below.

1. To achieve a high signal to noise with distinct peak signature the DNA origami needs to be engineered in a more robust format. For this one could increase the length of the linker sequences connecting the monomers (figure 10.4b) to separate out the DNA nanostructures for achieving better differentiation.
2. Also, the DNA nanostructures used throughout this thesis is of single layer, i.e., the thickness of the structures is equal to a single DNA duplex. By designing DNA nanostructures with multiple layers (figure 10.4c) one could increase the thickness thus arriving at an even more robust geometry subsequently capable of better signal to noise owing to the overall increase in mass and charge. This robust design will also reduce/eliminate any broken or fragmented DNA structures.

This improved nanostructure design could then be used for detecting various protein molecules, using different aptamers, in one sample mixture simultaneously. For example, the empty chain of DNA nanostructures without any aptamers will act as the barcode section. The barcode section will be followed or preceded by specific aptamer incorporated DNA nanostructures which will accomplish the detection and quantification of specific proteins, including those present at a low concentration.

Here, the aptamers ensure specificity and a unique signal via the translocation event in relation to the size of a given protein. Using different aptamers in the DNA nanostructure chain for different proteins will enable multiple protein capture from a single sample

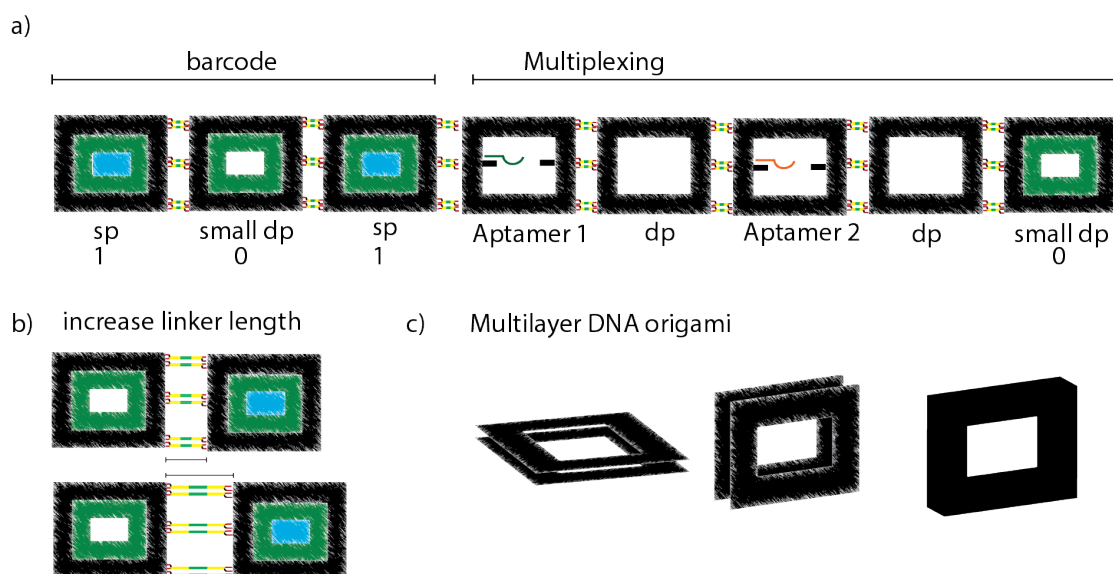


Figure 10.4: Schematic of a) the barcoded multiplexing system where, the empty nanostructures acts as the barcode with a specific binary output succeeded by the carriers with aptamers for multiple targets. b) Depiction of two DNA nanostructures connected by a linker sequence of increased length and c) multilayer DNA origami for a robust 3D origami structure.

volume. The barcodes can be designed to provide varying binary outputs (see figure 10.4a) succeeding or preceding specific protein specific carrier which would corroborate the results of the sensing system further. Another improvement to be targeted in this system is very high sensitivity with signal processing advancements.

As such, aptamer modified DNA origami carriers in combination with nanopore sensing has great potential for biosensing. In a clinical and medical perspective, these sensors do not require a large volume sample and are capable of low concentration detection, thus screening or quantifying a specific biomarker in biological samples like blood, urine and sweat becomes possible in a quick minimally invasive manner. More over, the nanopipettes with its versatility can be coupled or integrated to microfluidic devices, for further application.

Appendices

A Nanopipette pulling parameters

In this appendix, the different nanopipette pulling parameters tested in chapter 7 to arrive at the sample specific pore size are listed along with representative SEM micrograph of a nanopore pulled using the same parameters.

Table 1: Pulling parameters for quartz capillaries of 0.5 mm inner diameter and 1.0 mm outer diameter, producing pore diameters of $\sim 20\text{--}30$ nm.

HEAT	FIL	VEL	DEL	PULL
575	3	35	145	75
900	2	15	128	200

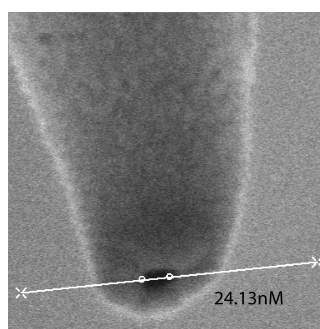


Table 2: Pulling parameters for quartz capillaries of 0.5 mm inner diameter and 1.0 mm outer diameter, producing pore diameters of ~10–20 nm.

HEAT	FIL	VEL	DEL	PULL
650	3	30	145	190
HEAT	FIL	VEL	DEL	PULL
650	2	30	145	170
HEAT	FIL	VEL	DEL	PULL
650	3	30	145	170

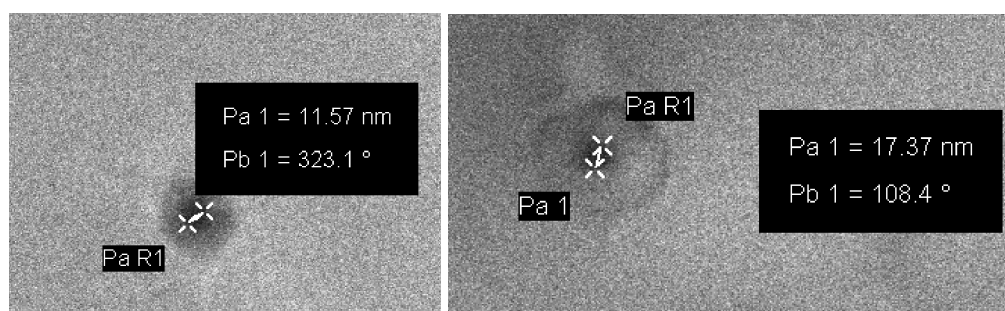


Table 3: Pulling parameters for brosilicate capillaries of 0.5 mm inner diameter and 1.0 mm outer diameter, producing pore diameters of ~250–280 nm.

HEAT	FIL	VEL	DEL	PULL
700	4	60	145	175

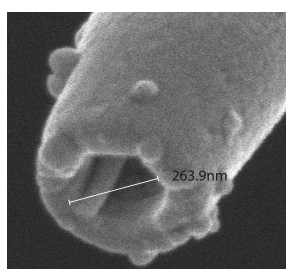


Table 4: Pulling parameters for brosilicate capillaries of 0.5 mm inner diameter and 1.0 mm outer diameter, producing pore diameters of $\sim 150\text{--}200$ nm.

HEAT	FIL	VEL	DEL	PULL
650	3	15	128	170

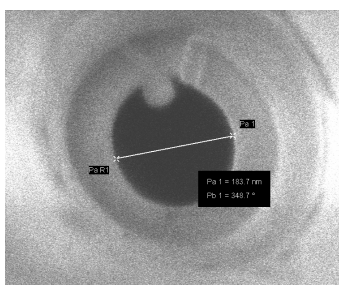


Table 5: Pulling parameters for quartz capillaries of 0.5 mm inner diameter and 1.0 mm outer diameter as listed in tables 1 and 5.1 in chapter 5, producing pore diameters of $\sim 20\text{--}30$ nm and $\sim 80\text{--}100$ nm.

pore size $\sim 20\text{--}30$ nm		pore size $\sim 80\text{--}100$ nm	
pore resistance (M Ω)	pore size (nm)	pore resistance (M Ω)	pore size (nm)
87.4	95.46	175.9	29.47
104.2	79.97	178.3	27.58
94.6	88.74	170	31.59
105.2	72.73	170.6	30.17
95.4	83.41	166.2	36.01
98.5	81.23	200	18.58
75.6	109.6	180.4	26.15
98.4	80.73	187.4	22.42
102.4	77.86	175	29.15
96.4	91.42	177.5	28.74
97.4	85.46	185.5	24.13
94.2	89.97	160.8	34.84
98.2	82.73	160	32.92
85.4	93.41	180.3	26.48
88.5	91.23	202.3	16.8
80.6	100.6	204.8	16.21
88.4	90.73	189.2	20.88
92.4	87.86	180.2	21.34

B DNA origami scaffold routing

In this appendix, the different DNA origami nanostructure used throughout this thesis is provided as schematics. The scaffold and staples strand routing design to form the various structures, tiles and frames, are shown.

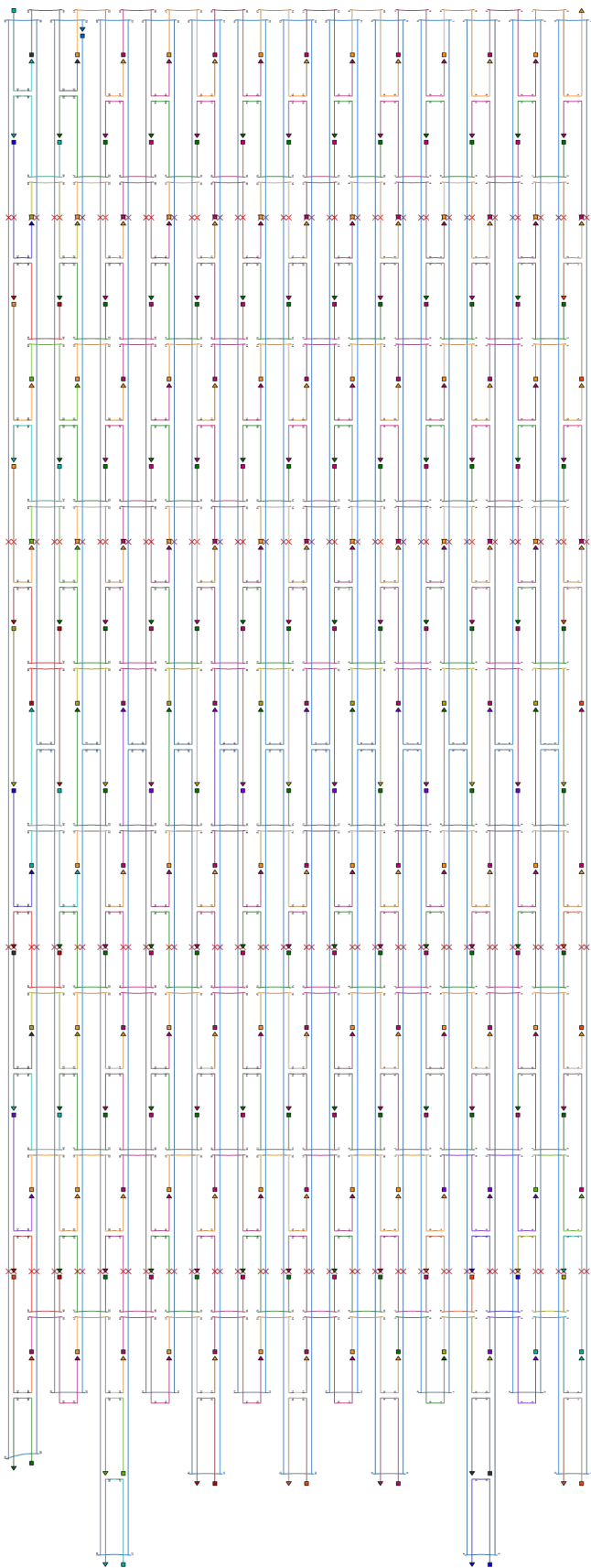


Figure B.6: Schematic portraying the scaffold and staple routing for plain tile origami T1, the scaffold is shown in blue while the staples are depicted in different colors.

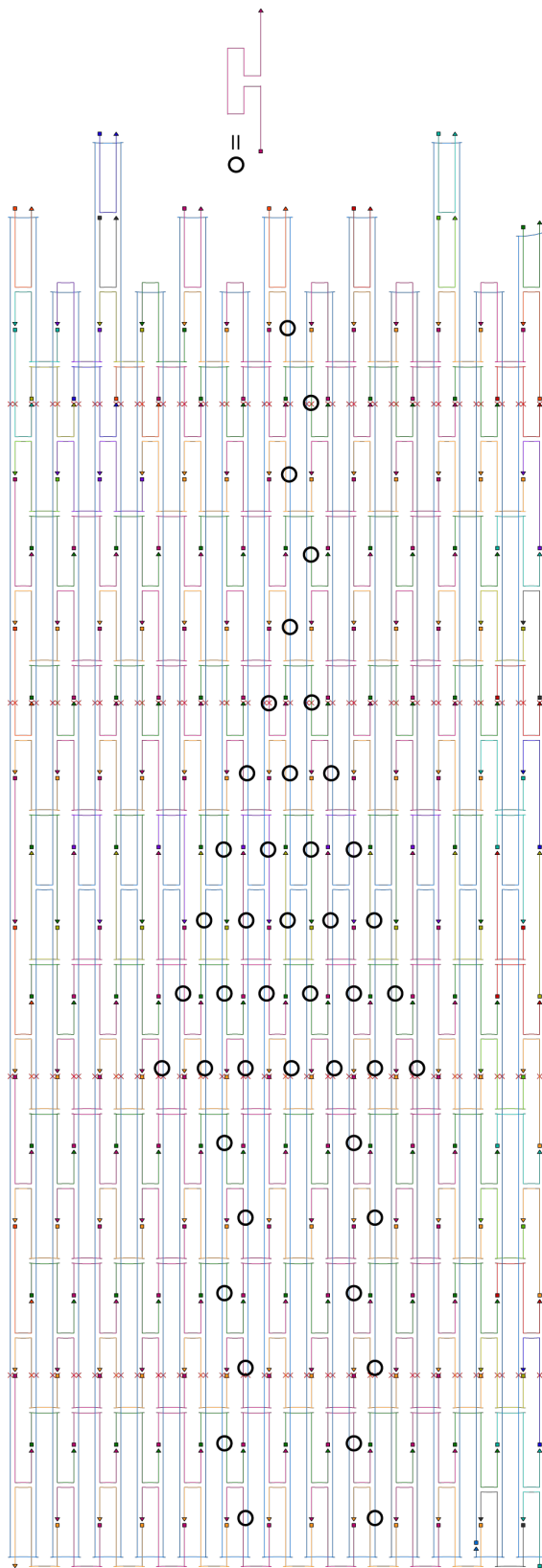


Figure B.7: Schematic portraying the scaffold and staple routing for Tile origami T2 with loops, the scaffold is shown in blue while the staples are depicted in different colors.

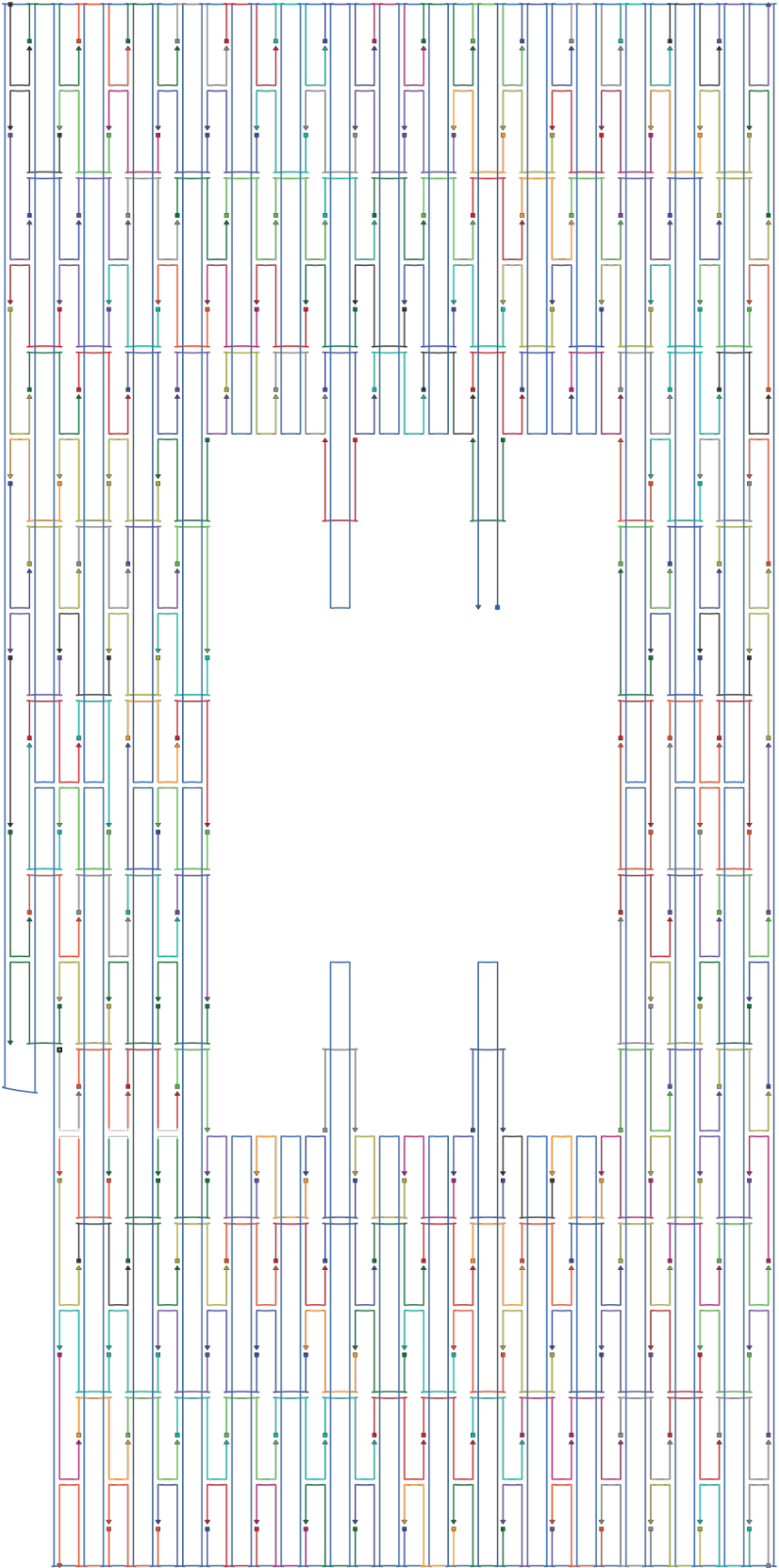


Figure B.8: Schematic portraying the scaffold and staple routing for frame origami F1, the scaffold is shown in blue while the staples are depicted in different colors.

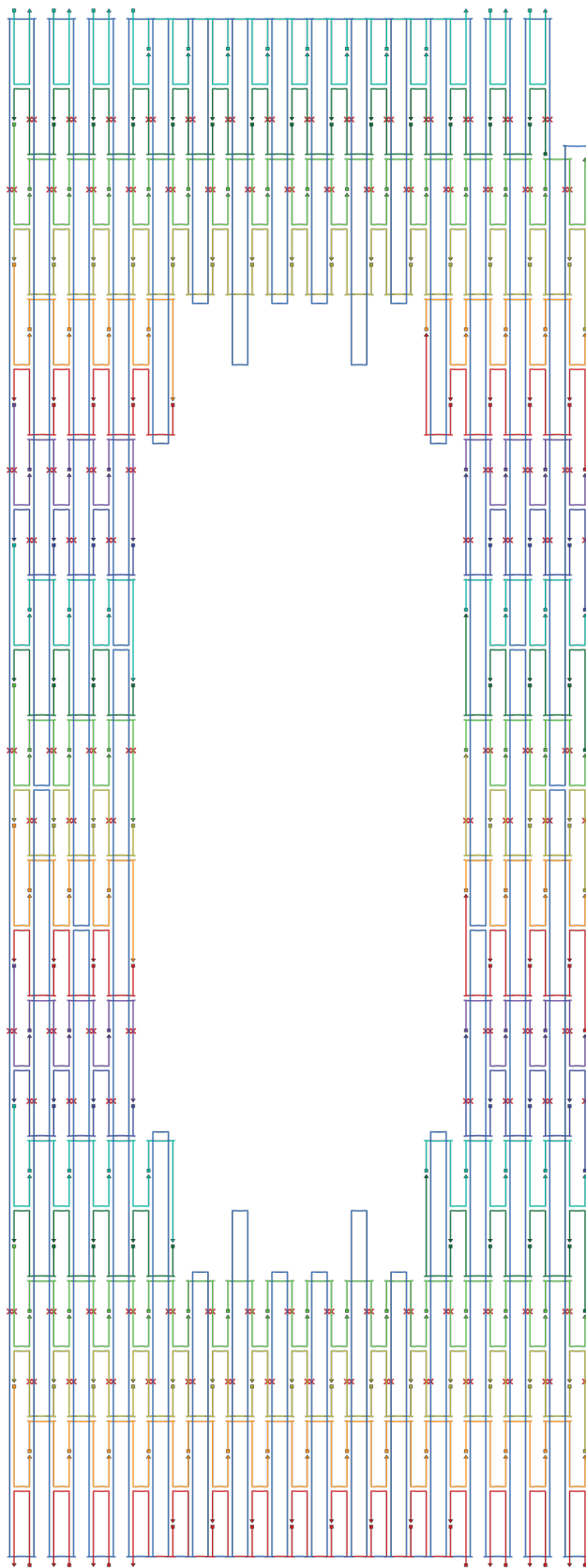


Figure B.9: Schematic portraying the scaffold and staple routing for frame origami F2, the scaffold is shown in blue while the staples are depicted in different colors.

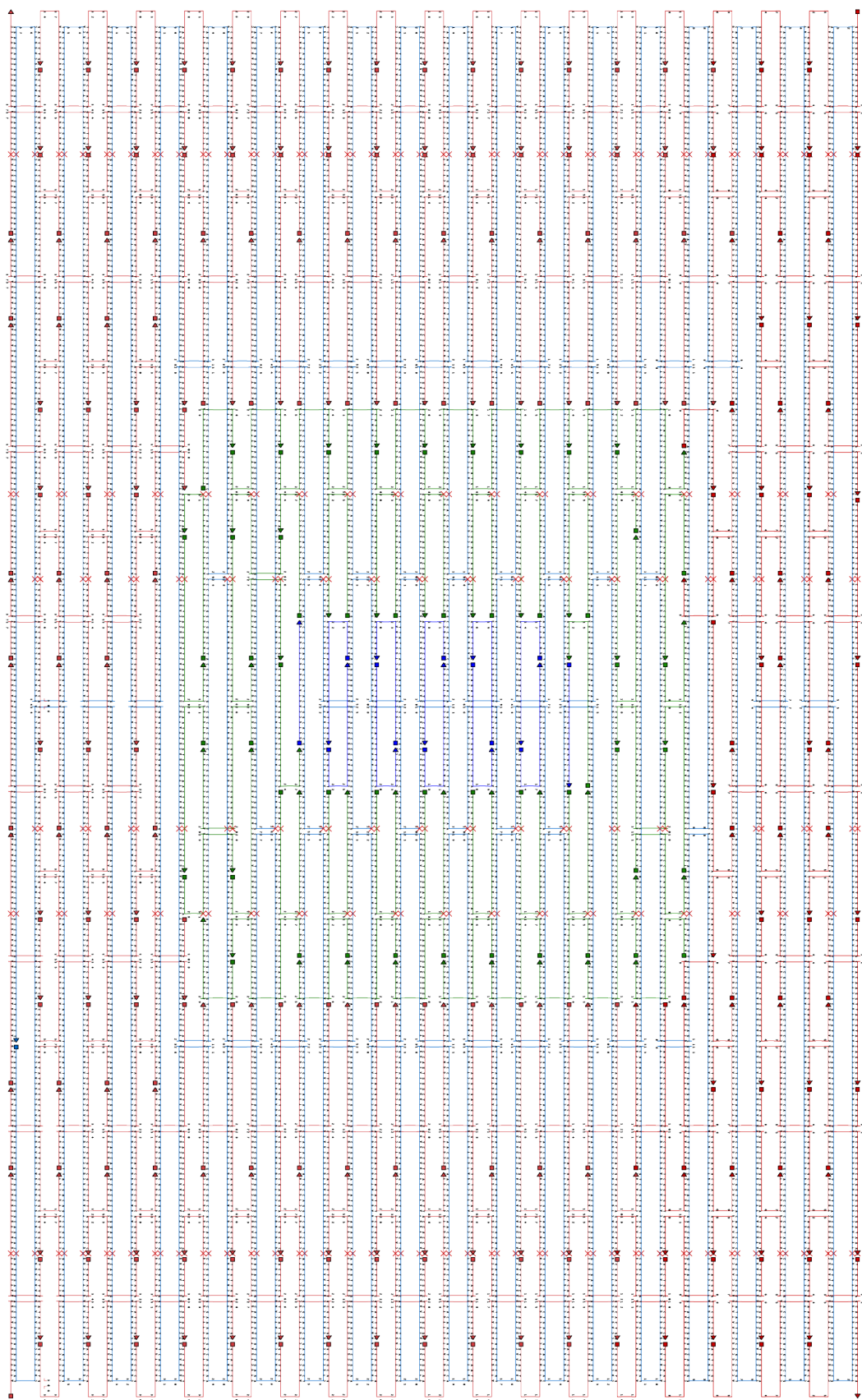


Figure B.10: Schematic portraying the scaffold and staple routing for ConA DNA origami, the scaffold is blue colored and the staples are shown in three colours depicting the parts of the design to be removed for forming ConB and ConC.

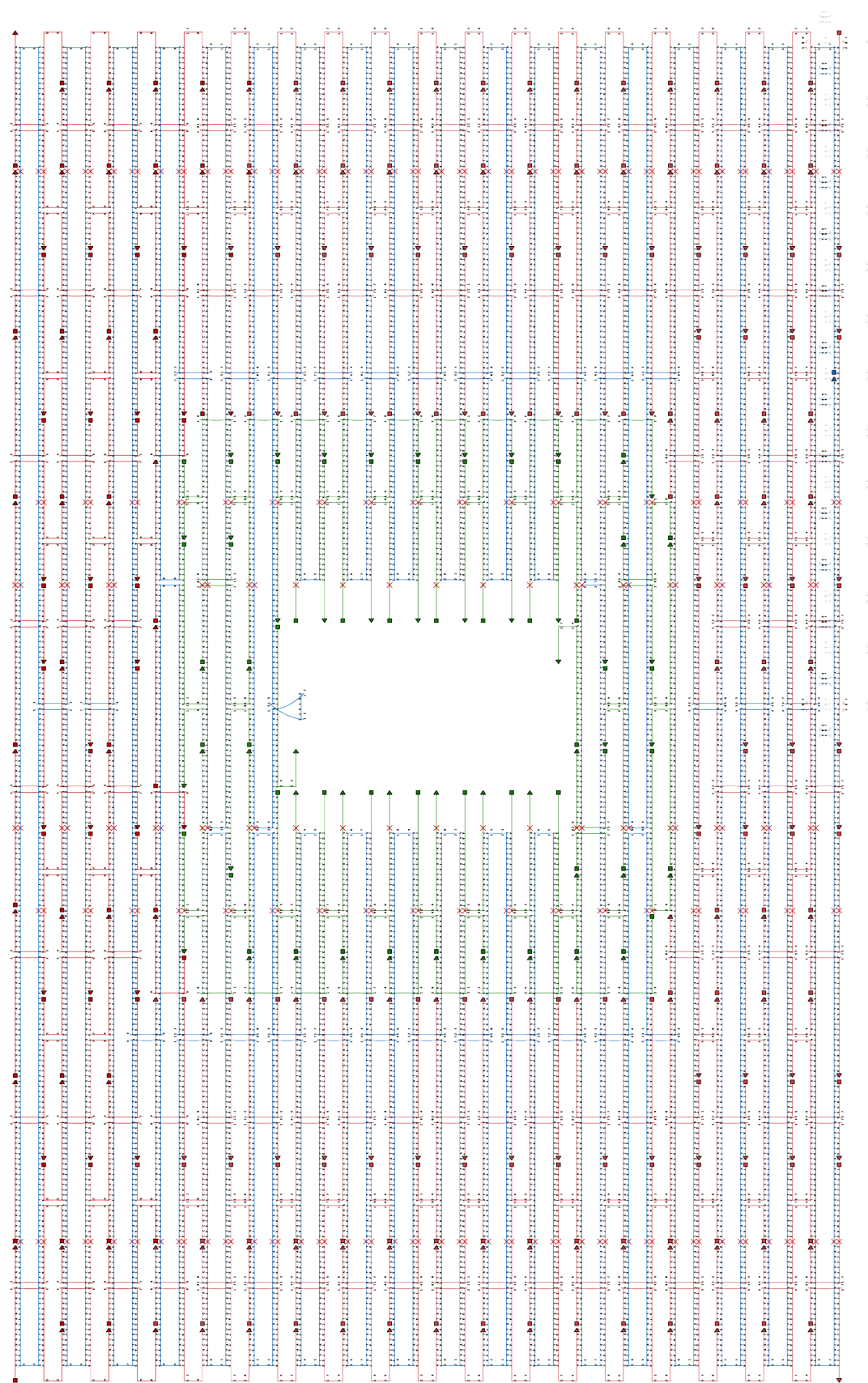


Figure B.11: Schematic portraying the scaffold and staple routing for ConB DNA origami, the scaffold is blue colored and the staples are shown in two colours depicting the part of the design to be removed for forming ConC.

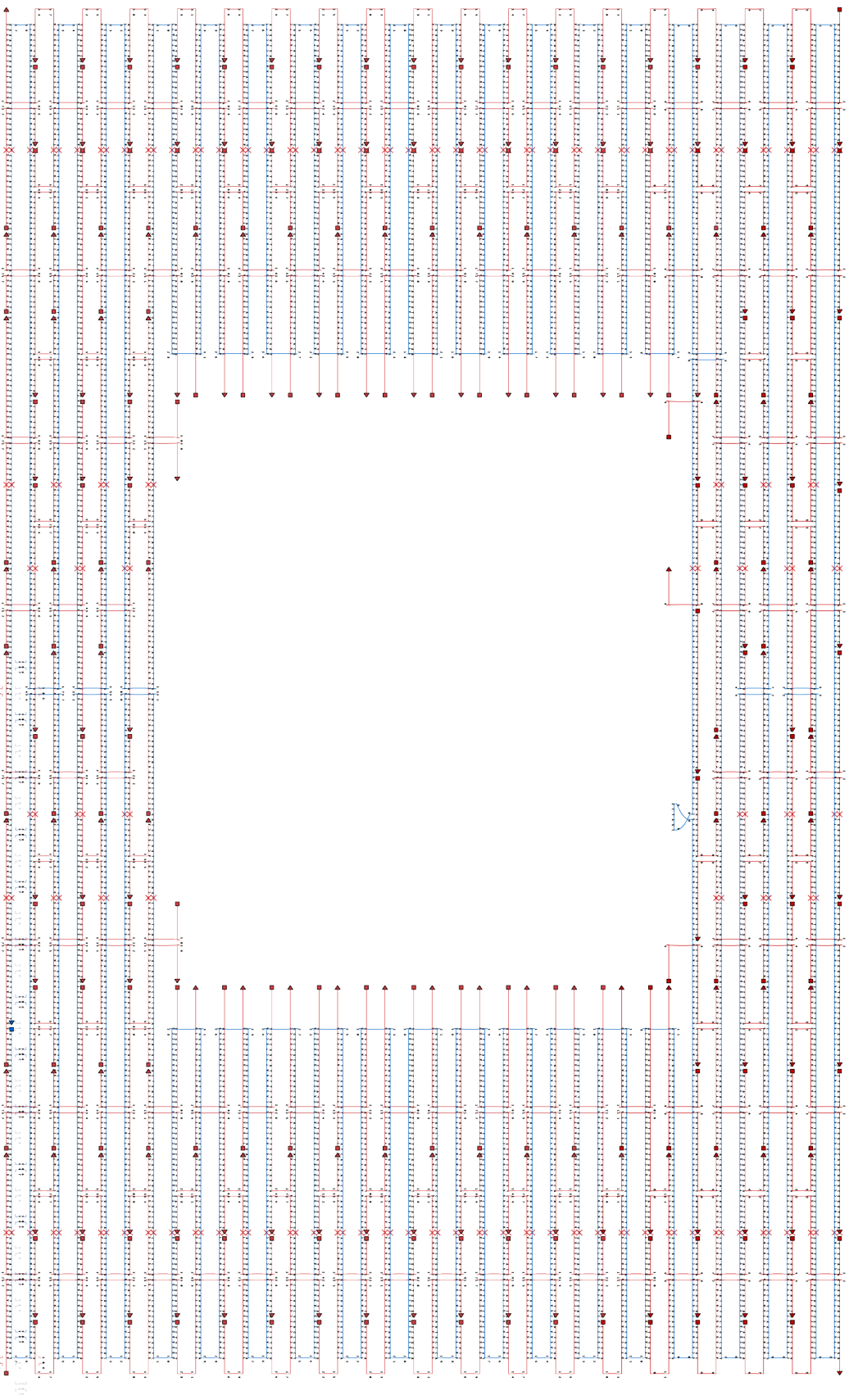


Figure B.12: Schematic portraying the scaffold and staple routing for Conc DNA origami, the scaffold is blue colored and the staples are all in red.

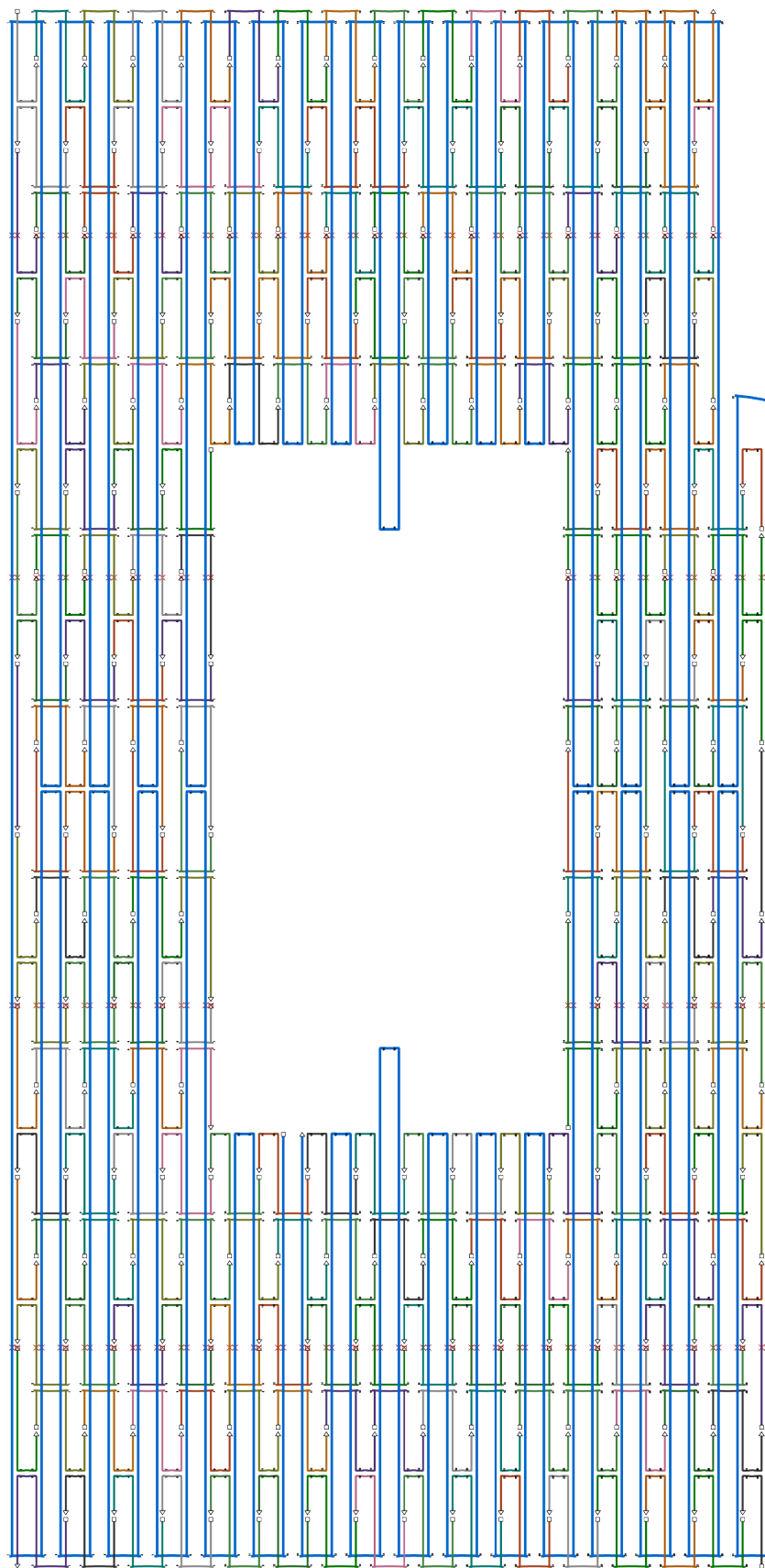


Figure B.13: Schematic portraying the scaffold and staple routing for DNA origami used as the carrier in chapter 9, the scaffold is blue colored and the staples are all colored differently.

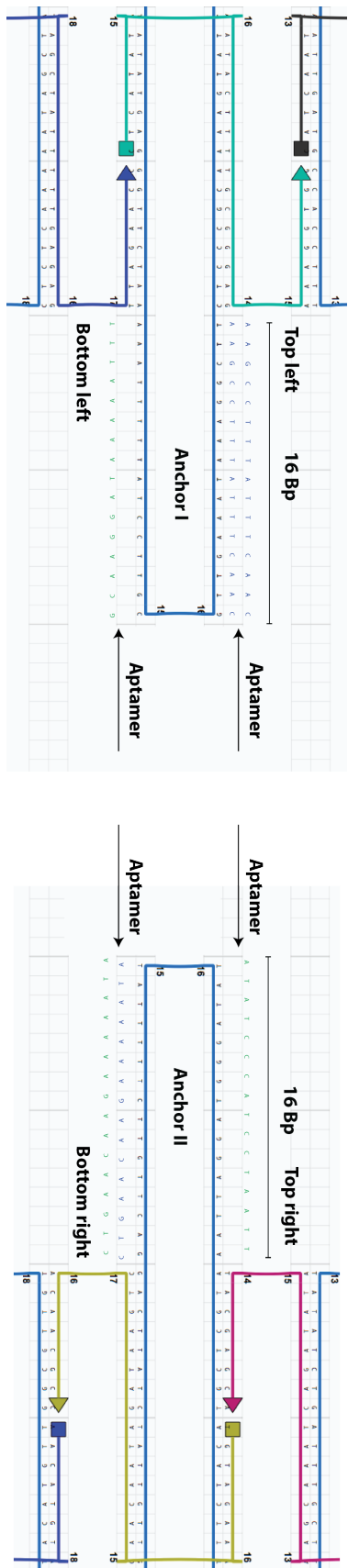


Figure B.14: Schematic portraying the anchor part of the DNA origami carrier, the 16 bp anchor extends into the inner window of the DNA origami onto which aptamers can be functionalized. As shown, the design provides possibility of attaching upto 4 aptamers to the top and bottom of the left and right anchors.

C Appendix for chapter 7

In this appendix, the different ion current signatures observed for the DNA origami nanostructures of different dimensions studied in chapter 7 is presented. Also, Gel electrophoresis study for the respective DNA nanostructures and the graph showing pore size to resistance correlation for a set of nanopipettes used in chapter 8 is provided.

Table 6: Number of double peaks (dp) observed for frame DNA origami (F1 and F2) and tile DNA origami (T1 and T2) for two nanopipette translocations conducted on different days.

Pipette	F1		F2		T1		T2	
	dp	total	dp	total	dp	total	dp	total
1	55	90	109	206	10	145	14	355
2	59	102	72	114	14	204	9	134

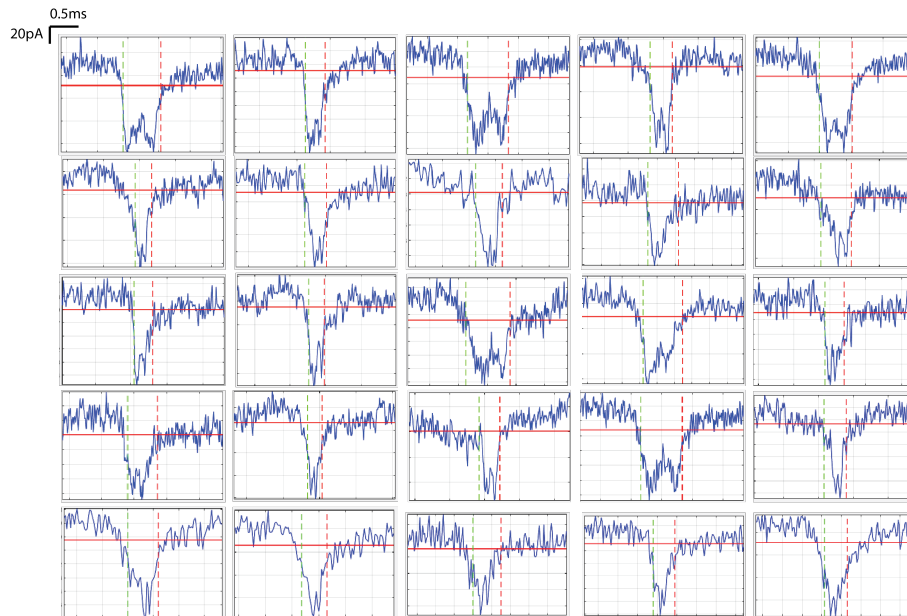


Figure C.15: Array of double peak signatures obtained for frame DNA origami samples *F1* and *F2*.

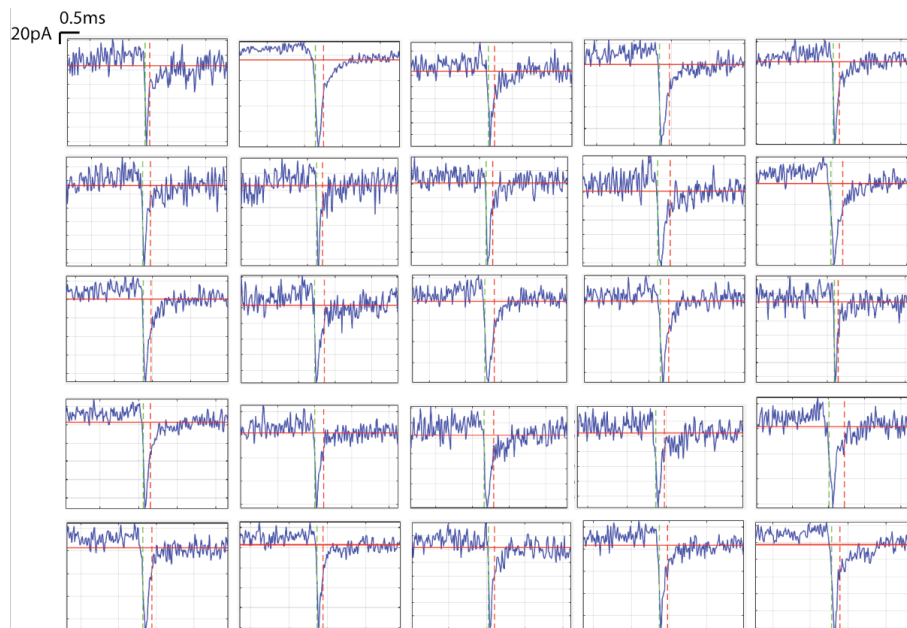


Figure C.16: Array of single peak signatures obtained for frame DNA origami samples *F1* and *F2*.

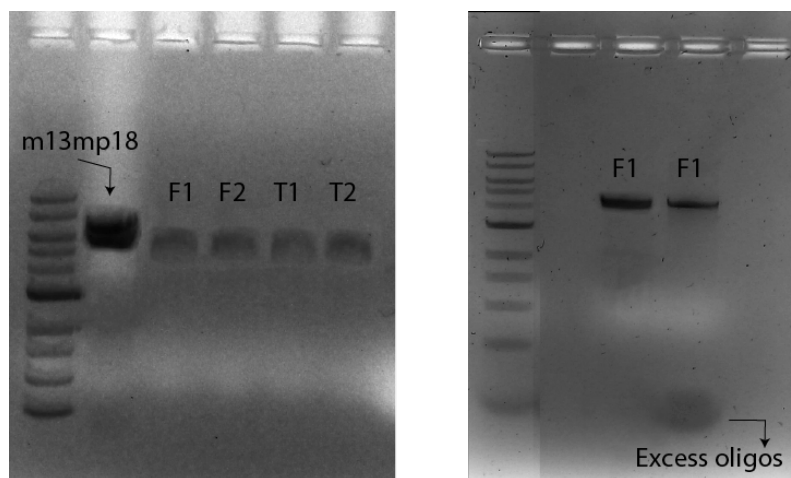


Figure C.17: Agarose gel electrophoresis analysis of a) the folded frames (F1 and F2) and tiles (T1 and T2) in 0.5% agarose run at 80V for 1 hour at 4 degree Celsius. The second lane contains the m13 scaffold run as control and the lanes 3, 4, 5, 6 have the respective intact DNA nanostructures. b) The adjacent gel contains the frame DNA origami F1 after and before purification via s400 columns to remove excess staples.

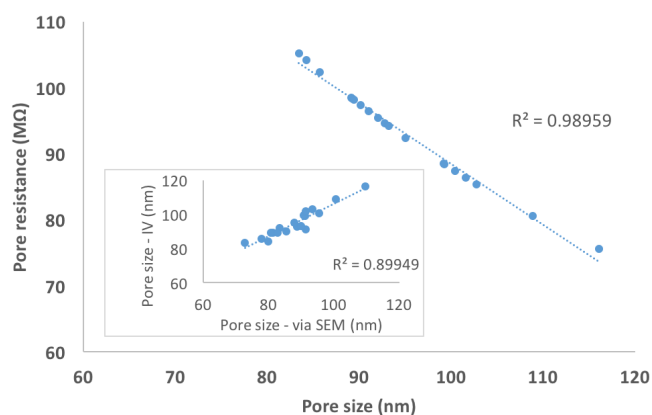


Figure C.18: Graph showing the correlation between pore resistance and pore diameter for seventeen \sim 80-100nm pore sized pipettes fabricated using parameters as outlined in methods and materials chapter. The inset shows the correlation between the measured and calculated pore diameter, D_s and D_a respectively. The dotted lines represent least square fits of a first order polynomial to the data.

D Appendix for chapter 8

This appendix accounts for the additional figures not included in the main content of chapter 9, this comprises the elaborate protocol for concentric square scaffold assembly along with design maps and ion current signatures of the concentric square samples.

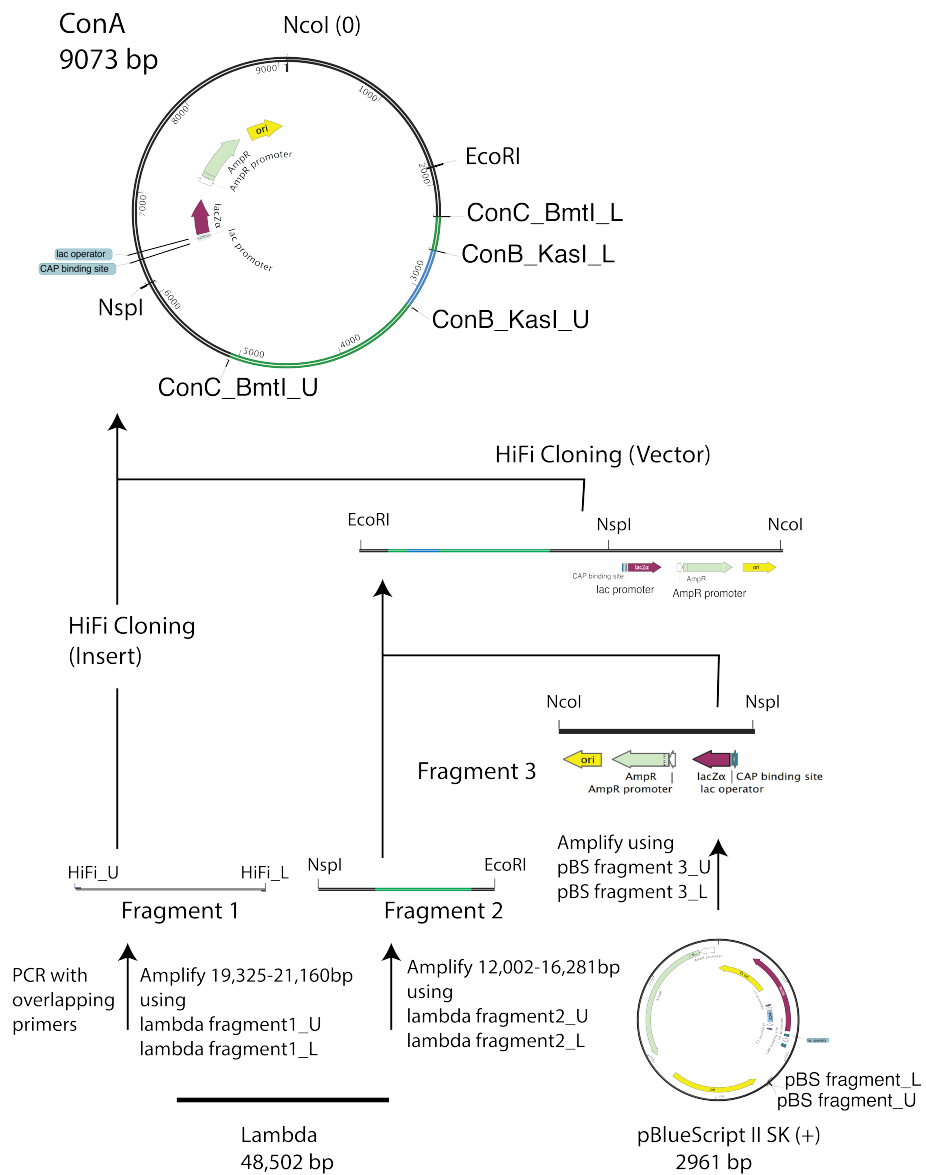


Figure D.19: Concentric square design map. The schematic portrays the different steps towards arriving at the ssDNA scaffold for concentric square A. Three fragments namely, fragment 1 and 2 derived from lambda phage DNA and fragment 3 from pBluescript II SK(+) plasmid are cloned together to form the 9073 bp scaffold.

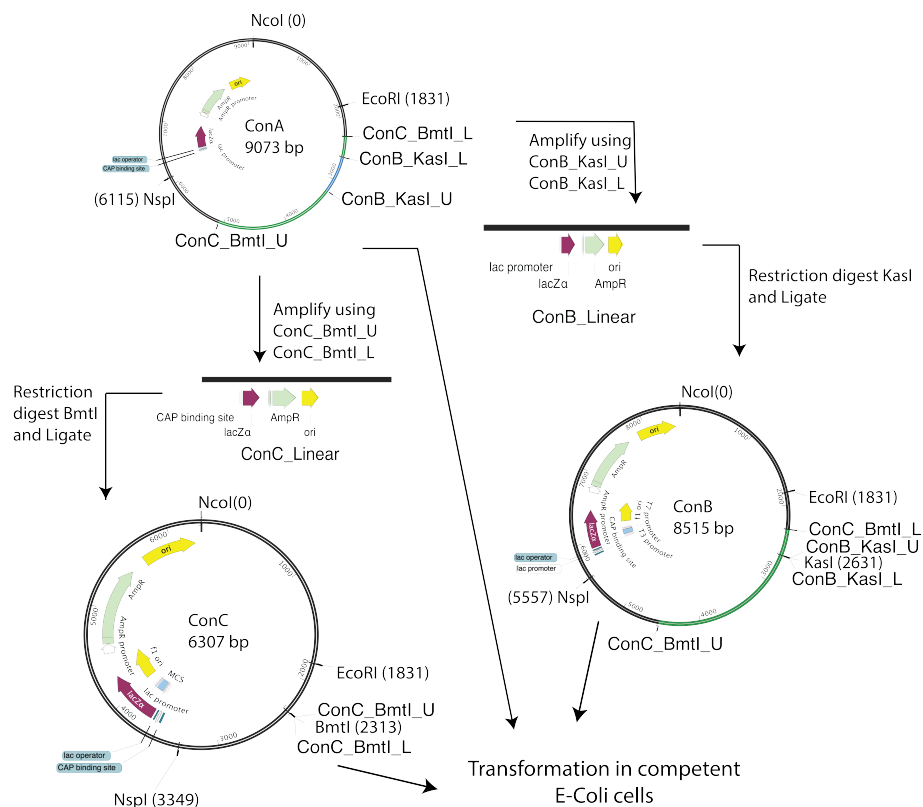


Figure D.20: Construction of concentric square B and C, is achieved by PCR amplification of ConA with specific primers incorporated with restriction digest sites, KasI and BmtI, for conB and C respectively. The resulting custom DNA is then transformed in E.coli.

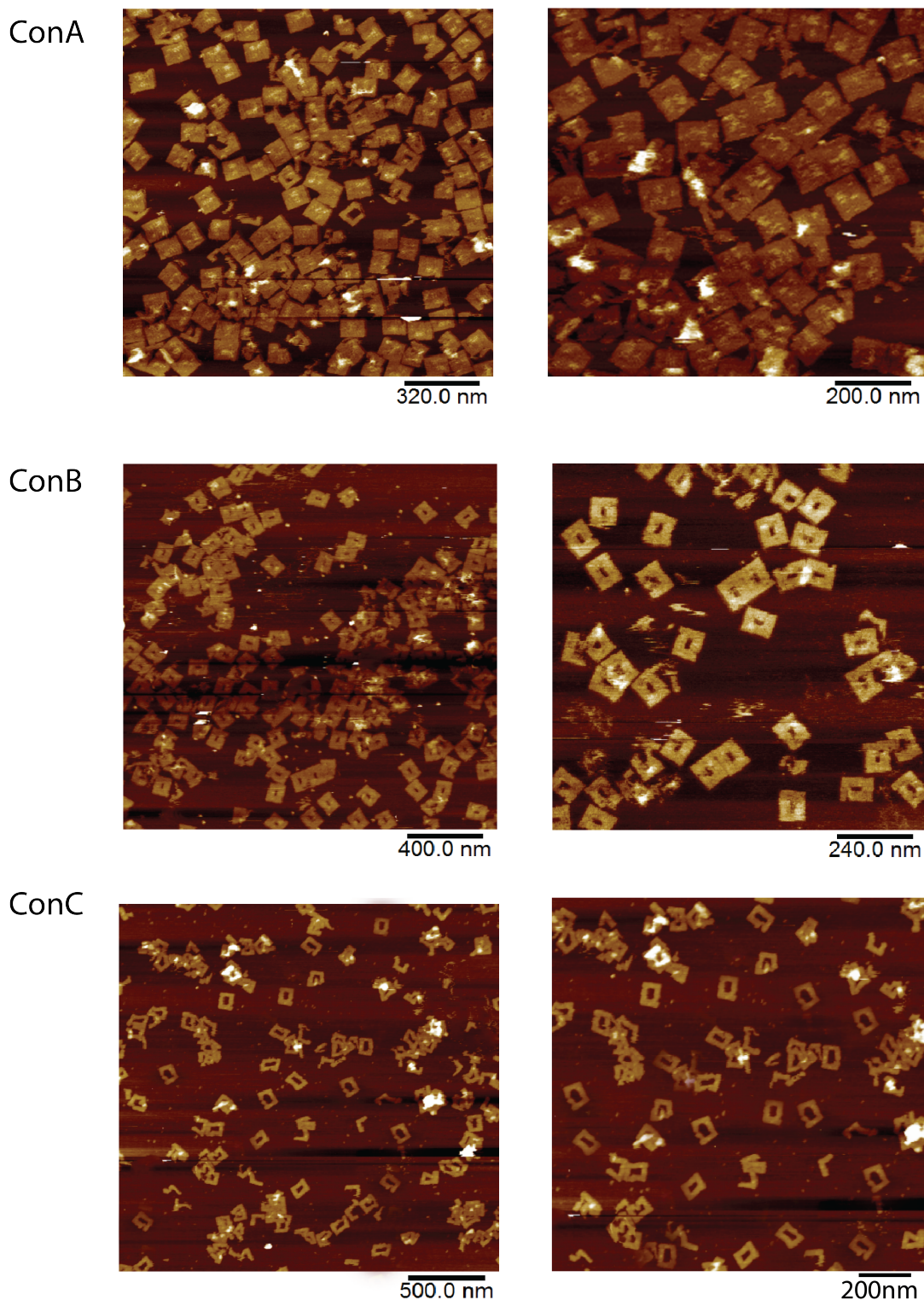


Figure D.21: AFM images of concentric squares ConA,B and C indicating effective folding. The folding efficiency of ConA sample and ConB with the smaller void was estimated to be $>80\%$, whereas the number of intact ConC DNA structure was $\sim 65\%$, the lower efficiency of ConC samples could be due to the mechanical fragmentation with the AFM tip.

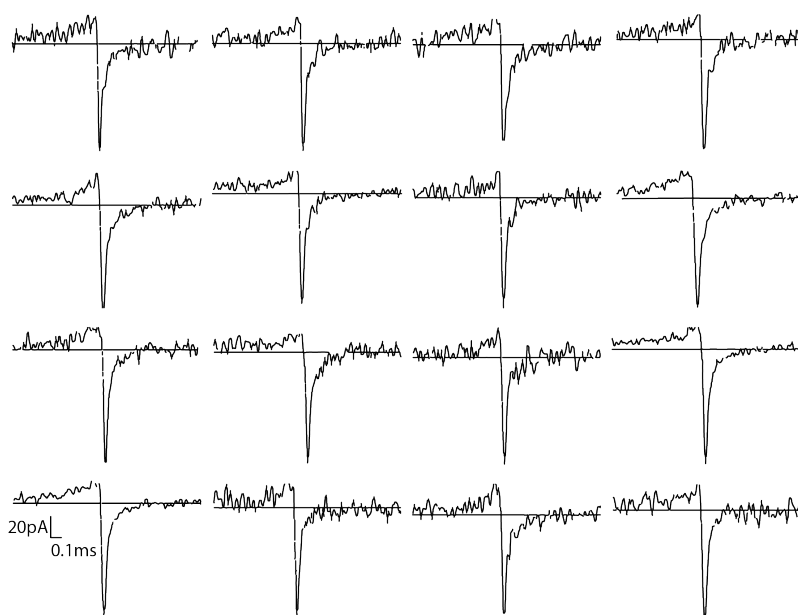


Figure D.22: Array of events representing the single peak ion current signatures as observed for concentric square ConA samples

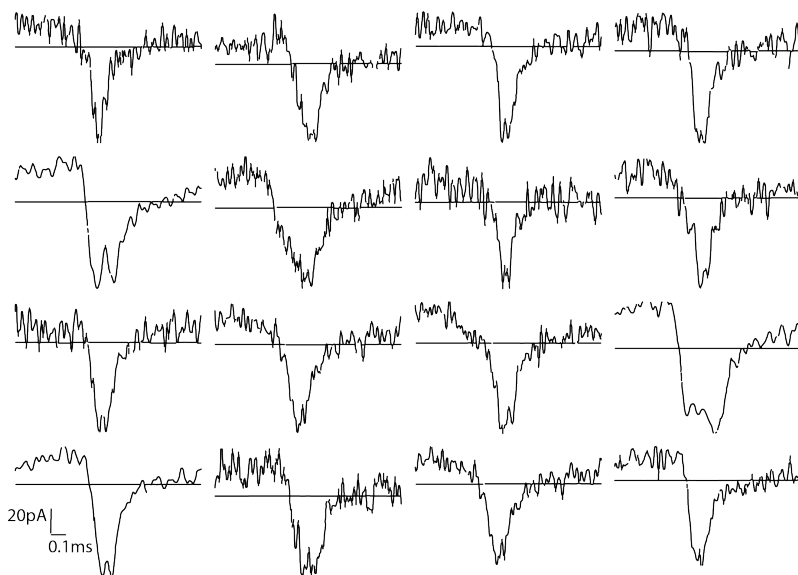


Figure D.23: Array of events representing the single peak ion current signatures as observed for concentric square ConB samples.

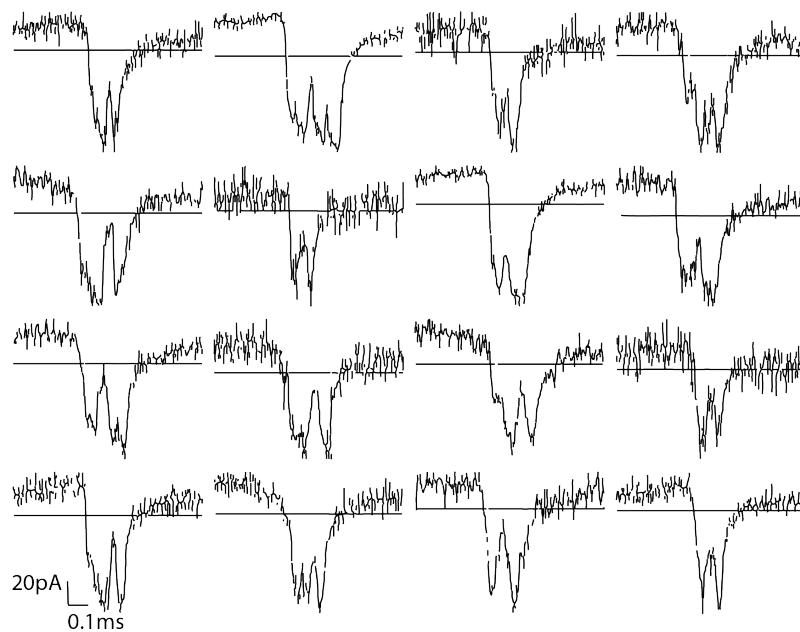


Figure D.24: Array of events representing the single peak ion current signatures as observed for concentric square ConC samples.

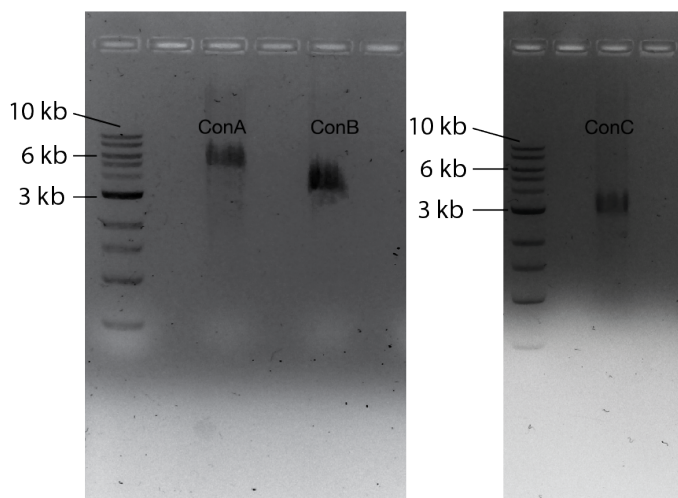


Figure D.25: Agarose gel electrophoresis of concentric squares ConA,B and C with one visible band indicating effective folding. The electrophoresis was conducted in 0.5% agarose for 2 hours at 4°C, the electrophoresis buffer was 1 X TAE with 11 mM MgAc.

Table 7: Number of double peaks (dp) observed for ConA, ConB and ConC for two nanopipette translocations conducted on different days.

Pipette	ConA		ConB		ConC	
	dp	total	dp	total	dp	total
1	13	90	107	112	117	138
2	7	85	68	125	102	87

E Appendix for chapter 9

Herein, ion current event data calculated for the samples used in chapter 9 in addition to those provided in the main content are presented in various figures and tables. The graphs and tables are grouped into different sections for ease. Section 1 consists of the various SPR data for the three aptamers tested. Section 2 and 3 contains all the data for carrier 1 and carrier 2 respectively.

Section 1 - SPR analysis

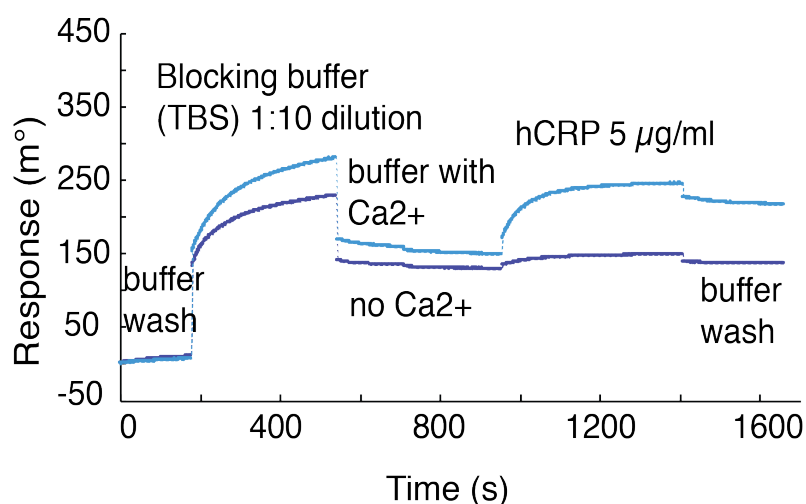


Figure E.26: SPR response data plotted against time shows an increased binding of CRP in the presence of calcium against aptamer 1.

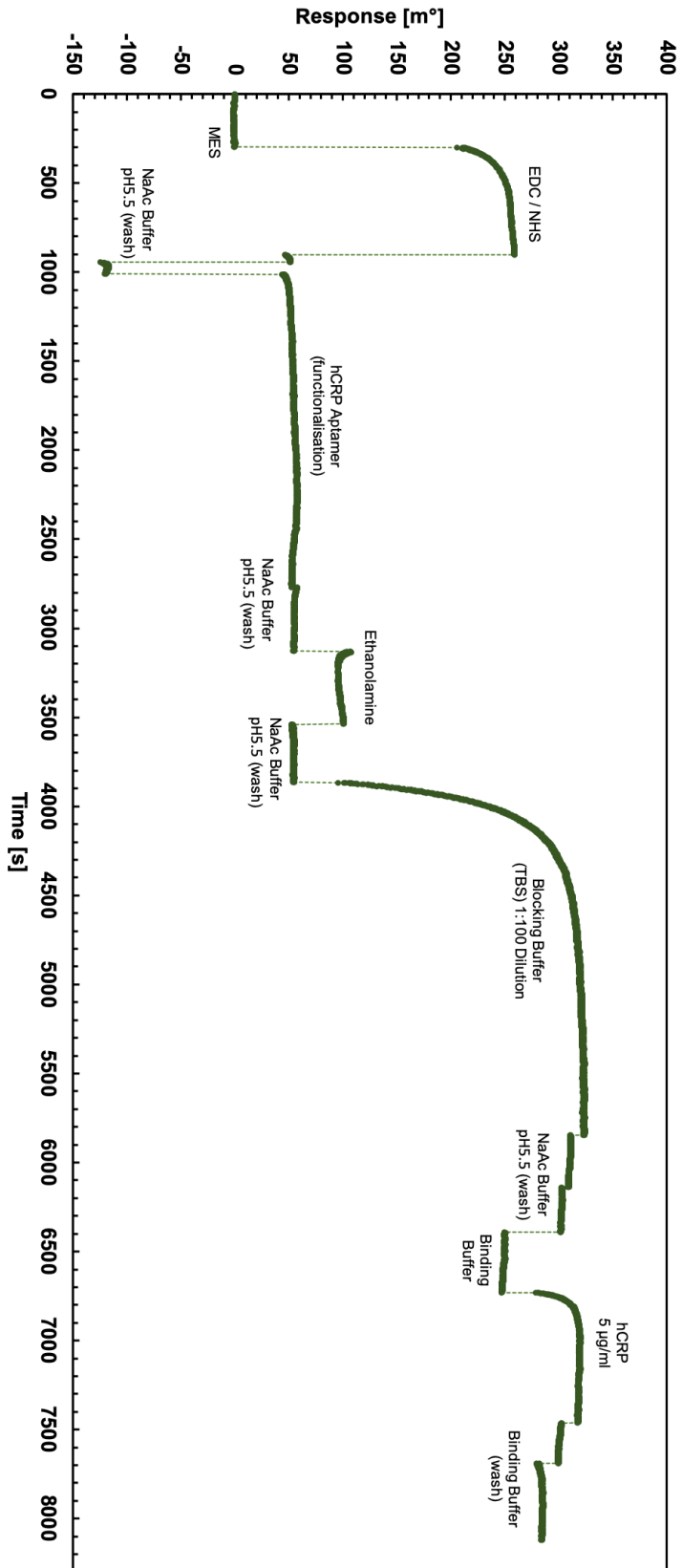


Figure E.27: SPR trace for aptamer I functionalization and subsequent CRP binding.

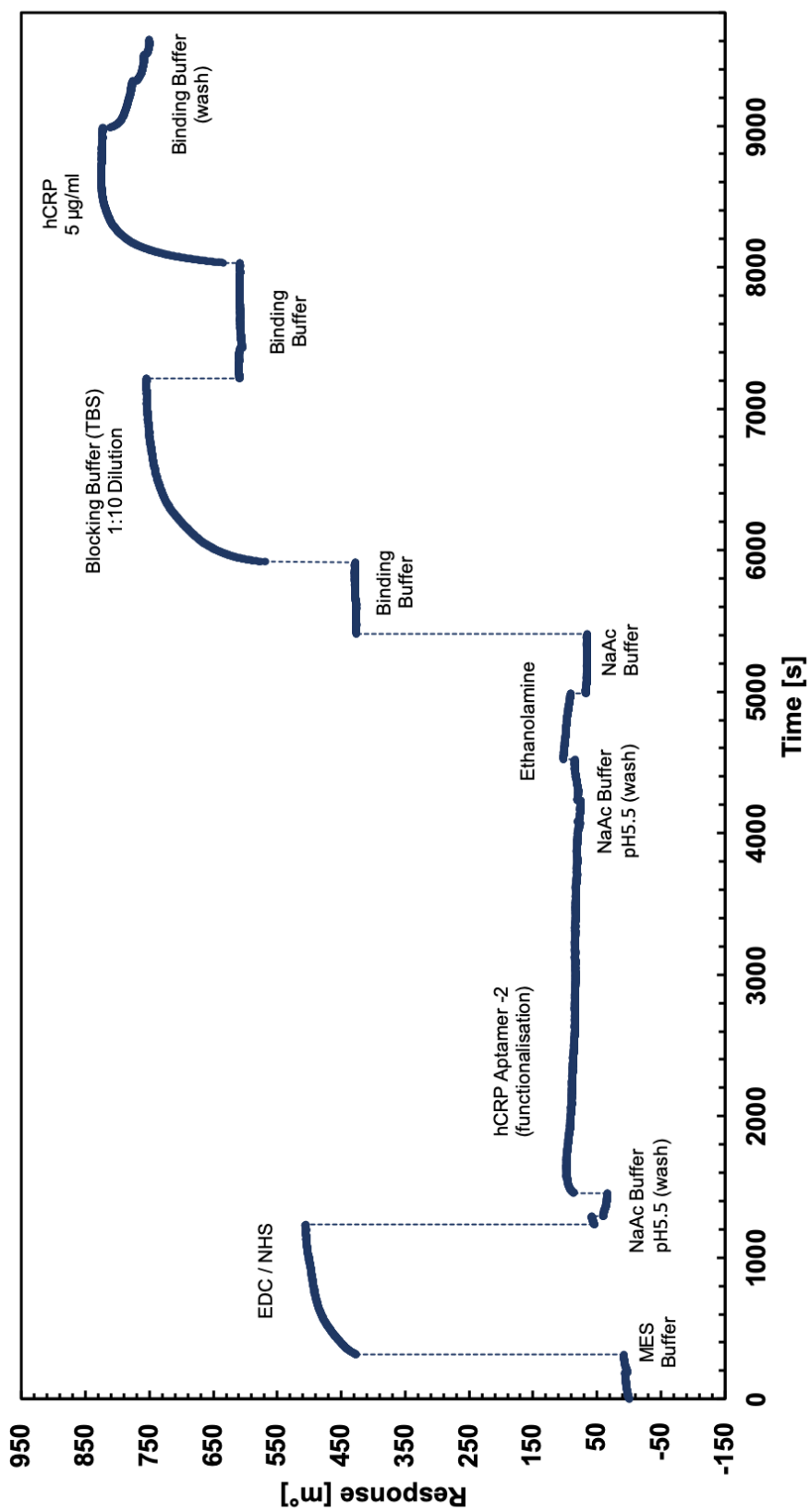


Figure E.28: SPR trace for aptamer 2 functionalization and subsequent CRP binding.

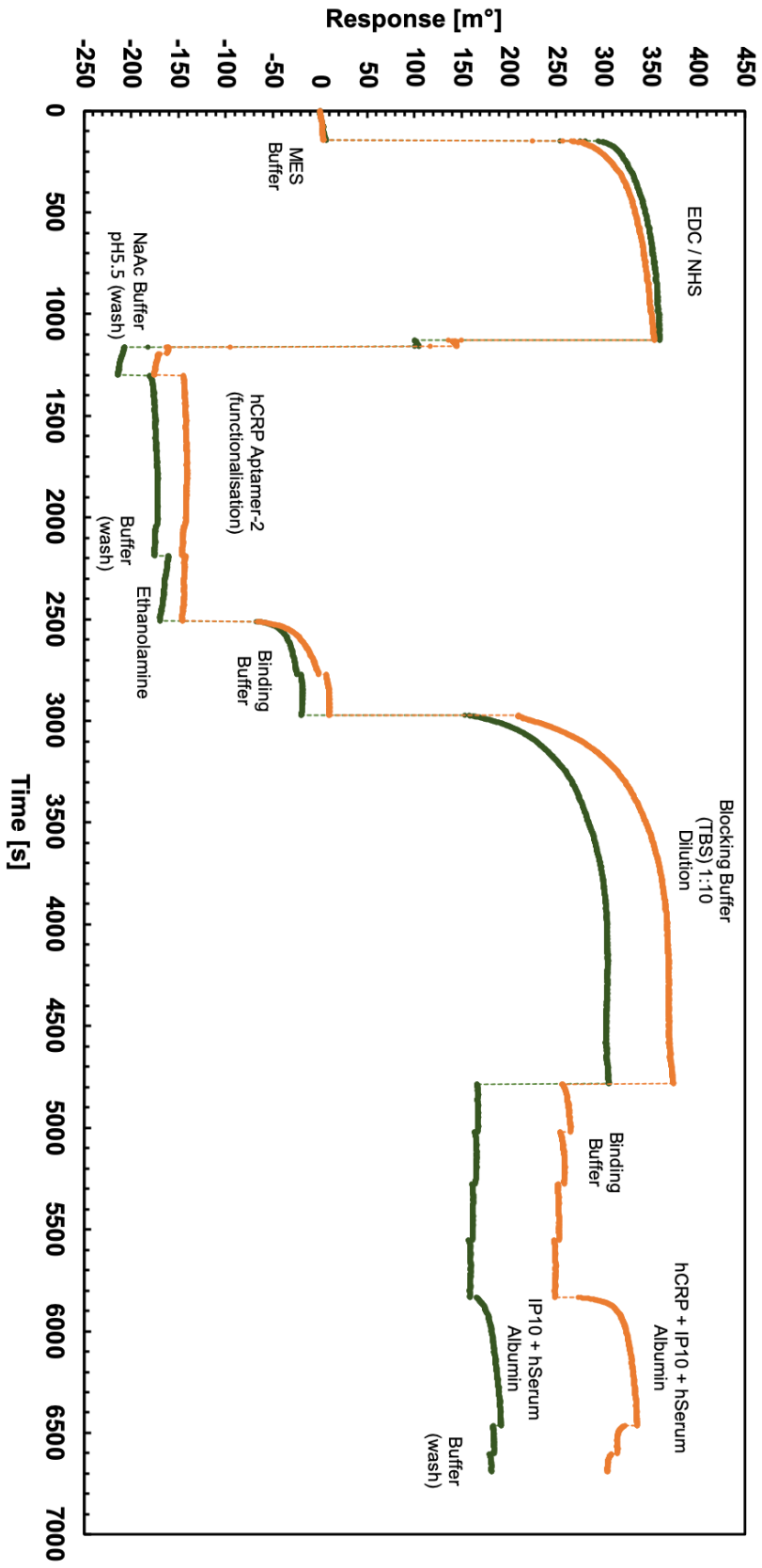


Figure E.29: SPR trace for aptamer functionalization and subsequent CRP binding in one channel and control in another channel.

Section 2 - Data for carrier 1

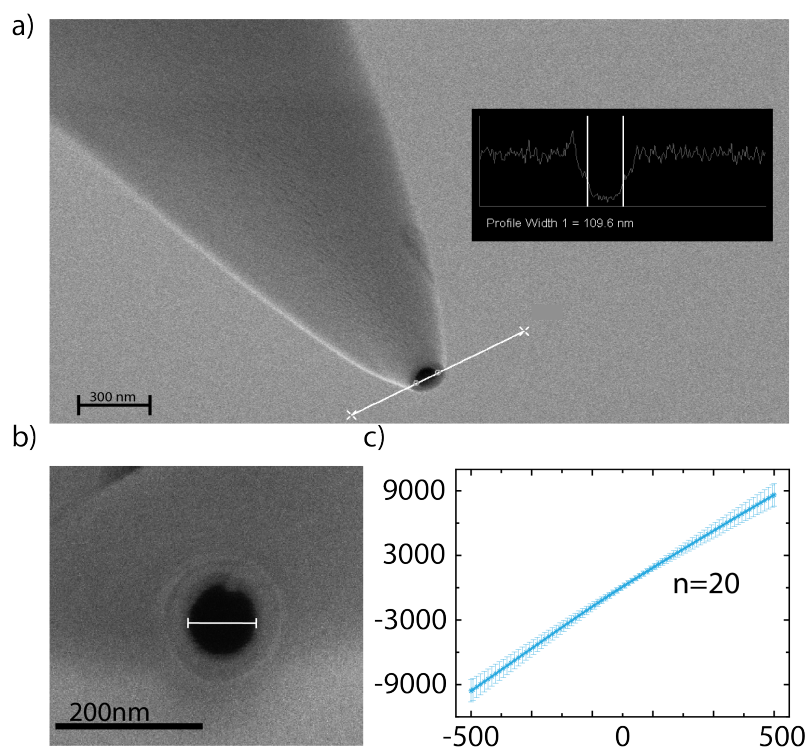


Figure E.30: SEM image of a) nanopipette tip with a b) pore diameter of approximately 100 nm. c) Representative Current - Voltage curves for 20 nanopipettes used in this study, the ion current was recorded in 0.1 M KCl.

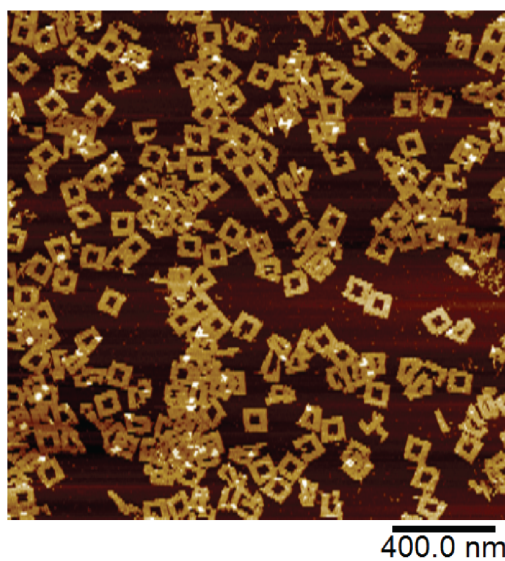


Figure E.31: AFM image of successfully folded DNA origami carrier.

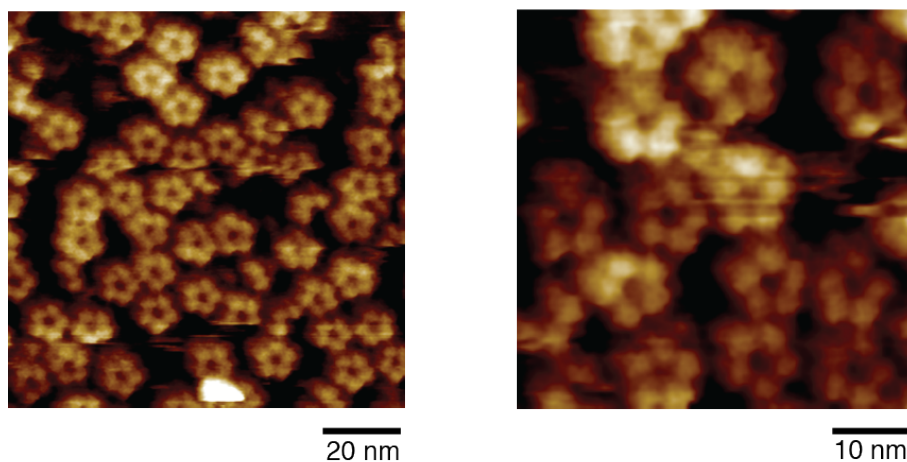


Figure E.32: AFM images of CRP deposited on mica.

Table 8: Normalised single peak counts (single peaks/(single peaks+double peaks)) for a 2 minute ion current trace for 3 different nanopipettes. The carrier concentration was 9 nM. This table is compiled from the data provided in table 9.

CRP nM	Carrier ratio			average	std
	sp/(sp+dp)				
	pipette1	pipette2	pipette3		
3	0.25	0.2	0.19	0.21	0.032
6	0.29	0.34	0.26	0.29	0.040
9	0.47	0.42	0.39	0.42	0.040
18	0.57	0.57	0.48	0.54	0.051
27	0.71	0.67	0.67	0.68	0.023
36	0.83	0.77	0.89	0.83	0.060
45	0.94	0.81	0.89	0.88	0.065
90	0.92	0.89	0.91	0.90	0.015

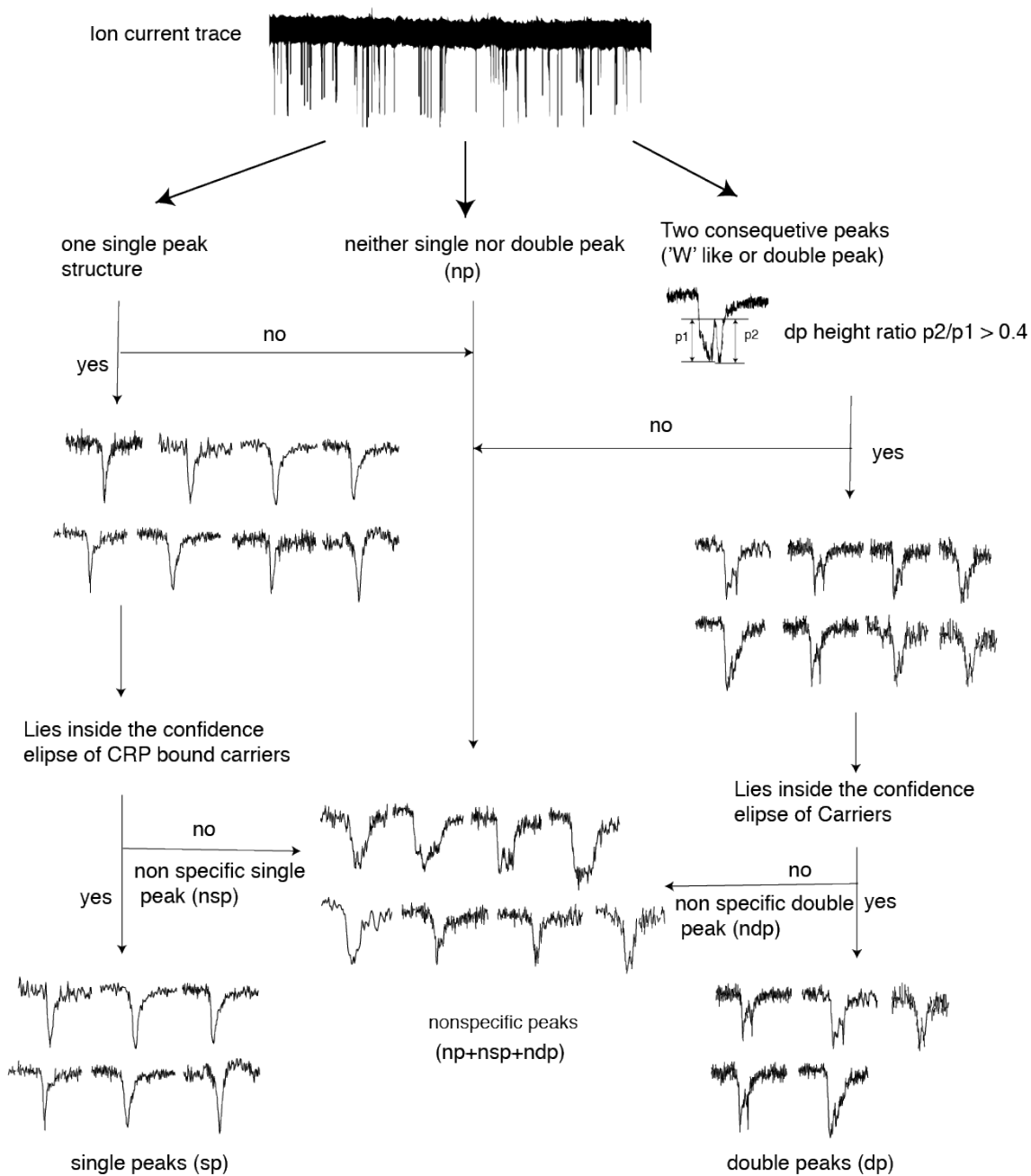


Figure E.33: A step wise schematic of classifying single peaks, double peaks and unclassified peaks using dwell time, peak amplitude and ion current structure.

Carrier 1

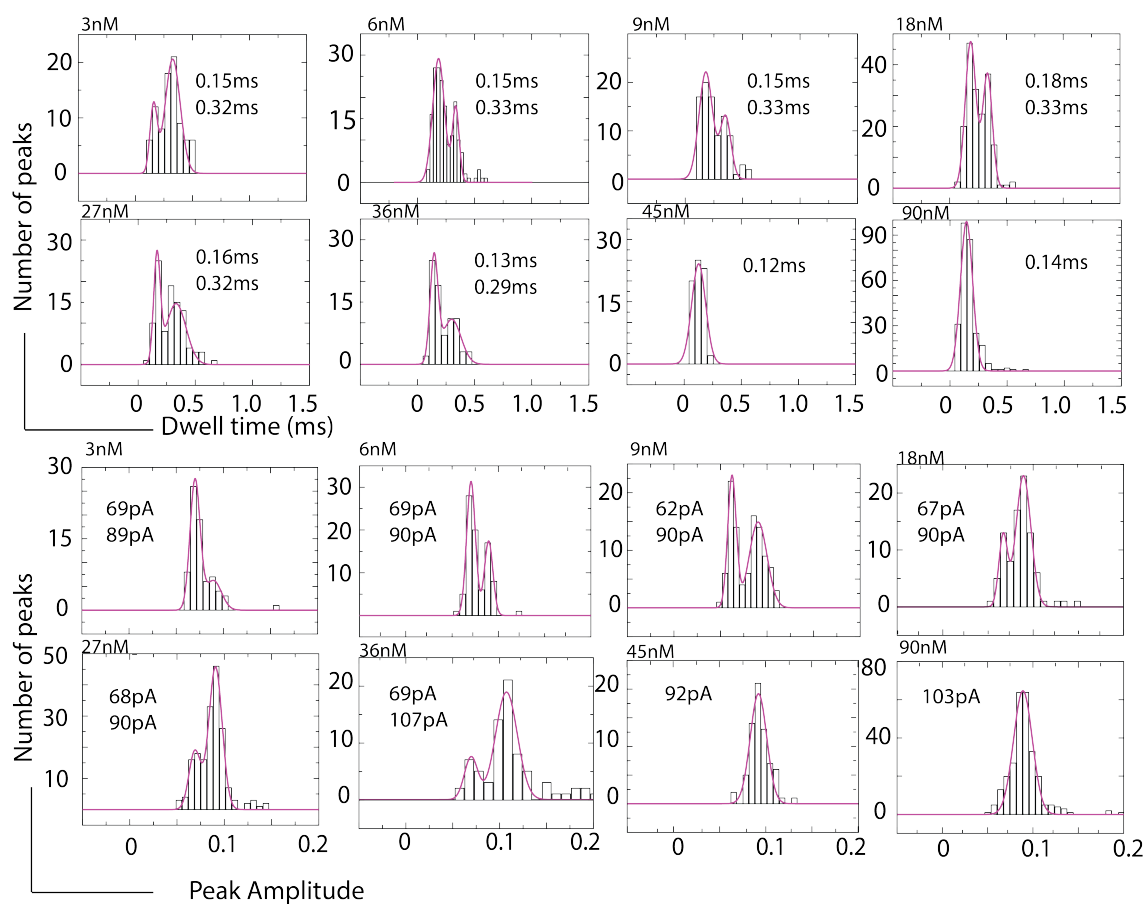


Figure E.34: Individual histograms of dwell time and peak amplitude observed for the carrier samples with aptamer 1 (carrier 1) incubated with varying concentration of CRP. The histograms are fitted with gaussian curves.

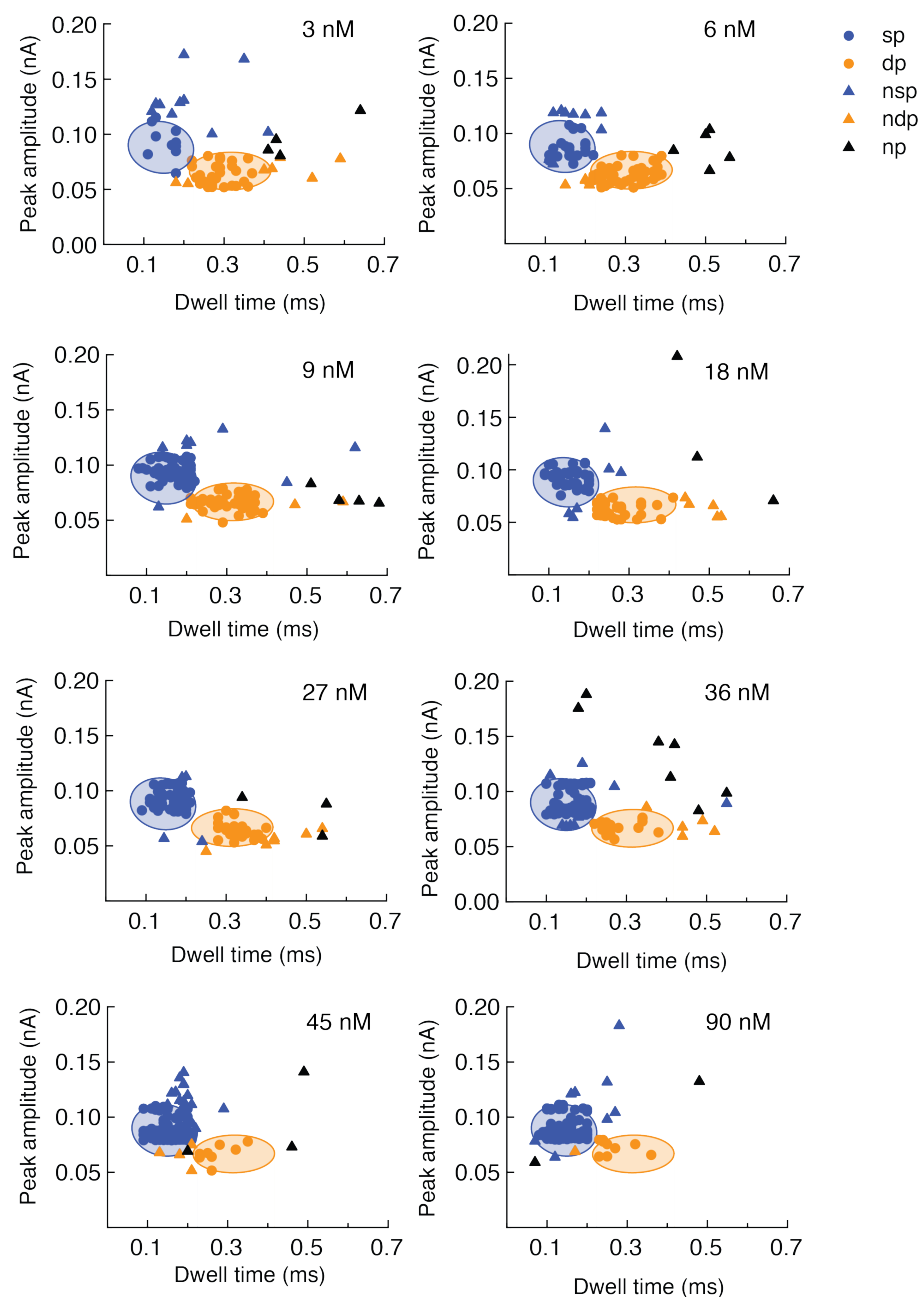


Figure E.35: Scatter plots of ion current events (peak amplitude versus dwell time) for carriers made with aptamer 1 incubated with different CRP concentration (3 to 90 nM). The individual observed ion peaks are classified as described in the main text and colour coded (double peaks orange and single peaks blue, triangles represent unclassified events which are not considered for analysis). The orange and blue ellipses represent the 95% confidence ellipses for double and single peaks and are taken from the analysis described in figure 9.7.

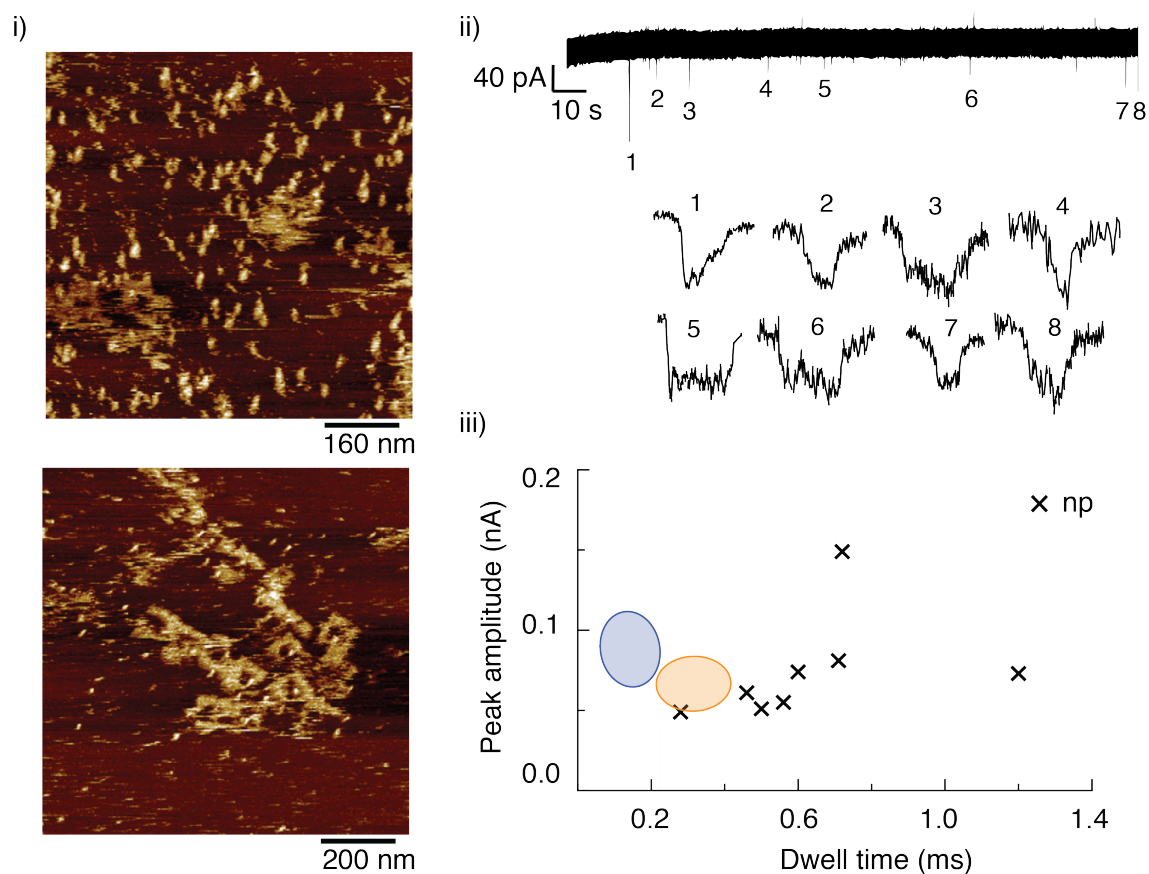


Figure E.36: To eliminate doubt of false positives due to broken or disintegrated carriers, the DNA nanostructures were degraded by incubation in 10 mM CaCl_2 at room temperature for 30 minutes. The presence of Ca disintegrates the DNA origami structure by replacing the Mg ions holding the origami together. (i) AFM micrographs showing degraded carriers. (ii) Ion current trace for the degraded samples recorded for about 2 minutes resulted in very few events. A range of different peak shapes were observed as shown. (iii). Scatter plot of peak amplitude versus dwell time, with the 95% confidence ellipses overlaid. The observed peaks fell outside the overlaid ellipses.

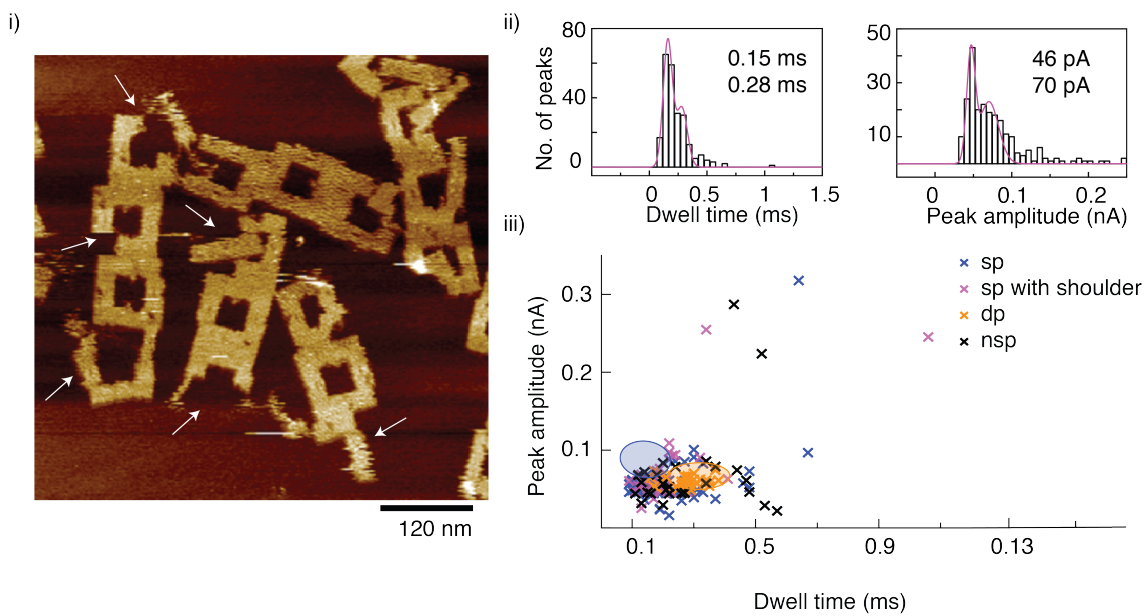


Figure E.37: To further confirm that there were no false positives resulting from broken carriers in the presence of calcium, the DNA nanostructures were incubated in the binding buffer with 2 mM CaCl_2 at room temperature for longer hours (4 hours). It was seen that long exposure to Ca^{2+} affects the stability of the DNA origami structure but the translocation experiment allows to exclude them from being counted as false positives. (i) AFM micrograph showing a mixture of intact and degraded carriers (indicated by white arrows). (ii) Peak amplitude and dwell time histograms of the translocation ion current peaks. A range of different peak shapes were observed, including ‘w’-like peaks, narrow single peaks and single peaks with shoulders. (iii). Scatter plot of peak amplitude versus dwell time, with the 95% confidence ellipses overlaid. Only around 10% of peaks which resemble single peaks also fall into the single peak 95% confidence ellipse.

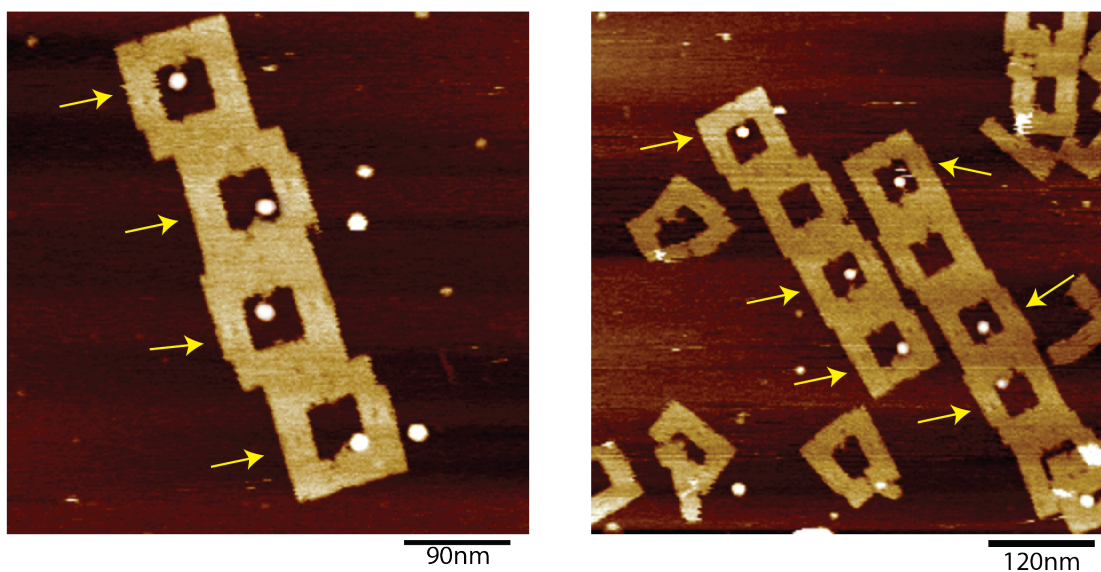


Figure E.38: AFM images of carrier incubated with CRP at ~ 36 nM, the binding efficiency calculated from the AFM images is $>60\%$ for a 1: 4 ratio.

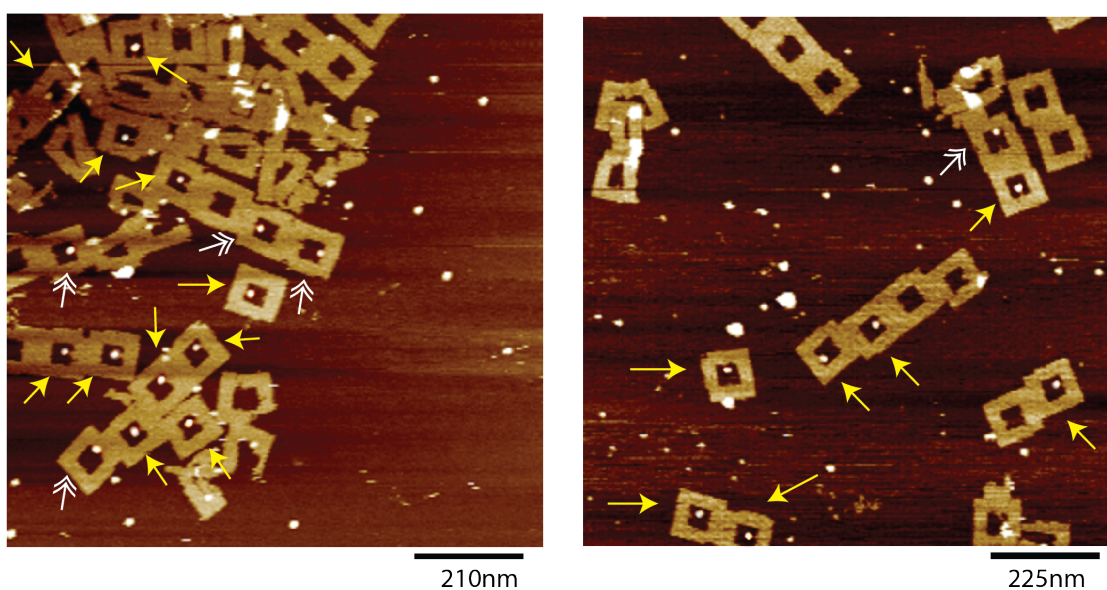


Figure E.39: AFM images of carrier with specific aptamer opposite to the polarity marker and nonspecific aptamer adjacent to the polarity marker incubated with CRP at ~ 9 nM. The yellow single arrow points out the CRP bound to the specific aptamer in the carrier (47–55%) and the white colored double arrow marks the few non specific binding (7–20%).

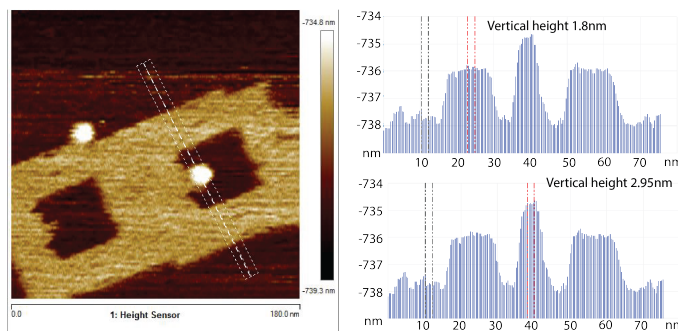


Figure E.40: AFM image shows an empty carrier and a carrier bound to CRP, step analysis using the nanoscope software as shown in the adjacent graphs shows the DNA carrier height from the mica surface to be 1.8 nm and height of the bound CRP to be 2.9 nm, i.e., ~ 1 nm higher than the carrier.

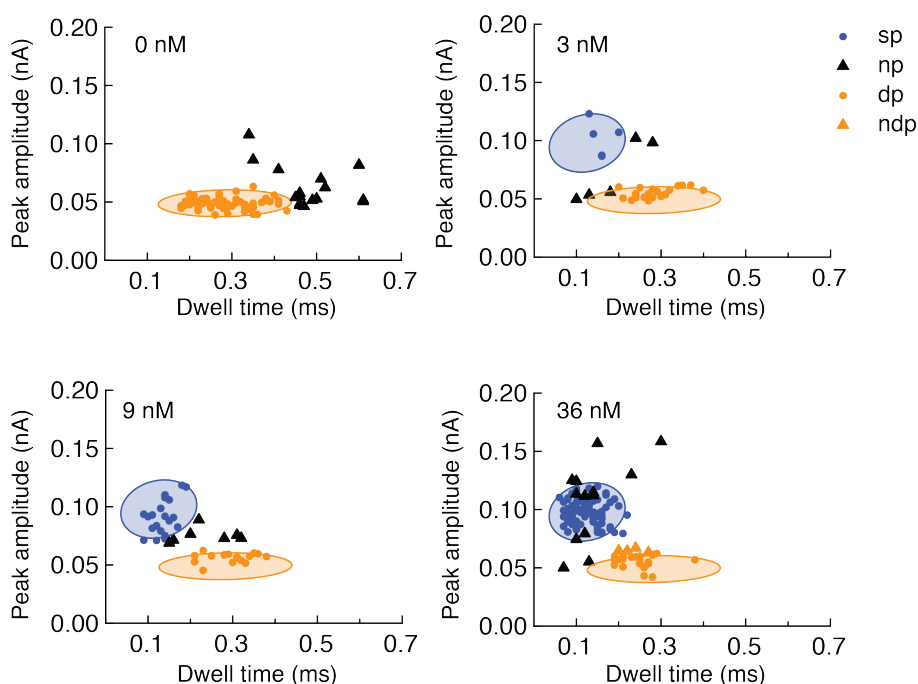


Figure E.41: Scatter plot of peak amplitude versus dwell time for carriers (9 nM) subjected to four different concentrations of CRP (0 nM, 3 nM, 9 nM and 36 nM) in plasma. For 0 nM, no single peaks were observed, and the cluster of double peaks was used to define the 95% confidence interval for the unoccupied carrier. Similarly, the 95% confidence ellipse for the single peaks was generated from the data of the highest CRP concentration.

Table 9: Number of single peaks, double peaks and unclassified events observed for carriers incubated with different concentrations of CRP for 3 different nanopipettes measured on different days. sp–single peaks, dp–double peaks, un–unclassified peaks

CRP	pipette1				pipette2				pipette3			
nM	sp	dp	un	total	sp	dp	un	total	sp	dp	un	total
3	10	29	21	60	9	36	11	56	9	38	13	60
6	19	46	18	83	18	34	30	82	12	34	16	62
9	46	52	16	114	19	26	12	57	31	49	27	107
18	41	31	14	86	19	14	17	50	32	35	17	84
27	58	24	13	95	36	18	15	69	39	19	12	70
36	84	17	17	118	67	20	36	123	58	7	24	89
45	132	8	22	162	59	14	9	82	72	9	16	97
90	105	9	11	125	48	6	13	67	64	6	11	81

Table 10: Normalised single peak counts (single peaks/(single peaks+double peaks)) for 3 different ion current traces. The carrier concentration was 9 nM. This table is compiled from the data provided in table 11.

CRP	trace1	trace2	trace3	average	std
3nM	0.14	0.13	0.18	0.15	0.02
9nM	0.61	0.64	0.55	0.6	0.04
36nM	0.95	0.84	0.77	0.85	0.09

Table 11: Number of single, double and unclassified events observed for CRP spiked plasma samples for three ion current traces of ~ 2 minutes each. sp–single peaks, dp–double peaks, un–unclassified peaks, total–total number of events.

CRP(nM)	trace 1				trace 2				trace 3			
	sp	dp	total	un	sp	dp	total	un	sp	dp	total	un
3nM	5	22	32	5	4	27	41	5	4	23	30	3
9nM	20	16	43	7	46	25	87	16	24	15	52	13
36nM	90	26	128	12	117	21	142	4	61	3	69	5

Section 3 - Data for carrier 2

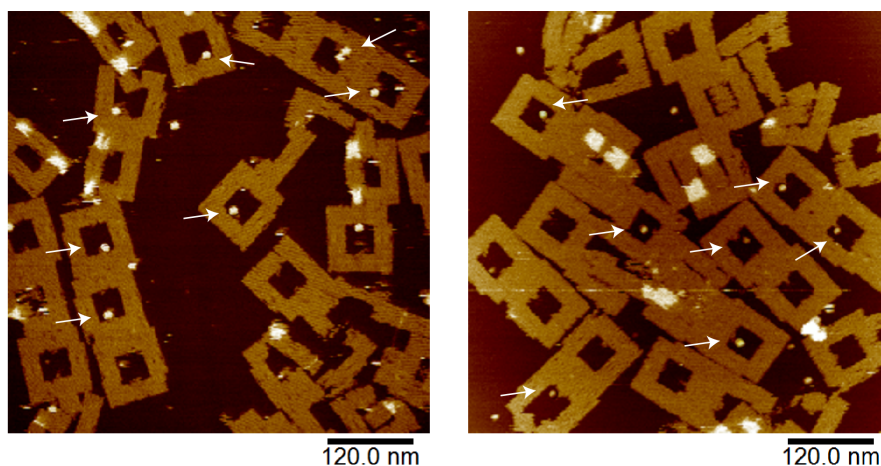


Figure E.42: AFM images of carrier 2 incubated with CRP at 6 nM (1: 1 ratio), the specific aptamer is placed opposite to the polarity marker. The arrows indicate CRP carriers, resulting in about $\sim 40\%$ occupied frames and $< 10\%$ non specific interaction with the nonspecific aptamer adjacent to the polarity marker.

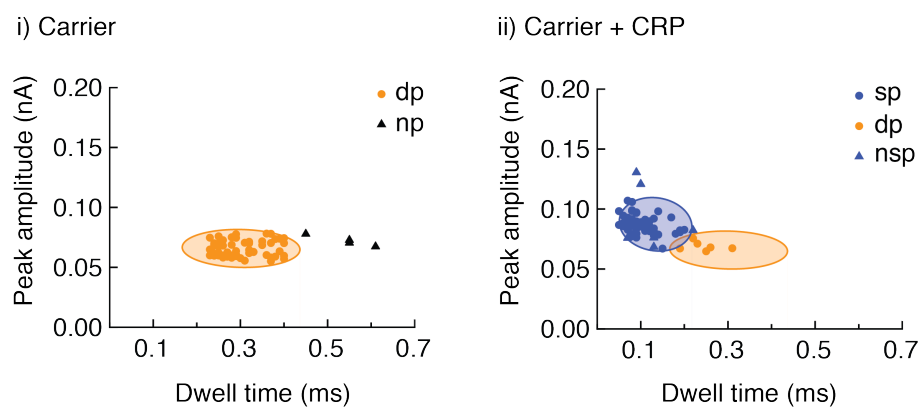


Figure E.43: Scatter plot of peaks for unoccupied carriers (left) and carriers incubated with a $17\times$ excess of CRP (100 nM). Ion current events which are double peaks are plotted on orange, and the ones that fall inside the 95% confidence ellipse are plotted as circles, the others as triangles. Only events that fall within the 95% confidence ellipse are considered double peaks. The same analyses were carried out for single peaks (plotted in blue). Ion current events which resembled neither a double nor a single peak are shown as black triangles and are excluded from the analysis.

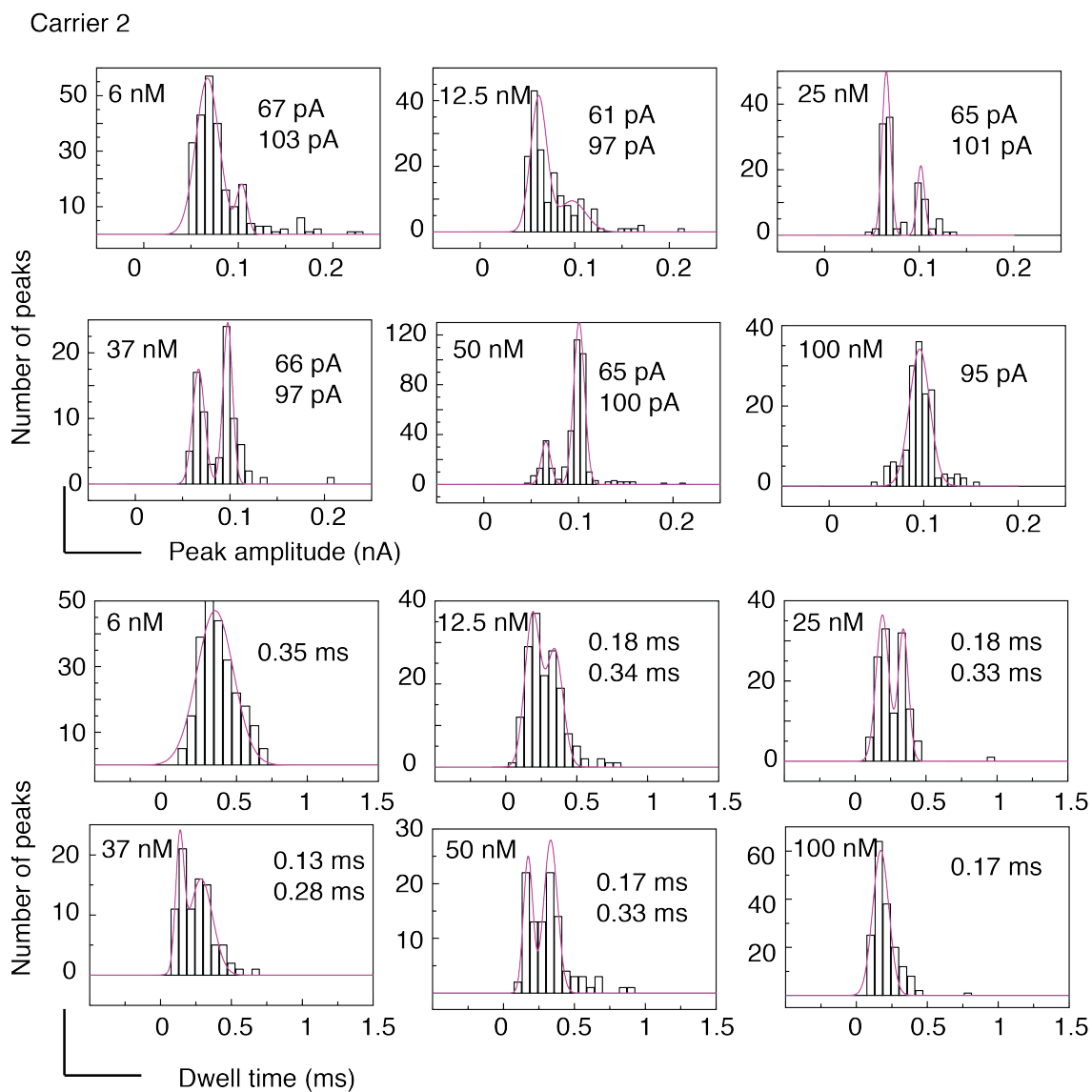


Figure E.44: Individual histograms of dwell time and peak amplitude observed for the carrier samples with aptamer 2 (carrier 2) incubated with varying concentration of CRP. The histograms are fitted with gaussian curves.

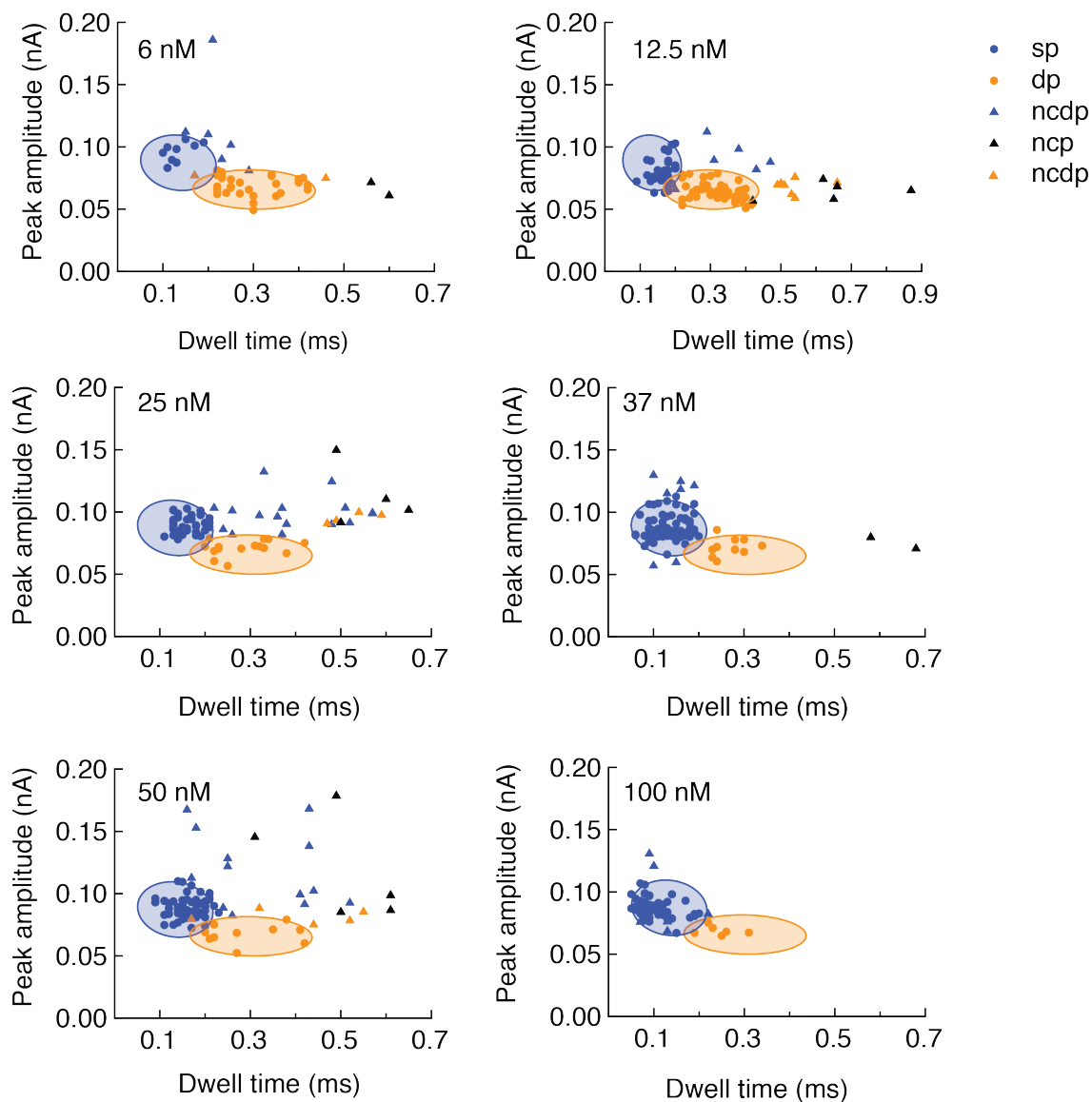


Figure E.45: Scatter plot of ion current events plotted with their peak amplitude against dwell time for carrier 2 incubated with different CRP concentration(6 to 100 nM), the ion peak signatures of double peak and single peaks observed for the samples are color coded orange and blue respectively and indicated by a 95% confidence ellipse obtained from figure E.43, unclassified events are represented as triangles.

Table 12: Normalised single peak counts (single peaks/(single peaks+double peaks)) for 2-minute ion current traces for 3 different nanopipettes. The carrier concentration was 6 nM. This table is compiled from the data provided in table 13.

CRP nM	Carrier ratio sp/(sp+dp)			average	std
	pipette1	pipette2	pipette3		
6	0.28	0.38	0.28	0.31	0.06
12.5	0.44	0.36	0.45	0.42	0.05
25	0.62	0.60	0.67	0.63	0.03
37	0.77	0.75	0.86	0.79	0.06
50	0.88	0.82	0.94	0.88	0.06
100	0.95	0.96	0.93	0.95	0.01

Table 13: Number of single peaks, double peaks and unclassified events observed for carriers incubated with different concentrations of CRP for 3 different nanopipettes measured on different days. sp–single peaks, dp–double peaks, un–unclassified peaks.

CRP nM	pipette1				pipette2				pipette3			
	sp	dp	un	total	sp	dp	un	total	sp	dp	un	total
6	8	31	12	51	12	37	9	58	8	33	13	54
12.5	35	48	19	102	17	31	17	65	24	30	11	65
25	40	15	25	80	30	13	28	71	35	12	11	58
37	78	11	10	99	38	9	22	69	55	9	12	76
50	58	10	23	91	174	22	39	235	77	8	22	107
100	58	6	6	70	53	4	12	57	111	11	22	144

F Appendix for chapter 10

Table 14: Number of single peaks (sp), double peaks (dp) and triple peaks (tp) observed for dimers formed from ConA and ConC for two nanopipette translocations conducted on different days.

Pipette	ConA and ConC dimer			
	sp	dp	tp	total
1	25	10	15	50
2	18	12	14	44

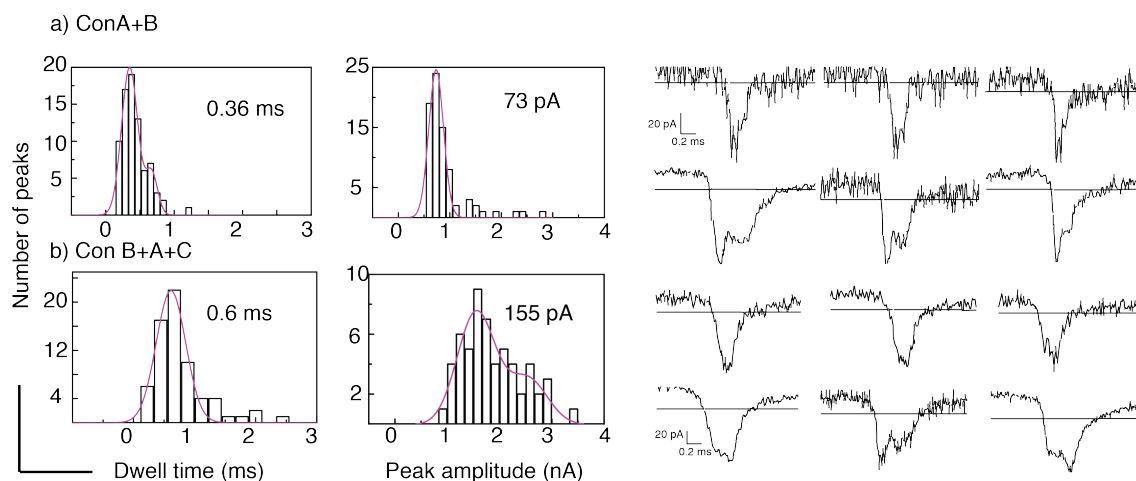


Figure F.46: Figure shows the individual histograms of dwell time (0.36 ms and 0.6 ms) and peak amplitude (73 pA and 155 pA) for a) ConAB dimer and b) ConABC trimer samples respectively. The Figure also includes the observed ion current peak structures for both the samples. The histograms are fitted with gaussian curve.

Bibliography

- [1] W. E. Moerner, “New directions in single-molecule imaging and analysis.” *Proceedings of the National Academy of Sciences of the United States of America*, vol. 104, no. 31, pp. 12 596–602, 2007.
- [2] H. Miller, Z. Zhou, J. Shepherd, and A. J. M. Wollman, “Single-molecule techniques in biophysics : a review of the progress in methods and applications,” *Rep. Prog. Phys*, vol. 81, no. 024601, 2018.
- [3] P. Actis, A. C. Mak, and N. Pourmand, “Functionalized nanopipettes: Toward label-free, single cell biosensors,” *Bioanalytical Reviews*, vol. 1, no. 2, pp. 177–185, 2010.
- [4] L.-Q. Gu and J. W. Shim, “Single molecule sensing by nanopores and nanopore devices,” *The Analyst*, vol. 135, no. 3, pp. 441–451, 2010.
- [5] E. M. Puchner, B. Huang, and H. E. Gaub, “Single molecule techniques - applications in biology,” *FEBS Letters*, vol. 588, no. 3519, 2014.
- [6] N. Bhalla, P. Jolly, N. Formisano, and P. Estrela, “Introduction to biosensors,” *Essays in Biochemistry*, vol. 60, pp. 1–8, 2016.
- [7] C. Karunakaran, K. Bhargava, and R. Benjamin, “Introduction to Biosensors,” in *Biosensors and Bioelectronics*. Elsevier, 2015, ch. 1, pp. 1–68.
- [8] M. C. Leake, “Analytical tools for single-molecule fluorescence imaging in cellulose,” *Physical chemistry chemical physics*, vol. 16, pp. 12 635–12 647, 2014.

- [9] T. Cordes, W. Moerner, M. Orrit, S. Sekatskii, S. Faez, P. Borri, H. P. Goswami, A. Clark, P. El-khoury, S. Mayr, J. Mika, G. Lyu, D. Cross, F. Balzarotti, W. Langbein, V. Sandoghdar, J. Michaelis, A. Chowdhury, A. J. Meixner, N. V. Hulst, B. Lounis, F. Stefani, F. Cichos, M. Dahan, L. Novotny, M. Leake, and H. Yang, "Plasmonics , Tracking and Manipulating , and Living Cells : general discussion," *Faraday Discussions*, vol. 184, pp. 451–473, 2015.
- [10] O. L. J. Harriman and M. C. Leake, "Single molecule experimentation in biological physics : exploring the living component of soft condensed matter one molecule at a time," *Journal of Physics: Condensed Matter*, vol. 23, p. 503101, 2011.
- [11] F. Ritort, "Single-molecule experiments in biological physics : methods and applications," *Journal of Physics: Condensed Matter*, vol. 18, pp. R531–83, 2006.
- [12] T. Lenn and M. C. Leake, "Experimental approaches for addressing fundamental biological questions in living , functioning cells with single molecule precision," *Open Biology*, vol. 2, no. 120090, 2012.
- [13] M. C. Leake, "Shining the spotlight on functional molecular complexes: the new science of single-molecule cell biology," *Communicative and Integrative Biology*, vol. 3, pp. 415–8, 2010.
- [14] M. C. Leake, "The physics of life : one molecule at a time," *Philosophical transactions of the Royal Society*, vol. 368, p. 20120248, 2013.
- [15] W. H. Coulter, "Means for counting particles suspended in a fluid," 1953.
- [16] H. Bayley and C. R. Martin, "Resistive-Pulse Sensing From Microbes to Molecules," *Chemical Reviews*, vol. 100, no. 7, pp. 2575–2594, 2000.
- [17] D. Fologea, J. Uplinger, B. Thomas, D. S. McNabb, and J. Li, "Slowing DNA Translocation in a solid state Nanopore," *Nano Letters*, vol. 5, no. 9, pp. 1734–1737, 2005.

- [18] S. W. Kowalczyk, D. B. Wells, A. Aksimentiev, and C. Dekker, “Slowing down DNA Translocation through a Nanopore in Lithium Chloride,” *Nano Letters*, vol. 12, pp. 1038–1044, 2012.
- [19] R. L. Fraccari, M. Carminati, G. Piantanida, T. Leontidou, and T. Albrecht, “High-bandwidth detection of short DNA in nanopipettes,” *Faraday Discussions*, vol. 193, pp. 459–470, 2016.
- [20] S. Sekar, D. J. Niedzwiecki, C.-C. Chien, P. Ong, D. A. Fleischer, J. Lin, J. K. Rosenstein, M. Drndic, and K. L. Shepard, “Measurement of DNA translocation dynamics in a solid state nanopore at 100ns temporal resolution,” *Nano Letters*, vol. 16, no. 7, pp. 4483–4489, 2017.
- [21] F. Sawafta, B. Clancy, A. T. Carlsen, and A. R. Hall, “Solid-state nanopores optimized for optical detection,” *Nanoscale*, vol. 6, pp. 6991–6996, 2014.
- [22] A. Singer, M. Wanunu, W. Morrison, H. Kuhn, M. Frank-kamenetskii, and A. Meller, “Nanopore Based Sequence Specific Detection of Duplex DNA for Genomic Profiling,” *Nano Letters*, vol. 10, pp. 738–742, 2010.
- [23] N. A. W. Bell and U. F. Keyser, “Digitally encoded DNA nanostructures for multiplexed, single-molecule protein sensing with nanopores,” *Nature nanotechnology*, vol. 11, no. 7, pp. 1–28, 2016.
- [24] J. Kong, N. A. W. Bell, and U. F. Keyser, “Quantifying Nanomolar Protein Concentrations Using Designed DNA Carriers and Solid-State Nanopores,” *Nano Letters*, vol. 16, pp. 3557–3562, 2016.
- [25] J. Y. Sze, A. P. Ivanov, A. E. Cass, and J. B. Edel, “Single molecule multiplexed nanopore protein screening in human serum using aptamer modified DNA carriers,” *Nature Communications*, vol. 8, pp. 1–10, 2017.

- [26] A. Yue, Y. Loh, C. H. Burgess, D. A. Tanase, G. Ferrari, M. A. McLachlan, A. Edward, G. Cass, and T. Albrecht, "An Electric Single-Molecule Hybridisation Detector for short DNA Fragments," *Analytical Chemistry*, 2018.
- [27] S. Cai, J. Y. Y. Sze, A. P. Ivanov, and J. B. Edel, "Small molecule electro-optical binding assay using nanopores," *Nature Communications*, vol. 10, no. 1, p. 1797, 2019.
- [28] L. J. Steinbock, A. Lucas, O. Otto, and U. F. Keyser, "Voltage-driven transport of ions and DNA through nanocapillaries," *Electrophoresis*, vol. 33, no. 23, pp. 3480–3487, 2012.
- [29] K. Chen, N. A. W. Bell, J. Kong, Y. Tian, and U. F. Keyser, "Direction- and Salt-Dependent Ionic Current Signatures for DNA Sensing with Asymmetric Nanopores," *Biophysical journal*, vol. 112, no. 4, pp. 674–682, 2017.
- [30] M. V. D. Hout, V. Krudde, X. J. A. Janssen, and N. H. Dekker, "Distinguishable Populations Report on the Interactions of Single DNA Molecules with Solid-State Nanopores," *Biophysical journal*, vol. 99, no. 11, pp. 3840–3848, 2010.
- [31] A. R. Chandrasekaran, N. Anderson, M. Kizer, K. Halvorsen, and X. Wang, "Beyond the Fold: Emerging Biological Applications of DNA Origami," *ChemBioChem*, pp. 1081–1089, 2016.
- [32] V. Kumar, S. Palazzolo, S. Bayda, G. Corona, G. Toffoli, and F. Rizzolio, "DNA nanotechnology for cancer therapy," *Theranostics*, vol. 6, no. 5, pp. 710–725, 2016.
- [33] A. Oswald T, M. Colin M, and M. Maclyn, "Studies on the chemical nature of the substance inducing transformation of pneumococcal types," *Journal of experimental medicine*, vol. 79, no. 2, pp. 137–158, 1944.
- [34] J. Watson and F. Crick, "A structure for deoxyribose nucleic acid," *Journal of the American College of Cardiology*, vol. 42, no. 2, pp. 373–374, 1953.

- [35] J. E. Krebs, E. S. Goldstein, and S. T. Kilpatrick, *Lewins Genes XI*. Jones and Bartlett, 2014.
- [36] B. Alberts, A. Johnson, J. Lewis, M. Raff, K. Roberts, P. Walter, J. Wilson, and T. Hunt, *Molecular Biology of the Cell*. Garland Science, Taylor and Francis Group, 2008.
- [37] R. Franklin and R. Gosling, "Molecular configuration in sodium thymonucleate," *Nature*, vol. 171, no. 4356, pp. 740–741, 1953.
- [38] J. Watson and F. Crick, "Genetic implications of the structure of DNA," *Nature*, vol. 171, pp. 964–967, 1953.
- [39] S. Neidle, *Principles of Nucleic Acid Structure*. Elsevier, 2008.
- [40] W. Rychlik and R. E. Rhoads, "A computer program for choosing optimal oligonucleotides for filter hybridization, sequencing and in vitro amplification of DNA," *Nucleic Acids Research*, vol. 17, no. 21, pp. 8543–8551, 1989.
- [41] Z. J. Tan and S. J. Chen, "Nucleic acid helix stability: Effects of salt concentration, cation valence and size, and chain length," *Biophysical Journal*, vol. 90, no. 4, pp. 1175–1190, 2006.
- [42] H. Lodish, A. Berk, P. Matsudaira, C. A. Kaiser, M. Krieger, M. P. Scott, L. Zipursky, and J. Darnell, *Molecular Cell Biology*. W.H. Freeman & Co Ltd, 2012.
- [43] A. Travers and G. Muskhelishvili, "DNA structure and function," *The FEBS Journal*, vol. 282, pp. 2279–2295, 2015.
- [44] D. A. Jackson, R. H. Symonst, and P. Berg, "Biochemical Method for Inserting New Genetic Information into DNA of Simian Virus 40: Circular SV40 DNA Molecules Containing Lambda Phage Genes and the Galactose Operon of Escherichia coli," *Proceedings of the National Academy of Sciences, USA*, vol. 69, no. 10, pp. 2904–2909, 1972.

- [45] S. N. Cohen, A. C. Y. Chang, H. W. Boyert, and R. B. Hellingt, "Construction of Biologically Functional Bacterial Plasmids In Vitro," *Proceedings of the National Academy of Sciences, USA*, vol. 70, no. 11, pp. 3240–3244, 1973.
- [46] N. C. Seeman, "Nucleic Acid Junctions and Lattices," *Journal of theoretical Biology*, vol. 99, no. 2, pp. 237–247, 1982.
- [47] R. Holliday, "A mechanism for gene conversion in fungi," *Genetics Research*, vol. 5, no. 2, pp. 282–304, 1964.
- [48] T. R. Broker and I. R. Lehman, "Branched DNA Molecules : Intermediates T4 Recombination," *Journal of Molecular Biology*, vol. 60, pp. 131–149, 1971.
- [49] N. C. Seeman, "DNA in a material world," *Nature*, vol. 421, pp. 427–431, 2003.
- [50] Y. Zhang and N. C. Seeman, "Construction of a DNA-Truncated Octahedron," *Journal of American Chemical Society*, vol. 116, no. 12, pp. 1661–1669, 1994.
- [51] R. P. Goodman, I. A. T. Schaap, C. F. Tardin, C. M. Erben, R. M. Berry, C. F. Schmidt, and A. J. Turberfield, "Rapid Chiral Assembly of Rigid DNA Building Blocks for Molecular Nanofabrication," *Science*, vol. 310, pp. 1661–1666, 2005.
- [52] X. Wang and N. C. Seeman, "Assembly and Characterization of 8-Arm and 12-Arm DNA Branched Junctions," *Journal of American Chemical Society*, vol. 129, pp. 8169–8176, 2007.
- [53] J. Chen and N. C. Seeman, "Synthesis from DNA of a molecule with the connectivity of a cube," *Nature*, vol. 350, pp. 631–633, 1991.
- [54] W. M. Shih, J. D. Quispe, and G. F. Joyce, "A 1.7-kilobase single-stranded DNA that folds into a nanoscale octahedron," *Nature*, vol. 427, no. February, pp. 618–621, 2004.
- [55] D. Liu, M. Wang, Z. Deng, R. Walulu, and C. Mao, "Tensegrity : Construction of Rigid DNA Triangles with Flexible Four-Arm DNA Junctions," *Journal of American Chemical Society*, vol. 126, pp. 2324–2325, 2004.

- [56] J. Zheng, J. J. Birktoft, Y. Chen, T. Wang, R. Sha, P. E. Constantinou, S. L. Ginell, C. Mao, and N. C. Seeman, "From molecular to macroscopic via the rational design of a self-assembled 3D DNA crystal," *Nature*, vol. 461, no. 7260, pp. 74–77, 2009.
- [57] Y. Ke, J. Sharma, M. Liu, K. Jahn, Y. Liu, and H. Yan, "Scaffolded DNA Origami of a DNA Tetrahedron Molecular Container," *Nano Letters*, vol. 9, no. 6, pp. 2445–2447, 2009.
- [58] N. C. Seeman, "Nucleic Acid Nanostructures and Topology," *Angewandte Chemie - International Edition*, vol. 37, pp. 3220–3238, 1998.
- [59] T.-J. Fu and N. C. Seeman, "DNA Double-Crossover Molecules," *Biochemistry*, vol. 32, pp. 3211–3220, 1993.
- [60] P. Sa-ardyen, A. V. Vologodskii, and N. C. Seeman, "The Flexibility of DNA Double Crossover Molecules," *Biophysical Journal*, vol. 84, pp. 3829–3837, 2003.
- [61] C. Lin, Y. Liu, S. Rinker, and H. Yan, "DNA Tile Based Self-Assembly : Building Complex Nanoarchitectures," *ChemPhysChem*, vol. 7, pp. 1641–1647, 2006.
- [62] Y. He, Y. Tian, A. E. Ribbe, and C. Mao, "Highly Connected Two-Dimensional Crystals of DNA Six-Point-Stars," *Journal of American Chemical Society*, vol. 128, pp. 15 978–15 979, 2006.
- [63] E. Winfree, F. Liu, L. A. Wenzler, and N. C. Seeman, "Design and self-assembly of two-dimensional DNA crystals," *Nature*, vol. 394, pp. 539–544, 1998.
- [64] C. Mao, W. Sun, Z. Shen, and N. C. Seeman, "A nanomechanical device based on the B - Z transition of DNA," *Nature*, vol. 397, pp. 144–146, 1999.
- [65] N. C. Seeman, "Biochemistry and Structural DNA Nanotechnology : An Evolving Symbiotic Relationship," *Biochemistry*, vol. 42, no. 24, pp. 7259–7269, 2003.
- [66] W. M. Shih and C. Lin, "Knitting complex weaves with DNA origami," *Current Opinion in Structural Biology*, vol. 20, no. 3, pp. 276–282, 2010.

- [67] T. H. Labean, H. Yan, J. Kopatsch, F. Liu, E. Winfree, J. H. Reif, and N. C. Seeman, "Construction , Analysis , Ligation , and Self-Assembly of DNA Triple Crossover Complexes," *Journal of American Chemical Society*, vol. 122, no. 14, pp. 1848–1860, 2000.
- [68] X. Zhang, H. Yan, Z. Shen, and N. C. Seeman, "Paranemic Cohesion of Topologically-Closed DNA Molecules," *Journal of American Chemical Society*, vol. 124, pp. 12 940–12 941, 2002.
- [69] Y. He, Y. Chen, H. Liu, A. E. Ribbe, and C. Mao, "Self-Assembly of Hexagonal DNA Two-Dimensional (2D) Arrays," *Journal of American Chemical Society*, vol. 127, pp. 12 202–12 203, 2005.
- [70] S. Hamada and S. Murata, "Substrate-Assisted Assembly of Interconnected Single-Duplex DNA Nanostructures," *Angewandte Chemie - International Edition*, vol. 48, pp. 6820–6823, 2009.
- [71] F. Zhang, J. Nangreave, Y. Liu, and H. Yan, "Structural DNA Nanotechnology : State of the Art and Future Perspective," *Journal of American Chemical Society*, vol. 136, pp. 11 198–11 211, 2014.
- [72] P. W. K. Rothmund, "Folding DNA to create nanoscale shapes and patterns," *Nature*, vol. 440, no. 7082, pp. 297–302, 2006.
- [73] H. Yan, T. H. Labean, L. Feng, and J. H. Reif, "Directed nucleation assembly of DNA tile complexes for barcode-patterned lattices," *Proceedings of the National Academy of Sciences*, vol. 100, no. 14, pp. 8103–8108, 2003.
- [74] S. M. Douglas, A. H. Marblestone, S. Teerapittayanon, A. Vazquez, G. M. Church, and W. M. Shih, "Rapid prototyping of 3D DNA-origami shapes with caDNAno," *Nucleic Acids Research*, vol. 37, no. 15, pp. 5001–5006, 2009.
- [75] S. M. Douglas, H. Dietz, T. Liedl, B. Hogberg, F. Graf, and W. M. Shih, "Self-assembly of DNA into nanoscale three-dimensional shapes," *Nature*, vol. 459, pp. 414–418, 2009.

- [76] Y. Ke, S. M. Douglas, M. Liu, J. Sharma, A. Cheng, A. Leung, Y. Liu, W. M. Shih, and H. Yan, "Multilayer DNA origami Packed on a Square Lattice," *Journal of American Chemical Society*, vol. 131, no. 43, pp. 15 903–15 908, 2010.
- [77] H. Dietz, S. M. Douglas, and W. M. Shih, "Folding DNA into Twisted and Curved Nanoscale Shapes," *Science*, vol. 325, pp. 725–731, 2009.
- [78] D. Han, S. Pal, J. Nangreave, Z. Deng, Y. Liu, and H. Yan, "DNA Origami with Complex Curvatures in Three-Dimensional Space," *Science*, vol. 332, pp. 342–347, 2011.
- [79] C. E. Castro, F. Kilchherr, D.-n. Kim, E. L. Shiao, T. Wauer, P. Wortmann, M. Bathe, and H. Dietz, "A primer to scaffolded DNA origami," *Nature Methods*, vol. 8, no. 3, pp. 221–229, 2011.
- [80] Y. Ke, N. V. Voigt, K. V. Gothelf, and W. M. Shih, "Multilayer DNA Origami Packed on Hexagonal and Hybrid Lattices," *Journal of American Chemical Society*, vol. 134, pp. 1770–1774, 2012.
- [81] T. Hermann and D. J. Patel, "Adaptive recognition by nucleic acid aptamers," *Science*, vol. 287, no. 5454, pp. 820–825, 2000.
- [82] A. B. Kinghorn, L. A. Fraser, S. Lang, S. C. C. Shiu, and J. A. Tanner, "Aptamer bioinformatics," *International Journal of Molecular Sciences*, vol. 18, no. 12, 2017.
- [83] J. Zhou and J. Rossi, "Aptamers as targeted therapeutics: current potential and challenges," *Nature Reviews*, vol. 16, pp. 181–203, 2017.
- [84] M. Jarczewska, R. Janusz, Ł. Górski, and E. Malinowska, "Development of DNA aptamer-based sensor for electrochemical detection of C-reactive protein," *Talanta*, vol. 189, pp. 45–54, 2018.

- [85] W.-B. Lee, Y.-h. Chen, H.-I. Lin, S.-C. Shiesh, and G.-B. Lee, "An integrated microfluidic system for fast , automatic detection of C-reactive protein," *Sensors and Actuators B*, vol. 157, no. 2, pp. 710–721, 2011.
- [86] C.-J. Huang, H.-I. Lin, S.-C. Shiesh, and G.-B. Lee, "Biosensors and Bioelectronics Integrated microfluidic system for rapid screening of CRP aptamers utilizing systematic evolution of ligands by exponential enrichment (SELEX)," *Biosensors and Bioelectronics*, vol. 25, no. 7, pp. 1761–1766, 2010.
- [87] J. Piccoli, R. Hein, A. H. El-sagheer, T. Brown, E. M. Cilli, P. R. Bueno, and J. J. Davis, "Redox Capacitive Assaying of C Reactive Protein at a Peptide Supported Aptamer Interface," *Analytical Chemisry*, vol. 90, pp. 3005–3008, 2018.
- [88] Z. Lu, Y. Wang, D. Xu, and L. Pang, "Aptamer-tagged DNA origami for spatially addressable detection of aflatoxin B1," *Chemical communications*, vol. 53, pp. 941–944, 2017.
- [89] P. Wang, T. A. Meyer, V. Pan, P. K. Dutta, and Y. Ke, "The Beauty and Utility of DNA Origami," *Chem*, vol. 2, no. 3, pp. 359–382, 2017.
- [90] F. Haque, J. Li, H.-C. Wu, X.-J. Liang, and P. Guo, "Solid-State and Biological Nanopore for Real-Time Sensing of Single Chemical and Sequencing of DNA," *Nanotoday*, vol. 8, no. 1, pp. 56–74, 2013.
- [91] M. D. Graham, "The Coulter Principle : Foundation of an Industry," *Journal of the Association for Laboratory Automation*, vol. 8, no. 6, pp. 72–81, 2003.
- [92] R. W. DeBlois and C. P. Bean, "Electrokinetic Measurements with Submicron Particles and Pores by the Resistive Pulse Technique," *Journal of Colloid and Interface Science*, vol. 61, no. 2, pp. 323–335, 1977.
- [93] E. Neher and B. Sakmann, "Single-channel currents recorded from membrane of denervated frog muscle fibres." *Nature*, vol. 260, no. 5554, pp. 799–802, 1976.

- [94] J. J. Kasianowicz, E. Brandin, D. Branton, and D. W. Deamer, "Characterization of individual polynucleotide molecules using a membrane channel," *Proceedings of the National Academy of Sciences*, vol. 93, no. 24, pp. 13 770–13 773, 1996.
- [95] L. Song, M. R. Hobaugh, C. Shustak, S. Cheley, H. Bayley, and J. E. Gouaux, "Structure of staphylococcal alpha-hemolysin, a heptameric transmembrane pore." *Science (New York, N.Y.)*, vol. 274, no. 5294, pp. 1859–66, 1996.
- [96] G. Maglia, M. R. Restrepo, E. Mikhailova, and H. Bayley, "Enhanced translocation of single DNA molecules through alpha-hemolysin nanopores by manipulation of internal charge." *Proc. Natl Acad. Sci. USA*, vol. 105, no. 50, pp. 19 720–5, 2008.
- [97] W. Shi, A. K. Friedman, and L. A. Baker, "Nanopore Sensing," *Analytical Chemistry*, p. acs.analchem.6b04260, 2016.
- [98] B. Cressiot, E. Braselmann, A. Oukhaled, A. H. Elcock, J. Pelta, and P. L. Clark, "Dynamics and Energy Contributions for Transport of Unfolded Pertactin through a Protein Nanopore," *ACS Nano*, vol. 9, no. 9, pp. 9050–9061, 2015.
- [99] C. Merstorf, B. Cressiot, M. Pastoriza-Gallego, A. Oukhaled, J. M. Betton, L. Auvray, and J. Pelta, "Wild type, mutant protein unfolding and phase transition detected by single-nanopore recording," pp. 652–658, 2012.
- [100] M. Pastoriza-Gallego, L. Rabah, G. Gibrat, B. Thiebot, F. G. Van Der Goot, L. Auvray, J. M. Betton, and J. Pelta, "Dynamics of unfolded protein transport through an aerolysin pore," *Journal of the American Chemical Society*, vol. 133, no. 9, pp. 2923–2931, 2011.
- [101] M. Pastoriza-gallego, M.-F. Breton, and F.-O. Discala, "Evidence of Unfolded Protein Translocation through a Protein," *ACS Nano*, vol. 8, no. 11, pp. 11 350–11 360, 2014.
- [102] R. Stefureac, Y. T. Long, H. B. Kraatz, P. Howard, and J. S. Lee, "Transport of α -helical peptides through α -hemolysin and aerolysin pores," *Biochemistry*, vol. 45, no. 30, pp. 9172–9179, 2006.

- [103] M. A. Fahie, B. Yang, B. Pham, and M. Chen, “Tuning the Selectivity and Sensitivity of an OmpG Nanopore Sensor by Adjusting Ligand Tether Length,” *ACS Sensors*, vol. 1, no. 5, pp. 614–622, 2016.
- [104] M. Chen, Q.-H. Li, and H. Bayley, “Orientation of the monomeric porin OmpG in planar lipid bilayers,” *ChemBioChem*, vol. 9, no. 18, pp. 3029–3036, 2012.
- [105] L. Franceschini, M. Soskine, A. Biesemans, and G. Maglia, “A nanopore machine promotes the vectorial transport of DNA across membranes,” *Nature Communications*, vol. 4, no. 2415, 2013.
- [106] M. Soskine, A. Biesemans, B. Moeyaert, S. Cheley, H. Bayley, and G. Maglia, “An engineered ClyA nanopore detects folded target proteins by selective external association and pore entry,” *Nano Letters*, vol. 12, no. 9, pp. 4895–4900, 2012.
- [107] L. Franceschini, M. Soskine, A. Biesemans, and G. Maglia, “A nanopore machine promotes the vectorial transport of DNA across membranes.” *Nature communications*, vol. 4, p. 2415, 2013.
- [108] L. Franceschini, T. Brouns, K. Willems, E. Carlon, and G. Maglia, “DNA Translocation through Nanopores at Physiological Ionic Strengths Requires Precise Nanoscale Engineering,” *ACS Nano*, vol. 10, no. 9, pp. 8394–8402, 2016.
- [109] C.-Y. Fu and P. E. Prevelige Jr, “In Vitro Incorporation of the Phage Phi29 Connector Complex,” *Virology*, vol. 394, no. 1, pp. 149–153, 2009.
- [110] D. Wendell, P. Jing, J. Geng, V. Subramaniam, T. J. Lee, C. Montemagno, and P. Guo, “Translocation of Double-stranded DNA through membrane-adapted phi29 motor protein nanopores,” *Nature Nanotechnology*, vol. 4, no. September, pp. 765–772, 2009.
- [111] G. M. Cherf, K. R. Lieberman, H. Rashid, C. E. Lam, K. Karplus, and M. Akeson, “Automated Forward and Reverse Ratcheting of DNA in a Nanopore at Five Angstrom Precision,” *Nature Biotechnology*, vol. 30, no. 4, pp. 344–348, 2012.

- [112] T. Deng, M. Li, Y. Wang, and Z. Liu, "Development of solid-state nanopore fabrication technologies," *Science Bulletin*, vol. 60, no. 3, pp. 304–319, 2015.
- [113] Z. Yuan, C. Wang, X. Yi, Z. Ni, Y. Chen, and T. Li, "Solid-State Nanopore," *Nanoscale Research Letters*, vol. 13:56, pp. 1–10, 2018.
- [114] C. Dekker, "Solid-state nanopores," *Nature nanotechnology*, vol. 2, no. 4, pp. 209–215, 2007.
- [115] Z. Tang, D. Zhang, and W. Cui, "Fabrications , Applications and Challenges of Solid-state Nanopores : A Mini Review," *Nanomaterials and Nanotechnology*, no. 6, 2016.
- [116] C. C. Harrell, Y. Choi, L. P. Horne, L. A. Baker, Z. S. Siwy, and C. R. Martin, "Resistive-Pulse DNA Detection with a Conical Nanopore Sensor," *Langmuir*, no. 22, pp. 10 837–10 843, 2006.
- [117] P. Y. Apel, I. V. Blonskaya, S. N. Dmitriev, O. L. Orelvitch, A. Presz, and B. A. Sartowska, "Fabrication of nanopores in polymer foils with surfactant-controlled longitudinal profiles," *Nanotechnology*, pp. 3 053 021–7, 2007.
- [118] A. J. Storm, J. H. Chen, X. S. Ling, H. W. Zandbergen, and C. Dekker, "Fabrication of solid-state nanopores with single-nanometre precision," *Nature Materials*, vol. 2, no. 8, pp. 537–540, 2003.
- [119] A. Han, G. Schürmann, G. Mondin, R. A. Bitterli, N. G. Hegelbach, N. G. Hegelbach, N. F. D. Rooij, and U. Staufer, "Sensing protein molecules using nanofabricated pores," *Applied Physics Letters*, vol. 88, pp. 0 939 011–3, 2006.
- [120] J. Bai, D. Wang, S.-w. Nam, H. Peng, R. Bruce, L. Gignac, M. Brink, E. Kratschmer, S. Rossnagel, P. Waggoner, K. Reuter, C. Wang, Y. Astier, V. Balagurusamy, B. Luan, Y. Kwark, E. Joseph, M. Guillorn, S. Polonsky, A. Royyuru, S. Papa, and G. Stolovitzky, "Fabrication of sub-20 nm nanopore arrays in membranes with embedded metal electrodes at wafer scales," *Nanoscale*, vol. 6, pp. 8900–8906, 2014.

- [121] J. Li, D. Stein, C. McMullan, D. Branton, M. J. Aziz, and J. A. Golovchenko, “Ion-beam sculpting at nanometre length scales,” *Nature*, vol. 412, no. 6843, pp. 166–169, 2001.
- [122] R. Kox, C. Chen, and G. Maes, “Shrinking solid-state nanopores using electron-beam-induced deposition,” *Nanotechnology*, no. 20, 2009.
- [123] B. Min, J. Kim, M. Wanunu, D. C. Bell, and A. Meller, “Rapid Fabrication of Uniformly Sized Nanopores and Nanopore Arrays for Parallel DNA Analysis **,” *Advanced materials*, no. 18, pp. 3149–3153, 2006.
- [124] C. Danelon, C. Santschi, and H. Vogel, “Fabrication and Functionalization of Nanochannels by Electron-Beam-Induced Silicon Oxide Deposition ,” *Langmuir*, no. 21, pp. 10711–10715, 2007.
- [125] W. Zhang, Y. Wang, J. Li, J. Xue, H. Ji, Q. Ouyang, J. Xu, and Y. Zhang, “Controllable shrinking and shaping of silicon nitride nanopores under electron irradiation,” *Applied Physics Letters*, vol. 90, pp. 1631021–3, 2007.
- [126] S. Wu, F. Cao, H. Zheng, H. Sheng, C. Liu, Y. Liu, D. Zhao, and J. Wang, “Fabrication of faceted nanopores in magnesium,” *Applied Physics Letters*, vol. 103, no. December 2013, pp. 2431011–3, 2013.
- [127] J. A. Rodriguez-Manzo, M. Puster, A. Nicolai, V. Meunier, and M. Drndic, “DNA Translocation in Nanometer Thick Silicon Nanopores,” *ACS Nano*, vol. 9, no. 6, pp. 6555–6564, 2015.
- [128] P. Chen, T. Mitsui, D. B. Farmer, J. Golovchenko, R. G. Gordon, and D. Branton, “Atomic Layer Deposition to Fine-Tune the Surface Properties and Diameters of Fabricated Nanopores,” *Nano Letters*, vol. 4, no. 7, pp. 1333–1337, 2004.
- [129] M. Mayer, J. K. Kriebel, M. T. Tosteson, and G. M. Whitesides, “Microfabricated Teflon Membranes for Low-Noise Recordings of Ion Channels in Planar Lipid Bilayers,” *Biophysical Journal*, vol. 85, no. 4, pp. 2684–2695, 2003.

- [130] N. Fertig, M. Klau, M. George, R. H. Blick, and J. C. Behrends, “Activity of single ion channel proteins detected with a planar microstructure,” *Applied Physics Letters*, vol. 81, p. 4865, 2002.
- [131] R. J. White, E. N. Ervin, T. Yang, X. Chen, S. Daniel, P. S. Cremer, and H. S. White, “Single Ion-Channel Recordings Using Glass Nanopore Membranes,” *Journal of American Chemical Society*, vol. 129, no. 38, pp. 11 766–11 775, 2007.
- [132] A. R. Hall, A. Scott, D. Rotem, K. K. Mehta, H. Bayley, and C. Dekker, “Hybrid pore formation by directed insertion of a -haemolysin into solid-state nanopores,” *Nature Nanotechnology*, vol. 5, no. 12, pp. 874–877, 2010.
- [133] S. Hernández-Ainsa, N. A. W. Bell, V. V. Thacker, K. Göpfrich, K. Misiunas, M. E. Fuentes-Perez, F. Moreno-Herrero, and U. F. Keyser, “DNA origami nanopores for controlling DNA translocation,” *ACS Nano*, vol. 7, no. 7, pp. 6024–6030, 2013.
- [134] N. A. W. Bell, C. R. Engst, M. Ablay, G. Divitini, C. Ducati, T. Liedl, and U. F. Keyser, “DNA origami nanopores,” *Nano Letters*, vol. 12, no. 1, pp. 512–517, 2012.
- [135] R. Wei, T. G. Martin, U. Rant, and H. Dietz, “DNA Origami Gatekeepers for Solid-State Nanopores,” *Angewandte Chemie - International Edition*, vol. 51, pp. 4864–4867, 2012.
- [136] K. Göpfrich, C.-Y. Li, M. Ricci, S. P. Bhamidimarri, J. Yoo, B. Gyenes, A. Ohmann, M. Winterhalter, A. Aksimentiev, and U. F. Keyser, “Large-Conductance Transmembrane Porin Made from DNA Origami,” *ACS Nano*, p. acsnano.6b03759, 2016.
- [137] N. A. W. Bell, V. V. Thacker, S. Hernandez-Anisa, M. E. Fuentes-Perez, F. Moreno-herrero, T. Liedl, and U. F. Keyser, “Multiplexed ionic current sensing with glass nanopores,” *Lab Chip*, vol. 13, pp. 1859–1862, 2013.
- [138] J. R. Burns, K. Göpfrich, J. W. Wood, V. V. Thacker, E. Stulz, U. F. Keyser, and S. Howorka, “Lipid-Bilayer-Spanning DNA Nanopores with a Bifunctional

- Porphyrin Anchor,” *Angewandte Chemie - International Edition*, vol. 52, pp. 12 069–12 072, 2013.
- [139] J. R. Burns, E. Stulz, and S. Howorka, “Self-Assembled DNA Nanopores That Span Lipid Bilayers,” *Nano Letters*, vol. 13, pp. 2351–2356, 2013.
- [140] J. R. Burns, A. Seifert, N. Fertig, and S. Howorka, “A biomimetic DNA-based channel for the ligand-controlled transport of charged molecular cargo across a biological membrane.” *Nature nanotechnology*, vol. advance on, no. 2, pp. 1–16, 2016.
- [141] M. Langecker, V. Arnaut, T. G. Martin, J. List, S. Renner, M. Mayer, H. Dietz, and F. C. Simmel, “Synthetic Lipid Membrane Channels formed by designed DNA nanostructures,” *Science*, vol. 338, no. 6109, pp. 932–936, 2012.
- [142] S. M. Iqbal, D. Akin, and R. Bashir, “Solid-state nanopore channels with DNA selectivity,” *Nature Nanotechnology*, vol. 2, pp. 243–248, 2007.
- [143] S. Zhang, M. Li, B. Su, and Y. Shao, “Fabrication and Use of Nanopipettes in Chemical Analysis,” *Annual Review of Analytical Chemistry*, vol. 11, no. 1, pp. 265–286, 2018.
- [144] B. M. Kim, T. Murray, and H. H. Bau, “The fabrication of integrated carbon pipes with sub-micron diameters,” *Nanotechnology*, vol. 16, no. 8, pp. 1317–1320, 2005.
- [145] J. R. Freedman, D. Mattia, G. Korneva, Y. Gogotsi, G. Friedman, and A. K. Fontecchio, “Magnetically assembled carbon nanotube tipped pipettes,” *Applied Physics Letters*, vol. 90, pp. 103 108–103 110, 2007.
- [146] C. A. Morris, A. K. Friedman, and L. A. Baker, “Applications of nanopipettes in the analytical sciences,” *Analyst*, vol. 135, pp. 2190–2202, 2010.
- [147] L. Ying, “Applications of nanopipettes in bionanotechnology.” *Biochemical Society transactions*, vol. 37, pp. 702–706, 2009.

- [148] J. L. Rae and R. A. Levis, "A method for exceptionally low noise single channel recordings," *European Journal of Physiology*, vol. 420, pp. 618–620, 1992.
- [149] R. A. Levis and J. L. Rae, "The Use of Quartz Patch Pipettes for Low Noise Single Channel Recording," *Biophysical Journal*, vol. 65, no. 4, pp. 1666–1677, 1993.
- [150] J.-L. Munoz and J. A. Coles, "Quartz micropipettes for intracellular voltage microelectrodes and ion-selective," *Journal of Neuroscience Methods*, vol. 22, pp. 57–64, 1987.
- [151] N. Sa and L. Baker, "Experiment and Simulation of Ion Transport through Nanopipettes of Well-Defined Conical Geometry," *Journal of The Electrochemical Society*, vol. 160, no. 6, pp. H376–H381, 2013.
- [152] J. A. Bafna and G. V. Soni, "Fabrication of Low Noise Borosilicate Glass Nanopores for Single Molecule Sensing," *Plos One*, vol. 11, no. 6, p. e0157399, 2016.
- [153] M. A. Barber, "A new method of isolating micro-organisms," *Journal of Kansas Medical Society*, vol. 4, pp. 489–494, 1904.
- [154] M. A. Barber, "A technic for the inoculation of bacteria and other substances into living cells," *Journal of Infectious diseases*, vol. 8, pp. 348–360, 1911.
- [155] M. A. Barber, "The Pipette Method in the Isolation of Single Micro-organisms and in the Inoculation of Substances Into Living Cells: With a Technique for Dissection, Staining and Other Processes Carried Out Under the Higher Powers of the Microscope," *Philiphine journal of science*, vol. 9, pp. 307–360, 1914.
- [156] G. L. Kite, "The nature of the fertilization membrane of the egg of the sea urchin (*Arbacia punctulata*)," *Science*, vol. 36, pp. 562–564, 1912.
- [157] G. L. Kite, "Studies on the physical properties of the protoplasm," *American Journal of Physiology*, vol. 32, pp. 146–164, 1913.

- [158] G. L. Kite, "Studies on the permeability of the internal cytoplasm of animal and plant cells." *American Journal of Physiology*, vol. 37, pp. 282–299, 1915.
- [159] C. Taylor, "An accurately controllable micropipette," *Science*, vol. 51, pp. 617–618, 1920.
- [160] R. Chambers, "New apparatus and methods for the dissection and injection of living cells," *The Anatomical Record*, vol. 24, pp. 1–19, 1922.
- [161] R. Chambers, "The microvivisection method," *biology bull*, vol. 34, pp. 121–136, 1918.
- [162] I. Hyde, "A micro-electrode and unicellular stimulation." *biology bull*, vol. 40, pp. 130–133, 1921.
- [163] W. J. V. Osterhout, "On the importance of maintaining certain differences between cell sap and external medium," *Journal of general physiology*, vol. 7, pp. 561–564, 1925.
- [164] W. J. V. Osterhout, E. B. Damon, and A. G. Jacques, "Dissimilarity of inner and outer protoplasmic surfaces in valonia," *The Journal of General Physiology*, pp. 193–205, 1927.
- [165] W. J. V. Osterhout, "physiological studies of single plant cells," *Biological Reviews Cambridge Philisophical Society*, vol. 6, pp. 369–411, 1931.
- [166] E. Damon, "Dissimilarity of inner and outer protoplasmic surfaces in Valonia II," *The Journal of General Physiology*, vol. 13, pp. 207–221, 1929.
- [167] C. Taylor, "Microelectrodes and Micromagnets," *Proceedings of the Society for Experiemental Biology and Medicine*, vol. 23, no. 2, pp. 147–150, 1925.
- [168] C. V. Taylor and D. M. Whitaker, "Potentiometric determinations in the protoplasm and cell-sap of Nitella," *Protoplasma*, vol. 3, pp. 1–6, 1927.

- [169] L. R. Blinks, "Protoplasmic potentials in Halicystis," *The Journal of General Physiology*, no. 28, pp. 223–229, 1929.
- [170] S. Gelfan and R. W. Gerard, "Studies of single muscle fibres: II. A further analysis of the grading mechanism," *American Journal of Physiology*, vol. 95, pp. 412–416, 1930.
- [171] J. Graham, G. R. Carlson, and R. W. Gerard, "Membrane and injury potentials of single muscle fibers," in *Fed. Proc*, vol. 1, no. Part II, 1942, p. 31.
- [172] J. Graham and R. W. Gerard, "Membrane potentials and excitation of impaled single muscle fibers," *Journal of Cellular Physiology*, vol. 28, pp. 99–117, 1946.
- [173] G. Ling and R. Gerard, "The normal membrane potential of frog sartorius fibers," *Journal of Cellular Physiology*, vol. 34, pp. 383–396, 1949.
- [174] A. L. Hodgkin and W. L. Nastuk, "Membrane potentials in single fibres of the frog's sartorius muscle." *The Journal of physiology*, vol. 108, no. 3, pp. Proc–42, 1949.
- [175] W. L. Nastuk and A. L. Hodgkin, "The electrical activity of single muscle fibers," *Journal of Cellular Physiology*, vol. 35, pp. 39–73, 1950.
- [176] J. Alexander and W. L. Nastuk, "An Instrument for the Production of Microelectrodes Used in Electrophysiological Studies," *Review of Scientific Instruments*, vol. 24, pp. 528–531, 1953.
- [177] K. T. Brown and D. G. Flaming, *Advanced micropipette techniques for cell physiology*, ser. IBRO handbook series:Methods in the Neurosciences Vol9. Wiley, Chichester, UK, 1986.
- [178] K. T. Brown and D. G. Flaming, "New microelectrode technique for intracellular work in small cells," *Neuroscience*, vol. 2, no. 6, pp. 813–827, 1977.

- [179] D. Ammann, *Ion-Selective Microelectrodes: Principles, Design and Application*, ser. Advances in Experimental Medicine and Biology. Springer Berlin Heidelberg, 2013.
- [180] T. Solomon and A. J. Bard, "Scanning Electrochemical Microscopy . 30 . Application of Glass Micropipet Tips and Electron Transfer at the Interface between Two Immiscible Electrolyte Solutions for SECM Imaging," *Analytical Chemistry*, vol. 67, pp. 2787–2790, 1995.
- [181] C. Wei, A. J. Bard, and S. W. Feldberg, "Current Rectification at Quartz Nanopipet Electrodes," *Analytical Chemistry*, vol. 69, no. 22, pp. 4627–4633, 1997.
- [182] A. J. Bard, F.-r. F. Fan, D. T. Pierce, P. R. Unwin, D. Wipf, and F. Zhou, "Chemical Imaging of Surfaces with the Scanning Electrochemical Microscope," *Science*, vol. 254, pp. 68–73, 1991.
- [183] Y. Shao and M. V. Mirkin, "Scanning electrochemical microscopy (SECM) of facilitated ion transfer at the liquid/liquid interface." *Journal of Electroanalytical Chemistry*, vol. 439, pp. 137–143, 1997.
- [184] P. Hansma, B. Drake, O. Marti, S. Gould, and C. Prater, "The scanning ion-conductance microscope," *Science*, vol. 243, no. 4891, pp. 641–3, 1989.
- [185] P. Sun, Z. Zhang, Z. Gao, and Y. Shao, "Probing Fast Facilitated Ion Transfer across an Externally Polarized Liquid-Liquid Interface by Scanning Electrochemical Microscopy," *Angewandte Chemie - International Edition*, vol. 41, pp. 3595–3598, 2002.
- [186] A. I. Shevchuk, G. I. Frolenkov, D. Sanchez, P. S. James, N. Freedman, R. Jones, D. Klenerman, and Y. E. Korchev, "Imaging Proteins in Membranes of Living Cells by High-Resolution Scanning Ion Conductance Microscopy," *Angewandte Chemie - International Edition*, vol. 45, pp. 2212–2216, 2006.
- [187] P. Novak, C. Li, A. I. Shevchuk, R. Stepanyan, M. Caldwell, S. Hughes, T. G. Smart, J. Gorelik, V. P. Ostanin, M. J. Lab, G. W. J. Moss, G. I. Frolenkov,

- D. Klenerman, and Y. E. Korchev, "Nanoscale live cell imaging using hopping probe ion conductance microscopy," *Nature Methods*, vol. 6, no. 4, pp. 279–281, 2009.
- [188] Y. Takahashi, A. I. Shevchuk, P. Novak, Y. Murakami, H. Shiku, Y. E. Korchev, and T. Matsue, "Simultaneous Noncontact Topography and Electrochemical Imaging by SECM / SICM Featuring Ion Current Feedback Regulation," *Journal of American Chemical Society*, vol. 132, pp. 10 118–10 126, 2010.
- [189] A. M. Rothery, J. Gorelik, A. Bruckbauer, W. Yu, Y. E. Korchev, and D. Klenerman, "A novel light source for SICM SNOM of living cells," *Journal of Microscopy*, vol. 209, no. Pt 2, pp. 94–101, 2003.
- [190] R. Brunner, O. Hering, O. Marti, and O. Hollricher, "Piezoelectrical shear-force control on soft biological samples in aqueous solution," *Applied Physics Letters*, vol. 71, pp. 3628–3630, 1997.
- [191] R. Proksch, R. Lal, P. K. Hansma, D. Morse, and G. Stucky, "Imaging the internal and external pore structure of membranes in fluid: TappingMode scanning ion conductance microscopy," *Biophysical Journal*, vol. 71, no. 4, pp. 2155–2157, 1996.
- [192] G. Binnig and C. F. Quate, "Atomic Force Microscope," *Physical Review Letters*, vol. 56, no. 9, pp. 930–933, 1986.
- [193] A. Bruckbauer, L. Ying, A. M. Rothery, D. Zhou, A. I. Shevchuk, C. Abell, Y. E. Korchev, and D. Klenerman, "Writing with DNA and protein using a nanopipet for controlled delivery," *Journal of the American Chemical Society*, vol. 124, no. 30, pp. 8810–8811, 2002.
- [194] E. W. Froede and M. Rothenberger, "Past , Present , and Future : Nanopipette Applications to Single Cell Analysis," 2011.
- [195] *P - 2000 Laser based micropipette puller system Operation Manual*. Sutter Instrument Company, 2010, vol. Rev 2.2.

- [196] N. Laohakunakorn and U. F. Keyser, "Electroosmotic flow rectification in conical nanopores," *Nanotechnology*, vol. 26, no. 275202, 2015.
- [197] Y. Wang, D. Wang, M. V. Mirkin, and M. V. Mirkin, "Resistive-pulse and rectification sensing with glass and carbon nanopipettes Review Subject Areas : Author for correspondence :," *Proc.R.Soc. A*, vol. 473, no. 20160931, 2017.
- [198] D. Hlushkou, J. M. Perry, S. C. Jacobson, and U. Tallarek, "Propagating concentration polarization and ionic current rectification in a nanochannel-nanofunnel device," *Analytical Chemistry*, vol. 84, no. 1, pp. 267–274, 2012.
- [199] A. J. Bard and L. R. Faulkner, *Electrochemical methods: Fundamentals and Applications*. John Wiley & Sons, Inc., 2001.
- [200] J. B. Edel and T. Albrecht, *Engineered Nanopores for Bioanalytical Applications*. Elsevier Inc., 2013.
- [201] L. Yates D and H. T. S, "Site-Binding model of the electrical double layer at the oxide/water interface," *J Chem Soc Faraday Trans*, vol. 70, pp. 1807–1818, 1974.
- [202] Z. Siwy, E. Heins, C. C. Harrell, P. Kohli, and C. R. Martin, "Conical-Nanotube Ion-Current Rectifiers : The Role of Surface Charge," *Journal of American Chemical Society*, vol. 126, pp. 10 850–10 851, 2004.
- [203] S. m. Lu and Y. t. Long, "Confined Nanopipette - A new microfluidic Approach for Single cell analysis," *TrAC - Trends in Analytical Chemistry*, vol. 117, pp. 39–46, 2019.
- [204] N. Sa, W. J. Lan, W. Shi, and L. A. Baker, "Rectification of ion current in nanopipettes by external substrates," *ACS Nano*, vol. 7, no. 12, pp. 11 272–11 282, 2013.
- [205] K. McKelvey, S. L. Kinnear, D. Perry, D. Momotenko, and P. R. Unwin, "Surface charge mapping with a nanopipette," *Journal of the American Chemical Society*, vol. 136, no. 39, pp. 13 735–13 744, 2014.

- [206] W. Shi, N. Sa, R. Thakar, and L. A. Baker, "Nanopipette delivery: influence of surface charge," *The Analyst*, vol. 140, no. 14, pp. 4835–4842, 2015.
- [207] R. M. M. Smeets, U. F. Keyser, D. Krapf, M. Y. Wu, N. H. Dekker, and C. Dekker, "Salt dependence of ion transport and DNA translocation through solid-state nanopores," *Nano Letters*, vol. 6, no. 1, pp. 89–95, 2006.
- [208] M. Wanunu, "Nanopores : A journey towards DNA sequencing," *Physics of Life Reviews*, vol. 9, no. 2, pp. 125–158, 2012.
- [209] N. Calander, "Analyte Concentration at the Tip of a Nanopipette," *Analytical Chemistry*, vol. 81, no. 20, pp. 8347–8353, 2009.
- [210] Q. Liu, H. Wu, L. Wu, X. Xie, J. Kong, X. Ye, and L. Liu, "Voltage-Driven Translocation of DNA through a High Throughput Conical Solid-State Nanopore," *PLoS ONE*, vol. 7, no. 9, pp. 1–9, 2012.
- [211] R. W. Clarke, S. S. White, D. Zhou, L. Ying, and D. Klenerman, "Trapping of proteins under physiological conditions in a nanopipette," *Angewandte Chemie - International Edition*, vol. 44, no. 24, pp. 3747–3750, 2005.
- [212] L. Shi, A. Rana, and L. Esfandiari, "A low voltage nanopipette dielectrophoretic device for rapid entrapment of nanoparticles and exosomes extracted from plasma of healthy donors," *Scientific Reports*, pp. 1–12, 2018.
- [213] S. Ghosal, "Effect of Salt Concentration on the Electrophoretic Speed of a Polyelectrolyte through a Nanopore," *Physical Review Letters*, vol. 98, no. 238104, 2007.
- [214] W. Shi, A. K. Friedman, and L. A. Baker, "Nanopore Sensing," *Analytical Chemistry*, vol. 89, pp. 157–188, 2017.
- [215] D. Pedone, M. Firnkies, and U. Rant, "Data Analysis of Translocation Events in Nanopore Experiments," *Analytical Chemistry*, vol. 81, pp. 9689–9694, 2009.

- [216] C. Plesa, S. W. Kowalczyk, R. Zinsmeister, A. Y. Grosberg, Y. Rabin, and C. Dekker, "Fast Translocation of Proteins through Solid State Nanopores," *Nano Letters*, vol. 13, pp. 658–663, 2013.
- [217] J. Larkin, R. Y. Henley, M. Muthukumar, J. K. Rosenstein, and M. Wanunu, "High-Bandwidth Protein Analysis Using Solid-State Nanopores," *Biophysical Journal*, vol. 106, no. 3, pp. 696–704, 2014.
- [218] M. Karhanek, J. T. Kemp, N. Pourmand, R. W. Davis, and C. D. Webb, "Single DNA molecule detection using nanopipettes and nanoparticles," *Nano Letters*, vol. 5, no. 2, pp. 403–407, 2005.
- [219] E. C. Yusko, J. M. Johnson, S. Majd, P. Prangkio, R. C. Rollings, J. Li, J. Yang, and M. Mayer, "Controlling protein translocation through nanopores with bio-inspired fluid walls," *Nature Nanotechnology*, vol. 6, pp. 253–260, 2011.
- [220] S. Ding, C. Gao, and L.-q. Gu, "Capturing Single Molecules of Immunoglobulin and Ricin with an Aptamer-Encoded Glass Nanopore," *Analytical Chemistry*, vol. 81, pp. 6649–6655, 2009.
- [221] Z. Siwy, L. Trofin, P. Kohli, L. A. Baker, C. Trautmann, and C. R. Martin, "Protein Biosensors Based on Biofunctionalized Conical Gold Nanotubes," *Journal of American Chemical Society*, vol. 127, pp. 5000–5001, 2005.
- [222] R. Wei, V. Gatterdam, R. Wieneke, R. Tampe, and U. Rant, "Stochastic sensing of proteins with receptor-modified solid-state nanopores," *Nature nanotechnology*, vol. 7, pp. 257–263, 2012.
- [223] C. Wang, Q. Fu, X. Wang, D. Kong, Q. Sheng, Y. Wang, Q. Chen, and J. Xue, "Atomic Layer Deposition Modified Track-Etched Conical Nanochannels for Protein Sensing," *Analytical Chemistry*, vol. 87, pp. 8227–8233, 2015.
- [224] D. I. Cherny, A. Fourcade, F. Svinarchuk, P. E. Nielsen, C. Malvy, and E. Delain, "Analysis of Various Sequence-Specific Triplexes by Electron and Atomic Force Microscopies," *Biophysical Journal*, vol. 74, pp. 1015–1023, 1998.

- [225] X. Lin, A. P. Ivanov, and J. B. Edel, "Selective single molecule nanopore sensing of proteins using DNA aptamer-functionalised gold nanoparticles," *Chem. Sci.*, vol. 8, no. 5, pp. 3905–3912, 2017.
- [226] R. J. Yu, Y. L. Ying, Y. X. Hu, R. Gao, and Y. T. Long, "Label-Free Monitoring of Single Molecule Immunoreaction with a Nanopipette," *Analytical Chemistry*, vol. 89, no. 16, pp. 8203–8206, 2017.
- [227] S. Hernández-ainsa and U. F. Keyser, "DNA origami nanopores: developments, challenges and perspectives," *Nanoscale*, vol. 6, pp. 14 121–14 132, 2014.
- [228] L. M. Hellman and M. G. Fried, "Electrophoretic Mobility Shift Assay (EMS) for detecting Protein-Nucleic Acid Interactions," *Nature protocols*, vol. 2, no. 8, pp. 1849–1861, 2007.
- [229] Y. Tang, X. Zeng, and J. Liang, "Surface Plasmon Resonance: An Introduction to a Surface Spectroscopy Technique," *J Chem Educ*, vol. 87, no. 7, pp. 742–746, 2010.
- [230] D. Perry, D. Momotenko, R. A. Lazenby, M. Kang, and P. R. Unwin, "Characterization of Nanopipettes," *Analytical Chemistry*, vol. 88, no. 10, pp. 5523–5530, 2016.
- [231] J. Rheinlaender and T. E. Schäffer, "Image formation, resolution, and height measurement in scanning ion conductance microscopy," *Journal of Applied Physics*, vol. 105, no. 9, p. 094905, 2009.
- [232] Y. Takahashi, K. Ito, X. Wang, Y. Matsumae, H. Komaki, A. Kumatani, K. Ino, H. Shiku, and T. Matsue, "Nanoscale Cell Surface Topography Imaging using Scanning Ion Conductance Microscopy," *Electrochemistry*, vol. 82, no. 5, pp. 331–334, 2014.
- [233] D. Perry, R. Al Botros, D. Momotenko, S. L. Kinnear, and P. R. Unwin, "Simultaneous Nanoscale Surface Charge and Topographical Mapping," *ACS Nano*, vol. 9, no. 7, pp. 7266–7276, 2015.

- [234] A. I. Shevchuk, G. I. Frolenkov, D. Sánchez, P. S. James, N. Freedman, M. J. Lab, R. Jones, D. Klenerman, and Y. E. Korchev, “Imaging proteins in membranes of living cells by high-resolution scanning ion conductance microscopy,” *Angewandte Chemie - International Edition*, vol. 45, no. 14, pp. 2212–2216, 2006.
- [235] E. M. Yuill, W. Shi, J. Poehlman, and L. A. Baker, “Scanning Electrospray Microscopy with Nanopipets,” *Analytical Chemistry*, vol. 87, no. 22, pp. 11 182–11 186, 2015.
- [236] D. Sánchez, N. Johnson, C. Li, P. Novak, J. Rheinlaender, Y. Zhang, U. Anand, P. Anand, J. Gorelik, G. I. Frolenkov, C. Benham, M. Lab, V. P. Ostanin, T. E. Schäffer, D. Klenerman, and Y. E. Korchev, “Noncontact measurement of the local mechanical properties of living cells using pressure applied via a pipette.” *Biophysical journal*, vol. 95, no. 6, pp. 3017–27, 2008.
- [237] S. Del Linz, E. Willman, M. Caldwell, D. Klenerman, A. Fernández, and G. Moss, “Contact-free scanning and imaging with the scanning ion conductance microscope,” *Analytical Chemistry*, vol. 86, no. 5, pp. 2353–2360, 2014.
- [238] A. P. Ivanov, P. Actis, P. Jönsson, D. Klenerman, Y. Korchev, and J. B. Edel, “On-demand delivery of single DNA molecules using nanopipets,” *ACS Nano*, vol. 9, no. 4, pp. 3587–3594, 2015.
- [239] N. A. Bell, K. Chen, S. Ghosal, M. Ricci, and U. F. Keyser, “Asymmetric dynamics of DNA entering and exiting a strongly confining nanopore,” *Nature Communications*, vol. 8, no. 1, pp. 1–8, 2017.
- [240] V. Wang, N. Ermann, and U. F. Keyser, “Current Enhancement in Solid-State Nanopores Depends on Three-Dimensional DNA Structure,” *Nano Letters*, vol. 19, pp. 5661–5666, 2019.
- [241] S. Stretton, S. Techkarnjanaruk, A. M. McLennan, and A. E. Goodman, “Use of green fluorescent protein to tag and investigate gene expression in marine bacteria,” *Applied and Environmental Microbiology*, vol. 64, no. 7, pp. 2554–2559, 1998.

- [242] S. V. Dorp, U. F. Keyser, N. H. Dekker, C. Dekker, and S. G. Lemay, "Origin of the electrophoretic force on DNA in solid-state nanopores," *Nature Physics*, vol. 5, no. 5, pp. 347–351, 2009.
- [243] P. Chen, J. Gu, E. Brandin, Y.-R. Kim, Q. Wang, and D. Branton, "Probing single DNA molecule transport using fabricated nanopores," *Nano Letters*, vol. 4, no. 11, pp. 2293–2298, 2004.
- [244] M. A. Alibakhshi, J. R. Halman, J. Wilson, A. Aksimentiev, K. A. Afonin, and M. Wanunu, "Picomolar Fingerprinting of Nucleic Acid Nanoparticles Using Solid-State Nanopores," *ACS Nano*, vol. 11, no. 10, pp. 9701–9710, 2017.
- [245] Z. Zhu, Y. Zhou, X. Xu, R. Wu, Y. Jin, and B. Li, "Adaption of a Solid-State Nanopore to Homogeneous DNA Organization Verification and Label-Free Molecular Analysis without Covalent Modification," *Analytical Chemistry*, vol. 90, pp. 814–820, 2018.
- [246] P. Ketterer, A. N. Ananth, D. S. Laman Trip, A. Mishra, E. Bertolin, M. Ganji, J. Van Der Torre, P. Onck, H. Dietz, and C. Dekker, "DNA origami scaffold for studying intrinsically disordered proteins of the nuclear pore complex," *Nature Communications*, vol. 9, no. 1, pp. 1–8, 2018.
- [247] Y. Zhang, M. A. Edwards, S. R. German, and H. S. White, "Multipass Resistive-Pulse Observations of the Rotational Tumbling of Individual Nanorods," *The Journal of Physical Chemistry*, vol. 120, pp. 20781–20788, 2016.
- [248] L. J. Steinbock, O. Otto, C. Chimere, J. Gornall, and U. F. Keyser, "Detecting DNA folding with nanocapillaries," *Nano Letters*, vol. 10, no. 7, pp. 2493–2497, 2010.
- [249] M. M. Ali, F. Li, Z. Zhang, K. Zhang, D.-K. Kang, J. A. Ankrum, X. C. Le, and W. Zhao, "Rolling circle amplification: a versatile tool for chemical biology, materials science and medicine," *Chem Soc Rev*, vol. 43, pp. 3324–3341, 2014.

- [250] C. Ducani, C. Kaul, M. Moche, W. M. Shih, and B. Högberg, “Enzymatic production of monochromic stoichiometric single-stranded DNA oligonucleotides,” *Nature methods*, vol. 10, no. 7, pp. 647–652, 2013.
- [251] M. Erkelenz, D. M. Bauer, R. Meyer, C. Gatsogiannis, S. Raunser, B. Saccà, and C. M. Niemeyer, “A Facile Method for Preparation of Tailored Scaffolds for DNA-Origami,” *small*, vol. 10, no. 1, pp. 73–77, 2014.
- [252] B. Kick, F. Praetorius, H. Dietz, and D. Weuster-botz, “Efficient Production of Single-Stranded Phage DNA as Scaffolds for DNA Origami,” *Nano Letters*, vol. 15, no. 7, pp. 4672–4676, 2015.
- [253] L. Chasteen, J. Ayriss, P. Pavlik, and A. R. Bradbury, “Eliminating helper phage from phage display,” *Nucleic Acids Research*, vol. 34, no. 21, pp. 1–11, 2006.
- [254] S. Fischer, C. Hartl, K. Frank, J. O. Rädler, T. Liedl, and B. Nickel, “Shape and inter-helical spacing of DNA origami nanostructures studied by small angle X-ray scattering,” *Nano Letters*, vol. 16, no. 7, pp. 4282–4287, 2019.
- [255] P. W. Rothmund, “Design of DNA origami,” *IEEE/ACM International Conference on Computer-Aided Design, Digest of Technical Papers, ICCAD*, vol. 2005, pp. 470–477, 2005.
- [256] M. B. Pepys and G. M. Hirschfield, “C-reactive protein: a critical update,” *Journal of clinical Investigation*, vol. 111, pp. 1805–1812, 2003.
- [257] A. J. Lee, M. Endo, J. K. Hobbs, and C. Wälti, “Direct Single-Molecule Observation of Mode and Geometry of RecA-Mediated Homology Search,” *ACS Nano*, vol. 12, no. 1, pp. 272–278, 2018.
- [258] T. W. D. Clos and C. Mold, “C-Reactive Protein An Activator of innate immunity and a modulator of adaptive immunity,” *Immunologic Research*, vol. 30, no. 3, pp. 261–277, 2004.

- [259] C. Kielar, Y. Xin, B. Shen, M. A. Kostianen, G. Grundmeier, V. Linko, and A. Keller, “On the Stability of DNA Origami Nanostructures in Low-Magnesium Buffers,” *Angewandte Chemie - International Edition*, vol. 57, no. 30, pp. 9470–9474, 2018.
- [260] S. Ramakrishnan, H. Ijäs, V. Linko, and A. Keller, “Structural stability of DNA origami nanostructures under application-specific conditions,” *Computational and Structural Biotechnology Journal*, vol. 16, pp. 342–349, 2018.
- [261] J. Zenk, C. Tuntivate, and R. Schulman, “Kinetics and Thermodynamics of Watson Crick Base Pairing Driven DNA origami Dimerization,” *Journal of American Chemical Society*, vol. 138, pp. 3346–3354, 2016.